

Supernova / Acceleration Probe (SNAP)

An Experiment to Measure the Properties of the
Accelerating Universe

A Science Proposal to the Department of Energy
and the National Science Foundation

The Institutions of the SNAP Collaboration

University of California, Berkeley, CA
Lawrence Berkeley National Laboratory, Berkeley, CA
LPNHE, CNRS-IN2P3 and University Paris VI & VII, Paris, France
University of Maryland, College Park, MD
California Institute of Technology, Pasadena, CA
University of Chicago, Chicago, IL
Space Telescope Sciences Institute, Baltimore, MD
Cornell University, Ithaca, NY
University of Stockholm, Sweden
Institute for Astronomy, University of Edinburgh, UK
European Southern Observatory
CEA/DAPNIA, Saclay, France
CENTRA, Instituto Superior Tecnico, Lisbon, Portugal

15 December 2000

Version 1.6

Copyright
Regents of the University of California

The SNAP Collaboration and authors of this Proposal are

D. Curtis, G. Goldhaber, J. Graham, S. Harris, P. Harvey, H. Heetderks, A. Kim,
M. Lampton, R. Lin, D. Pankow, C. Pennypacker, A. Spadafora, G. Smoot
University of California, Berkeley, CA, USA

G. Aldering, S. Deustua, W. Edwards, B. Frye, D. Groom, S. Holland, D. Kasen,
R. Knop, R. Lafever, M. Levi (co-PI), P. Nugent, S. Perlmutter (PI), K. Robinson
Lawrence Berkeley National Laboratory, Berkeley, CA, USA

P. Astier, J.F. Genat, D. Hardin, J-M. Levy, R. Pain, K. Schamahneche
LPNHE, CNRS-IN2P3 and University Paris VI & VII, Paris, France

A. Baden, J. Goodman, G. Sullivan
University of Maryland, College Park, MD, USA

R. Ellis, M. Metzger
California Institute of Technology, Pasadena, CA, USA

D. Huterer
University of Chicago, Chicago, IL, USA

A. Fruchter
Space Telescope Sciences Institute, Baltimore, MD, USA

C. Bebek
Cornell University, Ithaca, NY, USA

L. Bergström, A. Goobar
University of Stockholm, Sweden

I. Hook
Institute for Astronomy, University of Edinburgh, UK

C. Lidman
European Southern Observatory

J. Rich
CEA/DAPNIA, Saclay France

A. Mourao
CENTRA, Instituto Superior Tecnico, Lisbon, Portugal

Contents

I	Executive Summary	1
1	Executive Summary	2
1.1	Abstract	2
1.2	Introduction	2
1.3	Scientific Motivation and Background	3
1.4	Proposed Experiment	9
1.5	Control of Statistical and Systematic Uncertainties	10
1.6	Why a New Satellite?: Design Requirements and Ground- or Space- Based Alternatives	14
1.7	Overview of Feasibility	17
1.8	Summary of Other Major Science	18
1.9	This Proposal	18
II	SNAP Physics	20
2	Theoretical Overview	21
2.1	Cosmological Parameters	21
2.2	The Dark Energy	21
3	Summary of Current Results from SNe Ia	25
3.1	Introduction	25
3.2	The Physics of Type Ia Supernovae	26
3.2.1	Progenitors to Explosion	26
3.2.2	Light Curves	26
3.2.3	Spectra	27
3.2.4	Environmental Influences	27
3.3	Results from the Observation of Type Ia Supernovae	30
4	Science Reach of the Proposed Satellite	35
4.1	Introduction	35
4.1.1	SNAP’s Data Set and the Assumed Fiducial Model	35
4.2	Cosmological Parameter Determination with SNAP	36
4.2.1	Exploring Higher Redshifts (z & 1)	36
4.2.2	Summary of the expected parameter uncertainties	38

4.2.3	Constraining Ω_M and Ω_Λ	39
4.2.4	Measuring the Equation of State Ratio of the Dark Energy . . .	39
4.2.5	Hubble parameter issues	39
4.2.6	Comparison with CMB and LSS	41
4.2.7	Breaking the Parameter Degeneracies	44
4.2.8	Comparison with Other Methods	46
4.2.9	Further Exploration of the Dark Sector	47
4.3	Previously Identified Sources of Systematic Uncertainty	50
4.4	Treatment of Proposed Systematic Errors	51
4.4.1	Gray dust	52
4.4.2	Evolution	53
4.4.3	Observables to Correct or Match SNe Ia	54
4.5	Systematic Correlations	57
4.6	Summary	58
5	Comparisons with Alternatives	63
5.1	Introduction	63
5.2	Advantages of Space-Based Observations	66
5.2.1	Reduced Foreground Emission	66
5.2.2	Reduced Foreground with Better Seeing	69
5.2.3	Further Ground-based Degradation	70
5.2.4	Improved Detection Efficiency	71
5.3	Detailed Comparison of SNAP and Ground-based Viewing	72
5.3.1	Searching with HST or NGST	73
5.3.2	Ground-based searching with follow-up using HST or NGST . .	75
6	Other Scientific Objectives	77
6.1	Introduction	77
6.2	Type II Supernova	77
6.3	Gravitational Lensing	79
6.3.1	The Role of SNAP	79
6.3.2	Introduction to Lensing Phenomena	81
6.3.3	Detailed Considerations - Strong Lensing	85
6.3.4	Detailed Considerations - Weak Lensing	89
6.4	Gamma Ray Bursts	94
6.4.1	Observational strategy	96
III	Baseline Instrument Description	99
7	Observational Strategy & Data Package	100
7.1	Observational Requirements	100
7.2	Observational Strategy & Data Package	104
7.2.1	Photometry	104
7.2.2	Spectroscopy	105

7.3	Instrument Performance	107
8	Optical Photometry	108
8.1	Optical Photometer Requirements	108
8.2	Technology	109
8.3	Supernova Detection	109
8.4	Optical Photometer Performance	109
9	NIR Photometry	111
9.1	NIR Photometer Requirements	111
9.2	NIR Photometer Performance	111
10	Spectroscopy	113
10.1	Optical/IR Spectrograph Requirements and Performance	113
10.1.1	Introduction	113
10.1.2	Achieving Wavelength Coverage with a Three-Arm Spectrograph	113
10.1.3	Resolution Requirements and Constraints	114
10.1.4	Integral Field Unit	116
10.1.5	Optics	121
10.1.6	Dispersive Elements	122
10.1.7	Very Low-resolution NIR Spectroscopy Option	122
10.1.8	Internal Adjustment and Calibration	123
10.2	Spectrograph baseline	124
11	Telescope	127
11.1	Optical Requirements	127
11.2	Baseline Optical Design	127
11.3	Imaging Performance	131
11.4	Active Steering Mirror	133
11.5	Mirror Technology	133
11.6	Conclusion	134
12	Calibration	135
12.1	Introduction	135
12.2	Imager Photometric Calibration	135
12.2.1	Internal Calibration	135
12.2.2	External Flux Calibration	140
12.2.3	Imager Calibration Summary	141
12.3	Spectrograph Wavelength and Photometric Calibration	141
12.4	Imager Astrometric Calibration	142
12.5	Spectrograph Astrometric Calibration	143
12.6	NIR Imager Calibration	143
12.7	Extinction from Foreground Dust in the Galaxy	144
12.8	Photometric Redshift Calibration	147

13 Electronics	149
13.1 CCD Clocking	149
13.2 Double Correlated Sampling	150
13.3 Analog to Digital Conversion.	150
13.4 Digital Processing	151
13.5 Power	151
14 Spacecraft Description	152
14.1 Orbit Properties	152
14.2 Spacecraft Description	154
14.2.1 Power system	154
14.2.2 ACS/Propulsion System	156
14.2.3 Telecommunications System	157
14.2.4 Observatory Control Unit	158
14.2.5 Spacecraft Structure	158
14.3 Launch Vehicle	159
14.4 Observatory Integration and Testing	160
15 Mission Operations	162
15.1 Mission Operations	162
15.2 SNAP Operations	163
15.3 Data Handling & Signal Processing	164
15.4 NERSC	165
IV Education/Public Outreach	166
16 SNAP Education and Public Outreach	167
16.1 SNAP and Science Literacy	167
16.1.1 Introduction	167
16.1.2 Identified Need	168
16.1.3 Target Audiences	168
16.1.4 Goals	168
16.1.5 K-14 Activities and Instructional Materials	169
16.1.6 Undergraduate Research Experience	170
16.1.7 Professional Staff Development	171
16.1.8 Public Outreach	171
16.1.9 Partnerships	172
16.2 SNAP Training Undergraduates Science Majors and Graduate Students	175
16.2.1 Overview	175
16.2.2 Goals and Objectives	175
16.2.3 Training Program	176
16.3 SNAP Administration of Education and Outreach Programs	178
16.3.1 Budget	179
16.3.2 Advisory Board	179

16.3.3 Personnel	179
V Bibliography	181
VI Appendix	192
A WBS	193
B CCD's	196
B.1 Overview	196
B.2 Benefits and Goals	199
B.3 Uniqueness of Fully-Depletion Devices	200
B.4 Comparison of CCD's	201
B.5 Technical features of high-resistivity CCD's	204
B.6 Radiation Tolerance	206
B.7 Cosmic Rays	207
B.8 Packaging with 4-side Abutment	209

List of Tables

1.1	Systematic errors.	12
1.2	Observational requirements.	15
2.1	Some candidates for the dark energy and their respective EOS's.	23
4.1	A summary of statistical and systematic uncertainties in parameter de- termination from one year of SNAP data.	38
4.2	SNAP constraints on Ω_M , Ω_Λ and Ω_k compared to those expected from SDSS, MAP, and Planck.	42
4.3	1- σ uncertainties in Ω_M and w assuming a flat universe.	43
4.4	Potential systematic errors given SNAP's capabilities.	55
4.5	Observables that constrain the various SNe Ia model parameters.	55
4.6	Host galaxy characteristics.	55
5.1	Alternative facilities.	65
5.2	Comparison of alternative facilities to SNAP for baseline mission.	66
5.3	Atmospheric and space foregrounds.	68
5.4	Wide-field imaging comparison.	73
5.5	OH suppression (follow-up) imaging comparison.	73
5.6	AO (follow-up) imaging comparison.	74
5.7	AO (follow-up) spectroscopy comparison.	75
7.1	Redshifted B-band filters.	102
7.2	One-year SNAP supernova discovery and follow-up summary.	107
8.1	Optical Imager/Photometer requirements.	108
8.2	Observation strategy.	110
8.3	Optical photometry.	110
9.1	NIR Imager/Photometer requirements.	111
9.2	NIR photometry.	112
9.3	NIR V-band photometry.	112
10.1	Optical Spectrograph Arm Requirements	125
10.2	IR Spectrograph Arm Requirements	125
10.3	Optical Spectroscopy	125
10.4	IR Spectroscopy	126

11.1	SNAP observatory requirements.	128
12.1	Imager calibration error budget.	141
12.2	Survey regions with low zodiacal background.	144
13.1	Power consumption of CCD readout chain.	151
14.1	Orbit trade study matrix.	152
14.2	Attitude control system components.	156
14.3	Propulsion system components.	157
B.1	UCB $2k \times 2k$ ($15 \mu\text{m}$) ² CCD's as compared with other detectors. . . .	203
B.2	Lunar-assist orbit cosmic ray hit rate.	207

List of Figures

1.1	Ω_M — Ω_Λ confidence regions with the current data and with SNAP. . . .	5
1.2	Ω_M — Ω_Λ confidence regions with current SN, galaxy cluster, and CMB results.	7
1.3	Confidence regions in the Ω_M — w plane.	8
3.1	Stretch luminosity relationship.	28
3.2	Observed M_B vs. $\mathcal{R}(\text{Si II})$ and $\mathcal{R}(\text{Ca II})$	29
3.3	Spectral temporal evolution of a SN Ia.	30
3.4	Metallicity effects in the UV.	31
3.5	Metallicity effects in the optical.	32
3.6	Hubble diagram for 42 high- z SNe.	33
3.7	Ω_M — w confidence region.	34
4.1	Parameter estimation as a function of maximum redshift.	37
4.2	Constraints on Ω_M and Ω_Λ expected from the proposed experiment in a closed universe.	40
4.3	SNAP constraint on parameters Ω_M and w	44
4.4	Degeneracy breaking in quintessence models.	45
4.5	Current plus SNAP constraints on dark energy models, viewed in the magnitude-redshift plane.	48
4.6	SNAP constraints on dark energy models	49
4.7	Gray dust FIR emission.	59
4.8	B -band magnitude residuals from the best-fit flat cosmology.	60
4.9	Peak-to-tail light curve differences.	61
4.10	Metal abundances of nearby and distant galaxies.	62
5.1	Ground and HST images of a distant SN.	64
5.2	High redshift SN discoveries.	65
5.3	Poisson and foreground errors due to the sky background.	67
5.4	Atmospheric emission.	68
5.5	Atmospheric absorption.	70
5.6	Ground-based image quality - Optical.	71
5.7	Ground-based image quality - NIR.	72
6.1	SNe II fit.	79
6.2	Strong lensing by A2218.	80

6.3	Lensing Phenomena	81
6.4	HDFS gravitational lens.	83
6.5	Light curves of a MACHO event.	84
6.6	Cosmic shear in the “Groth” strip.	85
6.7	Mass map of MS1054.	86
6.8	Thin lens diagram.	87
6.9	Microlensing detectability.	88
6.10	HST galaxy sizes.	91
6.11	Weak lensing power spectrum.	92
6.12	Weak lensing constraints on Ω_M and Ω_Λ	93
6.13	The Optical counterpart to GRB990123.	95
6.14	A simulated Lyman forest absorption spectrum out to a redshift of $z = 7$	98
7.1	B-band light-curve for SNe Ia.	101
7.2	SN Ia spectrum with B-band bandpass superimposed.	103
7.3	B-band light-curve sampling for SNAP SNe Ia.	105
7.4	SN Ia spectroscopic regions relevant for identification and systematic studies.	106
10.1	KAST spectrograph layout.	115
10.2	Spectral resolution trade-offs.	116
10.3	Reformatting of spatial and spectral information with integral field units.	118
10.4	Richardson focusing image slicer.	119
10.5	Durham IFU.	120
10.6	Durham IFU pseudo-slit.	121
10.7	NIR dispersive element.	123
11.1	Side view of our baseline optical configuration.	130
11.2	Spot diagrams taken at off axis angles ranging from 0.4 to 0.7 degrees. One tick = 0.1 arcsecond.	132
12.1	SNAP imager star counts.	139
12.2	Northern Galactic dust map.	145
12.3	Southern Galactic dust map.	146
13.1	Correlated double sampling chain block-diagram.	150
14.1	Lunar-assisted orbit.	153
14.2	Block diagram of the relationship between the science payload and the spacecraft subsystems.	155
14.3	Planetary mission capability of the Delta III rocket.	159
14.4	The 4.0m diameter composite spacecraft fairing for the Delta IV-M launch vehicle.	160
15.1	Ground system showing the flow of data.	162

15.2	Daily coverage from from the UCB/SSL ground station for the lunar assist orbit.	163
15.3	Percentage coverage from the UCB/SSL ground station as a function of the lunar assist orbit inclination and for different values of the angle of perigee.	164
16.1	SNAP EPO Structure: Broker for Scientists, Partners and the Public . .	178
B.1	Raw test image obtained at Lick Observatory of a back-illuminated $2k \times 2k$ ($15 \mu m^2$ -pixel) UCB high-resistivity CCD.	197
B.2	Measured response of the UCB “fully-depleted” CCD at $-100^\circ C$ for an unoptimized two-layer AR coating.	198
B.3	Absorption length of light in silicon.	202
B.4	Back-Illuminated test pattern imaged a back-illuminated $2k \times 2k$ UCB high-resistivity CCD tested at Lick Observatory.	204
B.5	Lick test CCD images of a heavily obscured region in the Orion Nebula.	205
B.6	Cross-section of the back-illuminated, fully-depleted CCD.	205
B.7	Differential proton flux in high earth orbit for solar maximum and solar minimum for different shielding thicknesses.	208
B.8	Conceptual design for “fully-depleted” CCD packaging.	209

Part I

Executive Summary

Chapter 1

Executive Summary

1.1 Abstract

A ~ 2 -meter satellite telescope with a 1-square-degree optical imager, a small near-IR imager, and a three-arm near-UV-to-near-IR spectrograph can discover over 2000 Type Ia supernovae at redshifts between $z=0.1$ and 1.7, and follow them with high-signal-to-noise calibrated light-curves and spectra. The resulting data set can determine the cosmological parameters with precision: mass density Ω_M to ± 0.02 , vacuum energy density Ω_Λ to ± 0.05 , and curvature Ω_k to ± 0.06 . The data set can test the nature of the “dark energy” that is apparently accelerating the expansion of the universe. In particular, a cosmological constant dark energy can be differentiated from alternatives including a range of “quintessence dynamical scalar-field models,” by measuring the ratio of the dark energy’s pressure to its density to ± 0.05 over a range of redshifts. The large numbers of supernovae across a wide range of redshifts are necessary but not sufficient to accomplish these goals; the controls for systematic uncertainties are primary drivers of the design of this space-based experiment. These systematic and statistical controls cannot be obtained with other ground-based and/or space-based telescopes, either currently in construction or in planning stages.

1.2 Introduction

In the past few decades the study of cosmology has taken some of its first major steps as an empirical science, combining concepts and tools from astrophysics and particle physics. The most recent of these results have already brought surprises. The universe’s expansion is apparently accelerating rather than decelerating as expected due to gravity. This implies that the simplest model for the universe – flat and dominated by matter – appears not to be true, and that our current fundamental physics understanding of particles, forces, and fields is likely to be incomplete.

The most clear evidence for this surprising conclusion comes from the recent supernova measurements of changes in the universe’s expansion rate that directly show

the acceleration. These measurements indicate the presence of a new, mysterious energy component that can cause acceleration. This conclusion is supported by current measurements of the mass density of the universe, when taken together with current Cosmic Microwave Background measurements or inflationary theory.

To address this new puzzle and begin to establish a solid cosmological picture, we propose a satellite experiment to carry out a definitive supernova study that will determine the values of the cosmological parameters and may unveil the unidentified accelerating energy. In this proposal, we will show that this experiment addresses these fundamental science questions with a necessary level of statistical and systematic rigor that cannot be matched by plausible alternatives, whether on the ground or in space.

This proposed supernova measurement will play a key role in the larger set of cosmological measurement approaches expected to yield results over the next decade. (This proposed satellite will also use some of these other approaches as part of its science mission.) Together these measurements will complement and cross-check our understanding of the cosmological model of the universe. Since the supernova approach is arguably the most direct and least model dependent, we expect it to provide a touchstone for this concordance of measurement results. Moreover, since this experiment is sensitive to the redshift range in which the accelerating energy is dominant, it will provide a nearly unique window on the properties of this entity of fundamental physics.

This experiment seizes upon the many recent advances in instrumentation and space technology to explore fundamental questions about the nature of our universe.

1.3 Scientific Motivation and Background

A Simple, Direct Approach to the Cosmological Parameters

Type Ia supernovae (SNe Ia) provide simple cosmological measurement tools. Each one is a strikingly similar explosion event whose physics can be analyzed in some detail from its intensity and spectrum as it brightens and fades. Most observed SNe Ia have nearly the same peak luminosity, and the variations that do exist can be correlated with other observables and hence calibrated to 5% in distance (Hamuy et al., 1996; Riess, Press, & Kirshner, 1996). The variation-corrected peak brightness (magnitude) is then a measure of the distance to the supernova.

The wavelengths of the photons from the supernova are stretched—“redshifted”—in exact proportion to the stretching of the universe during the period that the photon travels to us. Thus the comparison of SN Ia redshifts and magnitudes provides a particularly straightforward measurement of the changing rate of expansion of the universe: the apparent magnitude indicates the distance and hence time back to the supernova explosion, while the redshift measures the total relative expansion of the universe since that time.

This satellite project is designed to establish a Hubble-diagram (redshift vs. magnitude) plot dense with supernova events looking back over two-thirds the age of the universe. With such a history of the expansion of the universe we can determine the contributions of decelerating and accelerating energies—mass density Ω_M , vacuum en-

ergy density Ω_Λ , and/or other yet-to-be-studied “dark energies”—as the expansion rate changes over time.

This is an extremely transparent methodology. Almost everyone, even non-scientists, can appreciate and perhaps critique every step. Aside from the basic cosmological equations, there is no model dependence in this empirically-based method, and it is sensitive to only a few parameters of cosmology so there is no fit required in a large-dimensional parameter space. (Conversely, this method of course does not help determine these other parameters, except by narrowing down the whole phase space, as discussed below.) This transparency is an unusual and important feature of this particular very fundamental measurement.

The Current Results: Questions Answered and Posed by an Accelerating Universe

The cosmological results from the magnitude/redshift measurements of a few score SNe Ia already present surprises and puzzles (Perlmutter et al., 1999; Riess et al., 1998). Most striking is the indication that we live in an accelerating universe, which must be dominated by a positive cosmological constant or other vacuum energy whose pressure is negative and large. The very simplest cosmological model, the Einstein-de Sitter ($\Omega_M = 1$) universe, which is flat and has zero cosmological constant, is strongly inconsistent with the data. Of the two arguably next-simplest models, only the flat model with the cosmological constant, Λ , fits the data, while the low-mass open universe with zero Λ does not. (All of these statements can be made with very strong statistical confidence; even stretching the range of imagined systematic uncertainties, it is very difficult to fit the data without a cosmological constant in a flat universe.)

These current results immediately raise important questions. Although the data indicate that an accelerating dark energy density—perhaps the cosmological constant—has overtaken the decelerating mass density, they do not tell us the actual magnitude of either one. These two density values are two of the fundamental parameters that describe the constituents of our universe, and determine its geometry and destiny. The proposed satellite project is designed to obtain sufficient magnitude-redshift data for a large enough range of redshifts ($0.1 < z < 1.7$) that these absolute densities can each be determined to unprecedented accuracy (see Figure 1.1). Taken together, the sum of these energy densities then provides a measurement of the curvature of the universe.

The current data also do not tell us the nature of the dark energy; all we know is that it must have a sufficiently negative pressure to cause the universe’s expansion to accelerate. Our one long-known physical model for the dark energy, the vacuum energy density that Einstein called “the cosmological constant,” presents difficult theoretical problems. Why, for example, is the vacuum energy density so small when compared to the natural energy scales of the particles and fields that would be expected to account for it: the values that are consistent with the current SN Ia results are 10^{120} times smaller than the Planck scale. Moreover, why would a vacuum energy density that remains constant throughout history turn out just now to be within a factor of two or three of the mass energy density, which has fallen by many orders of magnitude since the Big Bang?

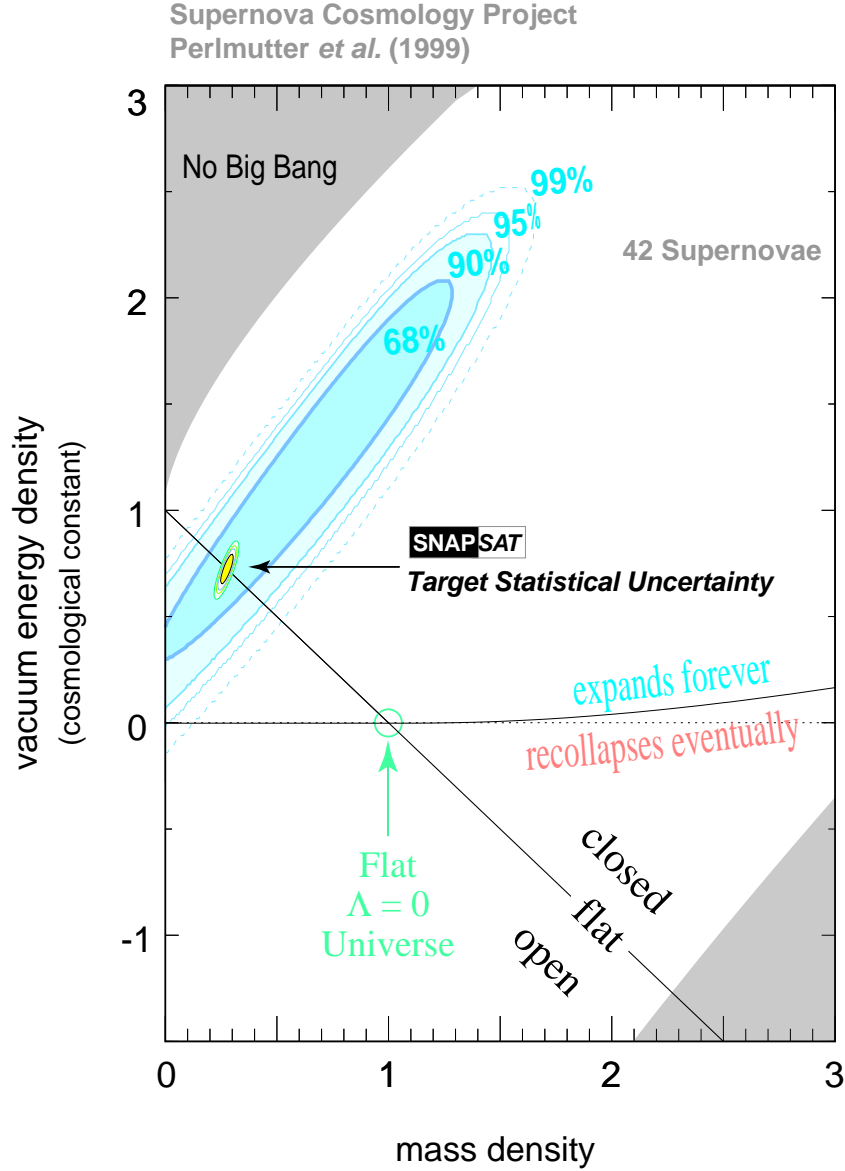


Figure 1.1: 68%, 90%, and 99% confidence regions in the Ω_M — Ω_Λ plane from the 42 distant SNe Ia in Perlmutter et al. (1999). These results rule out a simple flat, $[\Omega_M = 1, \Omega_\Lambda = 0]$ cosmology. They further show strong evidence (probability $> 99\%$) for $\Omega_\Lambda > 0$. Also shown is the expected confidence region from the SNAP satellite for an $\Omega_M = 0.28$ flat universe.

In response to these theoretical problems, several alternative physical models have been proposed as candidates for the dark energy. These models can generally be characterized by their equation of state, $p = w\rho$ (the speed of light, c , is set to unity).

The ratio of pressure to density, w , can be constant or time-varying depending on the model, and has a constant value of -1 in the case of the cosmological constant. The current SN Ia data allow some crude constraints on the alternative dark energy models, since not all equations of state fit the data. With the proposed satellite project we can begin to study these alternative dark energy models in some detail, by determining w to much higher accuracy and by studying it over a range of redshifts.

The existence of a negative-pressure vacuum energy density is in remarkable concordance with combined galaxy cluster measurements (Bahcall et al., 1999), which are sensitive to Ω_M , and current CMB results (Lange et al., 2000; Balbi et al., 2000), which are sensitive to the curvature Ω_k (see Figure 1.2). Two of these three independent measurements and standard Inflation would have to be in error to make the cosmological constant (or dark energy) unnecessary in the cosmological models. If this were, in fact, to be the case, a definitive accounting of the systematic uncertainties for the supernova measurements would be particularly crucial, and any new cosmological models would still require the basic product of the SNAP mission, a history of the scale of the universe.

Scientific Goals of SNAP

The primary scientific objective of this mission is to measure important cosmological parameters with low statistical and systematic errors. Assuming that the dark energy is the cosmological constant, this experiment can simultaneously determine mass density Ω_M to accuracy of 0.02, cosmological constant energy density Ω_Λ to 0.05 and curvature $\Omega_k = 1 - \Omega_M - \Omega_\Lambda$ to 0.06.

The proposed experiment is one of very few that can study the dark energy directly, and test a cosmological constant against alternative dark energy candidates. Assuming a flat universe with mass density Ω_M and a dark energy component with a non-evolving equation of state, the proposed experiment will be able to measure the equation-of-state ratio w with accuracy of 0.05, at least a factor of five better than the best planned cosmological probes. With such a strong constraint on w we will be able to differentiate between the cosmological constant and such theoretical alternatives as “topological defect” models and a range of dynamical scalar-field (“quintessence”) particle-physics models (see Figure 1.3). Moreover, with data of such high quality one can relax the assumption of the constant equation of state, and begin simple tests of its variation with redshift. These determinations would directly shed light on physics at high energy/small scale and physics of the early universe.

It is important to add that these SN Ia results are not the only available cosmological measurements, nor will they be at the time of the proposed satellite. The estimates of the mass density from large-scale structure (LSS) surveys and cluster evidence are constantly improving. The MAP and Planck satellite experiments are expected to give high-precision fits of ~ 11 cosmological and model-dependent parameters, both before and after the proposed satellite’s SN Ia measurements. Perhaps surprisingly, these supernova measurements will provide stronger constraints on Ω_M and Ω_Λ than those expected from either LSS or CMB measurements, and constraints on curvature Ω_k that are comparable with those expected from MAP and Planck. The important cosmolog-

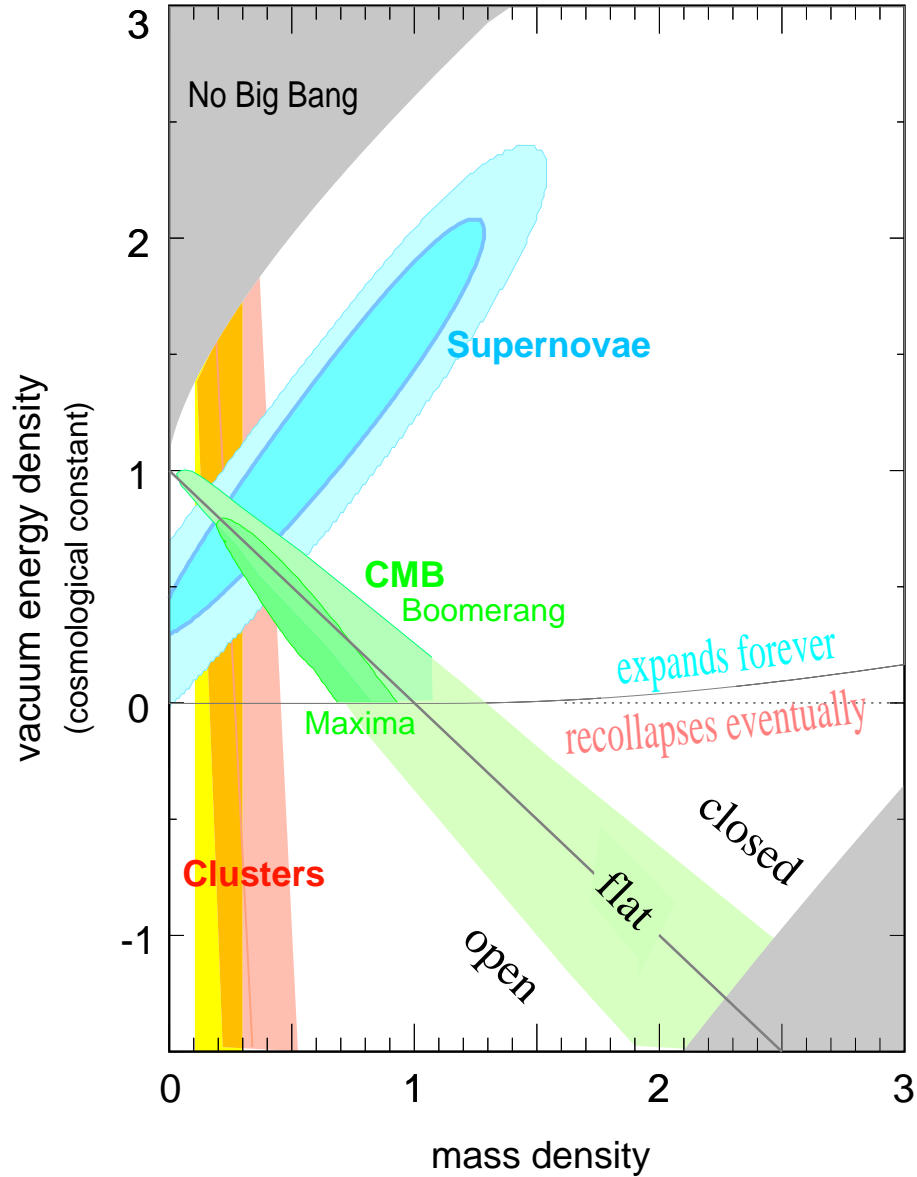


Figure 1.2: There is strong evidence for the existence of a cosmological vacuum energy density. Plotted are Ω_M — Ω_Λ confidence regions for current SN, galaxy cluster, and CMB results. Their consistent overlap is a strong indicator for dark energy.

ical test will be the cross comparison of these and other fundamental measurements — and it is even possible that cosmology will next progress when we discover that they do not agree. In any case, it will be all of these measurements fit simultaneously, that will provide us with our best understanding of the cosmology of the universe; the final results can be as much as an order of magnitude better than the constraints from any

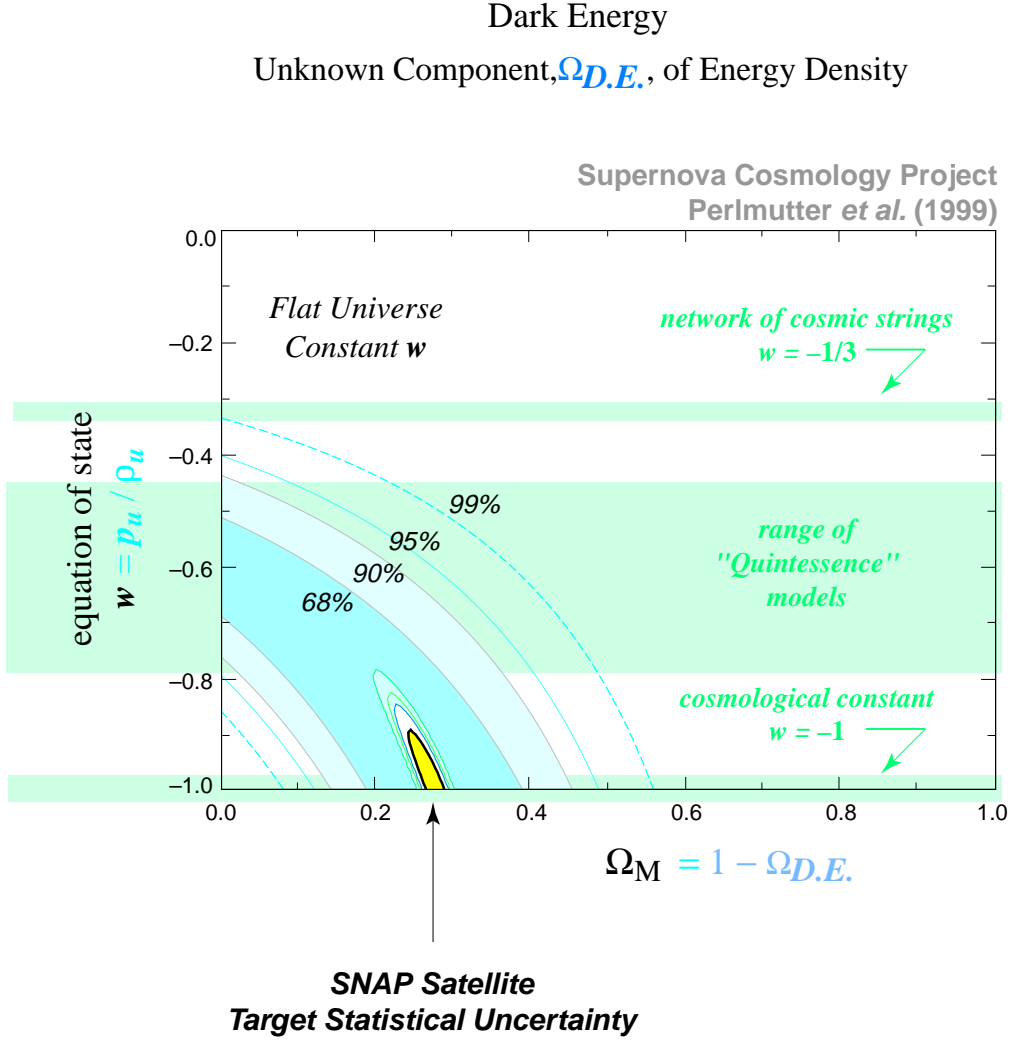


Figure 1.3: Best-fit 68%, 90%, 95%, and 99% confidence regions in the Ω_M - w plane for an additional energy density component, Ω_w , characterized by an equation-of-state $w = p/\rho$. (If this energy density component is Einstein's cosmological constant, Λ , then the equation of state is $w = p_\Lambda/\rho_\Lambda = -1$.) Also shown is the expected confidence region allowed by SNAP.

one measurement approach.

To accomplish these goals, it is not sufficient simply to discover and study more supernovae and more distant supernovae. The current SN Ia data set already has statistical uncertainties that are only a factor of two larger than the identified systematic uncertainties. There are also several additional proposed systematic effects that might confound attempts at higher precision, in particular the possibilities of “grey dust” or systematic shifts in the population of SN Ia host galaxy environments. Addressing each of these systematic concerns requires a major leap forward in the supernova mea-

surement techniques, and has driven us to the satellite experiment that we describe in this proposal.

1.4 Proposed Experiment

Instrumentation

The baseline proposed satellite experiment is based on a simple, dedicated combination of a 2.0-meter telescope, a 1-square-degree imager, a small near-IR imager, and a three-arm near-UV-to-near-IR spectrograph. The 1-square-degree wide field is obtained with a three-mirror telescope, and a feedback loop based on fast-readout chips on the focal plane to stabilize the image.

The wide-field imager is completely filled with a CCD mosaic for the “optical” wavelengths between 0.35 and 1.0 microns. The near-IR imager will be a single HgCdTe detector to obtain images of specific targets in the wavelengths between 1.0 and 1.7 microns.

The spectrograph uses dichroic beam-splitters to send the light into two optical arms ($0.35 - 0.6 \mu\text{m}$ and $0.55 - 1.0 \mu\text{m}$) and one near-IR arm ($0.95 - 1.7 \mu\text{m}$). Each of the three arms employs an “integral field unit” (IFU) to obtain an effective image of a $2''$ by $2''$ field, split into $0.07''$ by $0.07''$ regions that are each individually sent to the spectrograph to obtain a flux at each position and wavelength (sometimes called a three-dimensional “data cube”). In operation, these integral field units will allow simultaneous spectroscopy of a supernova target and its surrounding galactic environment; the $2''$ by $2''$ field of view also removes any requirement for precise positioning of a supernova target in a traditional spectrograph slit. This point is particularly important for absolute flux calibration, because all of the supernova light is collected with the integral field units. The spectrograph is thus designed to allow the spectra to be used to obtain photometry in any “synthetic” filter band that one chooses.

Observation Strategy and Baseline Data Package

This instrumentation will be used with a simple, predetermined observing strategy designed to monitor a 20-square-degree region of sky near the north and south ecliptic poles, discovering and following supernovae that explode in that region. Every field will be visited frequently enough with sufficiently long exposures that at any given redshift up to $z = 1.7$ every supernova will be discovered within, on average, two restframe days of explosion. Every supernova at $z < 1.2$ will be followed as it brightens and fades, while at $z > 1.2$ there will be sufficient numbers of supernovae that it will only be necessary (and possible) to follow a subsample to obtain comparable numbers of supernovae.

The wide-field imager makes it possible to find and follow approximately 2000 SNe Ia in a year and a half. The 2.0-meter aperture of the mirror, along with high throughput instruments, allow this dataset to extend to redshift $z = 1.7$.

This prearranged observing strategy will provide a uniform, standardized, calibrated dataset for each supernova, allowing for the first time comprehensive com-

parisons across complete sets of supernovae. The standardized dataset will have the following measurements that will address, and often eliminate, each of the statistical and systematic uncertainties that have been identified or proposed.

- A light curve sampled at frequent, standardized epochs that extends from ~ 2 restframe days to ~ 80 restframe days after explosion.
- Multiple color measurements, including optical and near-IR bands, at key epochs on the light curve.
- Spectrum at maximum light, extending from $0.35 \mu\text{m}$ to $1.7 \mu\text{m}$.
- Final reference images and spectra to enable clean subtraction of host galaxy light.

The quality of these measurements is as important as the time and wavelength coverage, so we require:

- Control over signal-to-noise ratio for these photometry and spectroscopy measurements, to permit comparably high statistical significance for supernovae over a wide range of redshifts.
- Control over calibration for these photometry and spectroscopy measurements, with constant monitoring data collected to ensure that cross-instrument and cross-wavelength calibration remains stable over time.

Note that to date not one single SN Ia has ever been observed with this complete set of measurements, either from the ground or in space, and only a handful have a dataset that is comparably thorough. With the observing strategy proposed here, *every one* of ~ 2000 followed SN Ia will have this complete set of measurements.

In addition to this minimum-required-dataset, a still more extensive set of observations will be performed for a randomly selected subset of SNe Ia (with more at lower redshifts and fewer at higher redshifts). These additional observations will include:

- A time series of spectra, sampled frequently over the entire 80 restframe days of the observed light curve.
- Multiple filter-band light curves. (These are not necessary when the time series of spectra is obtained, since this provides synthetic-filter photometry.)

1.5 Control of Statistical and Systematic Uncertainties

The satellite instrumentation and observation strategy is designed to provide comprehensive control of the previously identified or proposed sources of uncertainty. The completeness of the resulting dataset will make it possible to monitor the physical properties of each supernova explosion, allowing studies of effects that have *not* been previously identified or proposed.

At present, the identified systematic uncertainty is over half the size of the statistical uncertainty; this would provide the “floor” on the proposed measurement uncertainty, if it were not improved. However, almost every one of the sources of identified systematics is due to limitations of the previous (and even planned NGST baseline SN program) measurements. The dataset described here removes these limitations so that the relevant effects can be measured and the previous systematic uncertainties now become controllable *statistical* uncertainties.

Previously Identified Sources of Systematic Uncertainty

In Table 1.1, we summarize the identified sources of systematic error, and give the uncertainty that each contributed to previous measurements. With the proposed satellite experiment, each of these effects can either be measured so that it can become part of the statistical error budget, or else bounded (the target overall systematic uncertainty is kept below ~ 0.02 magnitudes, so that it will contribute comparably to the final statistical uncertainties). The final column of the table summarizes the observations required to reach this target systematic uncertainty. These previously identified sources of systematic uncertainty are each discussed in more detail in § 4.3.

Proposed Sources of Systematic Uncertainty

Extinction by Proposed “Gray Dust”: Models of “gray dust” have been proposed to evade detection by the usual measurements of reddening (Aguirre & Haiman, 1999). However, even grey dust cannot remain completely invisible, since it will re-emit absorbed light and contribute to the far-infrared (FIR) background. Current SCUBA observations indicate that FIR emission from galaxies is close enough to account for all the FIR background. Deeper SCUBA and SIRTf observations should tighten the constraints on the amount of gray dust allowed.

Another tell-tale observation will allow us to independently detect and measure gray dust. The physical models so far proposed have dust grains that are large enough that they dim blue and red light equally, however the near-IR light ($\sim 1.2 \mu\text{m}$) is less affected. The same technique can therefore be used to measure this dust as would be used to measure the “ordinary” dust, by extending the broad-wavelength measurements into the near-IR. This will measure dimming due to proposed large-grain gray dust out to $z = 0.5$, and this proposed systematic uncertainty, too, can become part of our statistical error budget.

Current space-based observations of existing supernovae are already being used in this way to test if gray dust in a non-accelerating universe can mimic the effects of an accelerating universe at $z = 0.5$. Results show that the observed color excess is too small to be compatible with the 30% opacity of gray dust needed in a $\Lambda = 0$ universe to be consistent with observations. Our proposed satellite measurements would improve greatly on these first results and allow detection and measurement of much smaller gray-dust opacity.

Requirement: Cross-wavelength calibrated spectra, at controlled SN-explosion epochs, that extend to rest-frame $1.2 \mu\text{m}$.

Systematic	Current ground-based δM	SNAP requirement to satisfy $\delta M < 0.02$
Malmquist bias	0.04	Detection of every supernova 3.8 magnitudes below peak in the target redshift range
K-Correction and Cross-Filter Calibration	0.025	Spectral time series of representative SN Ia and cross-wavelength relative flux calibration
Non-SN Ia Contamination	< 0.05	Spectrum for every supernova at maximum covering the rest frame Si II 6250Å feature
Milky Way Galaxy extinction	< 0.04	SDSS & SIRTf observations; SNAP spectra of Galactic subdwarfs
Gravitational lensing by clumped mass	< 0.06	Average out the effect with large statistics with ~ 75 SNe Ia per 0.03 redshift bin. SNAP microlensing measurements.
Extinction by “ordinary” dust outside the Milky Way	0.03	Cross-wavelength calibrated spectra to observe wavelength dependent absorption

Table 1.1: Listed are the main systematic errors in the measurement of the cosmological parameters. Their contribution to magnitude uncertainties in the current analyzed data set is tabulated, along with the observational requirements needed to reduce those uncertainties to $\delta M < 0.02$

In principle, gray dust models can be constructed that would evade these broad-wavelength measurements, either because the “gray dust” does not exist closer than $z = 0.5$ or because the dust grains are even larger than first proposed and thus absorb light equally at $0.4\ \mu\text{m}$ and $1.2\ \mu\text{m}$. (Such larger grain sizes are strongly disfavored by other astrophysical constraints, however.) Even these more contrived dust models can be measured by the proposed dataset because of its large redshift range: at redshifts beyond $z = 1.4$ models with dust would be distinguished from cosmological models with no dust but with Λ at the 50 standard-deviation level.

Requirement: A redshift distribution that extends to $z \geq 1.5$ for followed SNe Ia.

Proposed Uncorrected Evolution: Uncorrected “evolution” has also been proposed as a potential source of systematic uncertainty (Umeda et al., 1999). Supernova behavior may depend on properties of its progenitor star or binary-star system. The distribution of these stellar properties is likely to change over time—“evolve”—in a given galaxy, and over a set of galaxies.

As galaxies age, generation after generation of stars complete their life-cycles, enriching the galactic environment with heavy elements (the abundance of these elements is termed “metallicity”). In a given generation of stars, the more massive ones will complete their life cycles sooner, so the distribution of stellar masses will also change over time. Such statistical changes in the galactic environments are expected to affect the typical properties of supernova-progenitor stars, and hence the details of the triggering and evolution of the supernova explosions. Even the SNe Ia might be expected to show some differences that reflect the galactic environment in which their progenitor stars exploded, even though they are triggered under very similar physical conditions every time (as mass is slowly added to a white dwarf star until it approaches the Chandrasekhar limit).

Evidence for such galactic-environment driven differences among SNe Ia has in fact already been seen among nearby, low-redshift supernovae (Hamuy et al., 1996). The range of intrinsic SN Ia luminosities seen in spiral galaxies differs from that seen in elliptical galaxies. So far, it appears that the differences that have been identified are well calibrated by the SN Ia light curve width-luminosity relation. The standard supernova analyses thus already are correcting for a luminosity effect due to galactic-environment-distribution evolution. There are likely to be additional, more subtle effects of changes in the galactic environment and shifts in the progenitor star population, although it is not clear that these effects would change the peak luminosity of the SNe Ia. The proposed satellite experiment is designed to provide sufficient data to measure these second-order effects, which might be collectively called “proposed uncorrected evolution.”

In this discussion it is important to recognize that each individual galaxy begins its life at a different time since the Big Bang, at a different absolute time. Even today, there are newly formed, “young,” first-generation galaxies present that have not yet gone through the life cycles of their high-mass stars, nor yet produced significant heavy element abundance. Thus at any given redshift there will be a large range of galactic environments present and the supernovae will correspondingly exhibit a large range of progenitor-star ages and heavy-element abundances. (This is why we can currently

observe and correct an evolutionary range of SNe Ia using only low-redshift, nearby SNe Ia.) It is only the relative distribution of these environment ages that will change with universal clock time. By identifying matching sets of supernova that come from essentially the same progenitor stars in the same galactic environments, but across a wide variety of redshifts, we can then perform the cosmological measurements using SNe Ia in the same evolutionary state. This only requires that the SN Ia sample sizes are sufficiently large and varied at each redshift that we can find matching examples in sufficient quantities.

We have identified a series of key supernova features that respond to differences in the underlying physics of the supernova (see § 3.2.3 for a complete list and detailed description). By measuring all of these features for each supernova we can tightly constrain the physical conditions of the explosion, making it possible to recognize sets of supernovae with matching initial conditions. The current theoretical models of SN Ia explosions are not sufficiently complete to predict the precise luminosity of each supernova, but they are able to give the rough relationships between changes in the physical conditions of the supernovae (such as opacity, metallicity, fused nickel mass, and nickel distribution) and changes in their peak luminosities. We can therefore give the approximate accuracy needed for the measurement of each feature to ensure that the physical condition of each set of supernovae is well enough determined so that the range of luminosities for those supernovae is well below the systematic uncertainty bound ($\sim 2\%$ in total).

In addition to these features of the supernovae themselves, we will also study the host galaxy of the supernova. We can measure the host galaxy luminosity, colors, morphology, type, and the location of the supernova within the galaxy, even at redshifts $z \sim 1.7$. These observations are not possible from the ground.

1.6 Why a New Satellite?: Design Requirements and Ground- or Space-Based Alternatives

The science goals that we have described drive the design requirements of this experiment. The target statistical uncertainties are closely matched to the target systematic uncertainties, so that the numbers of supernovae, their redshift range, and the quality and comprehensive nature of the dataset of measurements for each supernova all together can achieve the stated cosmological measurements.

In particular, the mirror aperture is about as small as it can be before spectroscopy at the requisite resolution is no longer zodiacal-light-noise limited. A smaller mirror design would quickly degrade the achievable signal-to-noise of the spectroscopy measurements, and drastically reduce the number of supernovae followed. The field of view for the optical imager has been optimized to obtain the follow-up photometry of multiple supernovae simultaneously; a smaller field would require multiple pointings of the telescope and again would greatly reduce the number of supernovae that could be followed. The three-arm spectrograph covers precisely the wavelength range necessary to capture, over the entire target redshift range, the Si II 6250 Å feature that

Requirements	Addresses and Resolves
Detection of every supernova 3.8 magnitudes below peak for $z \leq 1.5$	<ul style="list-style-type: none"> • Rise time measurement • Eliminates Malmquist Bias
SNe Ia at $0.3 \leq z \leq 1.7$	<ul style="list-style-type: none"> • Statistics and lever-arm for the precision measurement of Ω_M, Ω_Λ • Detection of Gray Dust • Detection of SN Ia evolution
~ 75 SNe Ia per 0.03 redshift bin	<ul style="list-style-type: none"> • Statistics and lever-arm for the precision measurement of w • The effect of gravitational lensing by clumped mass is averaged out
Well sampled light-curves between ~ 2 restframe days to ~ 80 restframe days after explosion	<ul style="list-style-type: none"> • Determination of the peak magnitude of each SN Ia • Determination of the light-curve shape of each SN Ia • Detection of SN Ia evolution
Multiple IR and optical color measurements at key epochs	<ul style="list-style-type: none"> • Determination of extinction for each SN Ia • Confirmation of the light-curve shape of each SN Ia
Spectrum for every supernova at maximum covering the rest frame Si II 6250Å feature and that extend from rest frame UV to $1.2\mu\text{m}$	<ul style="list-style-type: none"> • Eliminates non-SN Ia contamination • Measures extinction due to “ordinary” dust outside the Milky Way • Spectral feature – peak magnitude relation
Spectral time series of representative SN Ia with cross-wavelength relative flux calibration	<ul style="list-style-type: none"> • Determine K-corrections • Allow cross-filter comparisons • Detection of Gray Dust • Detection of SN Ia evolution

Table 1.2: Observational requirements to ensure various statistical and systematic errors each contribute uncertainties of $\delta M < 0.02$. The particular sources of error that each requirement addresses are also listed.

both identifies the SNe Ia and provides a key measurement of the explosion physics to identify each supernova’s evolutionary state. In general, more than one critical design requirement has driven each of these instrument choices; for example, the wavelength range of the spectrograph also is required to measure the effects of any “gray dust” on the supernova magnitudes.

Although calculations based on Poisson noise would indicate that ground-based telescopes of sufficiently-large aperture can compete with a smaller space-based telescope, it ignores the difficulty inherent in obtaining accurate photometry of faint sources overwhelmed by a foreground $\sim 10^5\times$ brighter (typical for red/NIR observations for SNe of $z > 0.7$). Achieving photometry with an accuracy of 2% on such a source requires the foreground to be uniform and stable to 2×10^{-7} on small scales. This level of accuracy cannot be achieved from the ground. Furthermore, H_2O absorption will decimate the Si 6250Å and other other key spectral features.

Given this inherent limitation of ground-based observations, a comparison with plausible ground- and space-based alternatives makes it particularly clear why this satellite design is required to achieve the science. Simply finding the supernovae near their explosion date from the ground is the first challenge, even for an entirely dedicated 8-meter telescope with a special-purpose 9-square-degree imager. To detect SNe Ia within ~ 2 restframe days of explosion (as required for the risetime measurement) the photometry must extend to 3.8 magnitudes below peak with a signal-to-noise of 10. From the ground, with its bright sky and atmospheric seeing, this limits the search to redshifts less than $z = 0.6$ —and fewer than 300 SNe Ia per year would be measured. If one begins to degrade the experiment by removing this risetime measurement’s control on systematics, the next key requirement is a measurement of the plateau phase of the light-curve, approximately 2.8 magnitudes below peak, which would limit ground-based searches to redshifts less than $z = 0.7$. Finally, if we give up this plateau-measurement control on systematics, the fundamental measurement requirement is 2% photometry at peak and 15 days after peak (to determine lightcurve width). From the ground, even this minimal dataset is only obtainable to redshifts less than $z = 0.75$. (See Table 5.2 for a summary of these comparisons.)

Using the existing Hubble Space Telescope or even the planned Next Generation Space Telescope (NGST) does not improve the ability to discover these supernovae, since neither telescope has a wide-field camera. With the 8-meter NGST’s 16-square-arcminute field of view, it would require tens of years of full-time searching to obtain a comparable sample of SNe Ia in the target redshift range. The NGST does have a quite useful supernova program planned, but all at higher redshifts than this project, and without the extensive controls on systematic uncertainties that we require. This NGST program is aimed at different science, since it is not possible to study the “dark energy” at redshifts much beyond $z \sim 1.2$, when the universe had smaller scale and the matter-density dominated.

One might wonder if the NGST could be used simply to follow up the photometry of the supernovae discovered with this telescope. This would be possible, but it is a rather wasteful use of the 8-meter’s capabilities; most of time for over half a year would be spent simply slewing the NGST from supernova to supernova, with the shutter open for only a small fraction of the time. (A coordinated wide-field ground-based search with

NGST follow-up would suffer this same problem and further add the disadvantages of discovering the higher-redshift supernova late after explosion.)

1.7 Overview of Feasibility

The essential elements of the project's feasibility have already been studied. We were able to establish many of the baseline design feasibility issues by reference to other satellite missions that have successfully flown, or are currently being built.

- We made a top-down cost estimate based on other similar satellite designs and costs.
- We performed a study of orbit options. We found several options that allowed a workable combination of launch vehicle, mass-to-orbit, thermal control, cosmic-ray load, continuous observing duty cycle, telemetry rates, and power budget.
- We have baselined a three-mirror anastigmat telescope design which provides a diffraction limited wide field of view with minimum obscuration. We are also likely to adopt a flight-proven lightweight glass mirror technology.
- Pointing requirements can be met two ways: (1) using feedback from the focal plane detectors to the spacecraft attitude control system, or (2) using a fast-steering mirror. Both are legacy technologies developed for earth-observing satellites. This image-stabilizing option avoids the need to maintain a precisely stable spacecraft.
- At University of California at Berkeley and at Lawrence Berkeley National Laboratory's microfabrication facility, we have built and tested high-resistivity CCDs that provide greater than 90% quantum efficiency up to $1\text{ }\mu\text{m}$, and are at least ten times more radiation hard than conventional CCDs. This fabrication process has now been transferred to a high-volume commercial vendor, and two fabrication runs are currently in their final stages of processing.
- For some years, much larger CCD and silicon strip arrays have been routinely built by the high energy physics community and operated in comparably inaccessible locations, where they are exposed to high radiation levels.
- We have conducted extensive simulation and modeling of the science reach and performance of various observing strategies and instrument trade-offs.

Our collaboration has the technical experience and competence to formulate, implement, and manage a successful satellite-borne mission. The University of California Space Sciences Laboratory, in particular, has a long tradition in satellite experiments, and has been responsible for project management, spacecraft, scientific packaging, mission and science operations, and ground station operations. Recent and current satellite missions in which collaboration members have played key roles include the Cosmic Background Explorer, the Extreme Ultra-Violet Explorer, the Fast Auroral Snapshot Explorer, and the High Energy Solar Spectroscopic Imager Spacecraft.

1.8 Summary of Other Major Science

The dataset of images and spectra obtained with this wide-field imager and three-channel spectrograph can address other important science goals with very little additional effort in data collection or in the instrument specifications. Although these science goals will not be discussed in detail in this preview document, it is important in particular to note that we can obtain complementary measurements of the cosmological parameters with completely independent measurement methods.

Weak lensing. Because the observation strategy observes the same patches of sky repeatedly over a year of supernova observations, a very deep, high-resolution image can be added together from thousands of images taken at every orientation of the spacecraft. This is an ideal way to look for weak-lensing elongations of distant galaxies, since the optical distortions of the image will be small and well characterized. Such images of several dozen square-degree fields can constrain the cosmological parameters (see § 6.3.4) in a manner complementary to the SN Ia measurements, with different systematics.

Type II supernovae. As we discover and follow the SNe Ia, we will also discover and have the option of following SNe II. While these supernovae are not of predictable luminosity, they are close enough matches to a black body that their luminosities can be determined from the size and temperature of their photospheres, along with a fit to any spectral deviations from black body. (Since our experiment provides a very tight constraint on the date of explosion and the velocity of the expanding gas, the size of the photosphere will be easy to determine.) Most SNe II are about six times fainter than the prototypical SNe Ia, so most will not be studied with early detections beyond redshifts $z \sim 0.5$. However since SNe II are much more frequent than SNe Ia, we can afford to study the brightest few percent and this will extend the SN II study beyond $z = 1$. The sources of systematic uncertainty for these SNe II measurements would generally be different from the SNe Ia systematic uncertainties.

There is also important science to be gained from this project that is not aimed specifically at the cosmological models. It is clear, for example, that the final set of very deep, wide field images would become a resource for all of astrophysics, as the Hubble Deep Fields have been.

1.9 This Proposal

We envision this satellite project as a two-stage process, consisting of a first study phase followed by a final design and construction phase. This proposal presents the overall science goals of the project in its entirety, and a first look at the broad-brush technical design and feasibility. More specifically this proposal also presents the plans for the first phase of the project. In Phase I, we will prepare a ZDR (“zeroth-order design report”), followed by a CDR (“conceptual design report”) which will describe

in detail all technical aspects of the experiment and full cost and schedule analysis for the construction phase.

Phase I would complete the equivalent of a “Phase A” and the concept studies which would advance the critical technologies to a state of readiness that would minimize cost, schedule and technical risk follows. Examples of current development activities include CCD commercialization and telescope optics design.

During this same Phase I period, the ground-based studies will be carried forward to provide empirical support for the final science design of the SNAP mission. Further theoretical analyses of supernovae and their galactic environments will also contribute at this stage.

The fundamental questions and surprising discoveries of recent years make this a fascinating new era of empirical cosmology. This proposed satellite project presents a unique opportunity to extend this exciting work and advance our understanding of the universe. The origin and destiny of the universe have intrigued humanity for at least as long as there are written records. We live at a time when we can begin to find answers.

Part II

SNAP Physics

Chapter 2

Theoretical Overview

2.1 Cosmological Parameters

The Cosmological Principle states that the universe is homogeneous and isotropic. From this it follows that there is a universal expansion factor $a(t)$ describing the scale of the universe as a function of time. The dynamics of $a(t)$ are determined by General Relativity and depend on the universe's geometry and the energy density of the different components that fill the universe. A universe with nothing but a matter energy density equal to the critical value $\rho_c = 3H_0^2/(8\pi G) \approx 10^{-29} \text{ gm cm}^{-3}$ is poised between ultimate expansion and ultimate contraction. If there is a non-zero cosmological constant, it too contributes to the energy density. The relative importance of the two contributions is expressed by the dimensionless quantities

$$\Omega_M = \frac{8\pi G \rho_M}{3H_0^2}, \quad \Omega_\Lambda = \frac{\Lambda}{3H_0^2} \quad (2.1)$$

where $H_0 \equiv \dot{a}/a|_{\text{now}}$ is the Hubble parameter today and Λ the cosmological constant.

Within the Friedmann-Lemaitre-Robertson-Walker cosmological model, the bulk properties of the universe can be described by H_0 , Ω_M , and Ω_Λ . As the only parameters that determine the bulk kinematics of the universe, they fix the age of the universe and specify its past and future dynamics.

These three fundamental cosmological parameters have long been the subjects of investigation. Previous measurements of Ω_M have generally come from the study of self-gravitating dynamical systems. Previous Ω_Λ limits have generally come from counting statistics of high-redshift $z \gtrsim 1$ objects, which measure differential volumes. The measurement of H_0 has been controversial and only now are we seeing the slow convergence to a generally accepted value, $H_0 \approx 65 \text{ km/s/Mpc}$.

2.2 The Dark Energy

A standard cosmology based on inflation was established in the early 1980s. In this picture, inflation exponentially expands a small patch of space and produces a flat universe, one with total energy density precisely equal to the critical value. This

would explain why the universe does not have large curvature and why the Cosmic Microwave Background is so uniform across scales larger than the then-horizon of the universe. Inflation also generates adiabatic scale-invariant perturbations, which serve as seeds for large-scale structure (LSS) formation. Evidence for dark matter, on the other hand, has been present since the early work of Zwicky (1937) six decades ago, when he measured radial velocities of galaxies in the Coma cluster and concluded that they cannot be explained by the visible mass. Starting in the 1970s, comparisons of nuclear abundances with the predictions of big-bang nucleosynthesis established that most matter in the universe is non-baryonic and that baryons contribute no more than 5% of the critical energy density [for reviews of the dark-matter conundrums, see Trimble (1987); Turner (1999); Copi, Schramm, & Turner (1995)]. Observations of the radial motions of stars within galaxies revealed that there is non-luminous, dark matter.

The simplest cosmological model consistent with inflation, the one that was favored early on, is the Einstein - de Sitter universe with $\Omega_M = 1$. The Einstein - de Sitter universe is flat and contains matter only and no cosmological constant.

However, during the last 10-15 years cosmologists have begun to doubt this picture for several reasons. First of all, it has been established that there is not enough matter to make a flat universe, and that the energy density in matter (baryonic or otherwise) may be closer to $\Omega_M \approx 0.35 \pm 0.1$. These low values of Ω_M were obtained using several approaches: the evolution of the number-density of rich clusters of galaxies (Bahcall & Fan, 1998); mass estimates of galaxy clusters, either through the Sunyaev-Zeldovich effect (Carlstrom et al., 1999) or through measurement of the X-ray flux (J. Mohr & Evrard, 1999); and the power spectrum of Large Scale Structure (LSS), characterized by the “shape” parameter $\Gamma \approx \Omega_M h \sim 0.25$ (Efstathiou, Bond, & White, 1992) (where $H_0 = 100 h$ km/sec/Mpc), which for $h \approx 0.7$ implies $\Omega_M \sim 0.4$. Meanwhile, a flat universe is favored not only by theorists who believe in inflation, but also by preliminary evidence from Cosmic Microwave Background (CMB) data (Dodelson & Knox, 1999; Melchiorri et al., 1999). A flat universe ($\Omega_{\text{total}} = 1$) together with $\Omega_M < 1$ thus suggests that matter is not the only energy component of the universe.

New, direct evidence for this unidentified energy, which we will call the “dark energy,” came with the magnitude/redshift measurements of SNe Ia at high redshifts by two independent teams (Perlmutter et al., 1999; Riess et al., 1998). The observed high-redshift supernovae are fainter than would be expected if all energy density were due to matter or to matter together with space curvature.

This faintness can be understood if, contrary to expectation, the universe is accelerating. The General Theory of Relativity shows that this happens if the *total* equation of state ratio (that is, the total pressure divided by the total density in the universe) is less than $-1/3$. Since the equation of state ratio for (pressureless) matter is zero, this requires the existence of an energy component which has strongly negative pressure, and whose energy density is $\Omega \sim 0.6 \sim 1 - \Omega_M$. If the energy were nearly or exactly smooth, it would not have been seen in large-scale structure surveys. The most obvious candidate is energy of the vacuum, the cosmological constant (Λ).

The cosmological constant was first introduced by Einstein as a term in his equations of General Theory of Relativity in order to produce a static universe, only to be

rejected by him as his “greatest blunder” once Hubble discovered that the universe was expanding. Physicists have reintroduced Λ from time to time, only to discard it again. If there is a cosmological constant, its energy density cannot be much greater than the critical energy density. This “measurement” presents one of the most serious problems in all of particle physics: why is ρ_Λ so small? A straightforward dimensional argument taking its scale from Newton’s gravitational constant would predict an energy density of the vacuum 10^{120} times bigger than the upper limit quoted above. For an excellent review of the cosmological constant problem, see Weinberg (1989).

Dark energy candidate	w ($p = w\rho$)
Λ	-1
Cosmic strings	$-1/3$
Domain walls	$-2/3$
Quintessence (tracker)	$\& -0.8$
Quintessence (PNGB)	time-variable

Table 2.1: Some candidates for the dark energy and their respective equation of state ratios.

There are alternative sources of energy density whose equation of state $p = w\rho$ has $w < -1/3$. A scalar field rolling down its potential and providing significant energy density was proposed and investigated in the late 1980’s (Ratra & Peebles, 1987). With recent evidence for the accelerating universe, there was a surge of interest in these scalar fields, also called “quintessence” (Caldwell, Dave, & Steinhardt, 1998; Zlatev, Wang, & Steinhardt, 1999). For certain effective potentials the energy density in the quintessence field tracks that of the dominant component (radiation or matter) and can become dominant at late times (Steinhardt, Wang, & Zlatev, 1999). These “tracker” solutions can thus provide an answer to the “cosmic coincidence problem”: why do we live at a special time in the history of universe when the energy densities in matter and dark energy are the same order of magnitude? Quintessence couples to matter only gravitationally and clusters only on very large scales (larger than the horizon). In order for big-bang nucleosynthesis to proceed unhampered and for baryonic structure such as galaxies to grow sufficiently on small scales, quintessence is required to be sub-dominant throughout the past history of the universe and can begin dominating

the energy density only recently ($z \sim few$).

Another class of scalar-field models are Pseudo-Nambu-Goldstone Boson (PNGB) models (Frieman et al., 1995; Coble, Dodelson, & Frieman, 1997). In these models, the field is initially at rest on the potential, held by large friction (large Hubble parameter) in the early universe. The field starts rolling at late times, when the Hubble parameter drops to lower values. This generally happens at redshifts of a few, and that is when the field is dynamical.

Yet another class of candidates are cosmic defects (Vilenkin, 1984; Vilenkin & Shellard, 1994), of which cosmic strings and domain walls are the most likely dark energy candidates. Cosmic defects are produced during phase transitions in the early universe, and can be thought of as strings or walls with energy density. Cosmic defects have negative pressure ($w = -1/3$ for strings and $w = -2/3$ for domain walls) which makes them suitable candidates for the dark energy.

These dark energy candidates and their respective equations of state ratios are given in Table 2.1. “Ordinary” matter candidates like axions, primordial black holes, and lightest supersymmetric particles are candidates for dark matter, but cannot play the role of dark energy since their equation of state ratio is $w = 0$, not $w < -1/3$.

Chapter 3

Summary of Current Results from Type Ia Supernovae

3.1 Introduction

Numerous studies have shown that SNe Ia can be used as calibrated “standard candles” with an intrinsic dispersion in peak magnitudes, corrected for various understood effects, of ~ 0.1 mag (Hamuy et al., 1996; Riess, Press, & Kirshner, 1996). The mass density Ω_M , and the normalized cosmological constant Ω_Λ , together describe the space-time geometry of the universe and can be probed using the *relative* luminosity distances to such calibrated standard candles scattered throughout the observable universe. Over a modest range in redshift the luminosity distance is nearly degenerate for various combinations of $(\Omega_M, \Omega_\Lambda)$. However, Goobar & Perlmutter (1995) showed that it is possible to break this degeneracy if the data extend far enough in redshift. Using this approach, two independent research groups have presented compelling evidence for an accelerating universe from the observation of high-redshift SNe Ia (Perlmutter et al., 1999; Riess et al., 1998).

Measurements of Ω_M and Ω_Λ use the magnitude-redshift relation for SNe Ia over a range of redshifts (Perlmutter et al., 1997, 1998, 1999). The basic procedure consists of *a)* discovering large numbers of high- z SNe Ia (> 20 per observing run) while they are still on the rise, *b)* obtaining spectroscopic follow-up within a few days of discovery to confirm the SN type and redshift, *c)* acquiring ground-based and HST light curve photometry, and *d)* analyzing the data to obtain peak magnitudes and measure Ω_M and Ω_Λ .

In the following section, the physics behind a SN Ia explosion is reviewed in some detail. Following this, we briefly summarize the experimental results based on observations of several dozen supernovae.

3.2 The Physics of Type Ia Supernovae

3.2.1 Progenitors to Explosion

SNe Ia are among the brightest known objects in the universe. The classification of these objects is based purely on their optical spectra: “Type I” corresponds to the absence of hydrogen lines, and “a” for the presence of a strong Si II absorption feature (with a trough at ~ 6150 Å). Since they form a nearly homogeneous class and simple selection criteria can make the observed dispersion quite small, they are natural cosmological probes (Vaughan et al., 1995). The observed homogeneity has led to a search for a homogeneous progenitor that would satisfy the requirements of lacking hydrogen and occurring in both spirals and elliptical galaxies. This has led to the assumption that the SNe Ia progenitor involves the thermonuclear disruption of a Chandrasekhar-mass white dwarf. The current status of the search for the identification of the SNe Ia progenitor is reviewed in Branch et al. (1995), with the basic two models both involving white dwarfs in a binary system (one where hydrogen is accreted and turned into C/O through fusion on the surface layers until it approaches the Chandrasekhar limit, the other where two white dwarfs coalesce as gravitational radiation shrinks their orbits).

Observations of SNe Ia show that they have a characteristic light curve shape that can be understood in terms of the radioactive decay of ^{56}Ni (fused in the explosion) to ^{56}Co to ^{56}Fe (Arnett, Branch, & Wheeler, 1985), in which the γ -rays accompanying these decays get thermalized and power the optical light curve. They also have a characteristic development of their optical spectra: near the time of maximum light the spectrum contains lines of intermediate-mass elements from oxygen to calcium; and at late times the spectrum becomes dominated by iron-peak lines. Hydrodynamic explosion models to explain these observations have included deflagration models such as the “W7” model of Nomoto, Thielemann, & Yokoi (1984). While this model is somewhat hand-crafted to fit the observed spectra and suffers from an overproduction of neutron rich species, it remains the standard in the field. The “DD” (Khokhlov, 1991a; Woosley, 1991, delayed detonation,) and “PDD” models (Khokhlov, 1991b, Pulsating Delayed Detonation,) improve the predicted nucleosynthetic yield and gives qualitative agreement with the observed spectra and light curves (Höflich & Khokhlov, 1996).

3.2.2 Light Curves

The model for the photometric history of SNe Ia has been refined from a homogeneous description (Leibundgut, 1988; Branch & Miller, 1993; Sandage & Tammann, 1995) to one characterized by a relation between peak luminosity and light curve shape (Phillips, 1993; Hamuy et al., 1993, 1996; Riess, Press, & Kirshner, 1995; Kim et al., 2000). The slower, broader light curves are intrinsically brighter at peak than the faster, narrower light curves. Recognizing and exploiting such relations have led to a great increase in value of SNe Ia as extragalactic distance indicators. Extending luminosity/light curve relations to multiple passbands separates intrinsic brightness differences from the competing effects of dust and distance on the light of SNe Ia (Riess, Press, & Kirshner, 1996). Distances with $\sim 5\%$ uncertainty can be obtained using the light

curve shapes of well-observed supernovae.

In Figure 3.1 we see how knowledge of the B -band “stretch”, s , can help determine the relative luminosity of several well observed nearby SNe Ia. From an $s = 1$ template, which is similar to the Leibundgut template for SNe Ia (Leibundgut, 1988), all known light curves for SNe Ia can be reproduced quite reasonably from the U -band through the V -band (over the time range $-19 \cdot t - t_0 \cdot +40$) by stretching (or compressing) the time axis of the light curve about maximum light by the factor s . The correlation between the stretch and the SN Ia’s brightness is not surprising. SN Ia which produce more ^{56}Ni are more luminous, and hotter, leading to higher overall opacities (Höflich & Khokhlov, 1996). With higher opacities one increases the diffusion time and thus the time the SN Ia takes to reach peak and fade after peak (Arnett, 1982).

3.2.3 Spectra

The optical spectra of SNe Ia are rich in information [see Filippenko (1997) for a review]. Many of the elements synthesized and ejected in the explosion have been identified despite the blending of their high-velocity profiles (Branch et al., 1983; Nugent, 1997). In addition, the relative strengths of some spectral features have been shown to correlate with SN Ia peak luminosity (Nugent et al., 1995a). This is highlighted in Figure 3.2 where we see the ratios of various spectral features in the maximum light spectra of SNe Ia plotted against their relative peak brightnesses. As the supernova evolves, predictable casts of features appear and disappear, illuminated by the wavelength-dependent photosphere’s recession through the synthesized layers. Due to the amazing homogeneity of SNe Ia the temporal evolution of these features is sufficiently reliable to be used as a clock to determine the current age of a SN Ia to a precision of 1-2 days (Minkowski, 1939; Riess et al., 1997). Figure 3.3 displays the temporal evolution of a typical SN Ia starting at ~ 14 days before maximum light sampled from several nearby SNe Ia.

3.2.4 Environmental Influences

One of the more recent developments in SN Ia modeling has been the inclusion of differences in the progenitor’s make-up prior to exploding the model. This has led to a wonderful, and simple explanation for the stretch-luminosity relationship. As stated above, differences in the total fused ^{56}Ni mass can account for the relationship between stretch and peak brightness. Yet how do we wind up with these differences in the first place? One explanation can be seen in the models of Höflich, Wheeler, & Thielemann (1998). It is well known that differences in the metallicities of 7-10 M_{\odot} main sequence stars can produce both differences in the total C-O core mass as well as the C/O ratio [see Umeda et al. (1999) for a full explanation]. During the thermonuclear explosion white dwarfs with a smaller C/O ratio ($\approx 2/3$) than a typical white dwarf (≈ 1) will produce less ^{56}Ni and have a smaller amount of kinetic energy. This yields a SN Ia which has a smaller peak brightness and narrower light curve. This also has an effect on the spectral ratios mentioned above.

In simulations, Höflich, Wheeler, & Thielemann (1998) have altered the metallicity

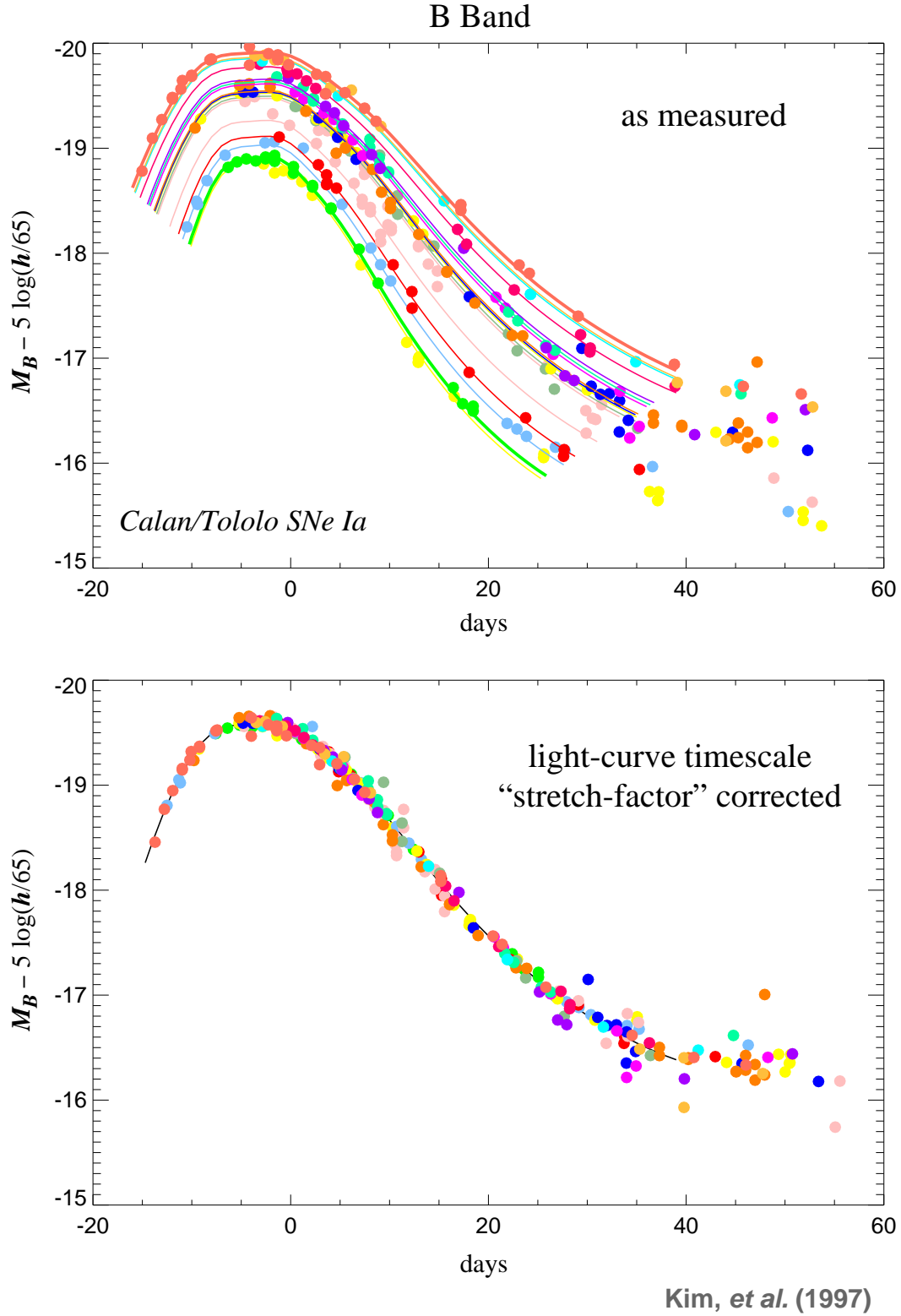


Figure 3.1: The relationship between “stretch” and the luminosity of a SN Ia is seen in these two panels. The top panel shows several SNe Ia from the Calán/Tololo Supernova Survey arranged by their observed relative luminosity (all objects were in the Hubble Flow). The bottom graph shows how “stretch” can be used to describe the light curves with one parameter.

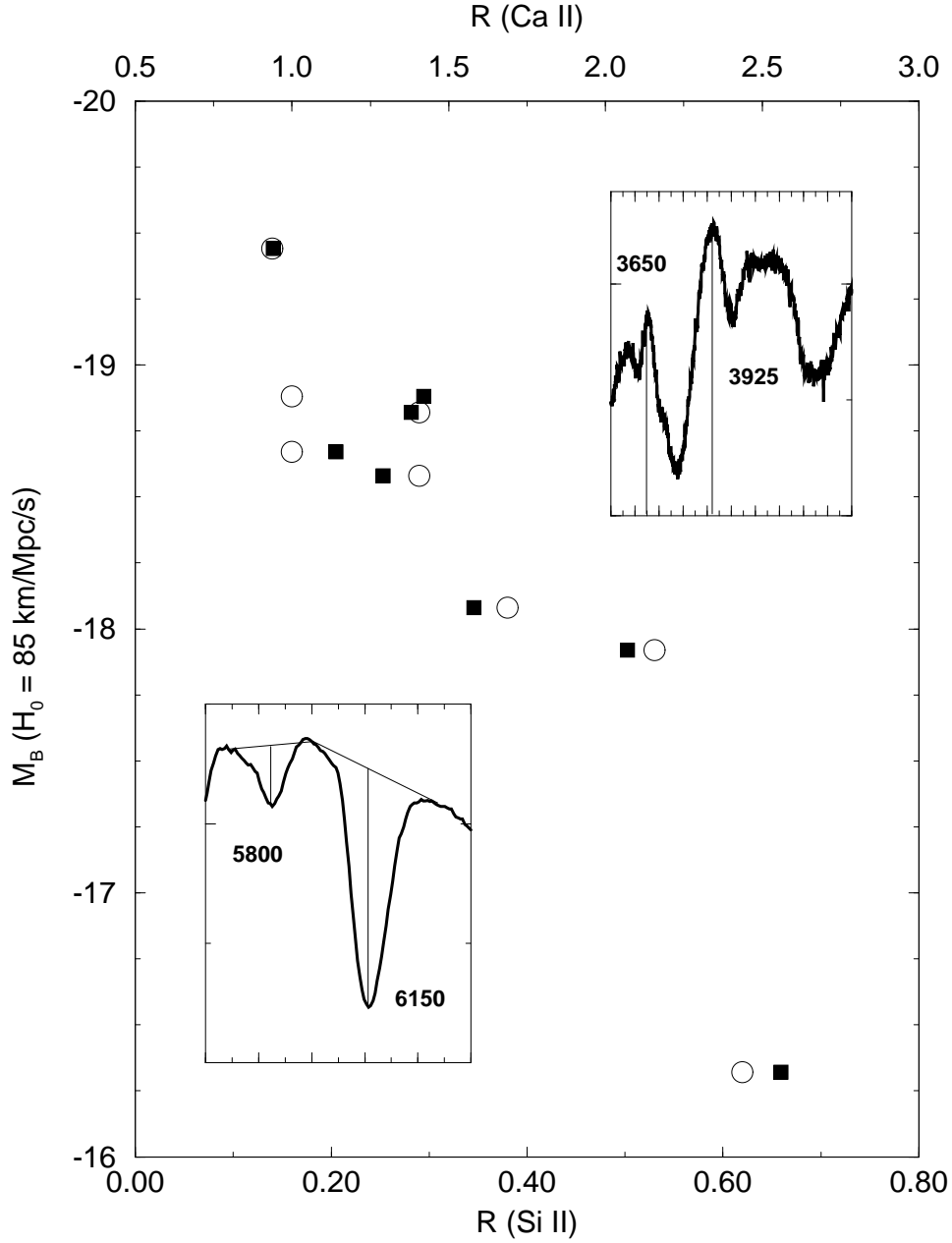


Figure 3.2: Observed M_B vs. $\mathcal{R}(\text{Si II})$ (open circles) and $\mathcal{R}(\text{Ca II})$ (filled squares). The inset graphs illustrate how the ratios were measured. (Nugent et al., 1995a)

of the progenitor in the outer, unburned layers. This has a strong influence on the UV spectrum. Lentz et al. (1999) has quantified these effects by varying the metallicity in the unburned layers and computing their resultant spectra at maximum light with the

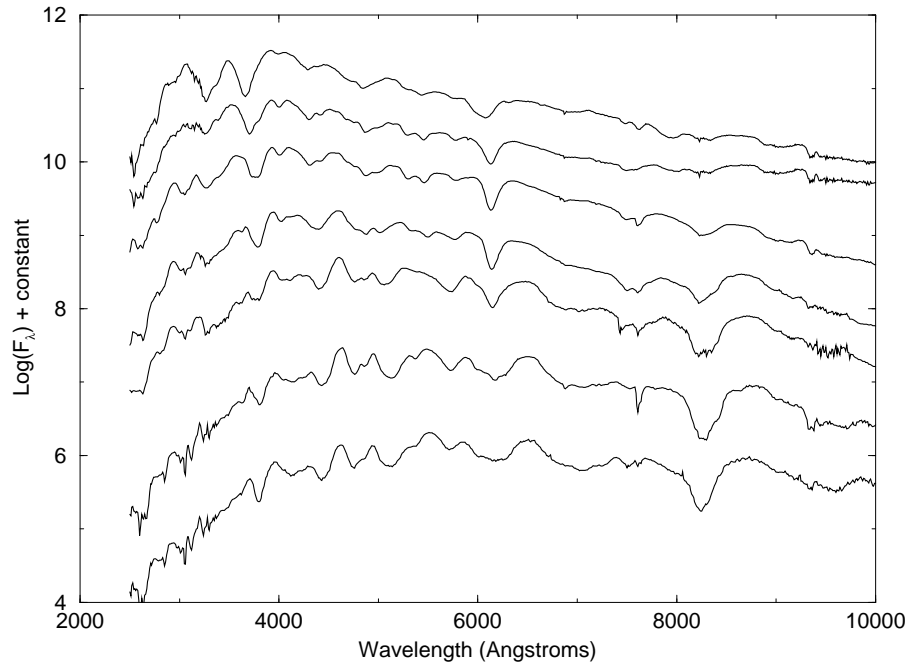


Figure 3.3: A graph of the weekly temporal evolution of a SN Ia starting at ≈ 14 days before maximum light and extending to ≈ 70 days after maximum (Nugent et al., 1999). Note the terrestrial atmospheric features at 7600\AA and 9500\AA .

spectrum synthesis code PHOENIX (Nugent et al., 1997; Nugent, 1997). In Figure 3.4 we see the large variations produced in the UV for SNe Ia of differing metallicity. This result is not surprising since the UV spectrum is created by millions of opaque iron-peak lines. Reducing the metallicity results in a lower opacity and higher flux in the UV. Further observations here will be able to quantify these differences at several epochs. In Figure 3.5 we see the affect on the Si II lines in the optical. The metallicity differences are most likely the cause of the “velocity differences” among SNe Ia that were seen in Branch & van den Bergh (1993).

Further observations in the UV and optical will allow us to quantify these differences at several epochs. We should then be able to look for correlations between these differences and peak brightness, light-curve shape and host galaxy type. With these additional data sets we will be able to put very tight constraints on acceptable progenitors, explosion mechanisms and peak luminosities.

3.3 Results from the Observation of Type Ia Supernovae

There are currently two independent teams that are running coordinated search and follow-up observations of high-redshift supernovae. They are the Supernova Cosmology Project (SCP) (Perlmutter et al., 1997, 1998, 1999) which was launched in 1989, and the High-Z Supernova Search Team (HIZST) (Schmidt et al., 1998; Garnavich et al.,

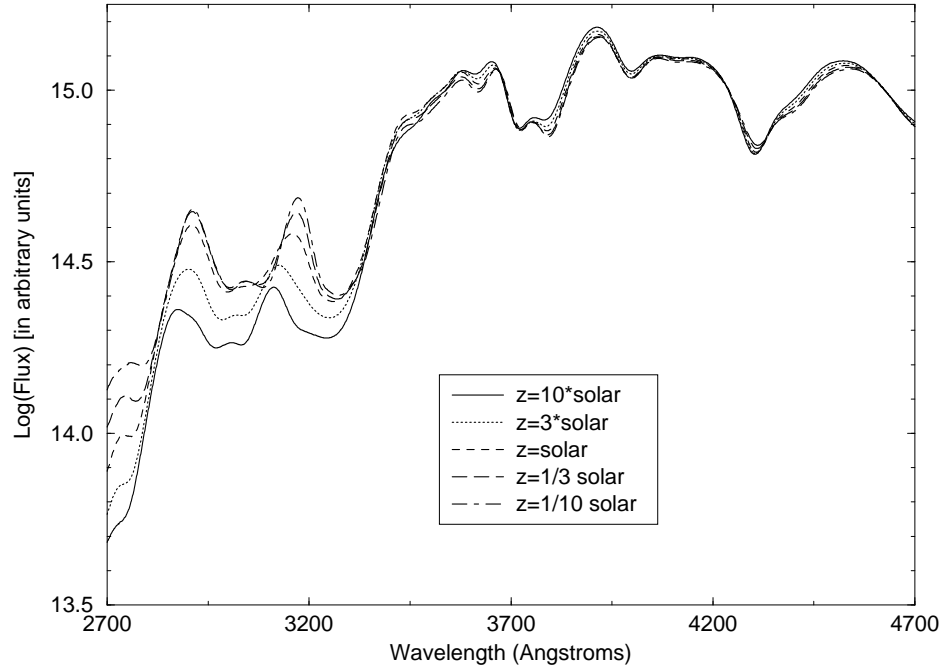


Figure 3.4: Maximum light spectrum synthesis models of W7 (a deflagration model by Nomoto, Thielemann, & Yokoi (1984) of a SN Ia) with varying metallicities.

1998; Riess et al., 1998) which found their first distant supernova in 1995.

Both groups use the same basic search techniques and resources and to date have together provided ~ 100 SNe Ia with spectral confirmation discovered at $z > 0.3$. The mean redshifts of the discovered supernovae have been steadily increasing with each successive search run, as we have specifically tailored the filters and exposure times to search at progressively larger distances. We have reached the point where we are now starting to build a statistically significant sample of $1 < z < 1.25$ supernovae.

The current results from both teams (Perlmutter et al., 1999; Riess et al., 1998) using a (largely) disjoint set of high-redshift supernovae studied with different photometry and analysis techniques lead to remarkably similar conclusions. We present here the Perlmutter et al. (1999) results which are statistically more significant.

A Hubble diagram based on results obtained by the SCP for 42 SNe with $0.18 < z < 0.83$ is shown in Fig. 3.6. It shows that we live in a low mass-density universe, and presents strong evidence for a cosmological constant [Perlmutter et al. (1999); see also Riess et al. (1998)]. These data indicate that $\Omega_M = 0.28 \pm 0.08$ for a flat universe, and constrain the combination $0.8\Omega_M - 0.6\Omega_\Lambda$ to -0.2 ± 0.1 . Similar results were obtained by HIZST.

The current data imply the existence of a dark energy which might be from the cosmological constant. Alternatively, it could be that this dark energy is due to some other primordial field for which $\rho \neq -p$, leading to different dynamical properties than a cosmological constant. By parameterizing the field's equation-of-state ratio as $w = p/\rho$, we can currently place some constraints on possible different dark energy

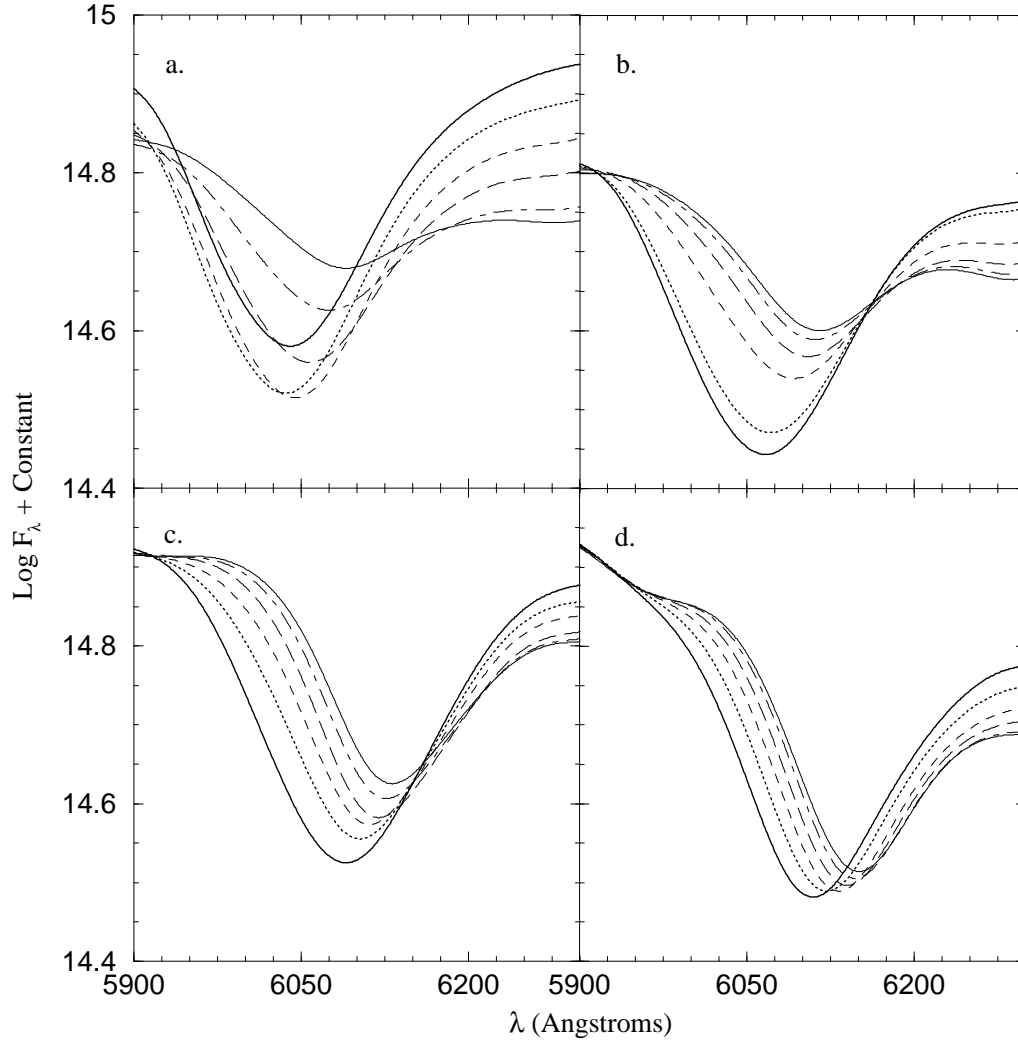


Figure 3.5: Spectrum synthesis models of W7 (a deflagration model by Nomoto, Thielemann, & Yokoi (1984) of a SN Ia) with varying metallicities starting at 2 weeks before maximum light and extending to a week after. The curves are the same as in Figure 3.4.

models. Perlmutter et al. (1999) find that for a flat universe, the data are consistent with a cosmological-constant equation of state with $0.2 \lesssim \Omega_M \lesssim 0.4$ (Figure 3.7). Cosmic strings ($w = -1/3$) are already strongly disfavored.

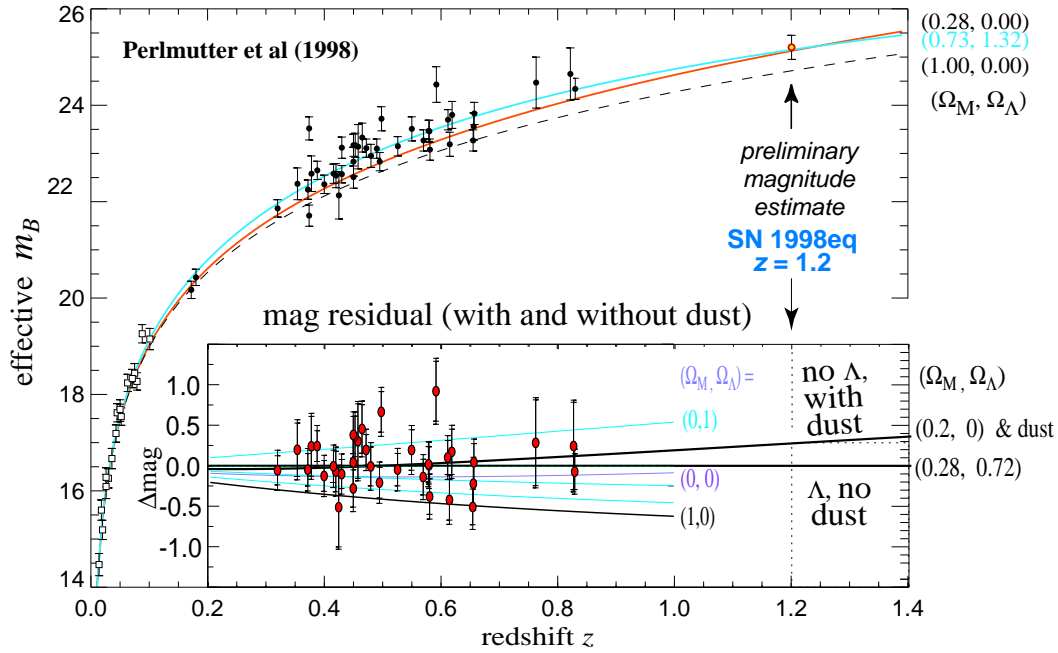


Figure 3.6: Hubble diagram for 42 high- z SNe (Perlmutter et al., 1999). The best-fit world model with $(\Omega_M, \Omega_\Lambda) = (0.73, 1.32)$ is drawn through the data (solid line). The Einstein-de Sitter case $(1.0, 0.0)$ is strongly excluded by the current data (dashed line). The case $(\Omega_M, \Omega_\Lambda) = (0.28, 0.00)$ indicates that some contribution from the cosmological constant is required for values of Ω_M favored by dynamical measurements. The magnitude difference between the best-fit world model and suitable ones with $\Omega_\Lambda=0$ show redshift dependencies which would be very hard to mimic within the context of SNe evolution or gray dust hypotheses (see inset panel). By extending our survey beyond $z=1$, the *form* of the Hubble diagram alone would become sufficient evidence to support a cosmological constant. The preliminary magnitude estimate of our highest redshift SN1999eq at $z = 1.2$ is suggestive, but more analysis and more SNe at this redshift are necessary.

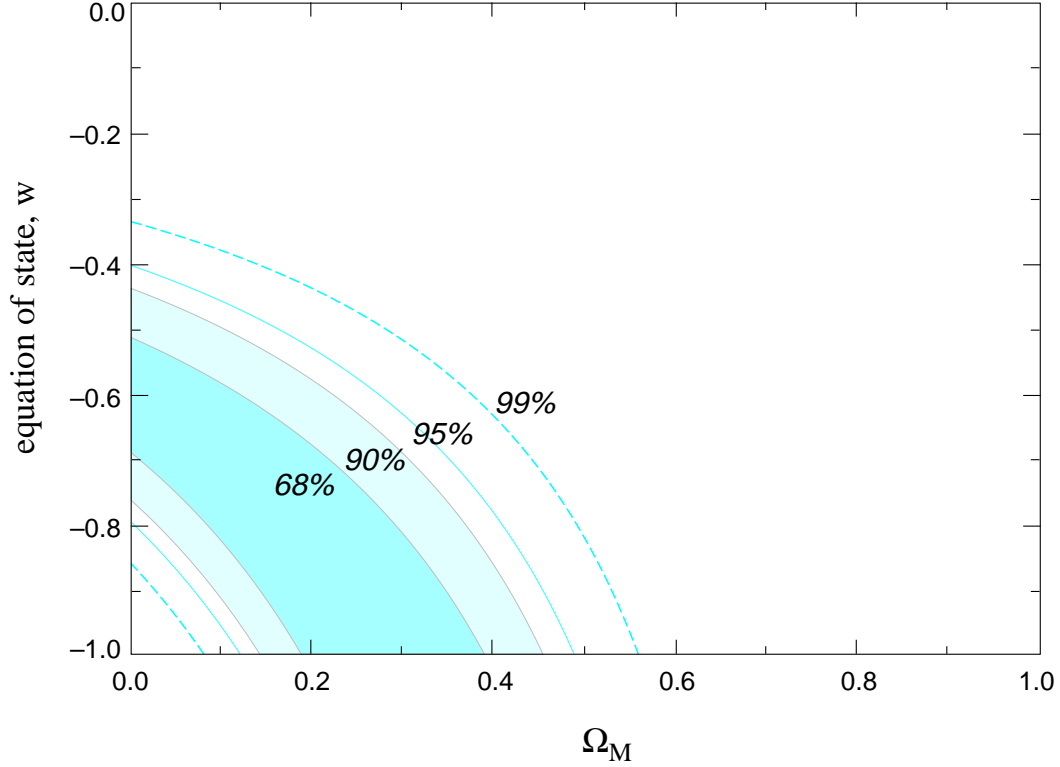


Figure 3.7: Best-fit 68%, 90%, 95%, and 99% confidence regions in the Ω_M - w plane for an additional energy density component, Ω_w , characterized by an equation-of-state ratio $w = p/\rho$. (If this energy density component is Einstein’s cosmological constant, Λ , then the equation of state is $w = p_\Lambda/\rho_\Lambda = -1$.) The fit is for the supernova subset of our primary analysis, Fit C, constrained to a flat cosmology ($\Omega_M + \Omega_w = 1$). The two variables \mathcal{M}_B and α are included in the fit, and then integrated over to obtain the two-dimensional probability distribution shown.

Chapter 4

Science Reach of the Proposed Satellite

4.1 Introduction

In this chapter we describe quantitatively the precision with which SNAP will allow us to pin down the cosmological parameters of the universe, and explain how it provides a unique capability to probe the dark energy sector and distinguish between various models. We then present a detailed analysis of the limiting systematic errors, and describe a program of observations that will constrain the sources of systematic error in supernova-based cosmology.

4.1.1 SNAP's Data Set and the Assumed Fiducial Model

The SNAP one-year baseline mission calls for the observation of ~ 2000 supernovae distributed per year from $z = 0$ to $z = 1.7$ with individual peak-brightness uncertainties of 0.15 mag per supernova, roughly the quadratic sum of the 0.1 mag intrinsic SN Ia magnitude dispersion after correction and the 0.1 mag uncertainty in the corrected peak magnitude targeted by SNAP. The distribution of supernovae in redshift will not be uniform; most will be in the interval $0 < z < 1.2$, and about a hundred at $z > 1.2$. In addition to the statistical uncertainties, we anticipate systematic errors of $\lesssim 0.02$ magnitudes, for each $\Delta z \sim 0.03$.

To estimate the accuracy of parameter determination from the proposed experiment, we performed Monte-Carlo simulations assuming a fiducial model with $\Omega_M = 0.28$, $\Omega_\Lambda = 0.72$ and $w = -1$. We only considered the part of the parameter space where the weak energy condition holds, i.e. where $w \geq -1$ ($w < -1$ is usually not considered, as accommodating such models requires a modification of General Relativity). We refer to the energy density in the dark component as $\Omega_{\text{D.E.}}$ (and not Ω_Λ) whenever its equation of state ratio is different from -1 .

As an example, we model the systematic error for each supernova as a correlated linear increase in magnitude, $\Delta m_{\text{sys}}(z) = 0.03 z/z_{\text{max}}$ with $z_{\text{max}} = 1.7$ and z the redshift of any given supernova. Thus, the most distant supernovae in this model appear

to be fainter by 0.03 mag (e.g. due to the presence of gray dust and/or evolutionary effects).

Unless otherwise noted, all simulations assume the baseline SNAP mission. Additional very-low-redshift supernovae that are planned to be observed from the ground are not included; their inclusion would further strengthen our arguments about parameter determination.

In the following sections we describe the expected uncertainties on the cosmological parameters using SNAP alone, and by combining SNAP with other complementary experiments. We also illustrate SNAP’s ability to distinguish between models that appear degenerate to other experiments, as well as its ability to explore the dark matter sector.

4.2 Cosmological Parameter Determination with SNAP

4.2.1 Exploring Higher Redshifts ($z \gtrsim 1$)

Energy density in any component scales with redshift as $(1+z)^{3(1+w)}$, where $w = p/\rho$ is its equation of state ratio. Matter is pressureless ($p = w = 0$), while strongly negative w is observationally favored for the dark energy ($w \lesssim -1/2$). Therefore, if the negative-pressure component is dominant or comparable to the energy density in matter today, it had to be sub-dominant in the early universe, until $z \sim 1$. There is another piece of evidence that the dark energy was sub-dominant until $z \sim 1$. Were it not the case and the universe were dominated by the negative-pressure component, the growth of structure would have been strongly suppressed, and galaxies and clusters would not have had time to form. Supernovae probe precisely the interesting redshift range where dark energy becomes important, $0 < z \lesssim 2$, which makes them a uniquely efficient probe of this mysterious component.

Figure 4.1 shows the statistical uncertainty in the cosmological parameters Ω_M , Ω_Λ , and Ω_k and that in the equation of state ratio of the dark energy, w , both as a function of maximum redshift probed. We assumed 2366 (selected from a 2 year sample, based on matching “normal” SN Ia criteria) supernovae in the range $0 \leq z \leq z_{\max}$ with a distribution scaled from the $z_{\max} = 1.7$ distribution targeted by our experiment. Each supernova is given an individual calibrated statistical uncertainty of 0.15 magnitudes. Fisher-matrix analysis was used to obtain the uncertainties [the Fisher matrix uses expansion of the log-likelihood function about its maximum in parameter space, and estimates the best possible statistical errors on parameters calculated from a given data set; see Tegmark, Taylor, & Heavens (1997)]. From this figure we conclude the following: 1) using SNe Ia that extend to redshifts of $z = 1$ and higher helps in obtaining higher accuracy because one covers a larger interval of “action” of the dark energy, and 2) going to redshifts much higher than $z \approx 2$ is not useful because dark energy’s contribution to the energy-density is negligible for $z \gtrsim 2$.

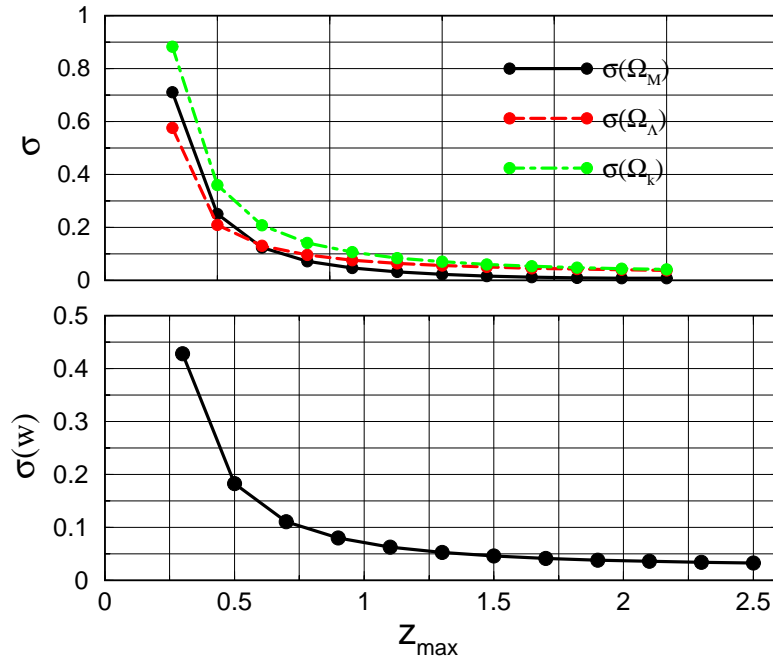


Figure 4.1: Accuracy in parameter estimation as a function of maximum redshift probed in SN Ia surveys. Shown is the statistical uncertainty in the determination of the cosmological parameters Ω_M , Ω_Λ , and Ω_k (upper panel; knowledge of w assumed) and equation of state ratio w (lower panel; flat universe assumed) each as a function of maximum redshift probed z_{\max} . In each case there are 2366 supernovae distributed from $z = 0$ to z_{\max} with statistical uncertainties only. Exploring redshifts between 0 and 1.5 is optimal, since this is where most of the dark energy action occurs. Going to redshifts beyond $z \sim 1.8$ would bring very little improvement in parameter-determination accuracy, as the dark energy is dynamically unimportant at such high redshifts.

4.2.2 Summary of the expected parameter uncertainties

The proposed experiment would put very strong constraints on the energy contents of the universe. Because the distance-redshift relation depends only on a handful of parameters, these parameters would be well determined by the high-quality data provided by our mission. Since the experiment would probe redshifts at which the dark energy contributes significantly to the total energy density and where it affects evolution of the universe, this especially interesting component would be well characterized.

	σ_{Ω_M}		σ_{Ω_Λ} (or $\sigma_{\Omega_{D.E.}}$)		σ_w		$\sigma_{w'}$	
	stat	sys	stat	sys	stat	sys	stat	sys
$w = -1$	0.02	0.02	0.05	< 0.01	—	—	—	—
$w = -1$, flat	—	—	0.01	0.02	—	—	—	—
$w = \text{const}$, flat	—	—	0.02	0.02	0.05	< 0.01	—	—
Ω_M, Ω_k known $w = \text{const}$	—	—	—	—	0.02	< 0.01	—	—
Ω_M, Ω_k known $w(z) = w + w' z$	—	—	—	—	0.08	< 0.01	0.12	0.15

Table 4.1: A summary of statistical and systematic uncertainties in parameter determination from one year of SNAP data. These numbers (all $1\text{-}\sigma$) are obtained using Monte Carlo simulations with fiducial cosmological model and assumed data set as described at the beginning of this chapter. Further assumptions are listed in the left column. Note that the systematic errors in the data have varying influence on the parameter uncertainties that strongly depends on the parameter space considered and on the parameter in question.

Table 4.1 shows the predicted statistical and systematic errors on cosmological parameters, assuming statistical and systematic uncertainties in the data as described in Section 4.1.1. All numbers in the table are obtained using Monte Carlo simulations (Fisher matrix analysis gives statistical uncertainties that are comparable to those from Monte Carlo). As one can see, SNAP will not only be able to pin down the parameters Ω_M , $\Omega_{D.E.}$ and (constant) w , but will also be able to constrain the variation of the equation of state ratio, w , with redshift (here we parameterize the equation of state ratio as $w(z) = w + w' z$ where w and w' are constants).

4.2.3 Constraining Ω_M and Ω_Λ

Two of the most basic cosmological parameters are Ω_M and Ω_Λ , the scaled energy densities in matter and vacuum energy. Table 4.1 shows that the accuracies pertaining to Ω_M and Ω_Λ that can be expected from SNAP are about a factor of ten better than current SN Ia constraints. Note that when Ω_M and Ω_Λ are measured simultaneously, the linear systematic error model that we assume (one that models “gray dust”) would have the effect of moving the contour region along a constant Ω_Λ line, thus only influencing Ω_M .

Figure 4.2 shows expected constraints from the proposed experiment on the energy densities of matter and vacuum for the case of a closed universe. Also shown are the current constraints using 42 high-redshift and 18 low-redshift supernovae (Perlmutter et al., 1999).

4.2.4 Measuring the Equation of State Ratio of the Dark Energy

How can we distinguish between alternative models like quintessence and a cosmological constant? It turns out that the equation of state ratio of the dark energy $w = p/\rho$ makes a good parameter to characterize dark energy models. In models with adiabatic initial perturbations w governs the background evolution of the dark energy through Friedmann’s equations (Hu, 1999; Hu & Eisenstein, 1999) (the other two parameters in these models, effective and viscous speeds of sound, govern only the evolution of perturbations, which are super-horizon-sized and difficult to detect with any cosmological probe). The equation of state ratio also parameterizes cosmic defects, such as strings and domain walls, which generate isocurvature perturbations.

Accurate determination of the equation of state of dark energy is one of the most important and exciting tasks that cosmology faces. SNAP would be able to measure w to an accuracy of 0.05 (statistical). The proposed experiment would not only distinguish conclusively between, for example, the cosmological constant and domain walls, but would also probe the properties of dark energy. For example, since tracker quintessence models obey the Ω_M – w relation for any given scalar-field potential (Steinhardt, Wang, & Zlatev, 1999), obtaining a tight constraint in the Ω_M – w plane would rule out many potentials and possibly shed some light on physics in the early universe.

4.2.5 Hubble parameter issues

Our constraints on the cosmological parameters do not depend on the value of the Hubble parameter H_0 . However, one can determine H_0 using supernovae in two ways: 1) by using information from a Cepheid variable in the host galaxy, which would set an absolute distance scale for the given galaxy and 2) by using information from SNe II, which can yield the distance to the supernova using the expanding photosphere method (see § 6.2). Finally, we would be able to accurately determine the combination $H_0 t_0$ (where t_0 is the age of the universe), since the uncertainty regions in the Ω_M – Ω_Λ plane are almost parallel to contours of constant age (Perlmutter et al., 1999).

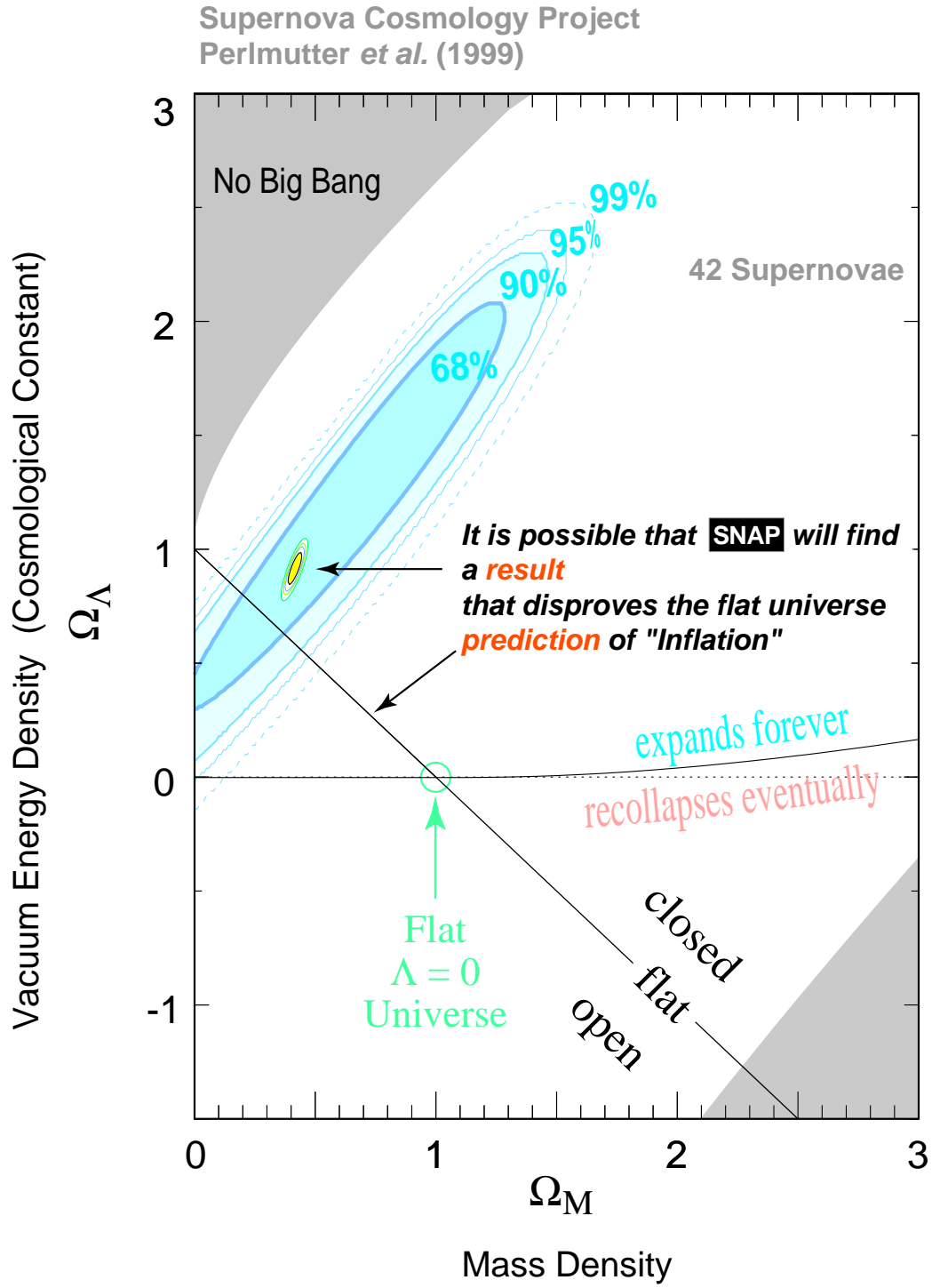


Figure 4.2: Constraints on Ω_M and Ω_Λ expected from the proposed experiment compared to current SN Ia constraints. This figure shows the case of a closed universe.

4.2.6 Comparison with CMB and LSS

SNAP's measurements of the dark energy will complement those of CMB experiments, which have more sensitivity to physics at higher redshifts ($z \lesssim 1100$). Dark energy affects the CMB in three ways: by contributing to the distance to the surface of last scattering, through the Integrated Sachs-Wolfe (ISW) effect, and through gravitational clustering. All three effects are small – the first one because dark energy contribution to the total energy diminishes at redshifts greater than a few, and the ISW and clustering because they are small and affect low multipoles of the CMB spectrum only, where cosmic variance is significant. As a consequence, CMB can determine Ω_M , Ω_Λ and w only to a moderate accuracy, although it can measure certain linear combinations of them, such as $\Omega_M + \Omega_\Lambda$, very accurately.

Galaxy surveys, such as Sloan Digital Sky Survey (SDSS), map the distribution of matter and measure Ω_M (as well as higher-order statistics of the large-scale structure), but do not shed much light on the properties of dark energy. However, when combined with CMB and/or SN Ia data, galaxy surveys help break the parameter degeneracies and improve measurements of contents of the universe.

Table 4.2 shows expected uncertainties in the aforementioned parameters for our experiment, for the CMB experiments MAP and Planck with and without the polarization information, for the SDSS, for MAP and Planck each combined with SDSS, and for MAP with polarization and combined with the knowledge that the universe is flat ($\Omega_k = 0$). Systematic uncertainties are available for SNAP only, while all other results are based on the Fisher matrix method (Eisenstein, Hu, & Tegmark, 1999) which assumes only statistical uncertainty in the data. From this table, it is apparent that the proposed experiment can determine Ω_M and Ω_Λ much more accurately than either MAP or Planck alone, and it can determine the curvature of the universe, Ω_k , about as well as MAP or Planck with polarization, which is remarkable given that CMB anisotropy probes will be able to measure curvature particularly well. Independent knowledge of cosmological parameters or combination with other experiments helps significantly decrease the (already small) CMB uncertainties; however, the same will in general be true for SNAP.

Figure 4.3 dramatically shows that our experiment is likely to be the strongest single probe of the dark energy. It shows constraints in the Ω_M - w plane, where w is equation of state ratio of the dark energy (assumed constant). A flat universe is assumed. Also shown are the constraints expected from MAP and Planck (both with polarization) and from SDSS, after marginalization over other relevant parameters [taken from Hu, Eisenstein, & Tegmark (1999)]. The proposed experiment would improve upon the present constraint on w by about an order of magnitude, and would also constrain the dark component much better than either CMB or LSS experiments.

Table 4.3 shows values for the uncertainties in Ω_M and w from upcoming LSS and CMB surveys and from the proposed SNAP experiment. Again, CMB and LSS results are based on the Fisher matrix analysis (Hu, 1999, private communication; Hu, Eisenstein, & Tegmark, 1999), while those for our experiment are based on a Monte-Carlo simulation. As this Table shows, the proposed experiment will constrain the equation of state ratio of the dark energy at least a factor of five better than the

	σ_{Ω_M}		σ_{Ω_Λ}		σ_{Ω_k}	
	stat	sys	stat	sys	stat	sys
SNAP	0.02	0.02	0.05	< 0.01	0.06	0.02
SDSS	0.23	<i>N/A</i>	∞	<i>N/A</i>	∞	<i>N/A</i>
MAP	1.40	<i>N/A</i>	1.10	<i>N/A</i>	0.31	<i>N/A</i>
MAP(P)	0.24	<i>N/A</i>	0.19	<i>N/A</i>	0.05	<i>N/A</i>
MAP(P)+ Ω_k	0.10	<i>N/A</i>	0.10	<i>N/A</i>	—	—
Planck	1.20	<i>N/A</i>	0.96	<i>N/A</i>	0.26	<i>N/A</i>
Planck(P)	0.14	<i>N/A</i>	0.11	<i>N/A</i>	0.03	<i>N/A</i>
MAP(P)+SDSS	0.036	<i>N/A</i>	0.042	<i>N/A</i>	0.015	<i>N/A</i>
Planck(P)+SDSS	0.027	<i>N/A</i>	0.024	<i>N/A</i>	0.005	<i>N/A</i>

Table 4.2: SNAP constraints on Ω_M , Ω_Λ and Ω_k compared to those expected from SDSS, MAP, and Planck with various assumptions as indicated. The (P) indicates the use of polarization information. MAP(P)+ Ω_k indicates that the universe is independently known to be flat ($\Omega_k = 0$). SDSS, MAP and Planck results are based on Fisher matrix analysis which included statistical errors in the data only (Eisenstein, Hu, & Tegmark, 1999), while SNAP constraint is obtained from Monte-Carlo simulations and includes estimates of systematic errors as well. Parameters considered and their fiducial values were $\Omega_M = 0.35$, $\Omega_B = 0.05$, $\Omega_\Lambda = 0.65$, $\Omega_\nu = 0.0175$ ($m_\nu = 0.7$ eV), $h = 0.65$, $n_s = 1$, $\alpha = 0$, $\tau = 0.05$, $Y_P = 0.24 \pm 0.02$, and $T/S = 0$. Here ν denotes a single massive neutrino species, $H_0 = 100 h$ km/s/Mpc, $n_s(k) = n_s + \alpha \ln(k/k_{fid})$ is the scale-dependent spectral index (with $k_{fid} = 0.025 Mpc^{-1}$), τ is the optical depth to reionization, Y_P is the primordial helium fraction, and T/S is the ratio of scalar to tensor perturbations.

	σ_{Ω_M}		σ_w	
	stat	sys	stat	sys
SNAP	0.02	0.02	0.05	< 0.01
SDSS	0.04	<i>N/A</i>	55.3	<i>N/A</i>
MAP	1.19	<i>N/A</i>	2.45	<i>N/A</i>
MAP(P)	0.86	<i>N/A</i>	1.96	<i>N/A</i>
Planck	0.11	<i>N/A</i>	0.27	<i>N/A</i>
Planck(P)	0.11	<i>N/A</i>	0.25	<i>N/A</i>

Table 4.3: $1\text{-}\sigma$ uncertainties in Ω_M and w assuming a flat universe. The (P) indicates use of polarization information. SDSS, MAP and Planck results are based on Fisher matrix analysis (Hu, 1999, private communication; Hu, Eisenstein, & Tegmark, 1999), while SNAP constraint is obtained from Monte-Carlo simulations.

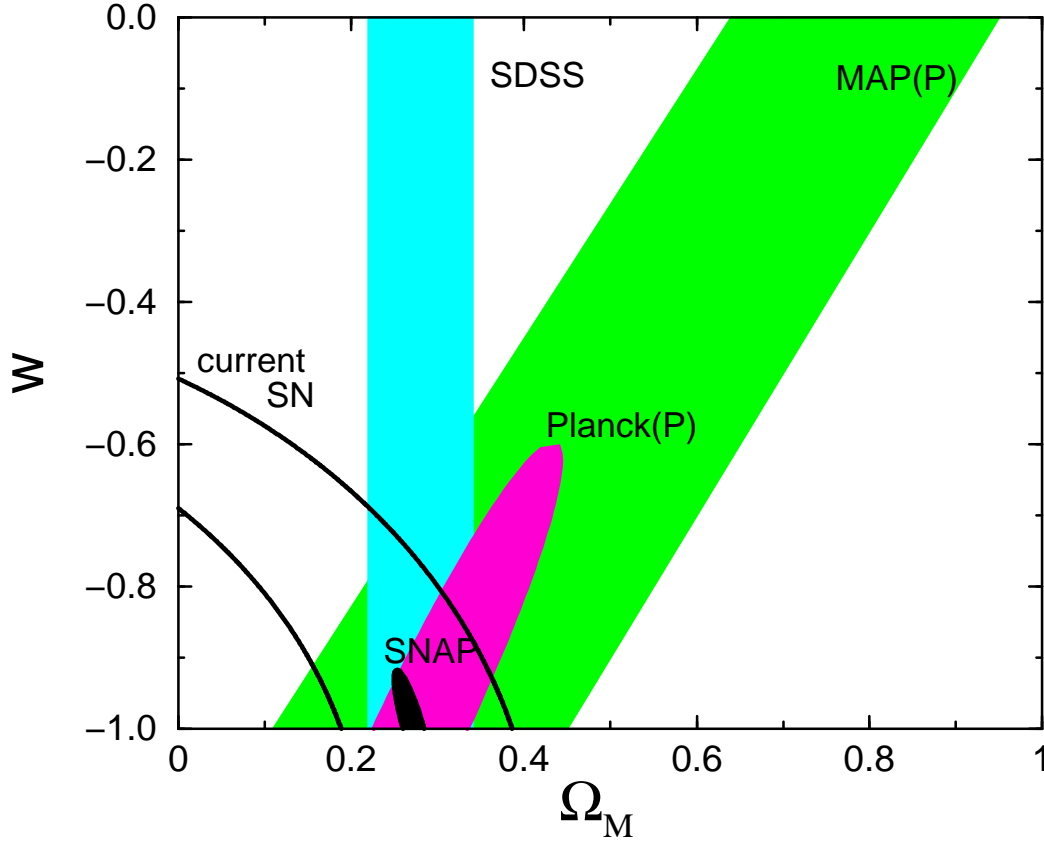


Figure 4.3: SNAP constraint on parameters Ω_M and w compared to those of MAP and Planck both with polarization information, and to SDSS (MAP, Planck and SDSS constraints are from Hu, Eisenstein, & Tegmark (1999)). Also shown are the present constraints using a total of 54 SN (Perlmutter et al., 1999). All constraints are $1-\sigma$ and include statistical uncertainties only. A flat universe is assumed, and fiducial values of the parameters are $\Omega_M = 1 - \Omega_{D.E.} = 0.28$, $w = -1$. MAP and SDSS constraint regions are obtained using Fisher matrix analysis, while SNAP constraint is obtained using Monte-Carlo simulation.

Planck satellite with polarization information.

4.2.7 Breaking the Parameter Degeneracies

It is well-known that cosmology experiments suffer from so-called degeneracies, or (strong) parameter correlations, where different combinations of parameters yield the same observable (Goobar & Perlmutter, 1995; Bond, Efstathiou, & Tegmark, 1997; White, 1998; Efstathiou & Bond, 1999). In experiments where the observable quantity depends on many parameters, these correlations can lead to drastic reductions in the accuracy of parameter determination.

Besides determining several important cosmological parameters to high precision,

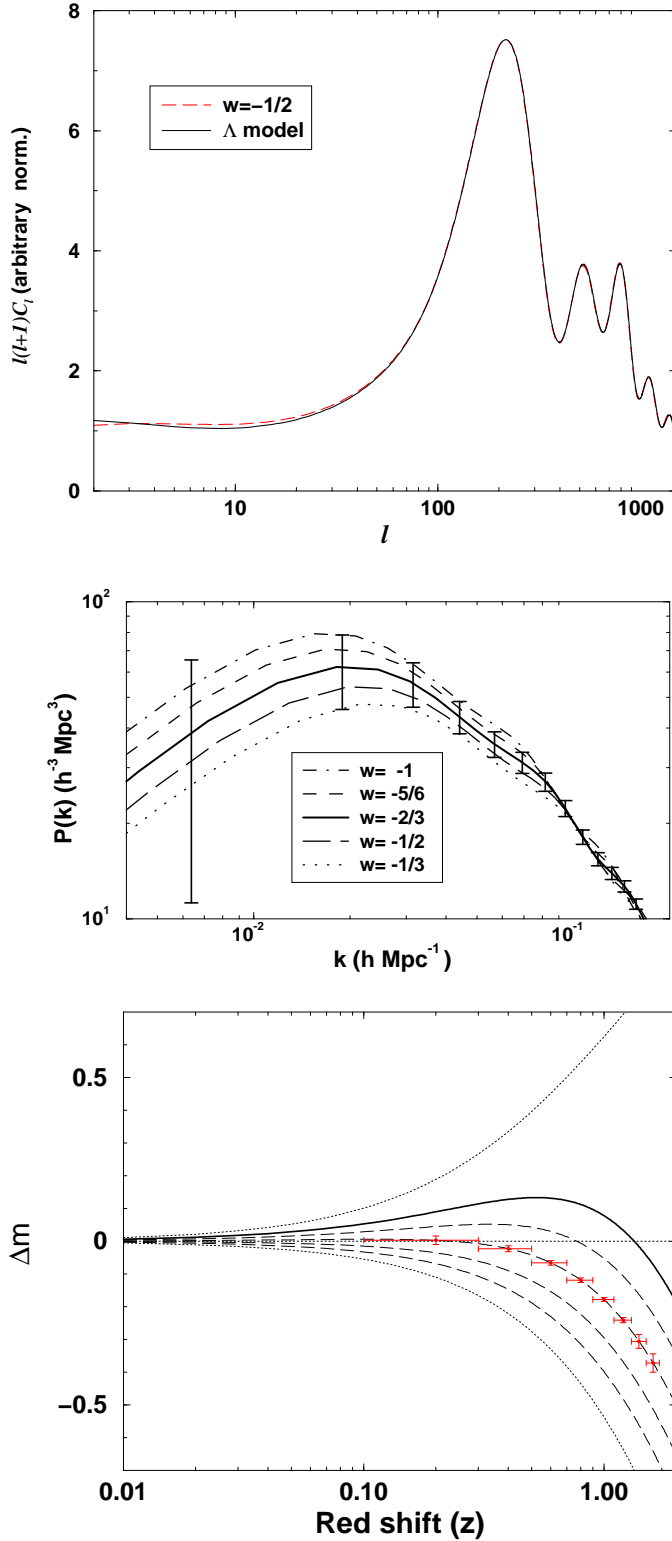


Figure 4.4: Breaking of the degeneracy. Four quintessence models are chosen (with $w = -5/6, -2/3, -1/2, -1/3$), each CMB-degenerate with a vacuum-energy dominated universe ($w = -1$). *Upper panel:* CMB power spectra for two of the five models; note that the power spectra overlap. *Middle panel:* matter power spectra for the same five models with SDSS projected standard errors. Note that the models still cannot be distinguished. *Lower panel:* the same five models shown on a magnitude-redshift graph, with errors predicted from SNAP. The dashed lines are the quintessence models, the solid line is the Λ CDM model, and $\Omega_\Lambda = 1$ (upper dotted) and $\Omega_M = 1$ (lower dotted) curves are added for reference. The models are readily distinguishable by our experiment.

the proposed SN experiment will have the ability to break parameter degeneracies from other experiments, notably CMB anisotropy probes and, to a lesser degree, LSS surveys. For example, Eisenstein, Hu, & Tegmark (1999) demonstrate that combining CMB and SN measurements can lead to improvement of up to a factor of 10 in determination of Ω_M and Ω_Λ due to breaking of degeneracies – much more than the naively expected $\sqrt{2}$ improvement.

As an example of just how strong the proposed experiment can be in breaking these degeneracies, we show the following example, based on Huey et al. (1999); Wang (1999, private communication). We consider four quintessence models (quintessence is a scalar-field candidate for the dark energy, and is discussed in the next section). These models have different equations of state ratios ($w = -5/6, -2/3, -1/2, -1/3$) and are all degenerate with the fifth, a model with a cosmological constant and cold dark matter. In other words, parameters of each model (quintessence energy density $\Omega_{D.E.}$, scaled Hubble parameter h , baryon energy density Ω_B) were chosen so that they are indistinguishable in the CMB data. The upper panel of Figure 4.4 shows overlapping CMB spectra for two of these models, while the middle panel shows matter power spectra for all five models, with SDSS projected standard errors (assuming $w = -2/3$ fiducial model). Note that the degeneracy remains even after the SDSS data are taken into account. The lower panel of the same figure shows the magnitude-redshift curves for the same models (with $\Delta m = m - m_{\text{empty}}$, where m is the magnitude for a given universe and m_{empty} that for an empty $\Omega_M = \Omega_\Lambda = 0$ universe) and error bars expected from the proposed experiment. The supernova telescope would be able to conclusively distinguish between the models and break the degeneracy.

4.2.8 Comparison with Other Methods

There are many other cosmological probes, existing or planned, that are likely to increase our understanding of the universe. Some of these are methods are still in development and not yet as powerful as CMB, LSS and SN Ia surveys, but it is reasonable to expect that in the future these probes will play a very important role in the progress of cosmology. Other methods have been recognized for a long time, but suffer from systematic and modeling uncertainties that prevent cosmologists from using them for accurate parameter determination.

Weak gravitational lensing [see (Bartelmann & Schneider, 1999) for a comprehensive review] is a very promising method based on weak distortions of distant objects due to large-scale structure. It turns out that for accurate parameter determination (in particular regarding Ω_M , $\Omega_{D.E.}$ and w) weak lensing lacks precision (Hu & Tegmark, 1999) because the power spectrum of the convergence from weak lensing is relatively structureless (unlike the power spectrum of the CMB), while it depends on about 8 parameters. However, when combined with other techniques, such as CMB or SN Ia, weak lensing can help pin down the cosmological parameters, for instance the neutrino mass (Cooray, 1999).

Classical number density vs. redshift (“ dN/dz ”) tests probe the desired redshift interval and are in principle capable of tightly constraining Ω_M , $\Omega_{D.E.}$ and w , as has been known for several decades. The most important among these tests are evolu-

tion of clusters of galaxies [with data either from X-ray surveys (Bahcall & Fan, 1998; Viana & Liddle, 1999) or from the proposed Sunyaev-Zeldovich survey (Holder et al., 1999)], evolution of galaxy abundance (Newman & Davis, 1999), and gravitational lensing counts as a function of redshift (Cooray & Huterer, 1999). With the upcoming observational data and new planned experiments, these tests have a potential to be quite powerful – for example, the proposed Sunyaev-Zeldovich survey might be able to measure (constant) w to 0.10 after two years of operation (Mohr, 2000). Unfortunately, in practice “dN/dz” tests are dependent on the intrinsic abundance of the objects in question (galaxies, galaxy clusters, gravitational lenses etc.), whose theoretical values are model-dependent and have to take into account complicated physics of these objects, e.g. evolution, formation rate, and mergers of galaxies.

4.2.9 Further Exploration of the Dark Sector

So far, we have assumed that the equation of state of the dark energy is constant. This may not be so. Some dark energy candidates, such as rolling scalar fields, generally produce a time-varying equation of state. While in the tracker quintessence models this change is often small out to $z \sim \text{few}$ (Zlatev, Wang, & Steinhardt, 1999), other models, such as Pseudo-Nambu-Goldstone-Boson models (Coble, Dodelson, & Frieman, 1997) can exhibit large variation of w at small redshifts.

As one considers more general candidates for the dark energy, one has to relax assumptions about its nature, that is, its equation of state ratio. However, this invariably leads to some loss of accuracy in parameter determination. In the preceding sections we have shown that the assumption that $w = -1$ leads to a very accurate determination of $\Omega_{\text{D.E.}}$ and, similarly, that if w is assumed constant then we can measure it very accurately. We now proceed to show that with SNAP we can go much further and determine properties of the dark energy with considerably less restrictive assumptions.

In Figure 4.5 we show constraints that SNAP would impose on dark energy models. We show the current set of 18+42 supernovae, plus a set of simulated SNAP supernovae (each SNAP point represents 50 supernovae). The magnitude-redshift relations shown are those expected from dark energy models motivated by particle physics and currently found in the literature. Figure 4.6 is the same as Figure 4.5, except that it has an expanded vertical axis for easier visualization. It is clear that SNAP would improve current constraints by an order of magnitude, and would be able to rule out the majority of numerous proposed models. Such a constraint would present a major step forward, as it would directly lead us to a small number of viable models and their corresponding physical mechanisms. It is important to note that models of dark energy can cross each other (see, for example, the crossings at $Z \sim 0.7$), and therefore the wide redshift range is a key element of this study.

Finally, accurate knowledge of the luminosity distance out to redshift of ~ 1.7 can be useful for other cosmological tests. For example, Starkman, Trodden, & Vachaspati (1999) derive a critical redshift out to which we need to verify acceleration of the universe to establish that the universe is entering an inflationary phase, and that we are not living in a cosmological-constant-dominated bubble. For the currently favored values of Ω_M and Ω_Λ , this critical redshift is $z \approx 1.8$. Clearly, the proposed experiment

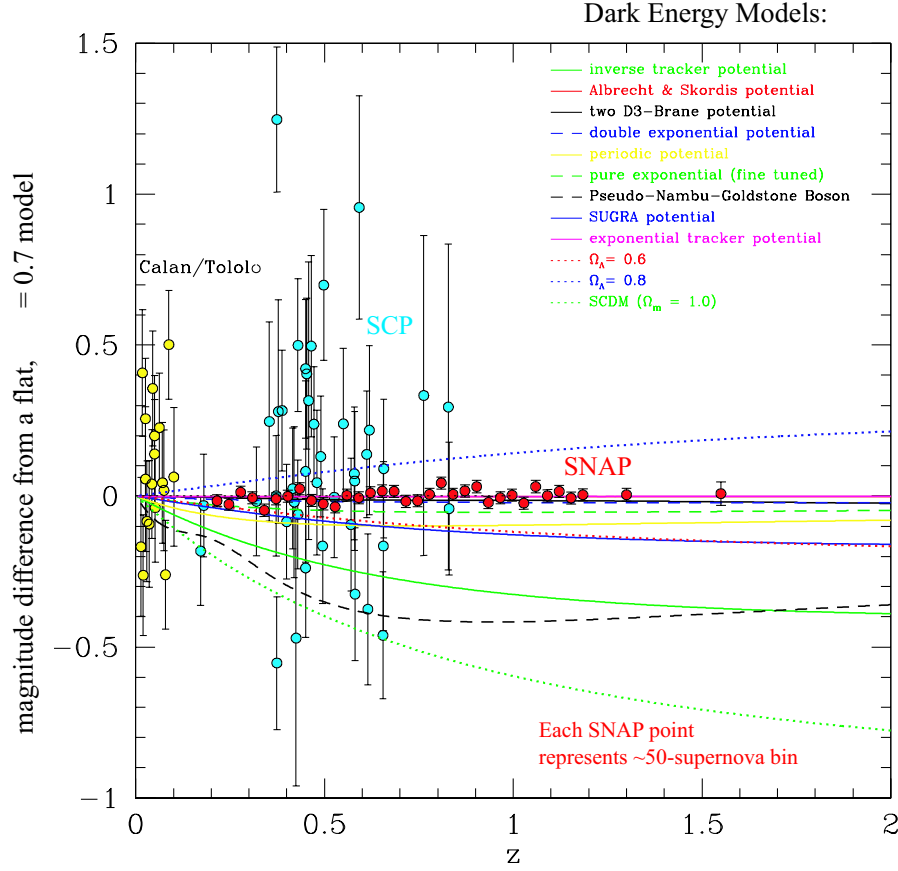


Figure 4.5: SNAP constraints on dark energy models, viewed in the magnitude-redshift plane. Shown is the current set of 18+42 supernovae, plus a set of simulated SNAP supernovae (each SNAP point represents 50 supernovae). Theoretical curves correspond to a variety of dark energy models currently found in the literature.

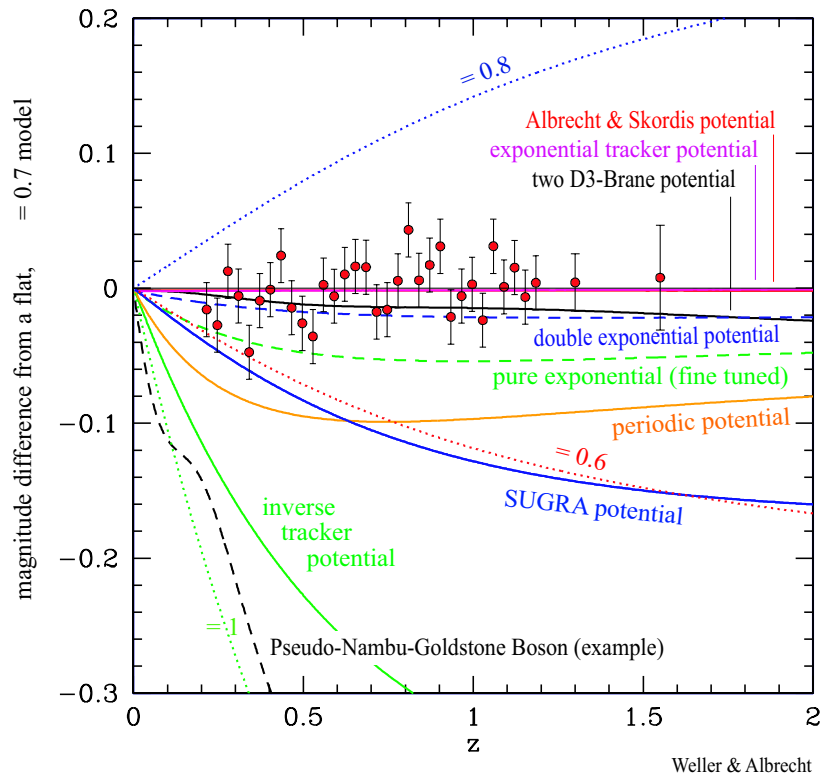


Figure 4.6: Same as Figure 4.5, but with no current data points and with an expanded vertical axis.

would be ideally suited to perform this cosmological test.

4.3 Previously Identified Sources of Systematic Uncertainty

To obtain high-accuracy measurements of the cosmological parameters and the time-dependent equation of state ratio for the dark energy, it will not suffice simply to discover and study more supernovae and more distant supernovae. The current SN Ia data set already results in statistical uncertainties that are within a factor of two of the identified systematic uncertainties. In Table 1.1, we summarized the identified sources of systematic error, and give the uncertainty that each contributed to previous measurements. With the proposed satellite experiment, each of these effects can either be measured so that it can become part of the statistical error budget, or else bounded (the target overall systematic uncertainty is kept below ~ 0.02 magnitudes, so that it will contribute comparably to the final statistical uncertainties). The final column of the table summarizes the observations required to reach this target systematic uncertainty.

Malmquist Bias: *Contributed 0.04 uncertainty on Ω_M^{flat} in previous studies.* This is the sampling bias due to any low-versus-high-redshift difference in detection efficiency of intrinsically fainter supernovae. For the target redshift range, the proposed experiment will detect every supernova in the observed region of sky at 10% of its peak brightness, eliminating this source of systematic uncertainty.

SNAP Requirement: Detection of every supernova at least 2.5 magnitudes below peak.

K-Correction and Cross-Filter Calibration Uncertainty: *Contributed 0.025 uncertainty on Ω_M^{flat} in previous studies.* The K -correction uncertainty is the systematic uncertainty due to any uncorrected redshift-dependent mismatch between the photometry filters’ transmission functions (in the supernova restframe). These generally small mismatches would be corrected perfectly if the supernova’s spectral time series were known. The proposed experiment will provide such time series for a representative sample of supernovae. Cross-filter calibration uncertainty reflects the lack of relative calibration of the magnitude systems of the different filters used at low and high redshifts. This “cross-filter,” cross-wavelength calibration has only been measured crudely from the ground (it requires a known source and detailed knowledge of the atmosphere transmission); the satellite experiment will be designed to fill this gap. *SNAP Requirement: Spectral time series of representative SN Ia sample and cross-wavelength relative flux calibration.*

Non-SN Ia Contamination Bias: *Bounded at < 0.05 uncertainty on Ω_M^{flat} in previous studies.* It is possible for occasional SNe Ib or Ic to appear very similar to SN Ia if the spectrum does not extend redward far enough—and with sufficient signal-to-noise—to include and detect the strong 6250 Å Si II feature that identifies the SN Ia. This feature is redshifted into the near-IR and thus becomes very difficult to observe

from the ground. The proposed SNAP spectrograph will study this feature for every SN in the target redshift range, eliminating this source of systematic uncertainty.

SNAP Requirement: Spectrum for every supernova at maximum light covering the 6300 Å restframe wavelength region, i.e. to 1.7 μm at $z = 1.7$.

Milky Way Galaxy Extinction: *Bounded at <0.04 uncertainty on Ω_M^{flat} in previous studies.* Maps of the extinction in our Galaxy provide good measurements of relative extinction, but there is still some residual systematic uncertainty in the absolute “zero point” of this extinction map. This zero-point uncertainty will be improved with observations by SIRTf and SDSS; SNAP itself will constrain this uncertainty using spectra of hot Galactic subdwarfs. *SNAP Requirement: Optical and near-IR spectra of ~ 100 hot Galactic subdwarfs in SNAP field.*

Gravitational Lensing by Clumped Mass (MACHOs): *Bounded at <0.06 uncertainty on Ω_M^{flat} in previous studies.* With the large data sample of ~ 2000 SNe Ia proposed here, it will be possible to average out the effect of any gravitational lensing on supernovae at a given redshift, by including both the rare amplified events and the common deamplified events—which average to give an undistorted value because the total flux is conserved in a lensed image. This is likely to be a quite small range of distortions at lower redshift, but possibly larger at $z > 1$. (Moreover, by studying the distribution of these amplification/deamplification events at redshifts above $z = 1$, it will be possible to statistically study the line-of-sight distribution of the dark matter that would be causing the lensing.) Note that this uncertainty will also be limited by microlensing studies; see § 6.

SNAP Requirement: Large samples of SNe Ia (~ 50 per 0.03 redshift bin) at all redshifts in target range.

Extinction by “Ordinary” Dust Outside the Milky Way: *Contributed 0.03 uncertainty on Ω_M^{flat} for all previously-observed dust that diminishes blue more than red light.* The proposed experiment will be able to obtain cross-wavelength-calibrated data with broad wavelength coverage for each supernova, so that the dimming of the spectrum as a function of wavelength can be measured with high signal-to-noise. This eliminates the systematic uncertainty due to “ordinary” dust that will absorb blue more than red light, since this systematic uncertainty now becomes part of our statistical error budget.

SNAP Requirement: Cross-wavelength calibrated spectra, at controlled SN-explosion epochs, that extend to rest-frame 1 μm.

4.4 Treatment of Proposed Systematic Errors

There are also several additional proposed systematic effects that might confound attempts at higher precision, in particular the possibilities of “gray dust” and systematic shifts in the initial conditions of supernova explosions through properties of their progenitor stars.

The satellite instrumentation and observation strategy were designed to obtain a dataset that provides comprehensive control of the major sources of systematic uncertainty. For each supernova, a set of observations is obtained that will monitor its physical properties. This will also allow studies of effects that have *not* been previously identified or proposed.

We address below the sources of systematic errors and then describe the full set of observables that constrain them.

4.4.1 Gray dust

Extinction of light from supernovae can lead to overestimation of their distances. Observed colors are an effective test, since typical dust reddens incoming light. However, it has been suggested by Aguirre (1999) that certain large (up to $\sim 0.1\mu\text{m}$), and possibly needle-like, dust grains can be expelled from galaxies via radiation pressure and can have an opacity curve that is shallow in optical bands, thus making them absorptive while producing only small color excess (see Fig. 4.7). The existence of such dust would lead the unwary cosmologist into underestimating Ω_M or overestimating Ω_Λ .

If there is gray dust that has had insufficient time to diffuse uniformly in intergalactic space, different lines of sight would have differing amounts of extinction due to clumping. This would result in an increase of observed supernova magnitude dispersion, an effect that is not seen in current observations. Figure 4.8 compares the magnitude-residual distributions to the Gaussian distributions expected given the measurement uncertainties and an intrinsic dispersion of 0.17 mag. Both the low- and high-redshift distributions are consistent with the expected distributions; the formal calculation of the SN Ia intrinsic-dispersion component of the observed magnitude dispersion ($\sigma_{\text{intrinsic}}^2 = \sigma_{\text{observed}}^2 - \sigma_{\text{measurement}}^2$) yields $\sigma_{\text{intrinsic}} = 0.154 \pm 0.04$ for the low-redshift distribution and $\sigma_{\text{intrinsic}} = 0.157 \pm 0.025$ for the high-redshift distribution.

The Hubble diagram extended to $z \sim 1.3$ also tests for gray dust. Sufficient dust to explain our $z \sim 0.5$ data without Λ predicts fainter SNe at $z \sim 1.2$ than the cosmology with Λ . *Preliminary* data for SN1998eq falls on the brighter (no dust) curve; Fig. 3.6.

As discussed in the Executive Summary, it is also possible to detect $z \lesssim 0.5$ gray dust by comparing optical and near-IR photometry of SNe (both Ia and II) found in this redshift range.

There are independent checks for gray dust. As Fig 4.7 shows, the light from galaxies and quasars permeating the intergalactic medium will heat any dust — whether gray or not — causing it to re-emit in the far-infrared (FIR). Observations limiting the strength, or even detecting, the FIR background place an upper limit on the amount of gray dust allowed. However, normal galaxies heat their own internal dust which also re-emits in the FIR. Only the difference between the FIR emission from galaxies and the total FIR background can come from intergalactic dust. Current SCUBA observations at $850\mu\text{m}$ are already close to ruling-out gray dust. Future deeper observations with SCUBA and possibly SIRTIF will provide even stronger constraints on the amount of gray dust allowed. Space-based observations of existing supernovae are now being used to test if gray dust in a non-accelerating universe can be mimicking the effects of an accelerating universe at $z = 0.5$. Results show that the observed color excess is

too small to be compatible with the 30% opacity of gray dust needed to be consistent with observations (Riess et al., 2000).

4.4.2 Evolution

SNe Ia with different progenitor properties should result in explosions with slightly differing properties, even if there is only one mechanism for creating them, and even if this mechanism has a set “trigger” such as the Chandrasekhar limit. If these differences are not corrected by the light curve width-luminosity relation presently in use, *and* if the *distribution* of key parameters of the progenitor stars changes with redshift, the SN Ia explosions observed at high redshift could differ in peak luminosity from those at low redshift, leading to a systematic error in the determination of the cosmological parameters. However, the SNAP dataset will allow corrections for these differences, or allow similar SNe Ia to be identified and matched at high and low redshifts thus mitigating against the effects of changing progenitor properties

Parameters which might affect the initial conditions of a supernova explosion include the masses, binary system orbital parameters, and abundance of elements heavier than helium (the abundance of elements starting with lithium is termed “metallicity”). The progenitor mass determines the timescale for a star to evolve from birth to the white dwarf stage, and affects the abundance and distribution of heavy elements in the core. The relative masses of stars in a binary system determines which star will become a white dwarf first (the most massive star will), how long that white dwarf will have to wait to accrete mass from — or coalesce with — its companion, and the mass accretion rate (for a Chandrasekhar WD). The binary system orbital parameters likewise affect the later two timescales. Finally, the heavy element abundance affects the stellar evolutionary timescales, the composition and structure of the core, and the mass accretion rate.

As a given galaxy ages, generation after generation of stars complete their life-cycles, enriching the galactic environment with heavy elements over time. In a given generation of stars, the more massive ones will complete their life cycles sooner, so the distribution of stellar masses within that generation will evolve. However, the star formation amongst — or even within — galaxies is not very well synchronized. Some galaxies form new stars fairly uniformly in time, while others experience bursts of star formation followed by billions of years without star formation. There are examples of very young, low-metallicity, galaxies even at the present epoch, and there are examples of old, high-metallicity galaxies at high redshift (see for example Fig. 4.10 where the metallicities of galaxies over the range $0 < z < 0.5$ are compared). Thus, the distribution of these progenitor parameters is very broad, not well correlated with redshift, and limited only by the age of the universe and the upper mass limit for forming a white dwarf.

There are two complementary paths to searching for and correcting the influence of progenitor properties, and the SNAP dataset will allow both to be pursued. First, the detailed form and development of the supernova spectrum and light curve offers important information of the initial conditions of the explosion itself. In addition, properties of the host galaxy globally and near the location of the supernova can suggest whether

a given supernovae might have been young or old, or metal-rich or metal-poor. In particular, although galaxy metallicity and age are difficult to determine, the luminosities, colors, morphology and location within a galaxy can provide an approximate means of determining likely properties of the progenitor of each supernova. Indeed, evidence for differences among SNe Ia with differing host galaxy environments has in fact already been seen among nearby, low-redshift supernovae. The range of intrinsic SN Ia luminosities seen in spiral galaxies differs from that seen in elliptical galaxies (Hamuy et al., 1996). So far, it appears that the differences that have been identified are well calibrated by the SN Ia light curve width-luminosity relation. The standard supernova analyses thus already correct for a luminosity effect due to the range in progenitor properties. Accounting for more subtle effects requires that the SN Ia sample sizes are sufficiently large and varied at each redshift so that at a minimum we can find matching examples in sufficient quantities, and possibly even a correction for such effects, turning a systematic error into a statistical one, and improving SNe Ia as distance indicators in the process.

4.4.3 Observables to Correct or Match SNe Ia

We have identified a series of key observable supernova features that reflect differences in the underlying physics of the supernova. By measuring all of these features for each supernova we can tightly constrain the physical conditions of the explosion, making it possible to recognize supernovae that have similar initial conditions and/or arise in matching galactic environments. The current theoretical models of SN Ia explosions are not sufficiently complete to predict the precise luminosity of each supernova, but they are able to give the rough correlations between changes in the physical conditions of the supernovae and the peak luminosity (Höflich, Wheeler, & Thielemann, 1998). These conditions include the velocity of the ejecta (a measurement of the kinetic energy of the explosion), the opacity (here we refer to the opacity of the inner layers, which affects the overall light curve shape), metallicity of the progenitor (which affects the early spectra), ^{56}Ni mass (a measurement of the total luminosity), and ^{56}Ni distribution (which might lead to small effects in the light curve shape at early time). We can therefore give the approximate accuracy needed for the measurement of each feature to ensure that the physical condition of each set of supernovae is well enough determined so that the range of luminosities for those supernovae is well below the systematic uncertainty bound ($\sim 2\%$ when all the constraints are used together). The following tables provides a list of these measurements. We also include a table that identifies several characteristics of the host galaxy that will also help us subdivide the SNe Ia into groups that come from very similar environments. There is currently some evidence that some of these host galaxy observables correlate with some of the SNe Ia parameters (Branch, Romanishin, & Baron, 1996).

Rise time from explosion to peak. The rise time to peak is an indicator of opacity, fused ^{56}Ni mass and potential differences in the ^{56}Ni distribution. Constraining it to within 0.3 days corresponds to a 0.03 magnitude constraint at peak. To achieve this accuracy requires discovery within ~ 2 days of explosion, on average, i.e. ~ 3.8 magnitudes below peak.

Observables X	$\partial M_{peak}/\partial X$	Requirement for $m_{sys} < 0.02$
Spectra		
Spectral feature minima	0.04/500 km/s	150 km/s
Spectral feature widths	0.12/100 Å	10 Å
Spectral Feature Ratios	$0.12(B)$, $-0.75(\lambda = 3000\text{Å})$, $1.5(\lambda = 6150\text{Å})$	5%
Light Curves		
Stretch	0.10/5%	1%
Rise Time	0.1/1 day	0.3 days
Peak to Tail Ratio	0.05/0.2 mag	0.05 mag

Table 4.4: A list of the potential sources and values (m_{sys}) of systematic errors due to unresolved differences among SNe Ia explosion models.

Observables	^{56}Ni Mass	^{56}Ni Distribution	Kinetic Energy	Opacity	Metallicity
Spectral feature minima	○	—	● ★	○	●
Spectral feature widths	○	—	● ★	○	●
Spectral Feature Ratios	●	—	○	○	● ★
Light Curve Stretch	●	○	○	● ★	—
Light Curve Rise Time	●	● ★	○	●	○
Light Curve Peak/Tail	● ★	—	○	○	—

Table 4.5: A list of the observables that constrain the various SNe Ia model parameters. ● = directly related to, ○ = indirectly related to, and — = slightly related to or no relation to the model parameter. The model parameters will be determined primarily from the ★'ed observable.

Parameter	Observable
Host galaxy luminosity	U, B, V, R, I, J, H band photometry
Host galaxy colors	U, B, V, R, I, J, H band photometry
Host galaxy absorption lines	0.3-1.7 μm spectroscopy
Host galaxy emission lines	0.3-1.7 μm spectroscopy
Host galaxy morphology	0.1'' spatial resolution
SNe Ia location in host galaxy	0.1'' spatial resolution

Table 4.6: Host galaxy observables which further constrain the progenitor environment of a SNe Ia.

Plateau level 45 days past peak. The light curve plateau level that begins ~ 45 days past peak is an important indicator of the C/O ratio of the progenitor star, and fused ^{56}Ni . A 0.1 magnitude constraint on this plateau level corresponds to a 0.02 magnitude constraint at peak. To achieve this accuracy requires a signal-to-noise ratio of 10 for photometry 2.8 magnitudes below peak. Figure 4.9 highlights these differences for two nearby supernovae.

Overall light curve timescale. The “stretch factor” that parameterizes the linear stretching or compression of the light curve time scale is affected by almost all the aforementioned parameters since it tracks the SN Ia’s evolution from early to late times. It is closely correlated with the two previously mentioned observables, which focus on details of the light curve timescale, and it ties this experiment’s controls for systematics to the controls used in the previous ground-based work. A 1.5% uncertainty in the stretch factor measurement corresponds to a ~ 0.02 magnitude uncertainty at peak. This requires signal-to-noise ratio of 10 for photometry extending from 10 days before peak to 45 days after peak.

Spectral line velocities. The velocities of several spectral features throughout the UV and optical make an excellent diagnostic of the overall kinetic energy of the SNe Ia. The kinetic energy directly influences the overall shape of the light curve. If the velocities are constrained to ≈ 150 km/s then the peak luminosity can be constrained to ~ 0.02 magnitude uncertainty at peak, given a typical SNe Ia expansion velocity of 15,000 km/s.

Spectral Feature Ratios. The ratios of various spectral features in the restframe UV are strong indicators of the metallicity of the SNe Ia. Since it is well known that the metallicities of *nearby* galaxies vary by large amounts (see Figure 4.10) this is another important parameter to constrain and correlate. As can be seen in Höflich, Wheeler, & Thielemann (1998) the metallicity of the progenitor has a strong influence on the UV spectrum. Lentz et al. (1999) has quantified these effects by varying the metallicity in the unburned layers and computing their resultant spectra at maximum light. By achieving a reasonable signal-to-noise per wavelength bin we will be able to constrain the metallicity of the progenitor to 0.1 dex.

We also note that the ratios of spectral features in the restframe optical (Ca II H&K and Si II at 6150 Å) provide additional constraints on the opacity and luminosity of the SN Ia (Nugent et al., 1995a). These features are easily observed given the velocity measurements mentioned above.

All these observables tightly constrain the physical properties of the SN Ia since they either directly or indirectly measure all of the physical parameters that control the light curve and spectral evolution. These parameters include the SN Ia’s overall opacity, total ^{56}Ni mass and distribution, and kinetic energy. Each will measure several of these parameters simultaneously, further refining and cross-checking their values. Based on our current understanding of the physics behind SNe Ia, the requirements

that we have placed on the observations will allow us to keep the systematics below the 2% level.

4.5 Systematic Correlations

The issue of systematic error is so crucial to the design of this experiment that it bears some further elaboration beyond the catalogs of Sections 1.5, 4.3 and 4.4. In particular it is important to determine whether each individual systematic error can be independently extracted from the data, using the approaches proposed.

First it should be recognized that the measurements that will control or eliminate each of the systematic errors cataloged are essentially independent of each other, with only a few exceptions to be discussed here. Thus the final uncertainty can be decomposed and estimated from the separate parts, without a Monte Carlo analysis of simulated data with all of the systematic errors simultaneously fitted.

Specifically, we note that key SN Ia input parameters (e.g. ^{56}Ni Mass, metallicity, opacity) produce evolutionary spectral indicators (e.g. well depth, equivalent widths, velocities) that will not be affected by the flat absorption of gray dust at optical wavelengths. The expected gray dust signature, an extreme decrease of opacity in the near infrared and flat opacity in the optical, will make evolutionary and dust effects distinguishable.

The exceptions to this independence are:

1. Ordinary dust vs. Evolution

The approach to measuring extinction due to ordinary (not gray) dust so far assumes that it is possible to identify the spectrum and/or color of representative SNe Ia in un-extincted or lowest-extinction environments. The low-redshift SN Ia data available to date, with a dominant spike at zero extinction, suggests that this is quite a reasonable expectation. However one can imagine scenarios in which certain sub-classes of SNe Ia only occur in dusty environments. This would require a somewhat different reddening-fit approach that might be expected to be less accurate – but only for the problematic subclasses. To the extent that these hypothetical subclasses could occur only in certain age stellar environments we might also expect some interdependence between the evolution controls and the dust controls.

2. Inhomogeneous gray dust vs. Gravitational lensing

As discussed earlier, gravitational lensing will increase the dispersion of observed supernova magnitudes as their light passes through different geodesics crossing under and overdense regions. Although more supernovae will appear fainter than brighter, there is no net average effect; using all the supernova to determine the cosmological parameters, even the outliers, will eliminate any potential bias. Inhomogeneous gray dust will also have the effect of increasing the magnitude dispersion with only subtle traces on supernova spectra and light curves. Standard techniques used to handle samples with an extincted component, such as the ridge-line method, are not compatible with the requirement that a full sample of supernovae be used to account for gravitational lensing.

3. Evolution parameters

Although each of the observables that we propose to use to identify the physical state of a supernova are themselves independent of the observables used to constrain other systematics, they are not one-to-one indicators of each of the SN Ia physical parameters; in general, two or more of these physical parameters determines each of these observables. However, as the chart of Table 4.5 shows, these physical parameters are overconstrained by the independent observables and we therefore consider it quite reasonable to use them iteratively to separate the evolutionary subclasses of SNe Ia to the level of the target systematic uncertainty. A possible methodology for determining the SN physical properties is as follows:

- (a) • ^{56}Ni Mass
Determined by the light curve peak-to-tail ratio (see Figure 4.9).
- (b) • Opacity
Determined with the ^{56}Ni Mass and stretch information.
- Metallicity
Determined from the ^{56}Ni Mass and line ratios (see Figures 3.4 and 3.5).
- (c) • Kinetic Energy
Determined from metallicity, spectral feature minima and widths.
- ^{56}Ni Distribution
Determined from ^{56}Ni Mass, opacity, and the rise time.

4.6 Summary

The satellite we propose would bring tremendous advances in our understanding of cosmology and the universe. By measuring energy densities of matter and the unknown component, we would accurately determine flatness and energy contents of the universe. By measuring equation of state of the dark energy, we would drastically narrow the list of dark-energy candidates, and quite possibly leave a very small subset of previously-considered theories viable. Combining our data with that of other cosmological experiments, notably CMB, would help break parameter degeneracies and make cross-checks among different probes. Finally, with the data from our experiment cosmologists could perform a number of other exciting tests, some of which were already proposed in literature. Given our current lack of knowledge about the energy contents of the universe, it is possible that some of these tests would give surprising and unexpected results.

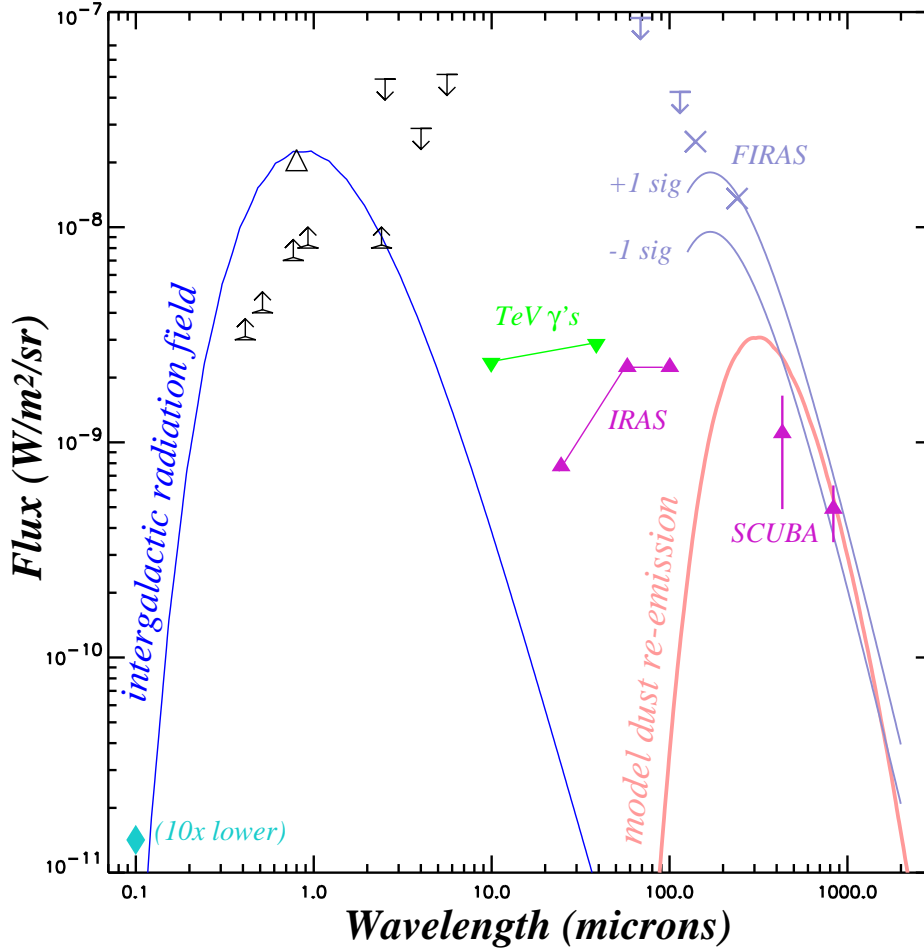


Figure 4.7: FIR model dust re-emission spectrum (solid line, right) and intergalactic radiation field spectrum (left) for the Aguirre & Haiman (1999) fiducial gray dust model (with the best-fit CMB subtracted) needed to make a $\Omega_M = 0.2$, $\Omega_\Lambda = 0$ cosmology fit the SNe results. Observational constraints are the DIRBE FIRB detections (crosses) and upper limits (down arrows), the UVB detections (triangles) and HDF-derived lower limits (up arrows). To the original Aguirre plot we have added lower limits from IRAS galaxy counts at 25, 60, and 100 μm , and from SCUBA source counts at 450 and 850 μm . These are represented with red upward-pointed triangles. We have further added the upper limits in the 10–40 μm region from modeling of the TeV spectra of nearby blazars (green downward triangles), and the EUV upper limits of Donahue, Aldering, & Stocke (1995) (diamond; plotted 10 \times too high to fit on the plot). Present SCUBA source counts are close to eliminating the fiducial dust model. Deeper FIR counts from SCUBA and SIRTf should settle the question of whether, or how much, gray dust is allowed.

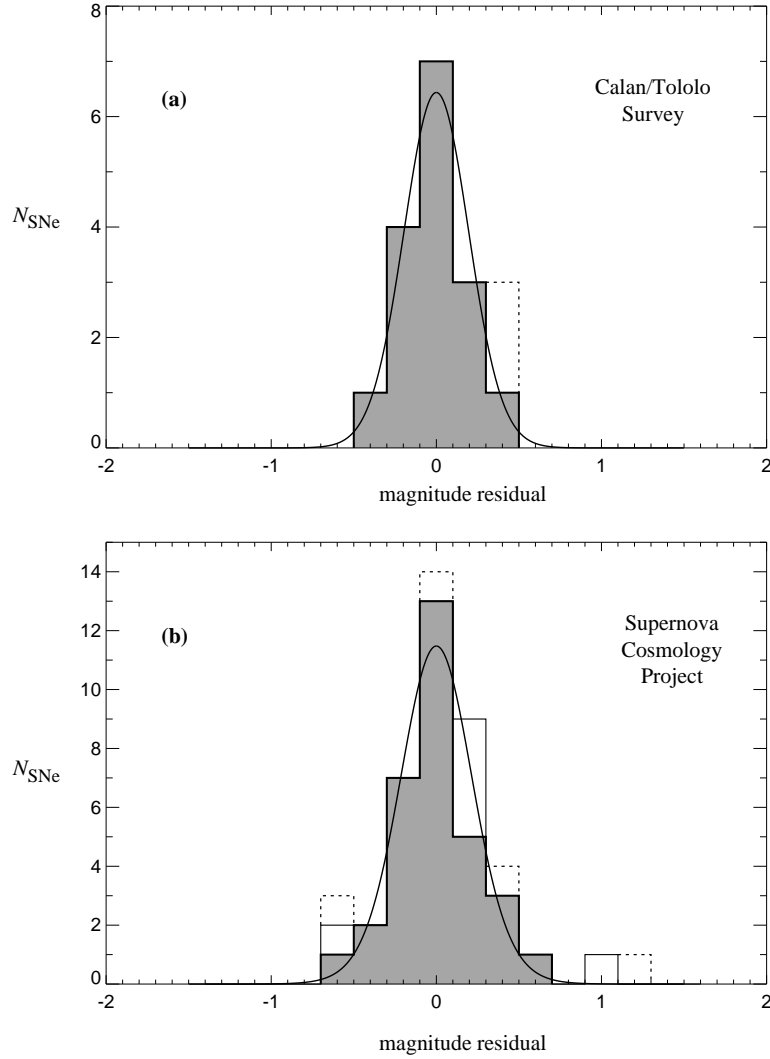


Figure 4.8: The distribution of restframe B -band magnitude residuals from the best-fit flat cosmology for the Fit C supernova subset, for (a) 18 Calán/Tololo supernovae, at redshifts $z \leq 0.1$ and (b) 42 supernovae from the Supernova Cosmology Project, at redshifts between 0.18 and 0.83. The darker shading indicates those residuals with uncertainties less than 0.35 mag, unshaded boxes indicate uncertainties greater than 0.35 mag, and dashed boxes indicate the supernovae that are excluded from Fit C. The curves show the expected magnitude residual distributions if they are drawn from normal distributions given the measurement uncertainties and 0.17 mag of intrinsic SN Ia dispersion. The low-redshift expected distribution matches a Gaussian with $\sigma = 0.20$ mag (with error on the mean of 0.05 mag), while the high-redshift expected distribution matches a Gaussian with $\sigma = 0.22$ (with error on the mean of 0.04 mag).

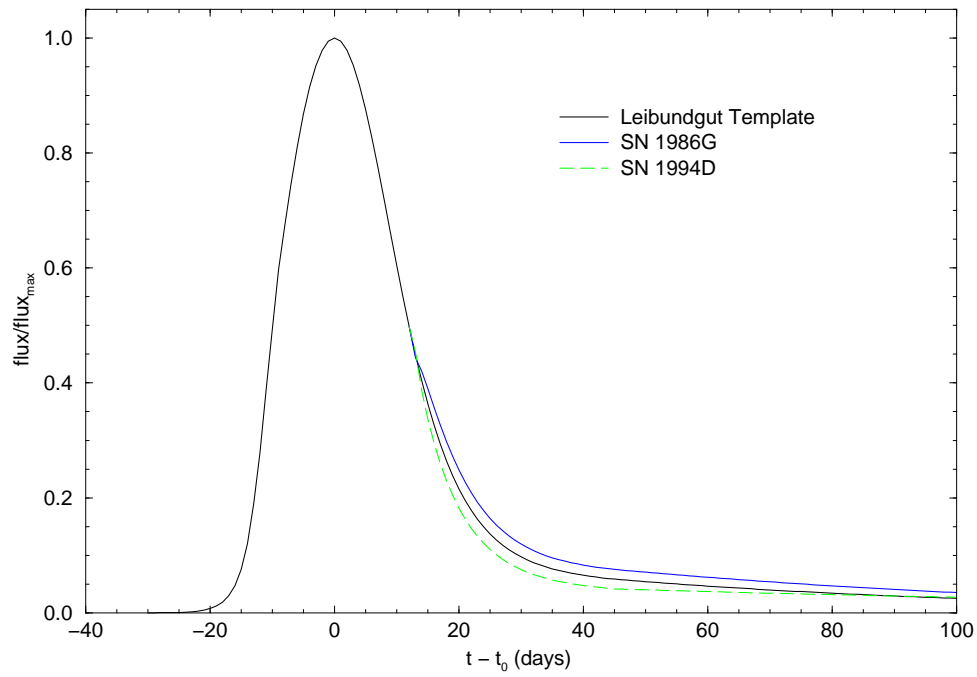


Figure 4.9: The black curve corresponds to the standard modified Leibundgut template. The solid-blue curve shows the late-time deviation exhibited by SN 1986G, while the dashed-green curve shows the late-time deviation for SN 1994D. These differences are expected for progenitors with differing C/O ratios (Aldering, Knop, & Nugent, 1999, in press).

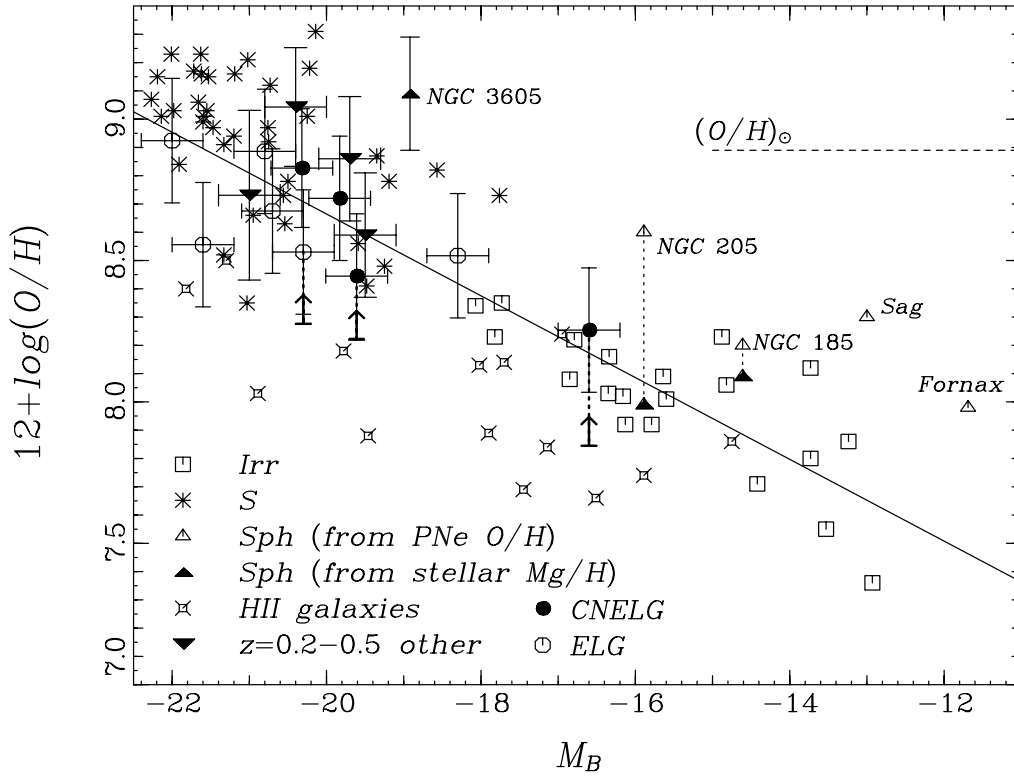


Figure 4.10: The oxygen abundance of $0.2 < z < 0.5$ star-forming galaxies, in comparison to those of nearby galaxies, versus the absolute blue magnitude, M_B , from Kobulnicky & Zaritsky (1999). This shows that metal-rich galaxies at $0.2 < z < 0.5$ (shown as inverted triangles) are common. [It also shows that if desired photometric redshifts from SNAP can be used to estimate M_B , and thus (relative) O/H , in advance of selection of which supernovae to follow at high redshift, then M_B can also serve as a surrogate measurement of O/H .] Normalization will have to be checked at even higher redshifts.

Chapter 5

Comparison with Alternative Approaches for Supernova Studies

5.1 Introduction

In choosing the best way to advance supernova cosmology, the capabilities, sensitivities, economics, and risk of various facilities need to be compared. Supernovae are point sources, and their study derives maximal benefit from the diffraction-limited imaging possible in space. This is nicely demonstrated by Figure 5.1, which compares ground-based and HST images of the same supernova explosion. The excellent resolution of the HST image allows for improved galaxy subtraction and less sky background and thus yields smaller photometric error.

The principle alternative to a dedicated space-based wide-field telescope like SNAP is to use much larger ground-based telescopes, possibly working in tandem with current (HST) and future (NGST) non-dedicated facilities in space. The current supernova work at high redshift involves the use of large ground-based telescopes equipped with wide-field imagers to find the supernovae near maximum light, followed by redshift determination and spectroscopic confirmation with the largest ground-based telescope (Keck 10-m) and subsequent photometric follow-up with HST. The quality and quantity of these current datasets are greatly inferior to what SNAP aims for. These data have been quite useful, but they are insufficient to fully test the underlying assumptions that the light-curve width-luminosity relation standardizes all SNe Ia luminosities at all redshifts, that there is no intergalactic extinction, and that no dispersion exists in host-galaxy dust extinction curves. Combining the discovery rate of both the SCP and the High- z Team, at best 20 high-redshift supernovae per year have adequate follow-up observations. Fig. 5.2 shows how the sample of distant SNe Ia has been built-up over time. This rate, in and of itself, indicates that vastly improved facilities are necessary to advance supernova cosmology.

The discussion below will make the case that a dedicated SNAP mission has significant advantages over a number of alternatives. Here we summarize how several

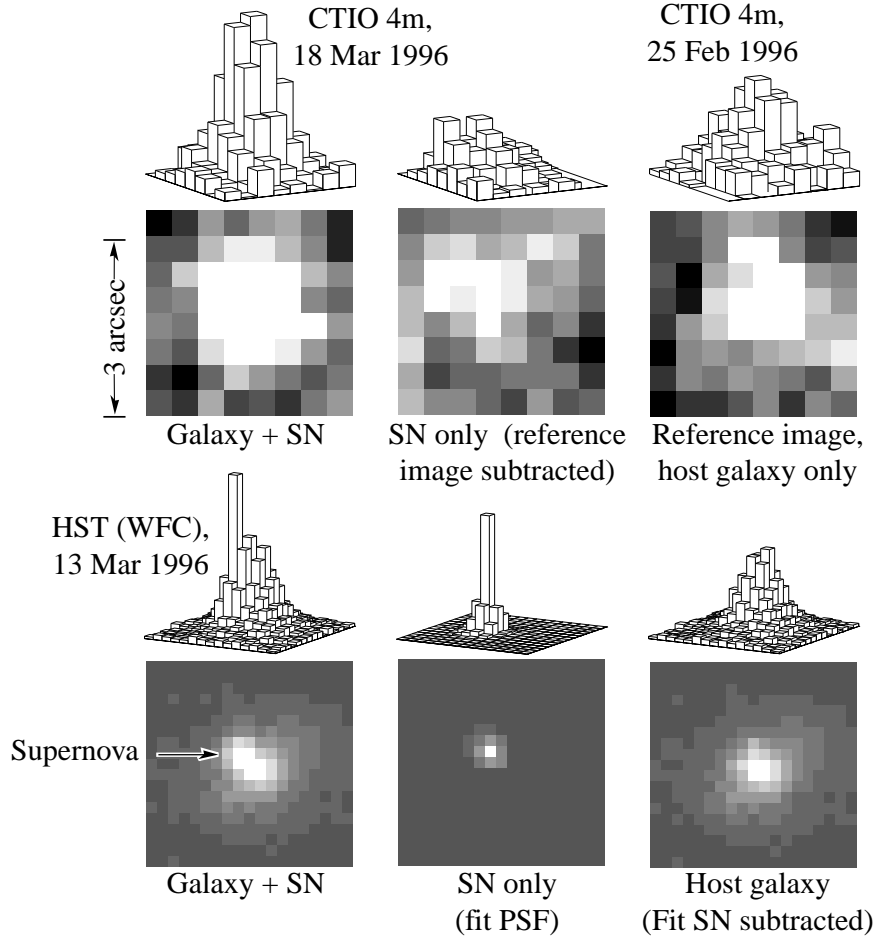


Figure 5.1: A comparison of ground-based and HST WF images of SN1996cl, a second $z = 0.83$ SN found by our project. This SN lies in the cluster MS1054.4-0321 which happened to be observed with HST when the SN was close to maximum light (HST image courtesy of Megan Donahue).

alternatives would perform were they to attempt the experiment for which SNAP is designed. This allows an examination of just which parts of the experiment would be compromised with each alternative.

The alternatives considered assumed the following dedicated facilities, which include a hypothetical wide-field telescope (WFT) and an overwhelmingly large telescope (OWLT) each which could be built within a decade:(see Table 5.1)

We do not consider wide-field AO or OH-suppression systems; these are impractical, as discussed in the next section.

We have determined how well these facilities, alone or in tandem, can actually execute the SNAP baseline mission. We examine whether discovery and follow-up photometry can be done in a batch mode, with several targets in a single field. The ability to discover distant supernovae within the allocated time, and to find supernovae

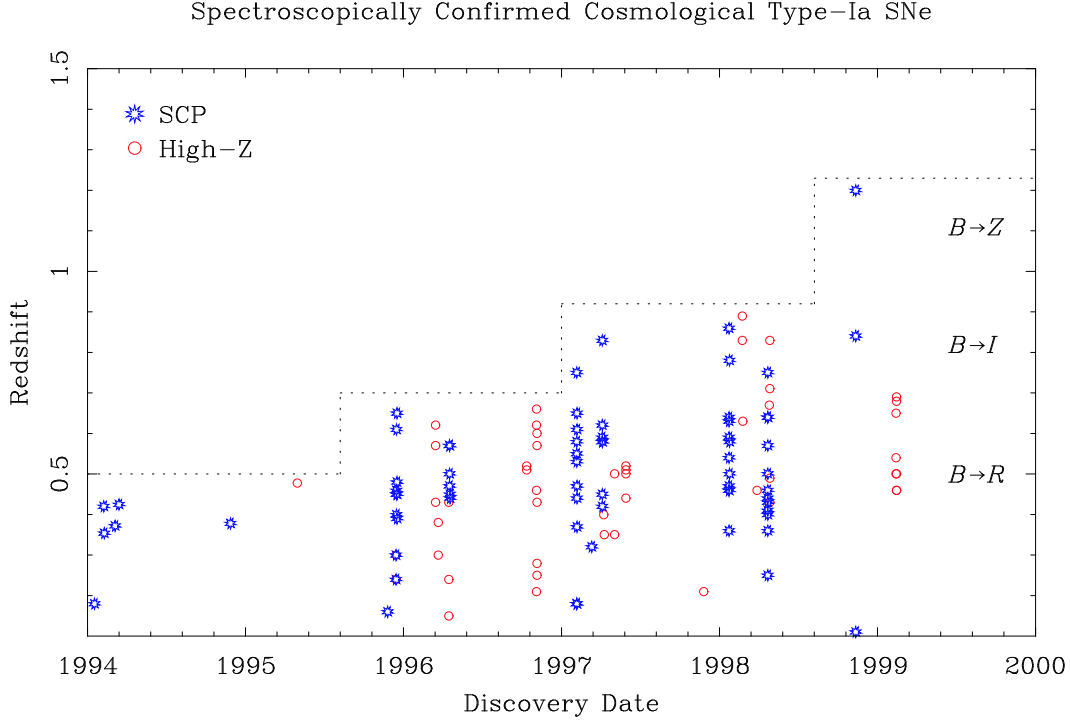


Figure 5.2: Distant, spectroscopically confirmed SNe Ia discoveries reported in the IAU Circulars this decade. Discoveries by the SCP and the High- Z Team are shown separately. The dashed boundary shows how the maximum distance has increased with time as facilities and time allocation have improved. Along the right margin the observer frame filter needed for restframe B -band discoveries and follow-up is indicated.

Description	Location	Aperture	FOV	AO?	OH-suppression?
CFHT	ground	3.6-m	1 \square°	no	no
Keck	ground	10-m	NA	no	no
Keck+AO	ground	10-m	NA	yes	no
Keck+AO+OH	ground	10-m	NA	yes	yes
WFT	ground	8-m	7 \square°	no	no
OWLT	ground	24-m	1 \square°	no	no
OWLT+AO	ground	24-m	NA	yes	no
OWLT+AO+OH	ground	24-m	NA	yes	yes
HST+ACS+NIC	space	2.4-m	0.003 \square°	NA	NA
NGST	space	6-m	0.004 \square°	NA	NA

Table 5.1: Alternative Facilities. WFT and OWLT refer to a hypothetical wide-field telescope and an overwhelmingly large telescope that would each require a decade to construct. CFHT refers to the Canada–France–Hawaii Telescope, AO refers to an adaptive optics system, OH refers to an OH suppression system, and NGST refers to the Next Generation Space Telescope. The Advanced Camera for Surveys (ACS) and the Near Infrared Camera (NIC) are both Hubble Space Telescope (HST) instruments.

shortly after explosion, are included in this comparison. In accord with the discussion

of contrast in the next section, we assume in addition to Poisson errors a contribution equal to 10^{-4} of the foreground signal (due, e.g., to flat-fielding errors or instrument sensitivity variations). We find that ground-based searches with a WFT hit a photon noise wall, whereas an OWLT search hits a noise wall set by the additional foreground signal error. These considerations prevent such facilities from finding distant supernovae early. The results of this analytic comparison are summarized in Table 5.2.

Search	Facilities Photometry + Spectra	Batch	SNe/yr	z Limit given time budget	Early Discovery (2 days)	Time (hrs) to Achieve S/N at max z	Magnitude Limit (AB)
SNAP	SNAP	Yes	2400	$z < 1.7$	Yes	4 ($S/N = 3$)	30
HST+ACS	HST+ACS+NIC	Yes	20	$z < 1.7$	Yes	2 ($S/N = 3$)	30
NGST	NGST	No	60	$z < 1.7$	Yes	0.1	-
CFHT	HST+ACS+NIC	No	350	$z < 0.6$	4 day	8 ($S/N = 5$)	26
WFT	Keck+AO	No	140	$z < 1.2$	Peak-0.5	8 ($S/N = 10$)	26
WFT	WFT	Yes	210	$z < 0.6$	Yes	6 ($S/N = 3$)	27
WFT	NGST	No	430	$z < 0.6$	4 day	8 ($S/N = 10$)	26
WFT	NGST	No	460	$z < 0.9$	6 day	7 ($S/N = 5$)	26.5
OWLT	OWLT	Yes	420	$z < 0.7$	Yes	9 ($S/N = 5$)	27.5
OWLT	OWLT+AO+OH	No	290	$z < 1.0$	5 day	4 ($S/N = 5$)	27

Table 5.2: Comparison of alternative facilities to SNAP for baseline mission.

The one basic theme these calculations show is that supernovae cannot be discovered very early on the light curve from the ground.

5.2 Advantages of Space-Based Observations

5.2.1 Reduced Foreground Emission

The principle advantage of space-based observation of distant supernovae is the large reduction in foreground noise compared to ground-based observations. The major source of foreground noise arises from the Poisson statistics of atmospheric airglow, light from the supernova host galaxy, and zodiacal light. For imaging applications with modern detectors, noise from dark current and readout amplifier noise make minor contributions. In the typical case where the photon foreground flux exceeds that from the supernova, the exposure time to reach a given signal-to-noise ratio is directly proportional to the foreground. Significant foreground reduction can be achieved in space because atmospheric airglow is eliminated, leaving only the foreground from zodiacal light and host-galaxy light. Thus space-based observation offers a very direct means of obtaining better brightness measurements of more distant supernovae beginning when they are quite faint, just days after explosion.

The redshifted B and V -band Poisson sky noise are plotted in Figure 5.3 as a function of redshift for a potential ambitious ground-based setup. The early detection at 3.8 mag below peak is seen to be impossible for $z > 0.6$ supernovae, and the equally important measurement of the plateau phase of the light curve at 2.8 magnitudes below peak would be limited to $z < 0.7$ supernovae. These limitations of ground-based observations are borne-out in more complete calculation in Table 5.2.

Emission from the atmosphere is strongly wavelength dependent, as shown in Fig 5.4. In the range 0.7 - 1.8 μm , of interest in observing distant (redshifted)

Sky Photon & Systematic Noise: Ground 8-meter, 3 hr

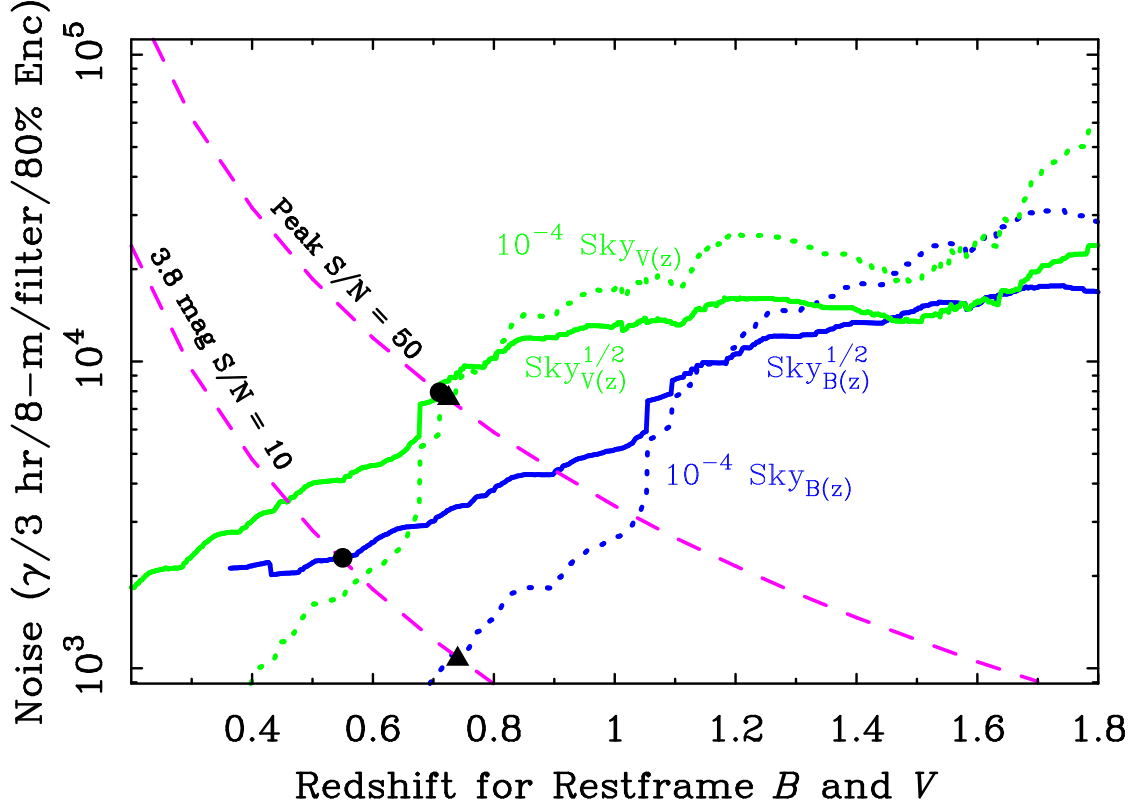


Figure 5.3: The sky background will introduce two forms of photometric uncertainty. The solid lines plot the redshifted B and V -band Poisson sky noise as a function of redshift. In addition to Poisson noise, the bright foreground can produce additional errors if it is not perfectly uniform; plotted as dots are 10^{-4} non-uniformity errors. The photometric search and peak color signal-to-noise requirements for the SNAP mission are given by the dashed lines. Ground-based searching and precise color measurements are impossible from the ground beyond $z = 0.7$, independent of exposure time and mirror aperture.

supernovae, the airglow is dominated by discrete emission lines from the OH radical. There is also a non-negligible continuum, thought to be caused by the reaction: $N + NO \rightarrow NO_2 + \gamma$. (Note that thermal emission is not important at these wavelengths, so observations at, e.g., the South Pole, do not lead to a significant reduction in sky emissions.) The relative contributions of important foreground sources are given roughly in Table 5.3.

These values indicate that for wide-field broadband imaging, as required for finding distant supernovae and obtaining light curve measurements simultaneously for all supernovae in the field of view, space-based images have an additional advantage of 12,

Wavelength (μm)	Airglow		Zodiacal
	Continuum	OH lines (photons/m ² /s/ μm /arcsec ²)	Light
0.8	130	400	43
1.2	600	16000	32
1.6	600	25000	21

Table 5.3: Atmospheric and space foregrounds.

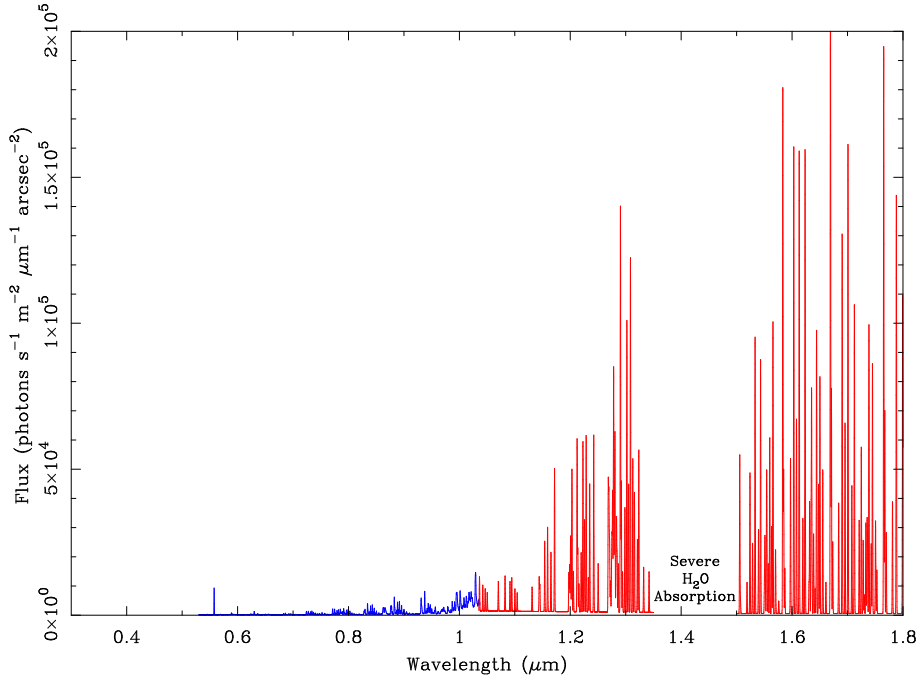


Figure 5.4: The optical and near-infrared spectrum of the atmosphere overhead at an excellent astronomical site such as Mauna Kea, Hawaii or Paranal, Chile. There is a faint continuum, punctuated by a series of bright emission lines, mostly due to OH. These emission lines are strong at the beginning of the night, and by midnight have decreased to the levels shown here. The sky brightness also correlates with increased solar activity, being roughly twice as bright as shown here at the peak of the solar cycle. Aside from these temporal variations, the sky brightness increases with the airmass of the source being observed. The intrinsic widths of the lines are quite narrow, thus their impact can be decreased for spectroscopic observations with resolution greater than $R \sim 3000$. The optical spectrum is from our own observations, while the NIR spectrum is constructed from the observations of Ramsay, Mountain, & Geballe (1992); Maihara et al. (1993); Oliva & Origlia (1992).

500, and 1200 at 0.8, 1.2, and 1.6 μm , respectively, from the reduced foreground emission alone. Some work has been done on filters attempting to suppress the OH emission lines; however, these filters also block significant spectral regions from the object being

observed, making accurate photometry dependent on *a priori* knowledge of the spectral energy distribution of the target. For supernovae the spectral energy distribution is time dependent, and of course shifts with redshift. Some test-bed instrumentation has shown the ability to suppress OH lines using an intermediate spectral image where the OH lines are masked (Iwamuro et al., 1994). Such instruments can only work over very small fields, and their additional optics reduce system throughput by $\sim 2 - 3\times$. This reduced efficiency and the need to observe each supernova individually eliminates any advantage of these systems compared to SNAP.

These benefits of space over ground-based observation are significant, but don't tell the whole story. Although calculations based on Poisson noise would indicate that ground-based telescopes of sufficiently large aperture might compete with a smaller space-based telescope, this ignores the difficulty inherent in obtaining accurate photometry of faint sources overwhelmed by a foreground $\sim 10^5\times$ brighter (typical of NIR observations). Photometry with an accuracy of 2% on such a source requires the foreground to be uniform to 2×10^{-7} on small scales. In our experience, accuracy of this type with CCD or NIR HgCdTe detectors has never been achieved. Indeed, we have found that whereas $S/N \sim 3.5$ supernova candidates discovered in ground-based *R*-band are generally genuine, candidates discovered in apparently well-flatfielded images at *I*-band – where the foreground is substantially brighter – with calculated S/N up to 5 have all been spurious. To achieve $S/N = 5$ rather than $S/N = 3.5$ requires twice the exposure; this penalty can only get worse as higher redshifts are attempted from the ground.

Figure 5.3 shows the noise introduced from 10^{-4} non-uniformity in the sky background expected from ground observations. From this plot we can conclude that ground-based searching and precise color measurements are impossible beyond $z = 0.7$ independent of exposure times and mirror aperture sizes.

5.2.2 Reduced Foreground with Better Seeing

Blurring by the atmosphere causes the light from a supernova to have a Gaussian point-spread-function (PSF) of ~ 0.7 arcseconds FWHM at optical wavelengths at the best ground-based sites (see Fig 5.6 and Fig 5.7), whereas in space the PSF is near the diffraction limit (0.12 arcseconds at a wavelength of $1 \mu\text{m}$ for a 2-m telescope). This blurring means that considerably more sky light and host-galaxy light [$(0.7/0.12)^2 = 34$ times more] is included in the (software) aperture used to measure a supernova from the ground. The improvement in image quality alone translates into a factor of 34 advantage for SNAP compared to a ground-based telescope of the same size. Prototype adaptive optics (AO) have demonstrated the ability to improve ground-based images to better than 0.1 arcsec. However, the corrected solid angle is small (less than one arcminute in radius), and laser guide stars (which are not available on nights with high cirrus) are needed for observations near the preferred regions towards the Galactic poles. In addition, absolute brightness measurements may be complicated by the significant and varying skirt of light typical of AO point-spread-functions (\sim Lorentzian). Kaiser, Tonry, and Luppino have proposed an array of many small telescopes applying tip-tilt correction based on coordinated monitoring of

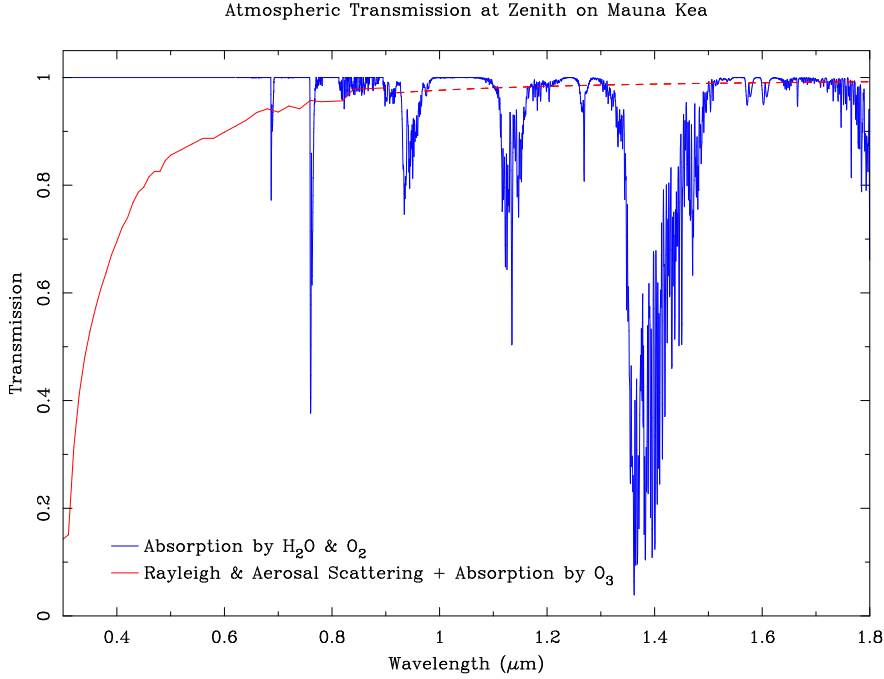


Figure 5.5: The optical and near-infrared transmission of the atmosphere at the zenith on Mauna Kea for an H_2O column of 1.6 mm. The transmission is broken into a smooth component mostly due to molecular and aerosol scattering, and a structured component due to H_2O and O_2 many discrete absorption lines. The resolution is approximately 1 nm, or $R \sim 1000$.

multiple guide stars, which can achieve some improvement in image quality and at the expense of having to build dozens of widefield imagers.

5.2.3 Further Ground-based Degradation

The clear-weather transparency of the atmosphere also has a non-trivial effect on the quality of supernova data attainable from the ground. Fig 5.5 breaks the atmospheric transmission into a smooth component — which can be corrected fairly accurately using standard observing procedures — and a second, finely structured, component which is difficult to accurately correct. The second component is composed of discrete, narrow, absorption lines at differing levels of saturation, making the correction dependent on airmass and spectral resolution. Narrow spectral features observed in these regions would be suspect, and the relative accuracy of the absorption correction no better than $\sim 10\%$. It is clear from this figure that key supernova observations can not be accurately obtained for some redshifts from ground-based observations (*e.g.* the 6250Å Si II feature for SNe Ia, H α for SNe II).

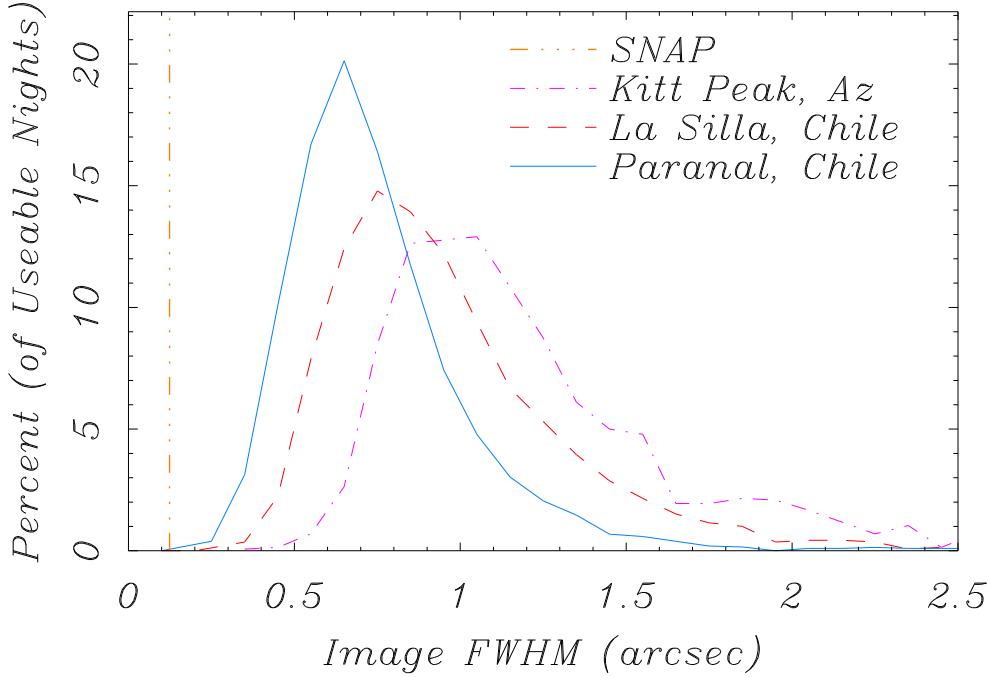


Figure 5.6: Percent of usable nights with given seeing for three representative sites and facilities, as compared with the diffraction limited ~ 0.12 arcsec seeing of the SNAP satellite. The Paranal data are applicable to an excellent site with state-of-the-art facilities, where careful attention has been paid to reducing telescope/dome seeing. The Kitt Peak data apply to a good site with old facilities which have been retrofitted to the extent possible to reduce telescope/dome seeing. La Silla is intermediate between these two. Measurements were obtained at optical wavelengths at zenith, using seeing measurement cameras and therefore do not include any degradation due to the astronomical instrument being used at the time. These measurements should scale with wavelength, λ , and airmass, X , roughly as $\lambda^{-0.2} X^{0.6}$. In determining the typical exposure time for foreground-limited observations, the appropriate value to use is not the mode, mean, or median of the seeing, but rather the RMS seeing, $\langle \text{FWHM}^2 \rangle^{0.5}$, since this reflects how seeing enters the signal-to-noise equation. $\langle \text{FWHM}^2 \rangle^{0.5}$ equals 0.80, 1.03, and 1.28 arcsec for Paranal, La Silla, and Kitt Peak, respectively. For constant signal to noise, exposure time goes as FWHM^2 .

5.2.4 Improved Detection Efficiency

Weather (cloudy skies, strong winds) make about $\frac{1}{3}$ of nights at the best sites unusable. For most astronomical observations this is simply counted as a direct loss in efficiency. However, for observations of transient sources, the impact of weather can be far greater. Our simulations indicate that a site with $\frac{2}{3}$ clear nights has an effective efficiency of 50%, assuming weather correlated on a timescale of 3 days. If this factor is combined with the fraction of each night that is dark ($\sim 40\%$) and the fraction of that time which is not severely degraded by moonlight ($< 75\%$), the effective duty-cycle of a ground-

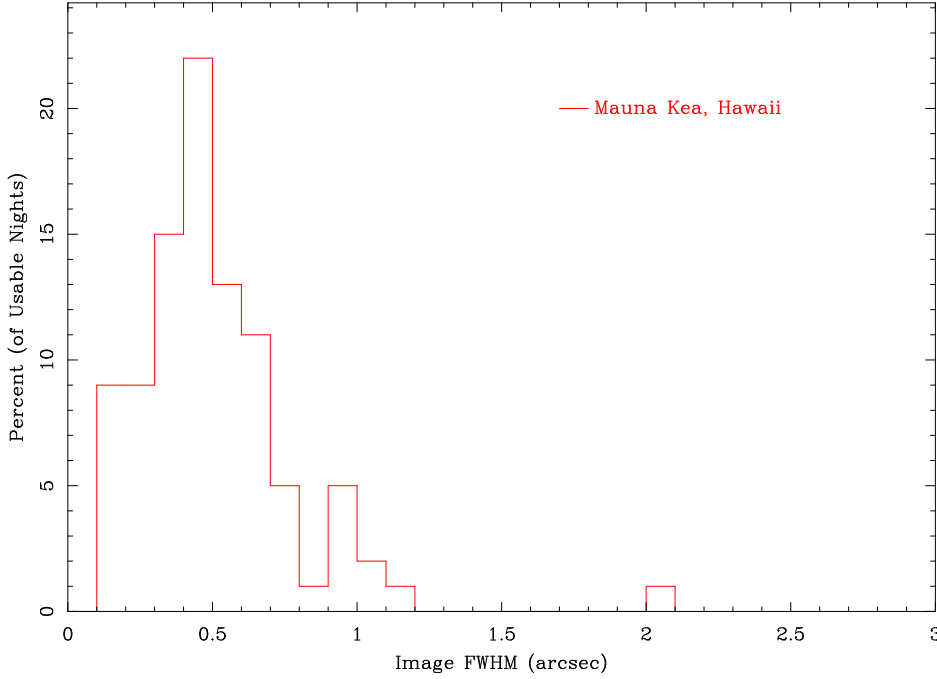


Figure 5.7: Percent of usable nights with given seeing in the near-infrared ($2.2 \mu\text{m}$) from the UK Infrared Telescope on Mauna Kea. UKIRT is at an excellent site, but the telescope and enclosure are not now state-of-the-art. The value of $\langle \text{FWHM}^2 \rangle^{0.5}$ equals 0.62 arcseconds if all the observations are included. Rejecting nights with seeing worse than 0.9 arcseconds (10% of nights) reduces $\langle \text{FWHM}^2 \rangle^{0.5}$ to 0.48 arcseconds.

based telescope is $\sim 15\%$. In addition, interference from the moon will preclude early discovery with wide-field ground-based imaging for $\sim 25\%$ of supernovae.

5.3 Detailed Comparison of SNAP and Ground-based Viewing

As background to the previous section, in Tables 5.4 through 5.7 a number of comparisons between various space-based and ground-based observing factors are explored as they pertain to the discovery and follow-up of supernovae. How these factors translate into overall mission capabilities has already been summarized in Table 5.2. There we found that in no case – neither wide-field imaging, OH-suppressed photometry, AO-assisted photometry, nor AO-assisted spectroscopy – can ground-based facilities perform as effectively as a 2-m SNAP satellite for the types of measurements required for supernova-based cosmological studies, including the necessary checks on potential sources of systematic error. Details of the space-based versus ground-based comparisons are provided in the table captions, and are based on the general discussion earlier in this section. The product of the dehydration factors yields the Ground/Space Efficiency ratio, and reflects the efficiency of equal aperture telescope in ground and

space.

Wavelength (μm)	Degradation Factors						Ground/ Space Efficiency
	Image Quality	Night Sky Brightness	Trans- mission	Weather	Sun- light	Moon- light	
0.5—0.7	0.028	0.22	0.89	0.5	0.4	0.6	7×10^{-4}
0.7—0.9	0.031	0.079	0.95	0.5	0.4	0.7	3×10^{-4}
0.9—1.1	0.034	0.014	0.95	0.5	0.4	0.9	8×10^{-5}
1.1—1.3	0.049	0.0018	0.85	0.5	0.4	1.0	1×10^{-5}
1.3—1.5	0.071	0.0012	0.50	0.5	0.4	1.0	9×10^{-6}
1.5—1.7	0.098	0.00077	0.90	0.5	0.4	1.0	1×10^{-6}

Table 5.4: Wide-field Imaging Comparison. This comparison assumes background-limited wide-field imaging, where adaptive optics and OH line suppression is not practical. The image quality comparison assumes the maximum of four $0.1''$ square pixels or $1.86\lambda/D$ (80% encircled flux) for SNAP. The ground-based image quality was based on an aperture with diameter equal to $1.52\times$ the *RMS* seeing FWHM, which encloses 80% of the light for a 2-D Gaussian. An *RMS* seeing of $0.8''$ at $0.55 \mu\text{m}$ (as measured at Paranal, Chile) was assumed, and scaled as $\lambda^{-0.2}$.

Wavelength (μm)	Degradation Factors							Ground/ Space Efficiency
	Image Quality	Night Sky Brightness	Trans- mission	Weather	Sun- light	Moon- light	Suppressor Penalty	
1.1—1.3	0.049	0.015	0.85	0.5	0.4	0.7	0.50	4×10^{-5}
1.3—1.5	0.071	0.014	0.50	0.5	0.4	0.8	0.50	4×10^{-5}
1.5—1.7	0.098	0.012	0.90	0.5	0.4	0.9	0.50	1×10^{-4}

Table 5.5: OH Suppression (Follow-up) Imaging Comparison. This comparison assumes background-limited ground-based imaging with OH line suppression, but no adaptive optics. Other assumptions are as in Table 5.4. Here we add an additional column which is a rough estimate of the throughput penalty associated with the use of OH suppression devices. Only wavelengths where this penalty is potentially compensated by the gain due to sky suppression are shown. Note that with OH suppression, aerosol-scattered moonlight is more important at near-infrared wavelengths.

5.3.1 Searching with HST or NGST

Space-based discovery with existing and currently planned imagers is impractical. The fields of WFPC2 ($5.3\Box'$), WFPC3 ($7.1\Box'$), and ACS ($11.3\Box'$) are small, and the red response of their CCD's is poor compared to an UCB CCD. Searching $20\Box^\circ$ to depths reached by SNAP would require about $6\text{--}12\times 10^3$ second exposures or $\sim 3\text{--}8$ orbits (each orbit has 52 minutes on-source, 44 minutes in Earth occultation and guide-star reacquisition); this amounts to 3—15 yrs! Therefore, searching for large numbers of supernovae with current or future HST instrumentation is impossible. NGST ($16\Box'$) would be more sensitive than SNAP due to its significantly larger aperture, requiring discovery exposures of only 1 minute. However, the 20 min repointing time means that NGST would take 3 days *just repointing* to observe the 225 fields needed to cover one SNAP field. To cover $20\Box^\circ$, 60 days of dedicated NGST time would be required; this return rate is an order of magnitude slower than the 4—8 day return rate offered

Wavelength (μm)	Degradation Factors							Ground/ Space Efficiency
	Image Quality	Night Sky Brightness	Trans- mission	Weather	Sun- light	Moon- light	AO Optics Penalty	
0.5—0.7	0.033	0.22	0.89	0.5	0.4	0.6	0.50	4×10^{-4}
0.7—0.9	0.041	0.079	0.95	0.5	0.4	0.7	0.50	2×10^{-4}
0.9—1.1	0.050	0.014	0.95	0.5	0.4	0.9	0.50	6×10^{-5}
1.1—1.3	0.081	0.0018	0.85	0.5	0.4	1.0	0.50	1×10^{-5}
1.3—1.5	0.144	0.0012	0.50	0.5	0.4	1.0	0.50	9×10^{-6}
1.5—1.7	0.262	0.00077	0.90	0.5	0.4	1.0	0.50	2×10^{-5}

Table 5.6: AO (Follow-up) Imaging Comparison. This comparison assumes background-limited ground-based imaging with adaptive optics with the diffraction limit of a 20-m telescope. Since in this case OH suppression is not as important, we do not include it. The quality of an adaptive optics system is often given by the Strehl ratio, which is the ratio of attained peak intensity relative to that expected from the diffraction limit. The point spread function resulting when adaptive optics is used consists of a (nearly) diffraction-limited core, surrounded by a broad skirt. Here Strehl ratios of 0.24, 0.32, 0.40, 0.48, 0.57, and 0.65 are assumed, respectively, for each of the wavelength ranges given in the table. These values are given or estimated from the study of Le Louarn et al. (1998) for median seeing conditions at Paranal and the use of nearby bright natural guide stars (which give better correction than laser guide stars). They are, however, optimistic in comparison with typical results to date from the AO system on Keck. We have further assumed that the skirt is a Gaussian with FWHM given by the uncorrected seeing. The ratio is evaluated as before for SNAP, and using the 80% encircled flux radius for AO. Here we add an additional column which is a rough estimate of the throughput penalty associated with the optics of the adaptive optics system. Note that the value chosen for this throughput penalty is quite generous in comparison to current working AO systems.

Wavelength (μm)	Degradation Factors							Ground/ Space Efficiency
	Image Quality	Night Sky Brightness	Trans- mission	Weather	Sun- light	Moon- light	AO Optics Penalty	
0.5—0.7	0.11	0.29	0.89	0.5	0.4	0.6	0.50	2×10^{-3}
0.7—0.9	0.16	0.17	0.95	0.5	0.4	0.7	0.50	2×10^{-3}
0.9—1.1	0.29	0.05	0.95	0.5	0.4	0.9	0.50	1×10^{-3}
1.1—1.3	1.2	0.03	0.85	0.5	0.4	1.0	0.50	3×10^{-3}
1.3—1.5	31	0.03	0.50	0.5	0.4	1.0	0.50	5×10^{-2}
1.5—1.7	127	0.034	0.90	0.5	0.4	1.0	0.50	4×10^{-1}

Table 5.7: AO (Follow-up) Spectroscopy Comparison. This comparison assumes background-limited ground-based spectroscopy with adaptive optics. (Note that it is possible that not all ground-based or space-based spectroscopic observations will be background-limited; the exact S/N is used in the SNAP mission analysis in Table 5.2, below). Observations at high resolution ($R > 10000$) automatically result in OH suppression, so we use the OH-suppressed foreground. The assumptions regarding the quality of AO are similar to this in Table 5.6, however, the comparison is made for a 50% encircled energy (which is being quite generous) for the ground-based observations. This is justified under the assumption that the ratio between the 50%, 80%, and total encircled energy apertures will vary slowly with wavelength, and that spectroscopic observations are deep enough that profile wings can be traced well beyond the 80% encircled energy aperture after smoothing over wavelength. A typical spectrum will cover a larger wavelength range than any of the ranges given in the table. Over the range of a real spectrum, the AO point spread function and sky foreground will vary, and an exposure will usually be taken to cover the worst case.

by SNAP. Of course NGST can be an effective supernova-finder for redshifts beyond those in the baseline SNAP mission, where the surface density of supernovae should be higher, and it could help in obtaining spectra of supernovae discovered by SNAP.

5.3.2 Ground-based searching with follow-up using HST or NGST

Ground-based discovery in concert with space-based follow-up using HST or NGST presents another alternative. As already discussed, ground-based searching is drastically inefficient; even hypothetical 24-m telescopes cannot compete with SNAP for early discovery due to the extremely small contrast of supernovae against the bright night sky. Ground-based discovery at peak is of course possible, but is of little value for precision cosmology.

In addition, combining ground and space observations involve some logistical problems, which we have already encountered with our current program. Namely, for observations with HST the location of, and observing sequence for, a potential supernova must be given three weeks in advance, and the exact location must be given one week in advance. If spectroscopic confirmation comes from the ground, and allowing for the time needed to analyze the discovery and spectroscopy data, a supernova must be discovered almost three weeks (observer frame) before maximum for space-based follow-up observations to begin even as late as one week before maximum. As we found in Table 5.2, such early discovery is impractical beyond modest redshifts even for a

wide-field imager on a large ground-based telescope.

Alternate schemes, such as obtaining spectroscopic confirmation with NGST can reduce the necessary lead time, but would require NGST to obtain an additional spectrum at maximum to ensure a homogeneous dataset. Also, such a scheme will result in a non-negligible number of wasted exposures due to spurious candidates or over-prescription of exposure times which cannot be tailored to each object. The time lost there may not be large in the overall scheme, but is likely to be taken with a dim view given that HST and NGST are user facilities.

Chapter 6

Other Scientific Objectives

6.1 Introduction

The detailed study of SNe Ia is the driving science behind the SNAP satellite proposal. However, there are a number of other exciting scientific measurements that could be carried out with the proposed facility. In the following sections, a few examples of measurements that can provide independent information about cosmological parameters are described. In addition there are a wealth of possible measurements that will not be described here, but that would nevertheless be of general interest to the astronomical community.

6.2 Type II Supernova

The expanding photosphere method (EPM) was developed by Baade (1926) for use with variable stars and has been applied to SNe II (Kirshner & Kwan, 1974; Branch et al., 1981; Schmidt, Kirshner, & Eastman, 1992; Eastman, Schmidt, & Kirshner, 1996) in order to estimate the value of H_0 . For a particularly lucid description of the empirical application of the EPM to supernovae see Branch (1987).

These previous applications of the EPM have all been semi-empirical in nature, in the sense that the supernova is assumed to emit radiation as a blackbody or as a diluted blackbody. Then, one simply needs to determine the color temperature and the velocity of expansion in order to determine the total luminosity. This method is plagued by the fact that supernovae are not dilute blackbodies, as well as by uncertainties in the absolute value of the “dilution factor” (Schmidt, Kirshner, & Eastman, 1992; Baron et al., 1995).

The use of detailed spectral modeling has allowed this difficulty to be overcome, making the method much more precise (Baron et al., 1993; Baron, Hauschildt, & Branch, 1994; Baron et al., 1995; Nugent et al., 1995b; Baron et al., 1996). In the Spectral-fitting Expanding Atmosphere Method (SEAM), observed spectra and photometry are used and combined with detailed theoretical modeling of the observed spectra to actually determine distances to both SNe Ia and II. It is unnecessary to make any assumptions about the intrinsic luminosity of the supernova; no black body

or temperature assumptions need to be made. The SEAM method gives accurate distances for SN 1993J (Baron et al., 1993; Baron, Hauschildt, & Branch, 1994; Baron et al., 1995), which was a peculiar Type II supernova, and SN 1994I (Baron et al., 1996) a SN Ic. Normal SN IIP supernovae are both easier to model and give more reliable distances. Preliminary results on SN 1993W and SN 1999em (observed in the UV with HST) confirm that this is indeed the case. Furthermore, Mitchell et al. (2000); Baron et al. (in preparation) show that with accurate radiation hydrodynamical models, exceptional precision to the spectra of SN 1987A can be achieved. Long time-series of spectra are fit that have unprecedented coverage in both time and wavelength which allow one both to assess the uncertainties in the method and to independently determine a distance to the LMC, which still presents one of the major uncertainties in the *HST* measurements of Cepheids and hence in the uncertainty on the Hubble constant. This method rivals Cepheid-based distances in quality and has a much greater range.

With the early data that *will* be obtained by SNAP, we will be able to nail down and reduce the uncertainty on several of the parameters in the SEAM method, making the Type IIs exceedingly useful cosmological probes. Models of very early time spectra obtained for SNe 1993W and 1999em (Baron et al., in preparation) indicate that the early time data allows one to break the degeneracy between reddening and temperature, further increasing the accuracy of the method. This occurs since at early times: the models are quite hot; for “normal” Type IIs, nickel mixing is not an issue; and one has to fit both the Ca H+K lines, the Balmer lines and the overall shape in the red and blue (restframe) of the observed spectrum. This leads to severe constraints on the temperature, which then allows one to estimate the reddening (and even the reddening law with the large amounts of data to be obtained by SNAP). The early time spectra are sensitive to the choice of density profile and helium mixing also, which will help us in determining these parameters.

Clearly, with the thousands of SNe II to be discovered with SNAP we will be unable to perform detailed modeling of all the nearly 10,000 spectra. However, our preliminary results on individual spectra already show that the method is extremely accurate. By detailed modeling of several selected well-observed SNe, we will produce a grid of theoretical models which when combined with Monte-Carlo simulations will allow us to use the SNe II as independent distance indicators. Prior to the launch of SNAP, we will study the use of automated and quantifiable methods for determining how well a given model spectrum “fits” that of an observed supernova.

The most important aspect of the use of SNe II and the SEAM method for determining cosmological distances is that the physics and astronomy is completely independent of that of the SNe Ia and hence the statistical and systematic errors are also uncorrelated with those of the SN Ia search. This is a crucial check on the correctness of the cosmological parameter determinations of SNe Ia alone.

Figure 6.1 shows the current SEAM best fit for a typical plateau-type SN II. The agreement is remarkable.

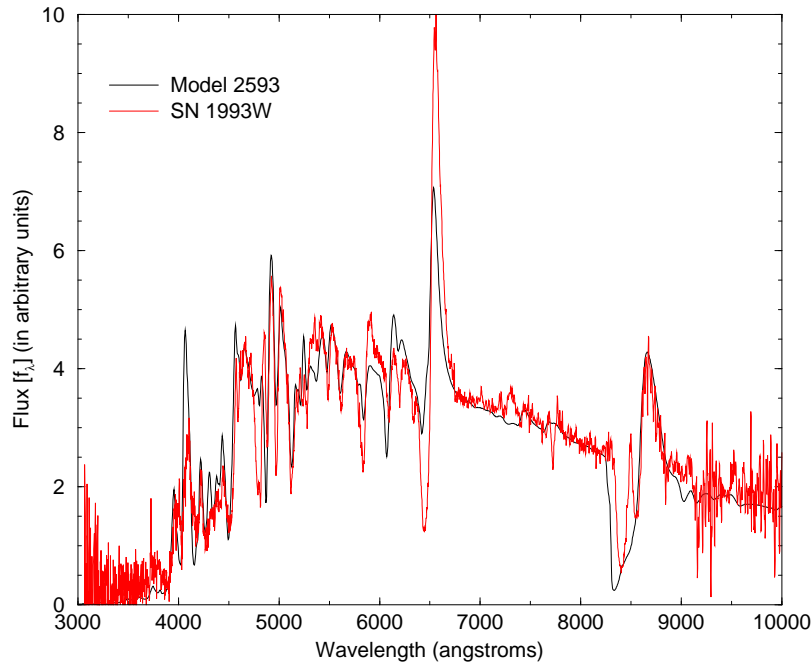


Figure 6.1: A fit to SN 1993W (courtesy D. Leonard) at roughly 40 days after max.

6.3 Gravitational Lensing

6.3.1 The Role of SNAP

According to General Relativity mass concentrations along the line of sight to distant sources produce image distortions and magnifications which can be measured both statistically and in individual cases. This phenomenon, called *gravitational lensing*, is one of the most rapidly-developing and promising observational tools in cosmology and large scale structure studies.

A particularly important bonus of gravitational lensing is its ability to trace mass structures *regardless of their baryonic or radiating component*. This ensures it can provide an independent probe of the amount (i.e. Ω) and distribution of dark matter in the Universe essential to constraining its nature and role in structure formation. Moreover, as lensing signals are also governed by the relative distances of the observer, lens and source, tests can be arranged to constrain the geometric properties of the world model. In summary, lensing can both extend and independently verify many of the conclusions drawn from studies of distant SNe Ia.

Although enormous progress has been made in demonstrating the rich variety of lensing phenomena using ground-based telescopes and, more recently, Hubble Space Telescope, this has been limited by many factors. For the most demanding studies, necessary to provide robust claims on the amount and distribution of dark matter, changes in the ellipticities of individual galaxies of only a few per cent are sought. Even at the best ground-based observatories, significant corrections for seeing and telescope-

induced effects are necessary. Reference is usually made to comparison images taken with Hubble Space Telescope to justify these corrections.

However, even with HST, there are severe restrictions in what can be accomplished because of its small field of view (2 arcmin). Lensing tests conducted along a few narrow sightlines may yield unrepresentative results. Most of the lensing work done by HST has, of necessity, been conducted along “interesting” sightlines such as those containing rich clusters of galaxies (Figure 6.2). As with all survey-based applications, panoramic samples are essential.



Figure 6.2: Image of the central portion of the massive cluster Abell 2218 ($z = 0.18$) recently taken with the Wide Field Planetary Camera 2 on the Hubble Space Telescope. The image shows foreground cluster members (bright oval-shaped sources) and a plethora of faint dramatically-distorted distant galaxies whose arc-like images are stretched tangentially about the cluster center. Multiple images of the same distant lensed galaxy can be recognized via their configuration and identical redshifts.

In this section we illustrate that SNAP has enormous potential in this area without in any way compromising the main mission to detect and study distant SNe. Its wide field and excellent image quality are perfectly suited to a new ambitious program in gravitational lensing.

We have organized the discussion as follows. In Section 6.3.2 we demonstrate the

various lensing phenomena discussing the scientific potential and requirements for each in turn. In Section 6.3.3 we introduce the mathematical treatment of lensing in both the strong and weak regimes. In Section 6.3.3 we discuss constraints on the cosmological parameters possible with SNAP and in Section 6.3.4 those aimed at constraining the distribution of dark matter on various scales.

6.3.2 Introduction to Lensing Phenomena

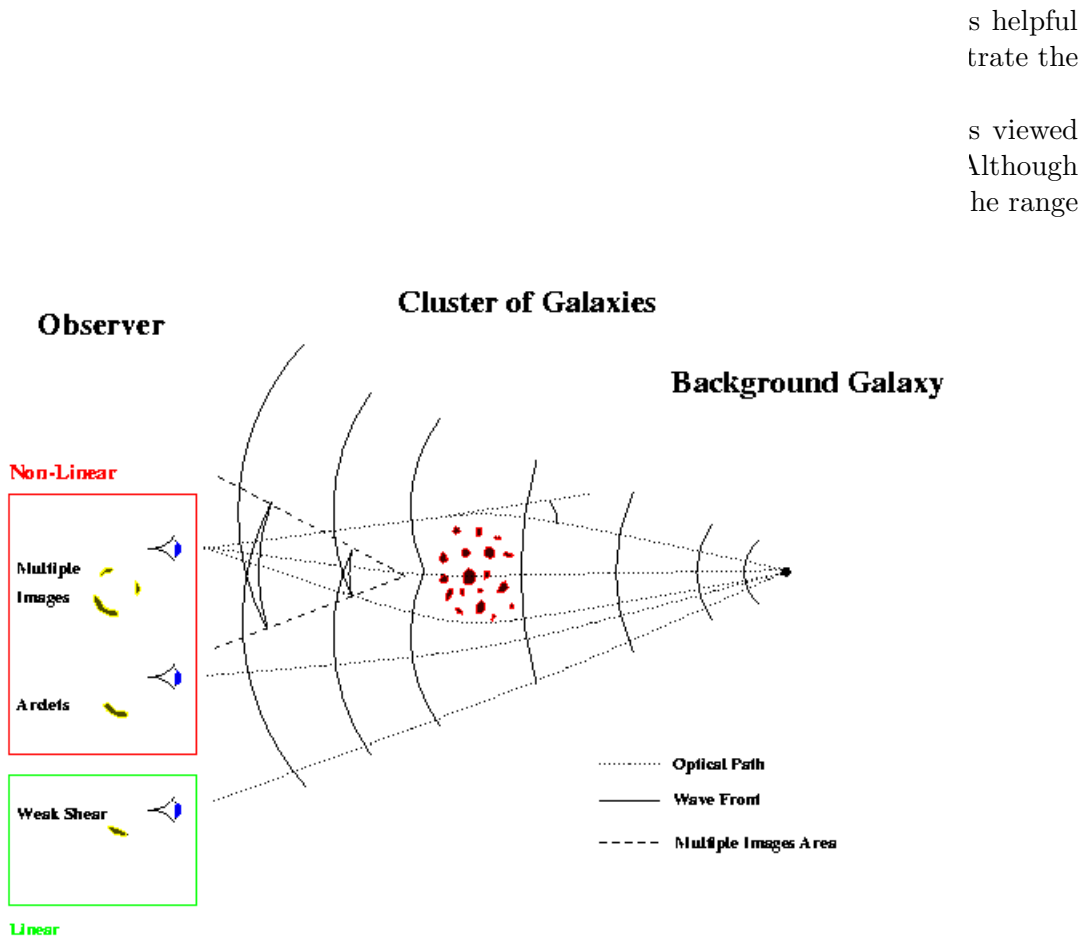


Figure 6.3: Schematic of various lensing regimes for a background population of galaxies viewed through a massive foreground galaxy cluster. Sources viewed inside of the critical curve or region of maximum amplification are multiply-imaged and highly magnified (“giant arcs”), those viewed outside the critical curve produce single tangentially-distorted images (“arclets”). Far from the cluster core, the weak shear is detectable only by averaging the elongations of statistical ensembles of faint galaxies.

Strong lensing: giant arcs, multiple images and microlensing: When a background galaxy is viewed through the dense core of the cluster, significant magnification and image distortion can occur. We will refer to this as “strong lensing” and defer

a more precise definition until Section 6.3.3. In favorable cases where the cluster is sufficiently dense in its core and the source alignment is precise, so-called “giant arcs” are produced. These are distant galaxies whose images are significantly elongated. As surface brightness is conserved by lensing, the image of a random background galaxy is highly magnified.

Typically more than one image of such a background source is produced. The arrangement of these “multiple images”, together with knowledge of the source and lensing redshifts, can provide very tight constraints on the lensing mass contained within a given radius.

If, instead of a rich cluster, the lensing potential is that produced by a single foreground galaxy, lensing features can still occur but, clearly the probability of a favorable alignment is much less than for a rich cluster whose cross-section on the sky is significant. Figure 6.4 shows an example “arc” produced by a foreground elliptical galaxy in the Hubble Deep Field. As the lensing elliptical is much less massive than a rich cluster, the distortion and image deflection is much smaller. Only with exquisite imaging like that from HST (or SNAP) could such features be seen.

As the deflector mass is further reduced, so is the separation between the lensed image and the foreground lens. Ultimately, for a stellar remnant or compact massive object (e.g. a black hole), the relative motion of lens and a background source will induce a temporal variability in the output of the latter at the moment when it is strongly lensed, as in Figure 6.5.

Each of these phenomena represent different manifestations of the same basic effect — the strong gravitational magnification of light from a background source. In the case of the rich clusters, many background sources may be affected offering a rich probe of the mass structure in a single system, particularly if the redshift of each lensed image can be determined. In the case of lensing by individual galaxies, because of the rarity of occurrence, it may not be possible to secure the redshifts involved. In this case, a statistical approach can still provide a very powerful constraint on the halo mass associated with different types of lensing galaxy, e.g. by utilizing the likely redshift distribution from which both lens and source are drawn. This is a good illustration of how a population of examples such as Figure 6.4 can convert an interesting phenomenon into a powerful tool.

Weak lensing: arclets, cosmic shear and large scale structure

Figure 6.3 also shows that gravitational lensing produces detectable effects even well away from the core of a dense cluster. The gradient in the gravitational potential induces a small tangential elongation, or “shear”, in the images of background galaxies (Figure 6.6). Elongated “arclets” have now been seen in the peripheral regions of HST images of rich clusters. In yet weaker regimes, the signal to noise can be improved by averaging the vectorial elongation over a population of randomly-oriented background galaxies in a given small area of sky.

The detection and mapping of this weak lensing signal is one of the most exciting and challenging areas of extragalactic astronomy. Sophisticated inversion techniques have been developed to derive projected mass distributions from maps of the weak shear. Impressive results are already emerging from mosaiced WFPC-2 cluster images taken with HST (Figure 6.7).



Figure 6.4: Strong lensing of a blue background galaxy with $V \sim 25$ by a foreground elliptical galaxy with $V \sim 22$, from the Hubble Deep Field South (Barkana, Blandford, & Hogg, 1999). The figure is centered on the lensing galaxy and measures $3''$ on a side. The separation is 0.9 arcseconds, which ground-based observations could just marginally resolve.

There is, however, a fundamental motivation for extending these weak lensing techniques into surveys of random areas. Models of structure formation are only partly constrained by galaxy surveys since these are most likely biased tracers of the underlying mass distribution. Simulations based on popular structure models indicate the coherent shear, i.e. that averaged over a given angular scale, observed for a population of background galaxies should be a few percent on arcmin scales. The variation of this “cosmic shear” as a function of angular scale is the most direct constraint on both the amount and statistical distribution of dark matter.

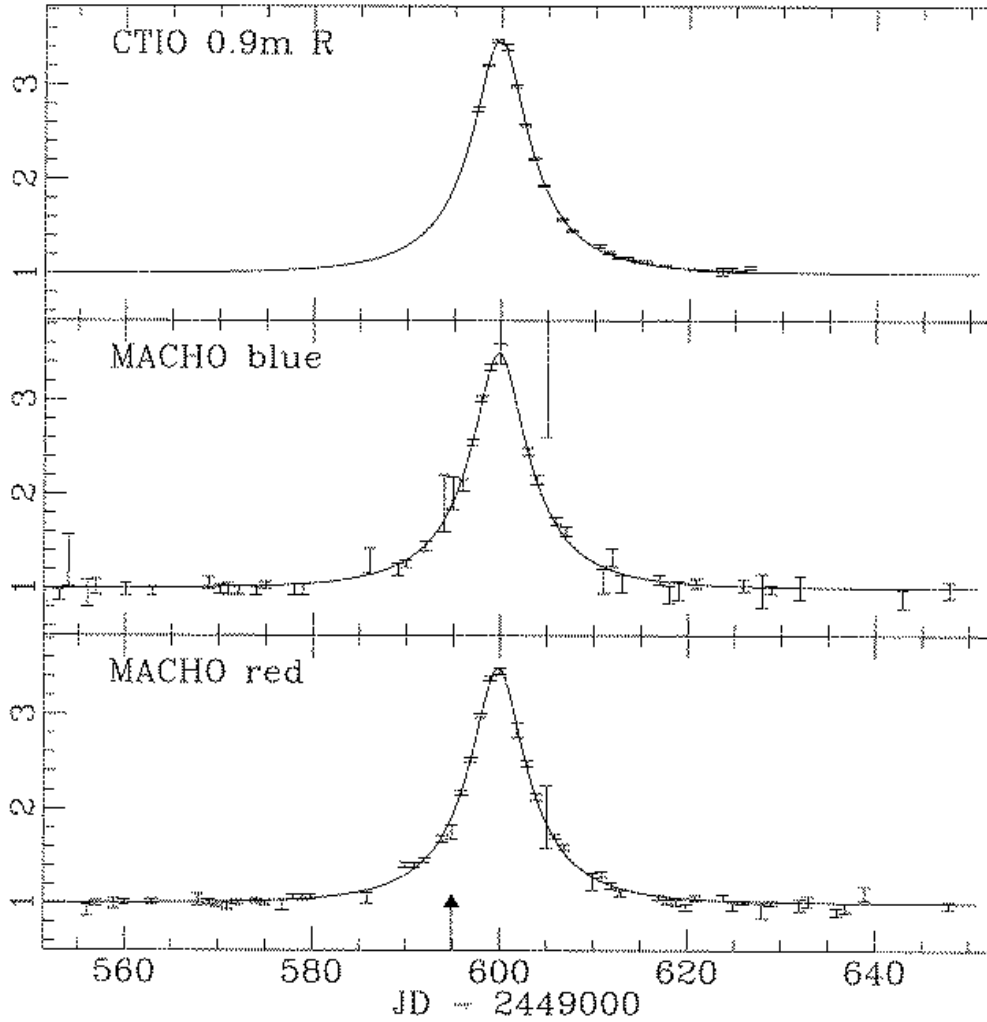


Figure 6.5: Light curves of a MACHO event. The relative motion of a compact lens in front of a background source produces an achromatic variation in the observed source flux.

With sufficient signal to noise, weak lensing methods can also be used to produce maps of the total projected mass distribution as a function of position. This raises the prospects of correlating such maps with the extensive galaxy redshift surveys now underway as well as for producing unbiased catalogs of clusters and groups.

Weak lensing has yet to realize much, if any, of the above potential because of the considerable technical challenges involved. Recovery of the signal necessitates averaging the image properties of large samples of galaxies over wide fields. The largest contiguous area imaged with HST is the Groth strip totalling 108 arcmin^2 where only marginal detections are reported (Rhodes, Refregier, & Groth, 1999). Since SNAP will routinely monitor some 20° of sky to very low flux levels and 100° to intermediate

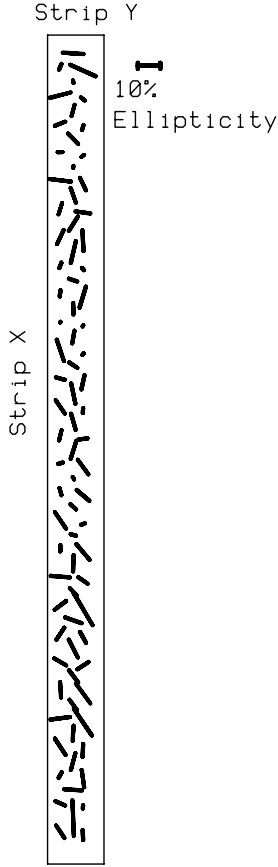


Figure 6.6: A gravitational lensing shear map of the HST Survey Strip (“Groth” Strip).

flux levels, with image quality comparable to that of HST, it can provide a weak-lensing dataset of unprecedented quality.

6.3.3 Detailed Considerations - Strong Lensing

In this section, we develop the above arguments more rigorously indicating the impact of typical experiments with SNAP. In the thin lens approximation, illustrated in Figure 6.8, input angles are mapped to output angles according to:

$$\theta^I = \theta^S + \frac{D_{LS}}{D_{OS}} \alpha(\theta^I)$$

where D_{LS} is the lens-source distance, D_{OS} is the observer-source distance, and $\alpha(\theta^I)$ is the deflection angle. The deflections depend on the projected surface mass density of the lens and the ratio of observer, lens, and source distances:

$$\alpha(\theta^I) = \frac{4G}{c^2} \int \Sigma(\theta^I) \frac{\theta^I - \theta'}{|\theta^I - \theta'|^2} d^2\theta'.$$

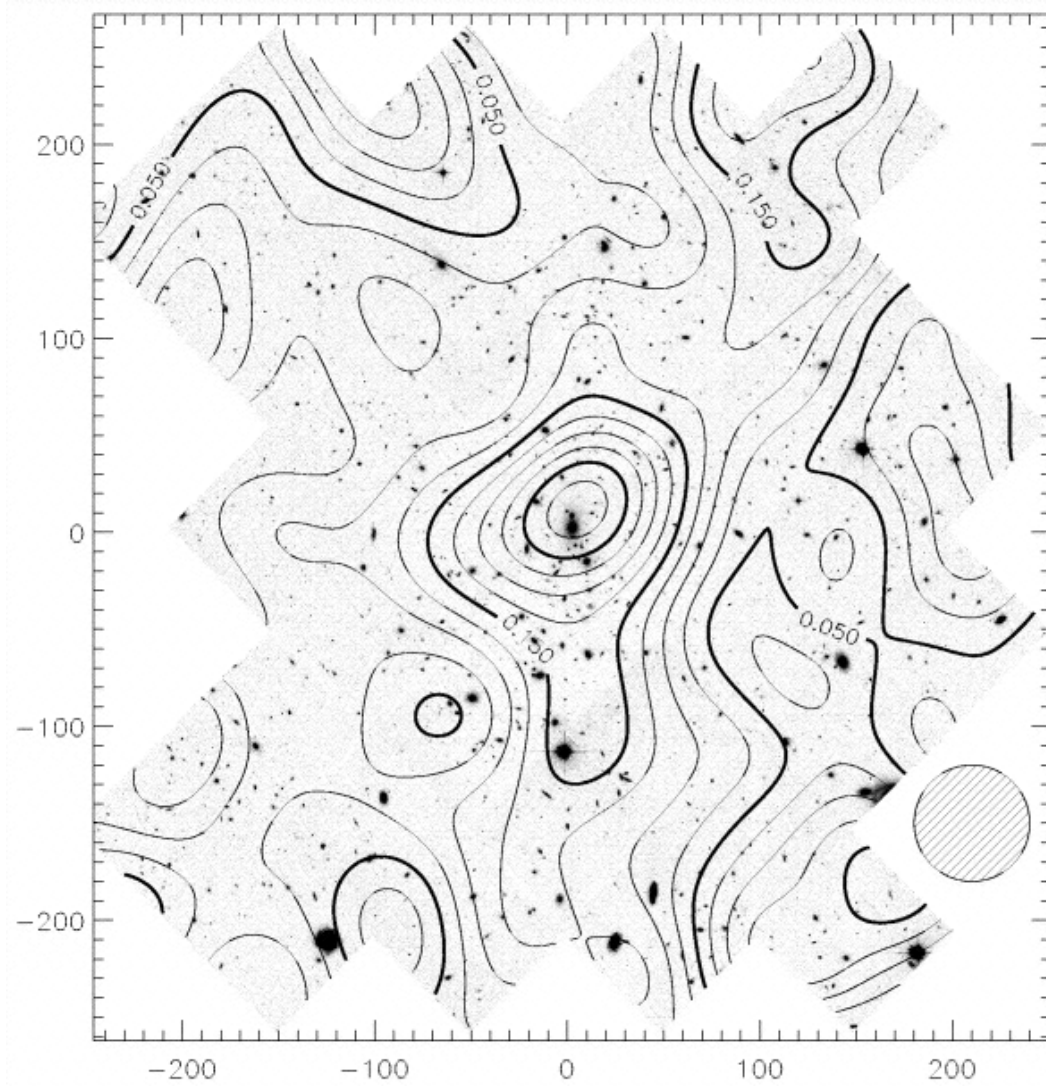


Figure 6.7: Detection and mapping of the weak lensing signal from MS1054 from mosaiced WFPC-2 images (Hoekstra et al., 1998). Note the central concentration of mass.

The surface mass density is related to the line-of-sight gravitational potential, φ , according to:

$$\frac{\Sigma(\theta^I)}{\Sigma_{crit}} = \frac{4\pi G}{c^2} \frac{D_{LS}D_{OL}}{D_{OS}} \Sigma(\theta^I) = \frac{1}{2} \Delta\varphi(\theta^I).$$

For galaxy clusters or elliptical galaxy halos, a singular isothermal sphere is often taken as an approximate model for the dark-matter dominated mass distribution. In this case the deflection angle is a constant, depending only on the line-of-sight velocity dispersion σ_{DM} (Turner, Ostriker, & Gott, 1984). Therefore, the deflection angle is

simply

$$\alpha \sim 4\pi \left(\frac{\sigma_{DM}}{c} \right)^2.$$

The halo of a typical massive elliptical galaxy with $\sigma_{DM} \sim 225$ km/s yields $\alpha \sim 1.5''$ while a rich cluster with $\sigma_{DM} \sim 1000$ km/s gives $\alpha \sim 30''$.

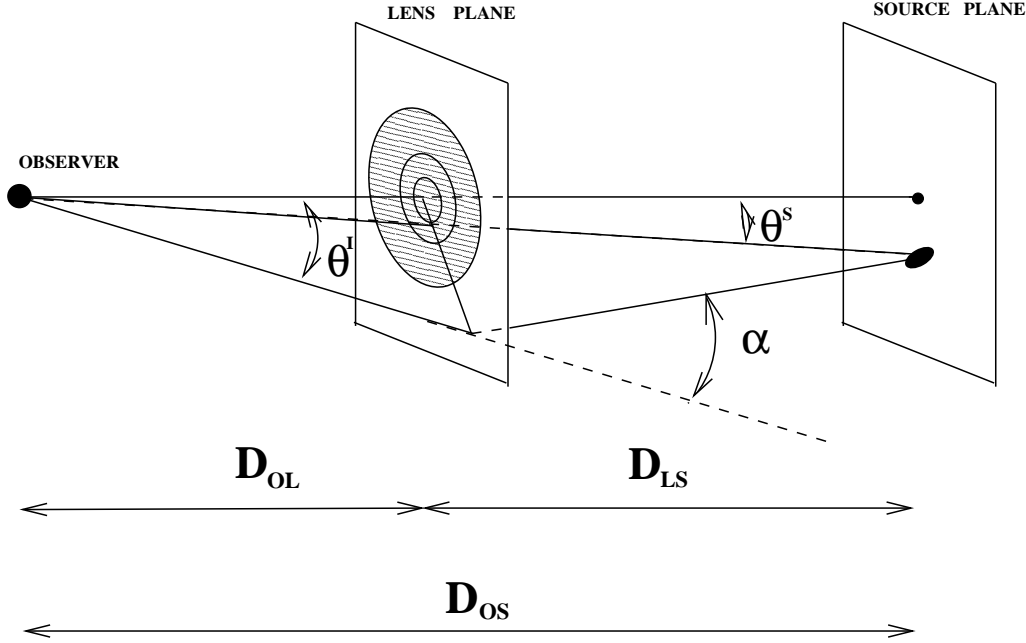


Figure 6.8: Schematic illustration of how light from a source, S , is deflected by an angle, α , as it passes by a mass concentration, L , acting as a gravitational lens. The distances between the observer, O , and the lens and source are angular-diameter distance, which depend on Ω_M , Ω_Λ , as well as any quintessence component.

Counts of multiply imaged sources (e.g. strongly-lensed quasars and galaxies) can be used to constrain Ω_M and Ω_Λ (Kochanek, 1996; Falco, Kochanek, & Munoz, 1998) in a manner complementary to the supernova limits. Such tests exploit the fact that the probability of lensing is a strong function of the volume over which potential background sources are distributed. One estimate of the surface density of such lenses comes from those discovered in blind optical searches with HST [most of which would not be recognized from the ground; Ratnatunga, Griffiths, & Ostrander (1999); Cooray, Quashnock, & Miller (1999)]. Such considerations suggest SNAP should easily find $\sim 10^3 - 10^4$ strong lenses over the 20° supernova monitoring region. Constraining Ω_M and Ω_Λ with strong lensing requires a knowledge of the lensing cross-section from foreground galaxies (or clusters), which goes roughly as $n (\sigma_{DM}/c)^4$, where n is the number of density of galaxies (which may evolve with redshift). SNAP will have reliable photometric redshifts for galaxies in the supernova monitoring region.

Since SNAP will be monitoring these strong lenses for a number of years, it may find some in which the source is strongly variable on short timescales. The time delay

between the light curve variation of the various lens components could then be used to place constraints on the Hubble constant. Since detailed lens modeling is required to interpret such observations, some follow-up spectroscopy with NGST would once again be an excellent complement to SNAP.

SNAP may also discover gravitational microlensing induced by compact masses in foreground galaxies [e.g., primordial black holes, stellar remnants, MACHOS, normal stars, gas clouds, etc.; Walker (1999); Dalcanton et al. (1994)]. If such a compact mass — in its orbit through its parent galaxy and as the galaxy moves through space — passes in front of a background quasar, it will produce a characteristic (nearly) achromatic enhancement. SNAP would be sensitive to such events on timescales from 2 days to 2 years (in the observer frame). Fig 6.9 shows the mass ranges and time scales that could be probed in this way.

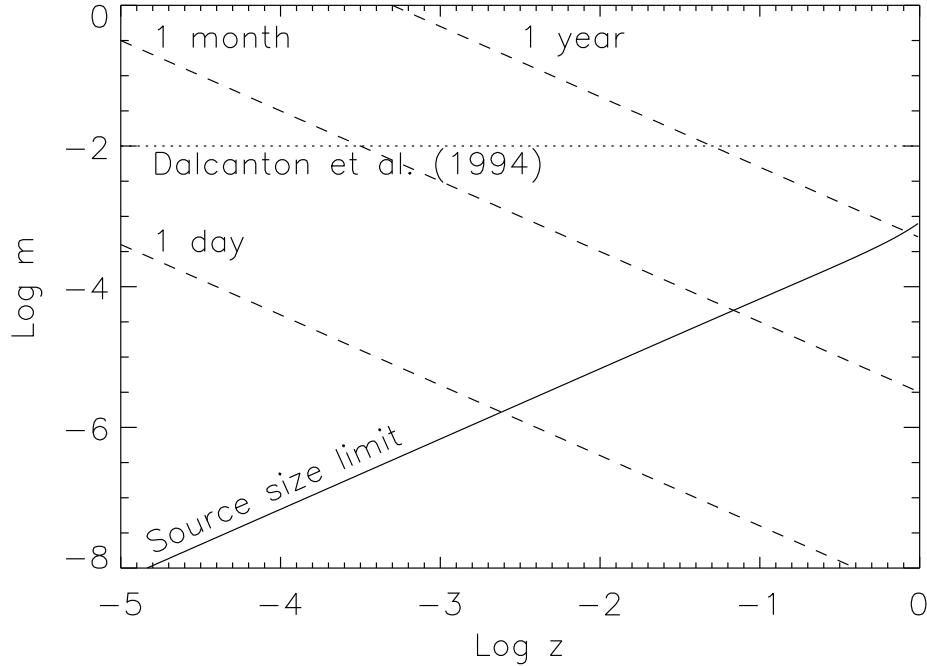


Figure 6.9: The microlensing detectability as a function of lens redshift, z , and lens mass, $m \equiv M/M_{\odot}$, from Walker (1999). In order for a microlens to introduce significant magnification, it must be more massive than indicated by the source-size limit. The adopted source size is taken as 10^{15} cm, located at $z \sim 2$, appropriate for a distant quasar. Approximate time-scales for microlensing events are shown by the dashed lines, assuming a transverse speed of 600 km/s. The limits already set by the Dalcanton et al. (1994) search for a change with redshift in quasar emission line equivalent widths which would be expected for lensing which resolved the quasar broad-line region are shown. SNAP would be most sensitive to planetary mass lenses in galaxies with redshift $0.1 < z < 1$ which varied on timescales less than 2 years.

Sets of multiply-imaged sources found in the same well-studied clusters allow a further way of constraining Ω_M and Ω_Λ (Link & Pierce, 1998). If spectroscopic redshifts are available for each multiple image set, their observed configuration is determined by the angular diameter distance-redshift relation, which is of course dependent on the cosmological parameters. It is unlikely that SNAP would happen to have a rich cluster with fortuitously-placed background galaxies in its survey field, so pursuit of this cosmological test would probably require special observations.

6.3.4 Detailed Considerations - Weak Lensing

The effect of line of sight density fluctuations on the properties of distant sources was discussed by Kristian & Sachs (1966); Gunn (1967); Valdes, Jarvis, & Tyson (1983); Miralda-Escude (1991); Blandford et al. (1991); Kaiser (1992); Metcalf & Silk (1998); Holz & Wald (1998); Bergström et al. (1999) and others. When lensing perturbations are $\ll 1$ (in dimensionless units), they are conventionally categorized in the weak regime. As discussed above, the net distortion and magnification contains information concerning the line of sight distribution of intervening mass. Via an optimal strategy, weak lensing therefore offers the prospect of new constraints on the amount of dark matter (Ω_M) and its spatial distribution (Tyson, Wenk, & Valdes, 1990; Luppino & Kaiser, 1997; Tyson, Kochanski, & Dell'Antonio, 1998). Statistically, the latter can be quantified via the normalization and slope of a power spectrum of mass fluctuations $P(l)$ (where $l=2\pi/L$ is the wavenumber corresponding to a physical scale L).

Determining the present-day mass power spectrum is a major goal in large scale structure as can be witnessed by the current preoccupation with ambitious galaxy redshift surveys. This is because it is intimately connected to the primordial fluctuation spectrum, as well as to the relative contributions of cold dissipationless particles (CDM), hot dissipationless particles (massive neutrinos), and baryons (which do dissipate).

The perturbation of light traveling to us from a distant source is given by the Jacobian mapping of input angles to output angles:

$$\frac{d\theta^I}{d\theta^S} = A(\theta^I).$$

where the amplification matrix, A , is given by:

$$A(\theta^I) = 1 - \partial_{11}\varphi\partial_{12}\varphi\partial_{12}\varphi - \partial_{22}\varphi \quad (6.1)$$

Here φ is the projected mass surface density. The overall image magnification is given by $1/\det(A)$.

The amplification matrix can be broken into an isotropic component due to focusing within the beam, termed the convergence κ , and an anisotropic component arising from the potential gradient termed the shear, $\gamma \equiv (\gamma_1, \gamma_2)$.

$$A(\theta^I) = 1 - \kappa - \gamma_1 - \gamma_2 - \gamma_2 1 - \kappa + \gamma_1. \quad (6.2)$$

The complex shear can be determined by measuring the distortions in the ellipticity of lensed background galaxies. If the complex ellipticity is defined as $\epsilon = \frac{1-r}{1+r}e^{2i\phi}$ where

ϕ is the position angle, $r = \frac{b}{a}$, and b and a are the major and minor axes of the ellipse, then the observed ellipticity ϵ_o is related to the intrinsic ellipticity ϵ_i in the weak lensing regime by

$$\epsilon_o = \frac{\epsilon_i + \mathbf{g}}{1 - \mathbf{g}^* \epsilon_i},$$

where $\mathbf{g} = \gamma/(1 - \kappa)$ is the reduced complex shear.

Using a large number of distant galaxies assumed to have random true orientations, $\langle \epsilon_i \rangle = 0$, a map of the convergence and shear fields due to lensing by foreground mass fluctuations can be obtained. If galaxies were intrinsically circular, the shear measurement would be trivial. Rather, since faint galaxies are observed to have an ellipticity dispersion of $\simeq 0.4$, the shear must be determined by spatially averaging over the ellipticities of many galaxies. The convergence map can then be reconstructed from the shear using

$$\langle \epsilon_o \rangle = \frac{|\gamma|}{1 - \kappa} \sim |\gamma| \text{ for } \kappa \ll 1,$$

or using a combination of shear information and galaxy surface density fluctuations (since the convergence component isotropically magnifies and demagnifies background galaxies).

As the lensing signal is effectively integrated along the line of sight, useful measurements are more practical to make if it is possible to statistically differentiate between foreground (lensing) and background (source) galaxies (Hui, 1999; Hu & Tegmark, 1999). Since the lensing signal changes only slowly with relative distance, galaxy redshifts accurate to $\sigma_z \sim 0.1$ are more than adequate. The main SNAP SN monitoring fields will have deep photometry in several optical filters spanning the wavelength range 0.35–1.0 μm ensuring photometric redshifts accurate to $\sigma_z < 0.1$ for most detected galaxies.

As discussed above, further limitations arise from the anisotropic component of the point spread function (PSF) and, for ground-based instruments, seeing circularization. Elaborate techniques have been developed to correct measured ellipticities for both effects (Kaiser, Squires, & Broadhurst, 1995; Kaiser, 1998; Rhodes, Refregier, & Groth, 1999). Since the expected distortions are at the 1-2% level (for popular models), clearly these corrections become less troublesome for resolved galaxies. An important motivation for a space-based lensing facility is not only the absence of seeing circularization but also, the greater surface density of galaxies which remain well-resolved (Fig 6.10).

We now discuss specific constraints that we expect to provide using the superlative performance of SNAP. Figure 6.12 gives an example of the constraints on Ω_M and Ω_Λ from a weak lensing survey of 100° (but with a galaxy surface density $10\times$ lower than appropriate for SNAP). Figure 6.11, from Hu & Tegmark (1999), shows a theoretical prediction for the convergence power spectrum, $P_\kappa(l)$, and its uncertainty from a $3^\circ \times 3^\circ$ survey to $m_{AB}(R) \sim 25$. Also shown is $P_\kappa(l)$ from a cosmology which would be degenerate within 0.1σ using the expected MAP CMB data.

The weak lensing power spectrum is able to significantly improve cosmological parameter estimates in combination with CMB or SN data by breaking degeneracies

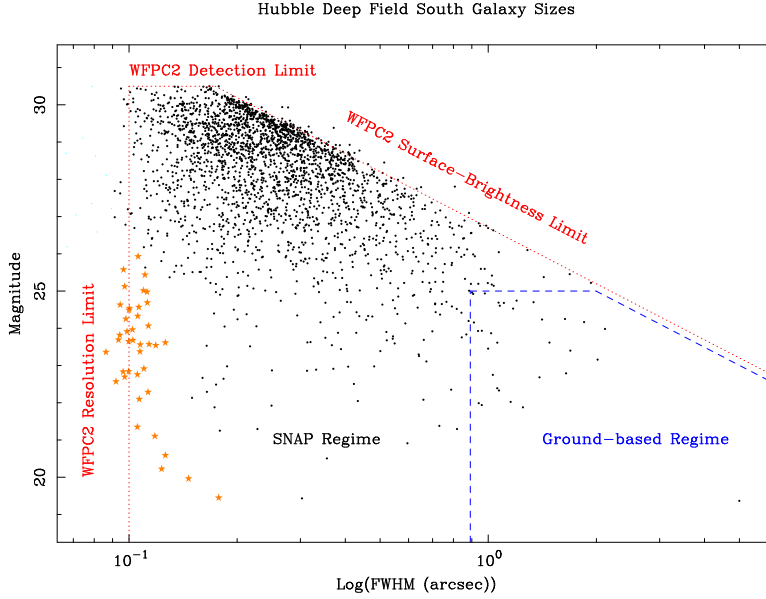


Figure 6.10: The sizes of galaxies detected by the HST Wide-Field/Planetary Camera (WFPC2) in the southern Hubble Deep Field (HDF-S) are shown, as a function of $V+I$ magnitude. The limits on faintness, resolution, and surface brightness for this sample are shown with dashed red lines, and are labeled accordingly. Brighter sources at the resolution limit are probably stars (possibly quasars as well; orange star symbols). Detections which are faint and below the resolution limit are likely spurious (cyan dots). The remaining detections are predominantly galaxies (black dots). The SNAP SN monitoring fields would deliver data of quality comparable to the HDF-S — with perhaps very slightly lower resolution but probably deeper surface-brightness limits — over a region of sky roughly $10^4\times$ larger. Galaxies which could be resolved with wide-field ground-based surveys are in the region bounded by dashed blue lines. Note that the resolution limits (vertical lines) indicate the point at which the FWHM of the point spread function (PSF) equals the FWHM of the galaxy, therefore, careful removal of PSF anisotropies is required or else the analysis must be confined to even larger galaxies. Given that the expected distortions are at the 1% level, it is very desirable to work only with well-resolved galaxies.

in those measurements. The uncertainties shown in Fig 6.11 can be improved by $2\times$ using galaxy redshift information (Hu, 1999). The larger sky coverage of the SNAP SN-monitoring fields would reduce the uncertainties by another $\sqrt{2}$, and the higher surface density of SNAP galaxies would reduce the uncertainties for $l > 100$ by another $\sim 5\times$. Finally, the higher mean redshift of the SNAP sample would increase the lensing signal, further improving the signal-to-noise. Better measurements for $l < 100$ would require observations in addition to the SNAP SN-monitoring fields.

Cosmic-variance overwhelmingly dominates the statistical noise at these angular frequencies, meaning that only a significant increase in sky coverage can reduce the uncertainties. Conversely, since shot noise is not an issue, such additional observations

need not go as deep. A promising prospect is a medium depth SNAP survey covering $100\text{--}1000^\circ$ [possibly with sparse sampling, as suggested by Kaiser (1998)] which would allow determination of the the slope of $P_\kappa(l)$ in the linear regime ($l < 100$).

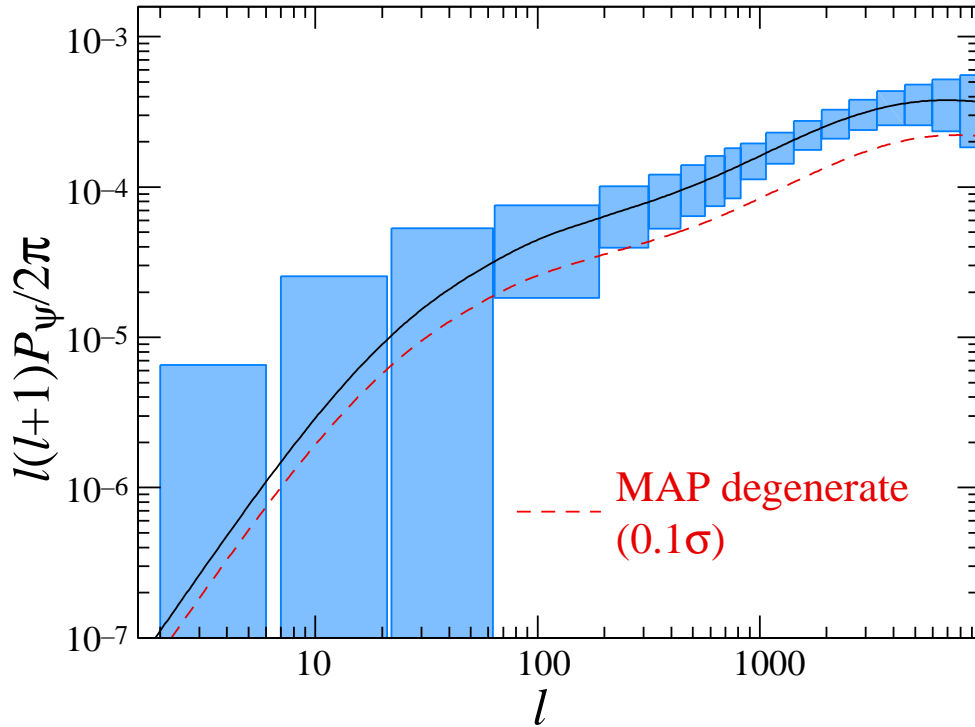


Figure 6.11: Example of the convergence power spectrum, $P_\kappa(l)$, and associated uncertainties, for a $3^\circ \times 3^\circ$ weak lensing survey (Hu & Tegmark, 1999). The surface density of galaxies assumed is roughly the geometric mean of what can be observed from the ground and what can be observed from space once spatial resolution requirements are imposed. Moreover, this example does not include the benefits of sorting lensed galaxies in different redshift bins, as advocated by Hu (1999). The larger areal coverage of the SNAP supernova monitoring fields, in combination with these other improvements should allow SNAP to reduce the uncertainties on $P_\kappa(l)$ by an order of magnitude compared to what is shown here for $l > 100$. Wider-field SNAP images taken for search and follow-up of the lowest redshift supernova, or dedicated weak lensing images, can substantially improve $P_\kappa(l)$ for lower multipoles.

Such a wider-field survey could be optimally arranged to overlap with other probes of large scale structure including the new generation of ambitious redshift surveys (Gunn, 1995; Colless, 1998). By correlating weak shear maps with foreground distributions of selected galaxy populations, mass/light ratios can be probed as a function

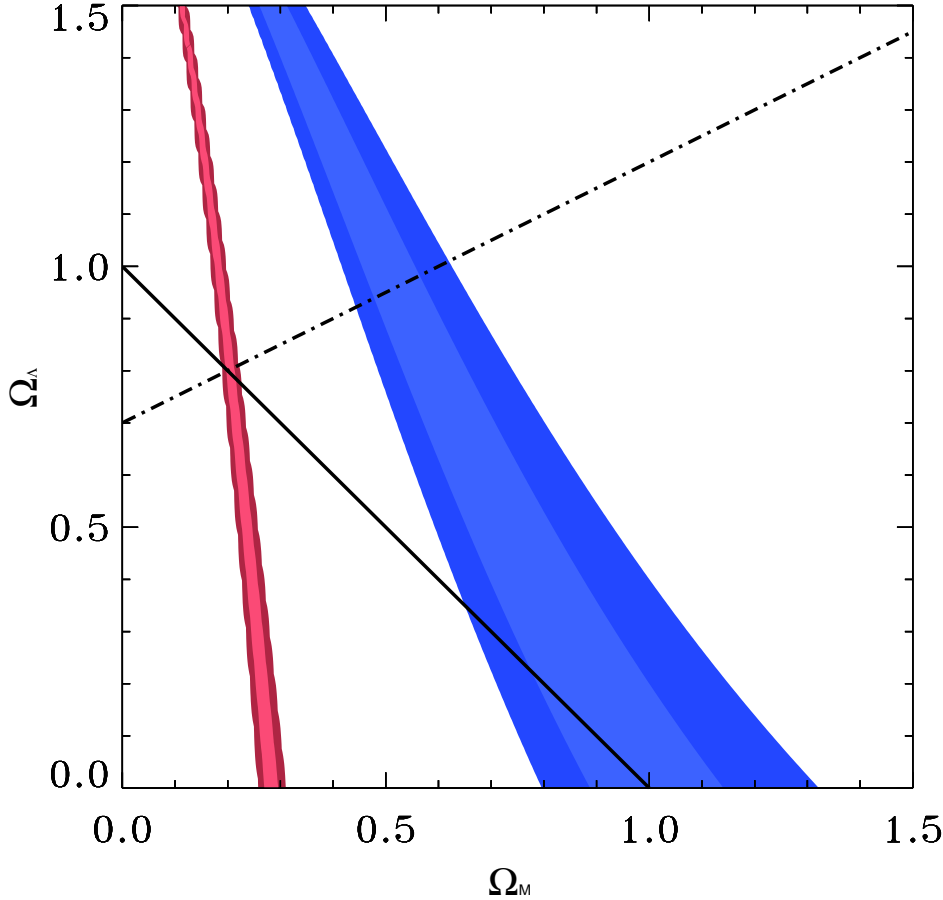


Figure 6.12: Example of the confidence regions in the Ω_M , Ω_Λ possible with a weak lensing survey of 100° , adapted from Van Waerbeke, Bernardeau, & Mellier (1999). Confidence regions are shown for $\Omega_M = 0.3$ (left bands) or $\Omega_M = 1$ (right bands) and $\Omega_\Lambda = 0$.

of environment. Such data is essential to testing concepts of biased galaxy formation (Benítez & Sanz, 1999) which have hitherto remained elusive.

Beyond direct measurement of the power spectrum, there are several additional methods for constraining cosmological parameters from weak lensing. Certain proposed estimators are sensitive to the combination $\sigma_8\Omega_M$, where σ_8 represents the normalized RMS density fluctuation on an 8 Mpc scale. These include measuring the skewness, S_3 , of the convergence field (Jain & Seljak, 1997; Schneider et al., 1998; Van Waerbeke, Bernardeau, & Mellier, 1999; Bartelmann & Schneider, 1999) measured on angular scales of several arcminutes. The amplitude distribution of peaks in maps of

the convergence (Jain et al., 1999; Van Waerbeke, Bernardeau, & Mellier, 1999) may provide an additional (and possibly more robust) method to constrain $\sigma_8\Omega_M$. Here the strongest signal comes from high angular frequencies, where SNAP can provide an enormous advantage over ground-based surveys by increasing the density of objects with well-measured shapes by a factor of more than 20 (see Fig. 6.6). Finally, the increased galaxy density can be used to make *differential* lensing measurements, impossible from the ground, to help constrain the evolution of the power spectrum. Applying a ratio of the convergence amplitude between two redshift intervals (estimated photometrically) removes the dependence on the cosmological geometry, and can provide an independent constraint on the power spectrum for $z > 1$. Measuring the non-linear power spectrum evolution far beyond the recombination epoch provides unique clues to the clustering behavior of the dark matter and its relation to the baryons, which may be key to determining what the dark matter is made of.

In summary, the unparalleled combination of wide area and high resolution of the SNAP surveys will have an impact far beyond the principal supernova cosmology. It will provide solutions to many of the fundamental problems that can be attacked through measurements of gravitational lensing. We will be able to detect signatures of structure from the primordial fluctuation spectrum of inflation to the present distribution of dark matter, its relation to the baryons, and its evolution with time. While deeper measurements and some science will be addressed with the larger aperture and resolution of NGST, many aspects of science through gravitational lensing require a very wide field, which will be a unique arena for SNAP.

6.4 Gamma Ray Bursts

Gamma ray bursters (GRBs) are among the most luminous phenomena in the universe. These intense bursts of γ -rays have recently been identified as residing in galaxies at redshifts ranging from $z \sim 0.01$ (980425) to larger than $z \sim 3.4$ (971214). The combination of great distance and large fluence leads to the conclusion that they are associated with isotropic energy releases of $10^{51} - 10^{54}$ ergs that these are some of the most energetic events since the Big Bang itself.

GRBs were discovered in the late 1960s, with detections limited to γ -ray energies only; until very recently it has been impossible to observe these mysterious phenomenon at longer wavelengths due to the low precision of celestial coordinates supplied by γ -ray observatories. Today, BATSE observes a burst rate of approximately 1/day, equally likely to originate from any direction in the sky. Optical observations were first made in 1997 in association with GRB 970228. GRB 970228 was detected on February 28, 1997, by the X-ray satellite BeppoSAX (Costa et al., 1997b). Eight hours after the event, Costa et al. (1997a) observed a transient X-ray source located at the edge of the GRB 970228 error box. Using the Ulysses satellite, Matz et al. (1997) reduced the error box of GRB 970228 and found that the X-ray error box overlapped partially that of the GRB. Within the intersection of the former error boxes Groot et al. (1997) discovered an optical transient related to GRB 970228 (van Paradijs et al., 1997).

Since the discovery of the optical transient (OT) of GRB 970228 incredible progress

has been made. It is now known that GRBs lie at cosmological distances, and that visible counterparts for GRBs can be incredibly bright. For example on Jan. 23, 1999 a very bright burst (GRB990123) was observed by the instruments aboard the Compton Observatory and Beppo-SAX, showing gamma-ray activity with a duration of more than 100 s. The precision of the X-ray position from SAX enabled the discovery of a rapidly fading optical transient. The holy grail of optical transient searches was found: a simultaneous OT/GRB (Akerlof et al., 1999).

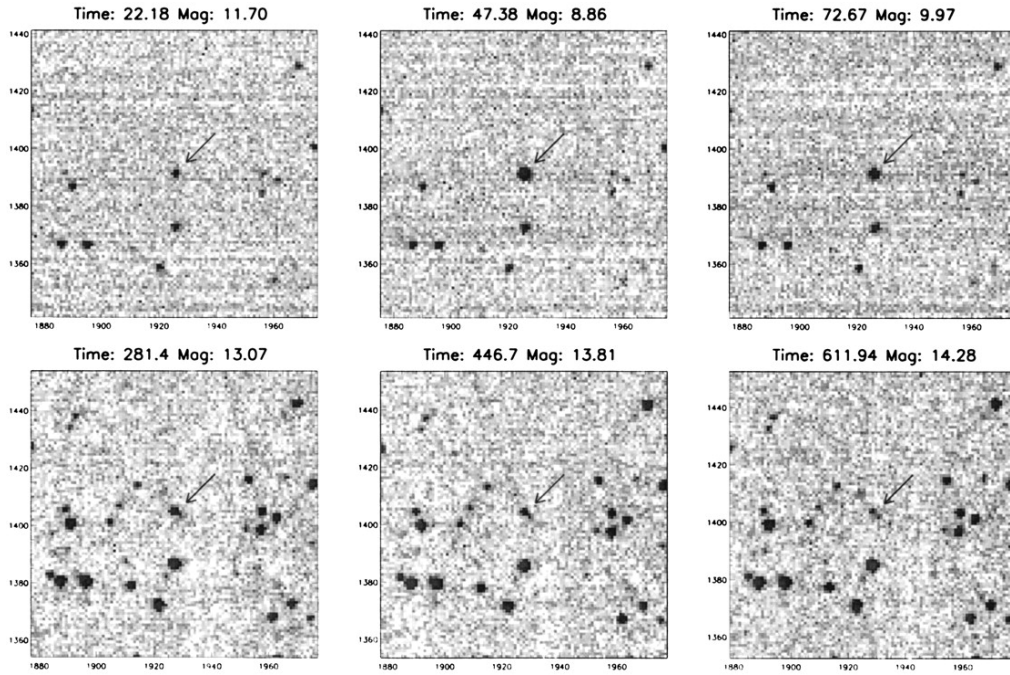


Figure 6.13: The LANL ROTSE-I wide-field-of-view cameras caught an incredibly bright ($R \sim 9$) optical transient simultaneously with GRB990123 (Akerlof et al., 1999). First exposure began 22 sec after the burst trigger. The light curve is complex, showing an increase by 3 magnitudes between the first and second image (5-sec exposures each), reaching a peak brightness of $R \sim 9$!

GRBs are likely an end product of massive star formation, e.g., the collapse of a single super massive star (Woosley, 1993) or merging neutron stars (Paczynski, 1986), and could signpost the first of star formation at high redshift. Since GRBs are now known at cosmological distances and have bright optical transients they may be the best probes of the ionization state of intergalactic gas in the early universe. Gamma ray burst afterglows display near-perfect featureless spectra, and by looking for the tell-tale absorption lines of red-shifted neutral hydrogen it should be possible to study the ionization state of the intergalactic medium. This observation could provide our first glimpse of the end of the “dark ages”, i.e., when the “first light” of the earliest stars and quasars reionizes hydrogen that recombined in the dying embers of the big bang at $z \simeq 1100$. Reionization is a key event in the history of the universe, and knowledge of when this singular event occurs is a principal constraint on theories of

the emergence and subsequent evolution of gravitational clustering in the universe.

6.4.1 Observational strategy

This visible light curve for GRB990123, which briefly reached 9th magnitude, shows an extremely intense but very brief burst of visible light (Akerlof et al., 1999). The sharp rise (a factor of $\times 10$ in 20 s) and short duration (several rise times) of the optical transient makes it an extremely difficult task for current detectors to observe if unaccompanied by a high-energy trigger. The typical astronomical mode of long exposures will miss such transients completely. The sharp rise (2.5 magnitudes in 20 seconds) is not seen in any other known astronomical object.

There is good reason to believe that GRBs suffer a large beaming effect which concentrates the γ -rays emission by factors of > 100 (Meszaros & Rees, 1999; Fruchter et al., 1999). If GRBs are beamed, then the number that are not observed in γ -rays is inversely proportional to the beaming fraction. Since the optical emission is likely to be isotropic, there will be many more optical transients associated with GRBs but with no gamma-ray trigger.

To estimate the number of untriggered optical transients (“orphans”), consider that BATSE sees about 300 GRBs per year over the whole sky (2π sr). If the beaming fraction is 0.001, then the number of orphans could be $\sim 5 \times 10^4 \text{ sr}^{-1} \text{ yr}^{-1}$. A telescope with a field of view of 1 degree should expect to detect ~ 14 orphans of the type that BATSE could have detected in a year of observing. If, as probable, there are many more bursts below the BATSE detection threshold this number could be many times higher. Either way SNAP will yield important information of the beaming fraction.

In devising a strategy for detecting orphan optical transients, we consider the only early-time OT yet observed. A possible search strategy for SNAP is to take at least two exposures as short as possible consistent with the readout time of the GigaPixel focal plane array, and quickly decide, based on what is seen in those two exposures (and a comparison with an archived baseline), on a subsequent observing strategy. If there is nothing new, continue with the program of short exposures, but if there is a candidate OT, a follow-up program begins, which may consist of progressively longer exposures for multi-band photometry, polarimetry, and spectroscopy. The spectroscopy requires an accurate enough position to fit the OT into the aperture of the spectrograph, which can be accomplished with the IFU.

That algorithm for detecting a candidate OT in the data stream has data mining aspects to it, but the demand of real-time response is unique to this application.

Making the connection of a candidate OT with GRBs is fairly straightforward. The rapid steep rise is seen in no other known object, though anything that acts so violently is going to be interesting in itself even if it is not a GRB. The t^{-1} power-law decay of the later emission is also fairly characteristic. Later longer exposures should show the faint host galaxy, the multi-color photometry should show the emission peak moving through the optical window as the shock decelerates, and the spectroscopy should show high-redshift absorption systems, from gas in the host galaxy and from intervening intergalactic matter. At some stage one might expect to see emission lines from the shocked gas around the blastwave as well.

We would then follow up those optical transients that are found to be visibly faint or apparently reddened. These may be high- z GRBs veiled by the absorption of intergalactic HI, extinguished by interstellar dust in the nuclei of protogalaxies, or hypernovae observed by their scattered light. GRB afterglows may be the only objects at high- z ($z \simeq 10 - 15$) with sufficient brightness to search for the Gunn-Peterson signature of the epoch of reionization. The IR channel of the SNAP spectrometer is a unique facility for this experiment. Since current estimates suggest that re-ionization occurs at $z \simeq 10$, the H Ly α line is redshifted to $\simeq 1.3 \mu\text{m}$. Figure 6.14 shows the infrared absorption spectrum of a GRB optical transient. In one case (top) the intergalactic medium is mostly ionized and only traces of neutral atomic hydrogen remain in clouds. In the second example (bottom) the intergalactic medium is predominantly neutral. The epoch of reionization, in this case at $z_i = 6$ is clearly identifiable.

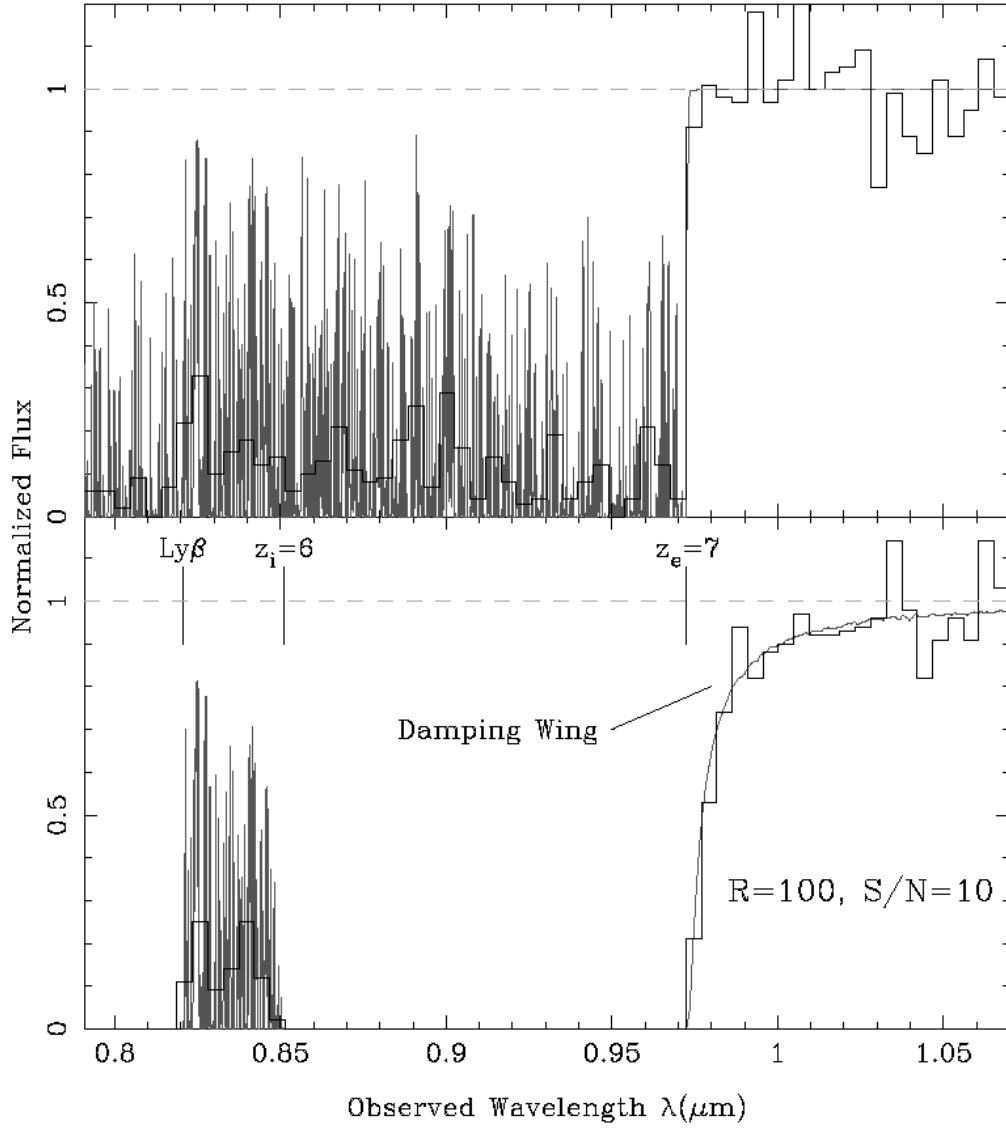


Figure 6.14: A simulated Lyman forest absorption spectrum out to a redshift of $z = 7$ (top). The lower frame shows the same absorption spectrum in the case where ionization of the intergalactic medium changes abruptly by a factor 10^4 at a redshift of $z_i = 6$. The thin curves show the true underlying spectra; the overlaid binned curves what would be observed at $R = 100$ and $\text{SNR} = 10$. Note the characteristic red damping wing $\text{Ly}\alpha$ of in the latter case.

Part III

Baseline Instrument Description

Chapter 7

Observational Strategy & Data Package

7.1 Observational Requirements

The SNAP baseline science objective is to use SNe Ia to perform a precision measurement of the cosmological parameters; a 2% measurement of the mass density of the universe, a 5% measurement of the vacuum energy density, a 6% measurement of the curvature, and a 5% measurement of the equation of state of the “dark energy” driving the acceleration of the universe. Achieving this ambitious goal requires large numbers of supernovae with excellent photometric and spectroscopic data to handle statistical and systematic errors. These conditions drive our observation strategy and thus our data package.

The satellite is expected to be able to discover and follow over 2,000 supernovae with redshifts ranging from 0.1 to 1.7. This is to be two orders of magnitude greater than the current published set of ~ 42 supernovae, and is to extend much farther in distance and time. The large numbers of supernovae will be found by cycling deep photometric observations of 20 fixed 1° fields in the north and south ecliptic poles. The fields will be selected to minimize zodiacal light background and extinction by Galactic dust. This “batch processing” method is a key to obtaining the required bias-free dataset.

The photometric and spectroscopic follow-up observations of the discovered supernovae need to satisfy both statistical and systematic requirements. It has been found experimentally that the supernova peak brightness can be standardized to 0.1 mag with supernova restframe B-band light curves and $B - V$ color (see Figure 7.1). To obtain corrected peak magnitudes with final statistical uncertainties of 0.1 mag for each SNAP supernova will require taking accurate photometric observations ($\Delta_m \sim 0.02$) over the light-curve for the next four to eight months while the luminosity waxes and wanes.

To minimize color and spectral correction error, we need to observe in passbands appropriate for the targeted redshifts of the supernova. The importance of this band-pass selection can be seen in Figure 7.2, where the B-band is superimposed over an

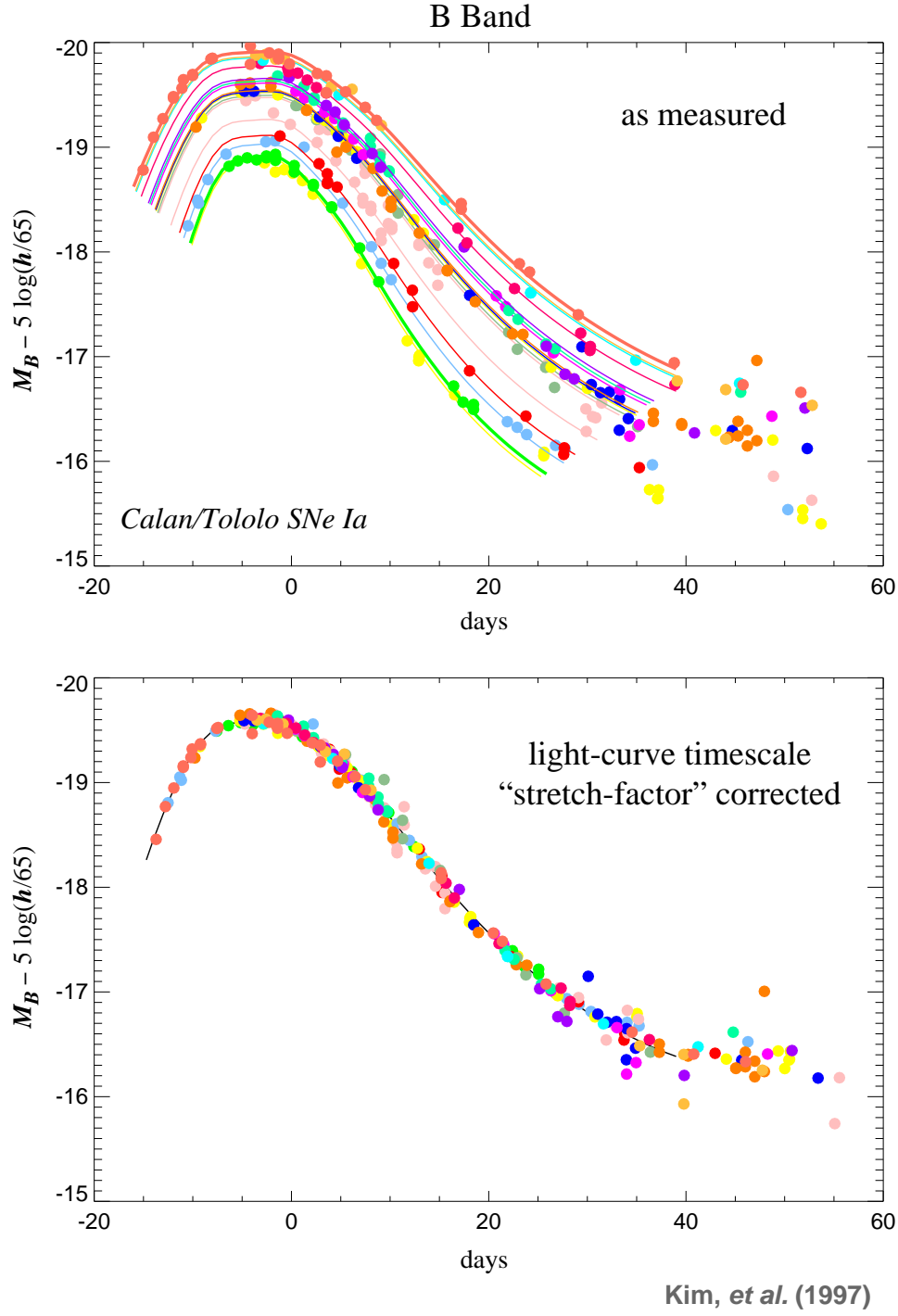


Figure 7.1: B-band light-curve for SNe Ia corrected for redshift and light curve timescale.

example SN Ia spectrum. The passbands can be defined either by having an extensive set of “redshifted B-band” filters, one for each small range of redshift, or by defining the passbands synthetically using spectrophotometry. Both are suitable and viable options. Given that a large field-of-view optical photometer is in the baseline for the mission, it is possible to “batch process” large numbers of supernovae in a given observation so that the objectives can be met with a large number of filters. An example of a possible set of bandpasses with an average 25% non-overlap are given in Table 7.1 below.

<i>Effective redshift</i>	<i>B-band Center λ (μm)</i>	<i>B-band Bandpass $\delta\lambda$ (μm)</i>
0	0.44	0.11
0.1	0.48	0.12
0.2	0.53	0.13
0.3	0.57	0.14
0.4	0.61	0.15
0.5	0.66	0.16
0.6	0.70	0.17
0.7	0.75	0.18
0.8	0.79	0.19
0.9	0.83	0.20
1.0	0.88	0.21
1.1	0.92	0.23
1.2	0.97	0.24
1.3	1.01	0.25
1.4	1.05	0.26
1.5	1.10	0.27
1.6	1.14	0.28
1.7	1.19	0.29

Table 7.1: Redshifted B-band filters.

We would like to constrain systematic errors to < 0.02 mag. Potential supernova evolution can be tracked both with photometry and rest-frame near-UV and optical spectroscopy. Effects correlated with host galaxy morphology and the position of the supernova in the host galaxy will also be studied. These properties may indicate differences in stellar population from which the supernova came and therefore can be used to test whether the intrinsic brightness of the supernova changes systematically with redshift. Potential “grey dust” sources will be identified at the restframe $\sim 1.2\mu m$ where a sharp dropoff in opacity is expected.

Advance knowledge of host galaxy properties is desirable. Specifically, we need photometric redshifts and morphology determinations of field galaxies to help us formulate observing priorities.

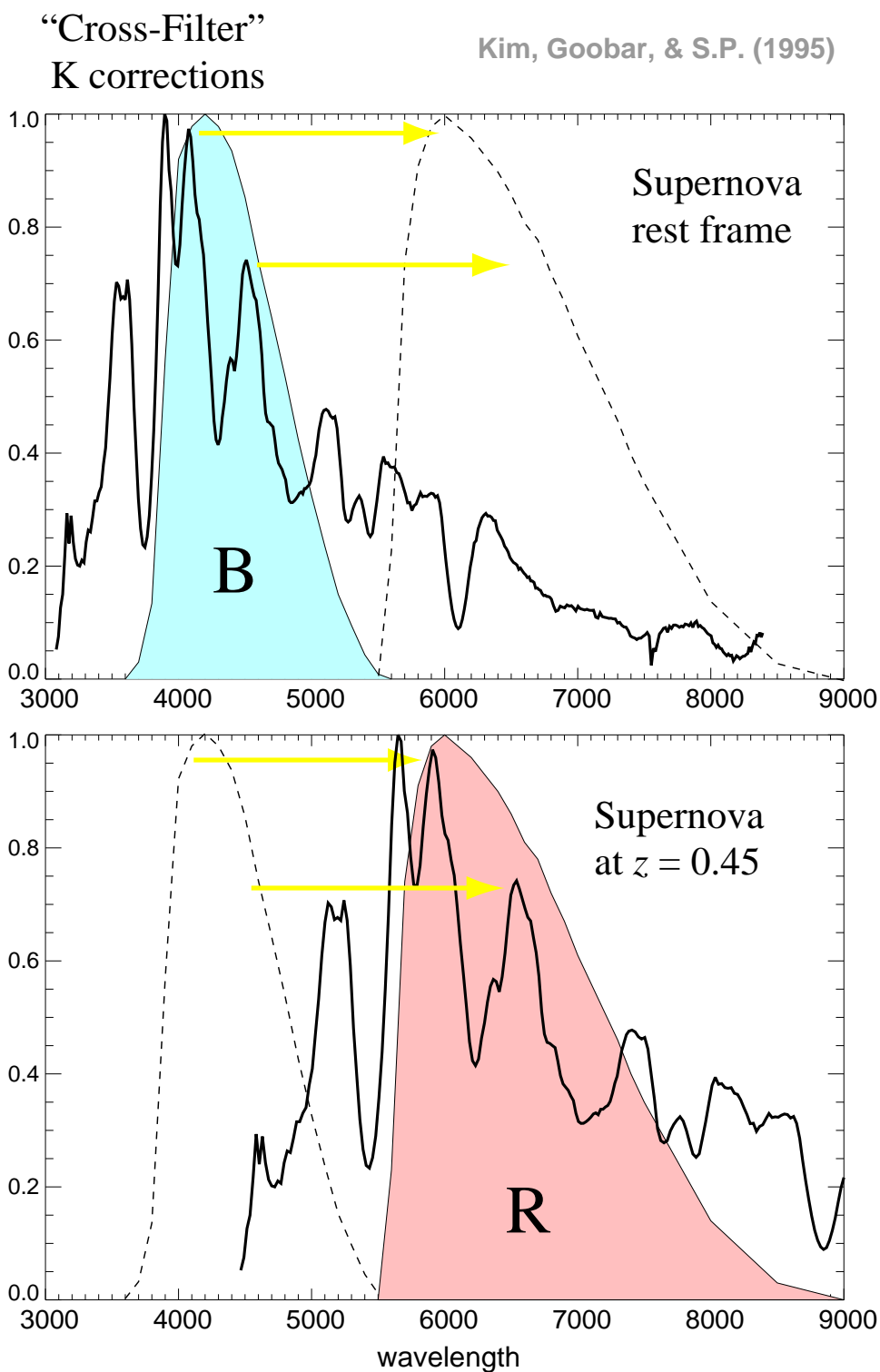


Figure 7.2: Example SN Ia spectrum with B-band bandpass superimposed.

7.2 Observational Strategy & Data Package

The satellite is expected to carry four key instruments, a $1^\circ \times 1^\circ$ wide-field optical imager/photometer, an optical spectrograph, a small IR imager/photometer, and an IR spectrograph. The capabilities of these instruments must be a good match to the science requirements for the satellite. In particular, the instrumentation must provide all the elements of the supernova studies, namely: 1) early detection of supernovae, 2) B-band restframe photometry to follow the photometric light curve of the supernova as it waxes and wanes, 3) supernova color at peak and near peak brightness, 4) spectra at near peak brightness to classify the supernova, 5) photometric redshifts of the host galaxies in advance of supernova follow-up, and 6) medium resolution spectra/photometry for a limited subset of supernovae sampled over the light-curve.

7.2.1 Photometry

Wide-field optical imager/photometer The data from the wide-field optical imager/photometer will serve both as search images and for follow-up photometry. Each field will have cycled observations through a series of filters, providing SN photometry every four restframe days that satisfies light-curve shape and systematic tracer requirements, as shown in Figure 7.3

Photometry for the supernova is obtained in the rest-frame B-band of the supernova using a filter set that approximates a redshifted B-band filter. Restframe photometry in the B-band is redshifted into the observer frame by $(1+z)$. Photometry can be obtained by multiple fixed filters, an integral field spectrograph which preserves photometry, or other low resolution spectrograph provided there are no photometric losses. An optimal redshifted B-band filter or synthesized filters applied to spectrophotometry would eliminate a principal source of systematic error from the K-corrections. The photometry will require both optical and NIR coverage. Both optical and IR Photometry are expected to be performed with a systematic accuracy of better than 1% over the redshift $0.3 < z < 1.7$.

At any given moment, a single field will have many supernovae at different redshifts in different stages of evolution. The photometric follow-up requirements for the faintest supernovae in each field are much more stringent than those necessary for detection; only a fraction of all images will be used for searching using optimized filter combinations. Our cycling strategy will at the least provide: Twenty $1^\circ \times 1^\circ$ fields would be repeatedly studied with a repetition rate of every four days for low-redshift supernovae $z \leq 0.3$ with magnitude $m_{AB}(1.0\mu) \leq 27$, every six days for supernovae $0.4 < z < 0.8$ with magnitude $m_{AB}(1.0\mu) \leq 28$, and every eight days for supernovae $0.8 < z < 1.2$ with magnitude $m_{AB}(1.0\mu) \leq 29$. Two $1^\circ \times 1^\circ$ fields would be repeatedly studied with a repetition rate of every eight days for high-redshift supernovae $1.2 < z < 1.7$ with magnitude $m_{AB}(1.0\mu) \leq 30$. Only a sub-sample of the supernovae with $z > 1.2$ would be selected for further study. Early detection of SNe Ia at $S/N > 7$ is required to identify the supernova within two days of explosion in the supernova restframe in order to probe potential systematics of the progenitor make-up.

Photometric redshifts are measured for host galaxies (only once per field) based on

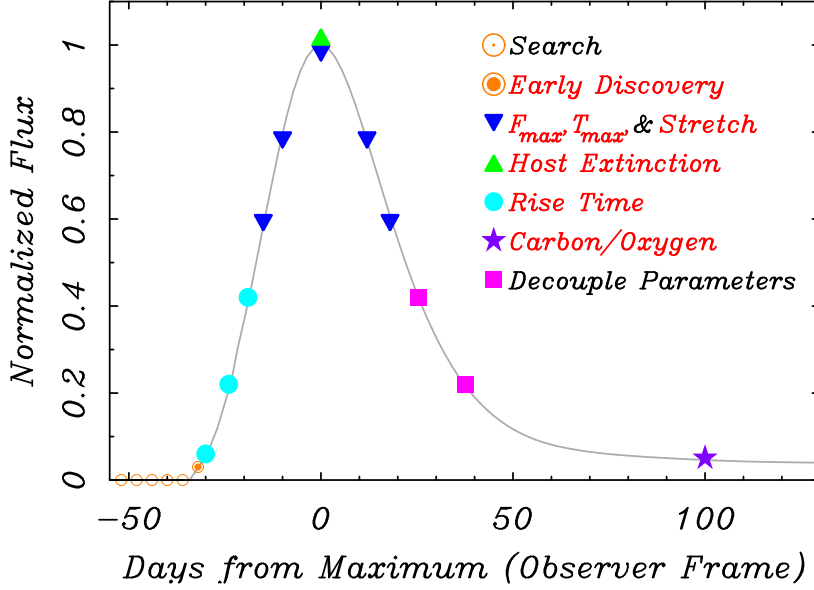
B-band Lightcurve Photometry for $z = 0.8$ Type Ia

Figure 7.3: B-band light-curve sampling for SNAP SNe Ia and the supernova physics they address.

images in multiple filters to $S/N > 30$.

Small IR imager/photometer The IR imager/photometer is necessary to obtain restframe V-band photometry that will help correct for supernova extinction from interstellar or intergalactic dust using color. At minimum, restframe V-band photometry is obtained at peak brightness to $S/N > 30$ band for all supernovae in the sample. Additional filter bands and near peak measurements (1 magnitude below peak) would be desirable.

For supernovae with redshifts beyond $z = 1.2$ a greatly limited sample of the discovered supernovae are followed as these can only be measured very slowly in the infrared.

7.2.2 Spectroscopy

Optical and IR spectrographs The two spectrographs combine to deliver the $0.35 - 1.7 \mu\text{m}$ coverage needed to exploit the interesting rest-frame wavelength range for the SNAP target redshifts. Figure 7.4 points out the relations between evolutionary tracers and spectral features that we need to observe with SNAP.

In order to classify the supernova as Type Ia a spectrum is obtained at peak magnitude. In the optical channel, for supernovae with redshift $0.02 < z < 0.4$ the resolution required is 15 \AA ($S/N > 10$), and 30 \AA ($S/N > 10$) for $0.4 < z < 1.2$, to study wavelengths between $3500\text{--}4800 \text{ \AA}$ in the restframe of the supernova. For supernovae with redshift $1.2 < z < 1.5$ the resolution required is 30 \AA ($S/N > 10$), to study wavelengths between

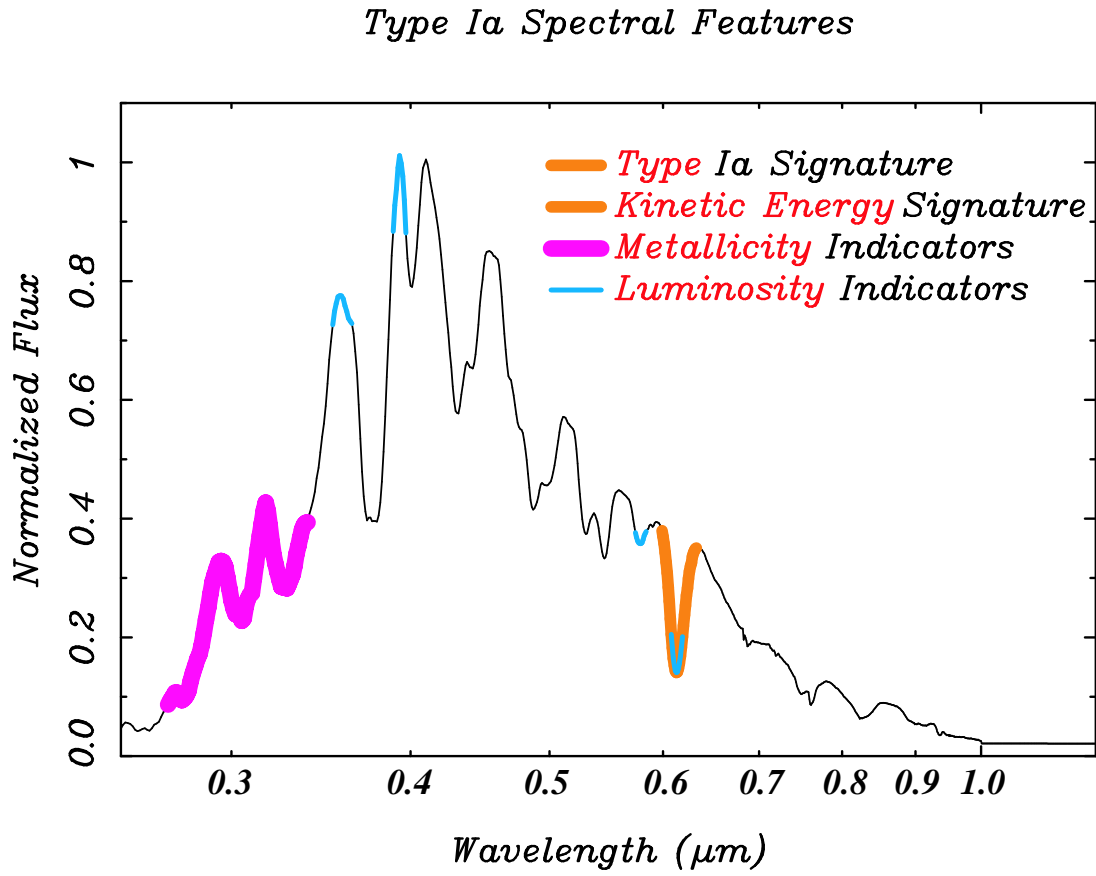


Figure 7.4: SN Ia spectroscopic regions relevant for identification and systematic studies.

3800-4200 Å (Ca II) in the restframe of the supernova. A single medium resolution optical spectrograph extending from 3500 Å to 10000 Å would appear to be sufficient to satisfy these requirements. For the highest redshift supernovae $z > 1.5$, a NIR channel would permit identification using the Ca II spectral features. In the IR channel, for supernovae with redshift $1.5 < z < 1.7$ the resolution required is 50 Å (S/N>10) to study wavelengths between 3800-4200 Å (Ca II) in the restframe of the supernova. For supernovae with redshift $0.02 < z < 1.2$ optical and IR spectra are obtained to 50 Å (S/N>10) at the Si II (6150 Å trough) to classify the supernova and study metallicity effects.

On a subset we obtain a spectrum or photometry at peak brightness in the laboratory frame wavelength range 4000 Å to 17000 Å to check for reddening of the supernovae for $z < 0.5$ from non-standard interstellar dust sources, emphasizing greater than 10000 Å. Only low-resolution of 1500 Å(S/N>30) is required for this systematic study.

7.3 Instrument Performance

In one year of study, as shown in Table 7.2, the satellite can discover, follow the light curve, and obtain spectra at peak brightness for 2366 supernovae. Most of these supernovae are obtained in the critical region of $0.5 < z < 1.2$ where the experiment has peak sensitivity to the value of the cosmological constant.

<i>Redshift</i>	<i>#SNe follow</i>	<i>Fields</i>	<i>Photometry</i>	<i>Spectroscopy</i> [days/yr]	<i>Color</i> [days/yr]
0.1	14	20	8.4	0.1	
0.2	44	20	8.4	0.2	
0.3	82	20	8.4	0.4	
0.4	124	20	5.6	0.7	
0.5	162	20	5.6	1.6	
0.6	196	20	11.3	2.8	
0.7	226	20	11.3	5.6	
0.8	250	20	11.6	8.7	
0.9	270	20	13.8	12.1	3.7
1.0	286	20	22.0	15.1	5.4
1.1	298	20	33.7	21.0	7.4
1.2	304	20	51.5	29.2	10.2
1.3	30	2	12.2	10.2	1.4
1.4	30	2	16.6	14.5	1.7
1.5	22	2	16.2	14.7	1.6
1.6	16	2	15.8	14.8	1.5
1.7	12	2	15.4	15.0	1.4
total	2366		268	167	34

Table 7.2: One-year SNAP supernova discovery and follow-up summary.

Chapter 8

Optical Photometry

8.1 Optical Photometer Requirements

The requirement for supernova detection and photometry is fulfilled by a large field imager based on CCD technology. The pixel size is chosen to be as low as attainable in science grade imagers to minimize the overall size of the device. The spatial sampling of one pixel per Airy disk FWHM is 20% better than for WFPC2 on HST, and is sufficient to ensure accurate photometry. The high-resistivity p-channel CCD technology provides high quantum efficiency at 10000 Å since the fully-depleted devices are 300 μm thick and back-illuminated. The longest single exposure is set by cosmic ray contamination, approximately 400 to 1000 sec. The longest aggregated exposure in the imager is one hour. For the parameters given in Table 8.1, which assumes a 2 meter primary mirror, the imager sensitivity is limited only by zodiacal light background.

Field-of-view	1° x 1°
Plate Scale	0.07 to 0.10 arcsec/pixel (0.10 nominal)
Pixelization	32k x 32k CCD mosaic
Wavelength coverage	350nm - 1000nm
Detector Type	High-Resistivity P-channel CCD's
Detector Architecture	2k x 2k, 10.5 or 12 micron pixel
Detector Array Temperature	135-150 K
Detector Quantum Efficiency:	65% @ 1000nm, 92% @ 900nm, >85% @ 400-800nm
Photometric Accuracy	1% relative
Read Noise	4 e-
Exposure Time	approximately ~200 sec
Dark Current	0.08 e ⁻ /min/pixel
Readout Time	20 sec
Limiting Magnitude Sensitivity	30th AB magnitude in I-band
Exposure control	Mechanical shutter
Filter Wheel	15 bands (U, V, R, I, Z, & 10 special filters)

Table 8.1: Optical Imager/Photometer requirements.

8.2 Technology

The optical photometer will be fabricated using a new state-of-the-art CCD based on ultra-high purity high-resistivity n-type silicon. These CCD's are fully-depleted and back-illuminated with superior response. The largest devices currently in operation at Lick Observatory are 2k x 2k with $15 \mu\text{m}^2$ pixels. Larger 2k x 4k devices are currently in fabrication as well as devices with 12.0 and $10.5 \mu\text{m}^2$ pixels. The technology has also been moved to a commercial foundry with the first lots currently in manufacture. Since the devices do not require thinning to obtain high sensitivity with back-illumination the devices are extremely robust and easy to fabricate in volume. For such back-illuminated devices, the intrapixel sensitivity variations (which are not removed by standard calibration techniques) will be very small, allowing accurate photometry even though undersampling the telescope point spread function (Lauer, 1999b; Jordon, Deltron, & Oates, 1994). Early measurements at the LBNL 88" cyclotron also indicate enhanced radiation tolerance. Additional studies will be required to validate the devices for the SNAP mission. Further information about this technology can be found at URL, <http://ccd.lbl.gov>, and in Appendix B.

Given the very large number of devices in the optical photometer, development of radiation hard multi-channel preamplifier/correlated double samplers developed on an integrated circuit has begun. Appropriate radiation hard 16-bit analog-to-digital converters are currently under investigation. These IC's would be fabricated in the radiation hard DMILL process through Temic Corp.

8.3 Supernova Detection

Detection of supernovae is accomplished by a repeated comparison of fixed fields to reference images. The imager would obtain twenty discovery fields from dark regions around the north and south ecliptic poles. These discovery fields would have a limiting detection magnitude of $m_{AB}(1\mu\text{m}) < 27$. This set of discovery fields would be recorded at intervals of four days. At six day intervals detection fields would be obtained to a limiting magnitude of $m_{AB}(1\mu\text{m}) < 28$. At eight day intervals detection fields would be obtained to a limiting magnitude of $m_{AB}(1\mu\text{m}) < 29$. Two of these fields would have a limiting detection magnitude of $m_{AB}(1\mu\text{m}) < 30$ taken every eight days. This strategy is summarized in Table 8.2. For this baseline study we considered a *Z*-band search; higher signal-to-noise may be achieved by combining the data from several filters. The average data transmission requirement from the images assuming 50% loss-free compression is 50 Mbit/s, these images represent the majority of the data to be transmitted.

8.4 Optical Photometer Performance

The follow-up optical photometry is obtained without specific knowledge of the location of new supernovae. The optical photometer obtains wide-field frames overlapping the positions of the discovery frames. Some of the photometry frames may be taken

<i>AB mag.</i> <i>B-band</i> <i>restframe</i>	<i>SN</i> <i>flux</i> <i>[e⁻/s]</i>	<i>Zodiacal</i> <i>Light</i> <i>[e⁻/s/pix]</i>	<i>Total Time</i> <i>per Field</i> <i>[hrs]</i>	<i>Filter Fields</i>	<i>Repeat</i> <i>Interval</i> <i>[days]</i>
27.0	0.4	0.17	0.2	Z-band	4
28.0	0.16	0.17	0.5	Z-band	6
28.5	0.06	0.17	2.9	Z-band	8
30.0	0.03	0.17	12.6	Z-band	8

Table 8.2: Observation strategy.

while the satellite is taking spectra of specific supernovae. The photometer obtains frames in each of a specified list of redshifted B-band filters with exposures of sufficient duration to obtain all the data points required to reconstruct the light curve. These total exposures will be comprised of numerous shorter exposures. These shorter exposures will be taken in dithered groups, allowing elimination of cosmic-rays without resampling of the image, while providing the subpixel offsets desirable for using resolution enhancing techniques (such as *DRIZZLE*; Fruchter & Hook (1998)) and averaging over any residual intrapixel sensitivity variations. The longest aggregate optical photometric exposure is one hour. The photometry is also obtained at regular intervals in order to obtain data points that reasonably approximate the required ten photometric points along the light curve. As shown in Table 8.3, the B-band photometry is divided into ranges of redshift for photometry in a specific filter. Given the correlation between brightness and redshift the exposure times are known a priori. The parameters given in Tables 8.2 & 8.3 assume a 2 meter primary mirror.

<i>Red-Shift</i>	<i>SNe</i> <i>Rate</i> <i>yr/1°</i>	<i>Peak AB</i> <i>mag.</i> <i>B-band</i> <i>restframe</i>	<i>Peak</i> <i>SNe</i> <i>flux</i> <i>[e⁻/s]</i>	<i>Zodiacal</i> <i>Light</i> <i>[e⁻/s/pix]</i>	<i>Longest</i> <i>Exposure</i> <i>[hrs]</i>	<i>B-band</i> <i>Filter</i> <i>Center</i> <i>[μm]</i>	<i>Fields</i>	<i>#SNe</i> <i>follow</i>	<i>Repeat</i> <i>Time</i> <i>[days]</i>	<i>Total</i> <i>Time/yr</i> <i>[days]</i>
0.1	0.7	18.95	634.0	0.10	0.11	0.48	20	14	4	8.4
0.2	2.2	20.59	145.3	0.12	0.11	0.53	20	44	4	8.4
0.3	4.1	21.60	57.8	0.13	0.11	0.57	20	82	4	8.4
0.4	6.2	22.33	29.5	0.14	0.11	0.61	20	124	6	5.6
0.5	8.1	22.91	17.3	0.15	0.11	0.66	20	162	6	5.6
0.6	9.8	23.39	11.1	0.16	0.11	0.70	20	196	6	11.3
0.7	11.3	23.80	7.6	0.16	0.12	0.75	20	226	6	11.3
0.8	12.5	24.16	5.5	0.17	0.18	0.79	20	250	6	11.6
0.9	13.5	24.47	4.1	0.17	0.33	0.83	20	270	8	13.8
1	14.3	24.76	3.2	0.17	0.44	0.88	20	286	8	22.0
1.1	14.9	25.02	2.5	0.17	0.67	0.92	20	298	8	33.7
1.2	15.2	25.25	2.0	0.17	0.89	0.97	20	304	8	51.5
total								2256		191.9

Table 8.3: Optical photometry.

The data payload from the photometry is large, so in studies we may consider transmitting data limited to pixel sets around star images over a 3σ threshold or around locations already identified as being supernova candidates, or around galaxies. Analysis of HST images indicate that this will provide a ten-fold reduction in the data. Given these assumptions, the data transmission requirement for the optical photometry data could be greatly reduced from 50 Mbit/s however, it could impact the utility of the data for other scientific measurements.

Chapter 9

NIR Photometry

9.1 NIR Photometer Requirements

The NIR photometer is constructed from one HgCdTe device with a $1.7\ \mu\text{m}$ wavelength cut-off. The requirements for the NIR photometer are shown in Table 9.1. The NIR photometer could have a single device with a filter wheel or there could be multiple devices each with a fixed filter. Using fixed filters may permit the placement of the HgCdTe devices within the focal plane of the optical photometer. The follow-up NIR photometry will require specific knowledge of the location of each new supernova. The NIR photometer obtains small frames determined by pointing the satellite at the supernova. Other options for the NIR photometer are currently under discussion.

Field-of-view	1.4 to 2.0 arcmin on a side
Plate Scale	0.08 - 0.12 arcsec/pixel (0.12 nominal)
Pixelization	1k x 1k, 18.5 micron pixel
Wavelength coverage	1000nm - 1700nm
Location	TBD
Detector Type	HgCdTe (1.7 μm cut-off)
Detector Array Temperature	130K-140K (to achieve dark current)
Detector Quantum Efficiency	70% average
Photometric Accuracy	1% relative
Read Noise	5 e^- (multiple samples)
Dark Current	3 e^- min/pixel
Exposure control	Mechanical or electrical
Filters	J&H, plus five special filters

Table 9.1: NIR Imager/Photometer requirements.

9.2 NIR Photometer Performance

The NIR photometer would be unable to follow all supernovae seen in each of the most distant discovery frames. Consequently a subset would be selected for follow-up. As shown in Table 9.2, the longest photometric NIR observation is 7 hours and would require a total of 31 hours of observing time to follow the complete light curve

of a $z=1.7$ supernova out to a limiting magnitude of $m_{AB}(1\mu\text{m}) < 28.2$. Following the supernova light curve in the infrared is the most “expensive” task of the satellite. This task will require the highest possible optical throughput and quantum efficiency. The parameters given in Table 9.2 assume a 2 meter primary mirror. With these parameters the NIR photometer is only limited by zodiacal light background. HgCdTe arrays are known to have strong intrapixel sensitivity variations (Lauer, 1999a; Finger et al., 1999). Therefore, a careful study of the appropriate scale and dithering pattern will be undertaken to ensure that the IR photometer will produce accurate, unbiased photometry. The data transmission requirement for the NIR photometry data is small in comparison to the optical imager.

<i>Red-Shift</i>	<i>Peak AB mag. B-band restframe</i>	<i>Peak SNe flux $[e^-/s/pix]$</i>	<i>Zodiacal Light $[e^-/s]$</i>	<i>Longest Expose $[hrs]$</i>	<i>Time per SNe $[hrs]$</i>	<i>B-band Filter Center $[\mu m]$</i>	<i>Fields</i>	<i>#SNe follow</i>	<i>Total Time/yr $[days]$</i>
1.3	25.47	1.25	0.18	2.2	9.8	0.95	2	30	12.2
1.4	25.67	1.02	0.17	3.0	13.2	1.01	2	30	16.6
1.5	25.85	0.87	0.17	4.0	17.6	1.07	2	22	16.2
1.6	26.03	0.73	0.17	5.5	23.6	1.13	2	16	15.8
1.7	26.19	0.63	0.17	7.2	30.8	1.20	2	12	15.4
total								110	76.1

Table 9.2: NIR photometry.

The highest redshift supernova followed photometrically by the optical photometer will require measurement of the V-band restframe color of the supernova at peak magnitude using the NIR photometer since the light will be redshifted into the infrared. Since these measurements are only performed at peak brightness the limiting magnitude for the measurements is $m_{AB}(1\mu\text{m}) < 25.2$, as shown in Table 9.3, and very little time is devoted to these measurements. It may be necessary to assign additional observing time to obtain color at additional epochs near maximum brightness. The data transmission requirement for the NIR V-band photometry data is negligible.

<i>Red-Shift</i>	<i>SNe Rate $yr/1^\circ$</i>	<i>Peak AB mag. B-band restframe</i>	<i>Peak SNe flux $[e^-/s/pix]$</i>	<i>Zodiacal light $[e^-/s]$</i>	<i>Time SNe $[hrs]$</i>	<i>Fields</i>	<i>#SNe follow</i>	<i>Total Time/yr $[days/yr]$</i>
0.9	13.5	24.47	3.08	0.18	0.33	20	270	3.7
1	14.3	24.76	2.36	0.18	0.45	20	286	5.4
1.1	14.9	25.02	1.86	0.18	0.60	20	298	7.4
1.2	15.2	25.25	1.50	0.18	0.81	20	304	10.2
1.3	15.4	25.47	1.23	0.18	1.11	2	30	1.4
1.4	15.5	25.67	1.02	0.17	1.34	2	30	1.7
1.5	15.4	25.85	0.87	0.17	1.72	22	22	1.6
1.6	15.3	26.03	0.73	0.17	2.20	2	16	1.5
1.7	15.1	26.19	0.63	0.17	2.77	2	12	1.4
total							1268	34.3

Table 9.3: NIR V-band photometry.

Chapter 10

Spectroscopy

10.1 Optical/IR Spectrograph Requirements and Performance

10.1.1 Introduction

Spectroscopy of supernova candidates discovered by SNAP is necessary to confirm and assign a type to the supernova, to establish the redshift of the host galaxy, and to further characterize the supernova based on its expansion velocity, metallicity, and luminosity-indicator absorption line ratios. The defining signature for SNe Ia is the Si II 6250Å absorption feature. SNe II, from which the SNe Ia are to be distinguished, are characterized by the presence of $H\alpha$ absorption and emission having a classic P-Cygni profile. In addition, numerous features, especially in the wavelength range 3800–5500Å can be used to distinguish SNe Ia from other types. Host-galaxy redshifts can in most cases be determined from emission lines, such as OII 3727Å $H\beta$, and O III 5007Å, as well as absorption features like the Ca II H and K lines at 3933 and 3969Å. The supernova expansion velocity can be obtained from numerous absorption lines throughout the rest-frame optical spectrum, while the metallicity is best determined from pseudo-emission features produced by Fe absorption in the UV (2700–3800Å). Promising spectral luminosity indicators include the $\mathcal{R}(\text{Si II})$ and $\mathcal{R}(\text{Ca II})$ ratios (Nugent et al., 1995a). Thus, to fully exploit the spectral information from SN Ia, rest-frame wavelength coverage from 2700–6600Å is desirable. For the redshift range of $0.3 < z < 1.7$ best probed by SNAP, a spectrograph covering 0.35–1.7μm is needed to obtain the optimal rest-frame spectral coverage.

10.1.2 Achieving Wavelength Coverage with a Three-Arm Spectrograph

The zero-th order requirements for a spectrograph capable of obtaining the above measurements are high throughput and broad wavelength coverage. These requirements, coupled with the need to prevent overlapping of spectral orders, lead naturally to the choice of a three-channel spectrograph. By initially splitting the light entering the spectrograph into blue (0.35–0.55 μm), red (0.50–1.00 μm), and non-thermal near-

infrared (0.95—1.70 μm) components, not only is order overlap handled automatically, but the detectors and optics (optical elements, materials, and coatings, and blaze wavelength for each grating) can be chosen to provide the best possible performance over the limited wavelength range of each channel. Conversely, no single dispersive element can cover the required wavelength range, so a single-channel spectrograph would require multiple gratings and serial observations of different wavelength ranges leading to a $2\text{--}3\times$ loss of observing efficiency. Even then, multiple detectors would be required since even fully-depleted CCD's do not perform beyond $\sim 1 \mu\text{m}$, while NIR detectors do not perform well, period, for space-based (low-background) spectroscopic applications. Finally, only reflective optics can perform over a large wavelength region, but their use would result in extremely low efficiency.

Several highly successful multi-channel spectrographs have been built for ground-based telescopes (Oke & Gunn, 1982; Miller et al., 1992; Oke et al., 1995), so the design and construction of a three-channel spectrograph does not present fundamental technical challenges. An example of a two-channel optical spectrograph, the KAST spectrograph at the Lick 3-m telescope, is shown in Fig 10.1. One modest compromise over a static three-channel spectrograph design is required by the fact that current dichroic beam splitters — used to achieve color separation — only perform well over a range in wavelength that is slightly smaller than required for SNAP. This limitation is easily accounted for by allowing the NIR/optical dichroic to be removed from the beam for blue-channel observations of the lowest redshift supernova. With this dichroic in the beam, the blue-channel performance from 0.35—0.42 μm will be degraded, however higher redshift supernova ($z > 0.6$), which do require NIR coverage, will not require blue coverage in this wavelength range.

10.1.3 Resolution Requirements and Constraints

The next most important spectrograph design parameter is the resolution needed to measure supernova and host-galaxy features of interest. Typical supernova expansion velocities of $v \sim 15000 \text{ km s}^{-1}$ imply that supernova spectral information is undeniably lost for a resolution worse than

$$R = \lambda/\delta\lambda \sim \lambda/((v/c)\lambda) \sim c/v \sim 20.$$

At the other extreme, host-galaxy absorption and emission lines will be diluted if the resolution is not sufficient to resolve the velocity dispersion or rotation velocity of the host. These velocities are typically 100—300 km s^{-1} , and would require $R \sim 1000\text{--}3000$ to properly resolve. Although this higher resolution can be achieved and would satisfy the resolution requirements for supernovae, for a 2-m aperture the light would then be so dispersed that detector dark current and read noise would dominate the noise budget, leading to lower performance compared to the photon-limited case. Thus, it is important to determine the minimum resolution needed for supernovae, and accept that this resolution is not ideal for galaxy spectroscopy.

Despite the large expansion velocities for supernovae, the locations and shapes of absorption and pseudo-emission features shift with changing metal abundance by amounts much smaller than the line velocity width. For example, the locations of the

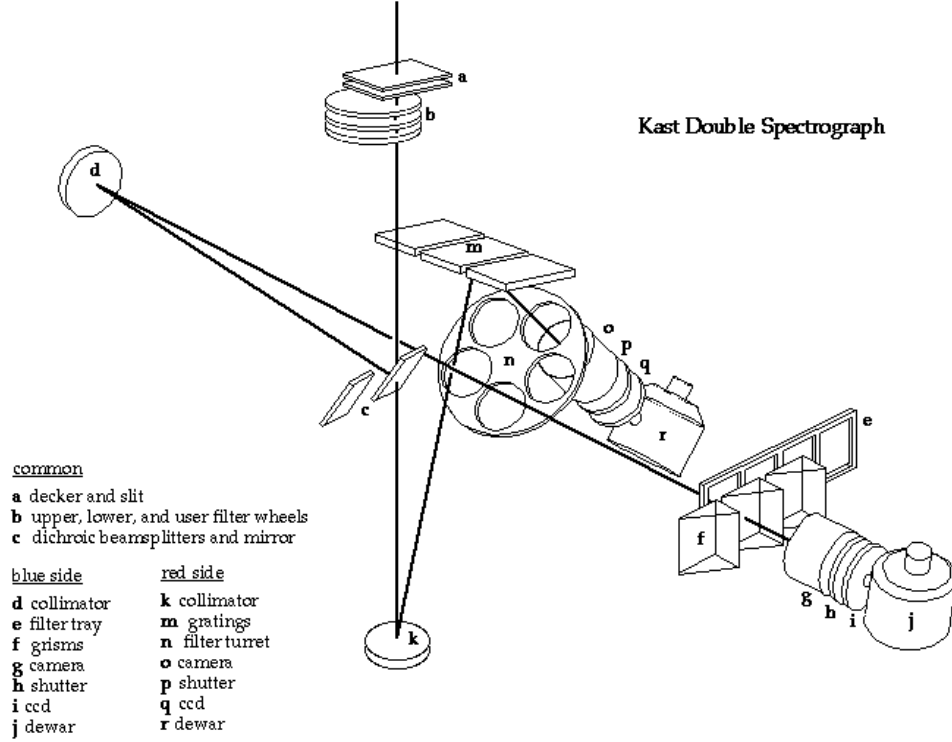


Figure 10.1: Schematic illustration of the light path for the KAST two-channel spectrograph of the Lick 3-m (Miller et al., 1992). The three-channel spectrograph for SNAP would use similar concepts, although it would employ an integral field unit, rather than a single slit (see below), would have one more spectral channel, and would include a more limited selection of filters, gratings, and transmission gratings (a.k.a. a grism). Note that a wide variety of geometric layouts is possible in addition to that shown for KAST.

UV pseudo-emission features shift by about 60 \AA over a 2 dex change in metallicity. In order to achieve an approximate indication of supernova metallicity, say to 0.3 dex, a resolution of

$$R \sim (3000 \text{ \AA} / 60 \text{ \AA}) (2 \text{ dex} / 0.3 \text{ dex}) \sim 300$$

is desired. A similar, but more detailed analysis is summarized in Fig. 10.2, where the expected error on the velocity of the Ca II H&K features in SN Ia for various combinations of signal to noise and resolution is shown. Also shown are the *statistical* errors in the supernova peak brightness associated with these velocity errors under the model discussed earlier where supernova absorption line velocity differences at a given light curve width lead to an additional source of error in the peak brightness. From this plot, and the previous discussion, it is clear that $R \sim 100\text{--}300$ is sufficient for obtaining the desired velocity measurements.

Assuming detectors with 2048 pixels in the wavelength direction and the wavelength coverage given above for each channel, the resolution limit set by the detectors (assuming Nyquist sampling of two pixels per resolution element) is $R \sim 2200, 1500$, and 1800 for the blue-, red-, and NIR-channel, respectively. Thus, the number of detector elements does not pose any significant limitation compared to the resolution desired for properly observing supernovae and their host galaxies.

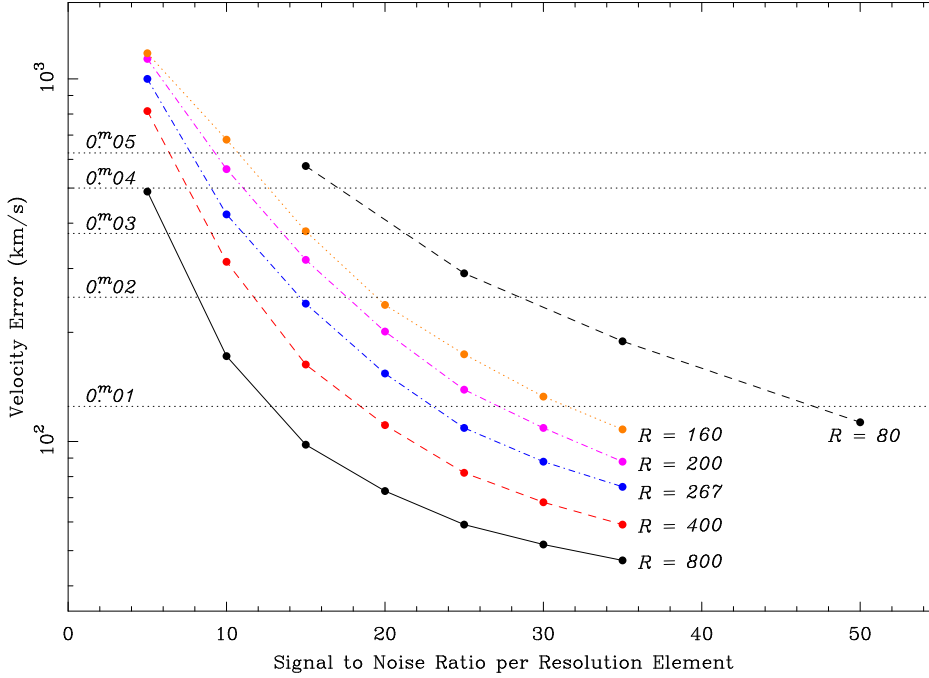


Figure 10.2: Calculation of the error in the position of the Ca H&K supernova absorption lines, expressed as a velocity, versus the signal-to-noise per spectral resolution element for various values of the resolution, R . The horizontal lines give the statistical error in the peak magnitude at a given light curve width for variations in the Ca II H&K velocity, as discussed in § 4.4.3. As an example, supernova absorption line velocities can be measured to 250 km/s, the peak magnitudes can be corrected to 0.02 magnitudes (2%). This accuracy can be achieved for a wide range of combinations of R and signal-to-noise. The ability of SNAP to meet such a goal is discussed in the text. Application of such a correction means that this effect will then be a statistical error rather than a systematic one.

10.1.4 Integral Field Unit

In typical spectroscopic observations a slit is placed at the focal plane of an astronomical telescope so that the region on the sky containing light from the object of interest can be selected (along with whatever background/foreground is superposed on the object), while light from regions on either side of the slit having only background light are prevented from entering the spectrograph. Along the spatial direction of the

slit, background light does enter, and can often be used to estimate and subtract light contaminating the object of interest. Introduction of a slit is also necessary to preserve spectral resolution, which is otherwise set by the spatial width of the target (not always a point source). The drawback of using a slit is that either some light from the target is also rejected (when the slit is too narrow), or an undesirable amount of background is admitted into the spectrograph (when the slit is too wide). For very faint targets, extremely precise astrometry, pointing, and stability is required to place the slit accurately on the target object; for diffraction limited imaging in space these requirements are severe. Moreover, if there is any chromatic aberration in the telescope — or atmospheric dispersion for ground-based observations — the amount of light entering from the target is wavelength dependent. This is very undesirable because unless this effect can be exactly reproduced when calibration stars are observed (which it cannot be unless the pointing is perfect), the final target spectrum will not be properly flux-calibrated as a function of wavelength.

A solution to these acquisition, pointing stability, calibration, and slit-loss problems is to employ an integral field unit (IFU) in place of a slit. An IFU spatially subdivides the region of the focal plane near the target, and sends each subregion to the spectrograph where its spectrum is produced. If the filling factor of the IFU is 100%, all the light of the target object enters the spectrograph, although it may be spread amongst the spectra of several subregions. All information is available to completely reconstruct the 3-dimensional (2 spatial and 1 wavelength) spectral image, allowing the spectrum from the target object to be extracted in software, using optimal weighting. The most common and useful types of IFU's are illustrated in Fig. 10.3. IFU's will soon become the norm at most major telescope facilities; they are in use at WHT and Palomar, are under construction for Keck, VLT, and Gemini, and one is under consideration for NGST.

The simplest form of IFU is an image slicer, composed of a stack of thin metal or glass plates, with each layer of the stack tilted slightly with respect to each other and with a reflective coating applied to the thin edge of each layer (Hunten, 1974). When the edge of such a stack is placed in the telescope focal plane, different slices of the focal plane image are reflected at slightly different angles. From the point of view of the spectrograph, this gives the appearance of a long slit (albeit with slight steps perpendicular to the slit along the length of the slit). An example of such an image slicer built for the Palomar 200-inch telescope is given in Murphy, Matthews, & Soifer (1999). In this simplest form of image slicer, only one slice can be in focus at the spectrograph entrance, and thus a very slow input beam is required to minimize aberrations. More advanced image slicers incorporate an additional optical element for each slice which corrects for such defocusing. Examples include the image slicer for Gemini discussed in Content (1998b) and those for NGST discussed in Content (1998a), Le Fevre, O. and the IFMOS Consortium (1999), and Richardson et al. (2000). Fig. 10.4 shows an especially elegant image slicer design by Richardson which uses internal reflection to obtain very high throughput, and which is made of a solid piece of glass which makes it impervious to changes in temperature. For the small field needed by SNAP, there will be no light loss due to shadowing by adjacent (micro) mirrors.

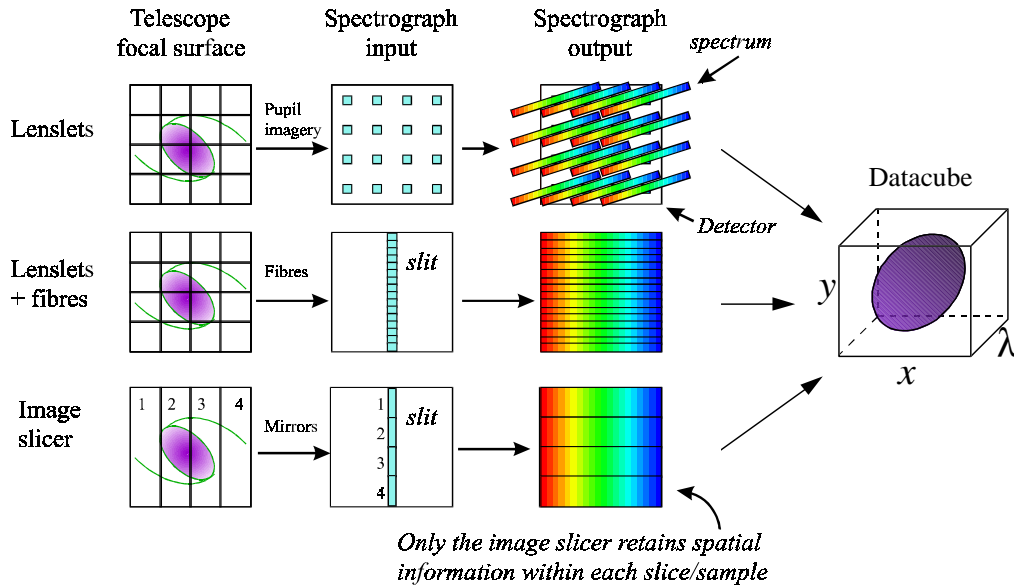


Figure 10.3: Illustration of how various types of integral field units are used to reformat spatial and spectral information from an astronomical scene. The top row shows a pure microlens array IFU, the middle row shows a microlens array feeding optical fibers, and the last row shows in image slicer.

Alternative IFU designs using microlens arrays directly, or microlens arrays feeding optical fibers are also possible, and examples are presented by Iye, Ebizuka, & Takami (1998), Allington-Smith, Content, & Haynes (1998), Haynes et al. (1999) and Larkin, Quirrenback, & Graham (2000). A microlens-array + fibers IFU is illustrated in Fig 10.5 and Fig 10.6. Care is required to avoid light losses due to focal ratio degradation induced by imperfections in the fibers, and it is critical that the microlens and fibers be properly aligned. In current designs, the fibers must be glued to the microlens arrays; typical glues have optical absorption features. Glue bonds may be susceptible to breakage from thermal and mechanical stresses (at launch). To avoid some of these drawbacks, Eisenhauer et al. (2000) have developed flared fibers with a spherical lens polished onto the end to simulate a microlens. Presently this is a custom process for each fiber, and would likely be expensive to implement for ~ 400 fibers.

The image slicer IFU has several advantages over those using microlens arrays. Unlike the image slicer IFU, both types of microlens array IFU's subdivide the image in two dimensions, so in the spatial direction the image is resampled twice — once by the microlens array and again by the detector. This requires a larger number of detector elements to ensure proper sampling. For the microlens array IFU, the spectrograph design is strongly intertwined with the scale and number of microlenses, thus reducing the flexibility in designing the spectrograph (Bacon et al., 1995). On the other hand, combining microlens arrays with optical fibers to make an IFU is very

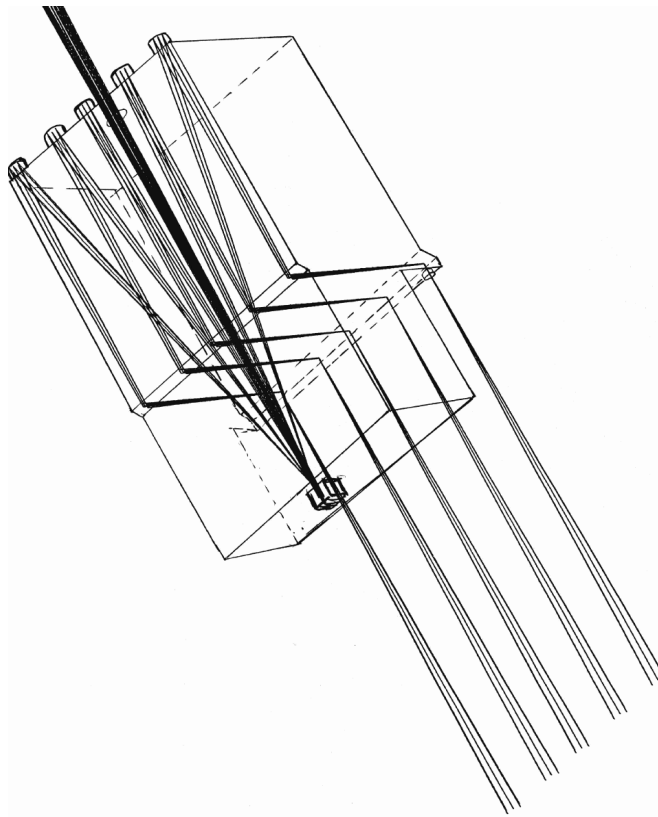


Figure 10.4: Schematic illustration of an advanced focusing image slicer design for NGST. The throughput of this IFU should be better than 90%. Here light from the telescope enters the glass block from the upper left, reflects off the first array of mirrorlets and back to another array of mirrorlets. It is then redirected through two 90 degree internal reflections and into an array of field lense, after which the light exits the glass block and forms a reformatted in-focus image on the entrance to a spectrograph (not shown). All reflections use backcoated optical surfaces. The first mirrorlet array can employ toroidal optics to produce magnification perpendicular to each slice. This helps reduce the size of the pupil image in the spectrograph and can be chosen to ensure proper (two pixel) sampling of the slit on the detector. [Adapted from Figure 1 of Richardson et al. (2000)].

delicate, involving glue bonds which can fail, and fibers and glue which have spectral absorption features. Furthermore, slicing in the image plane leads to diffraction in the pupil plane, requiring larger optics and grating, thus increasing mass and cost. An image slicer IFU only produces diffraction in one direction, and toroidal slicing optics can be used to introduce magnification, both of which lead to a smaller final pupil size. For these and other reasons, Content (1998a) and Le Fevre, O. and the IFMOS Consortium (1999) both conclude that an image slicer is the best choice for

space-based applications, and Le Fevre, O. and the IFMOS Consortium (1999) has produced a prototype for NGST.

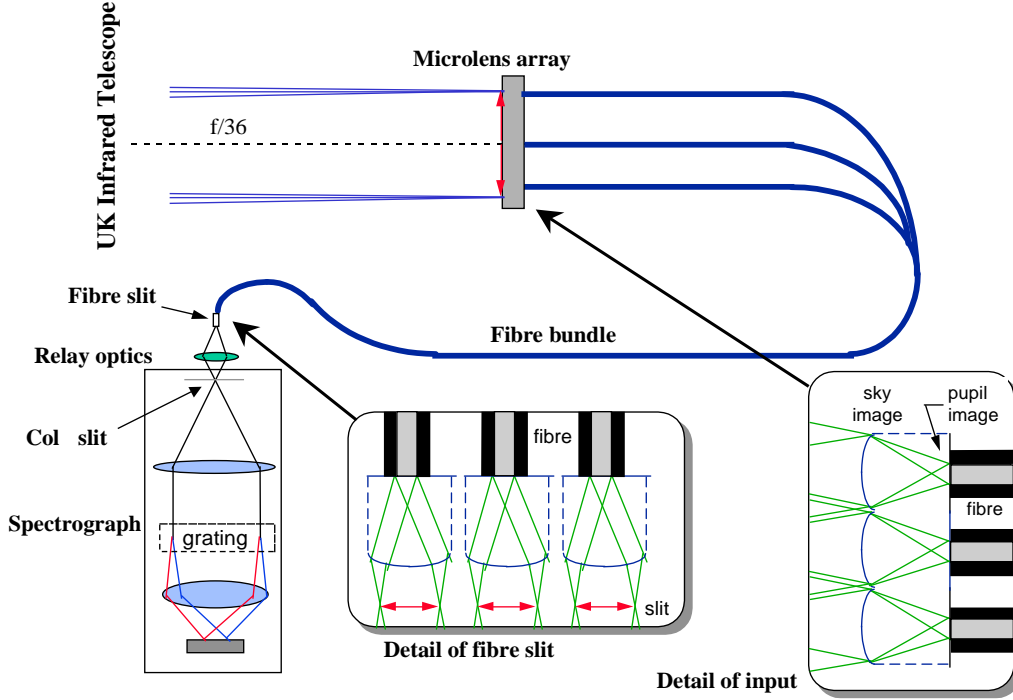


Figure 10.5: Schematic illustration of how an integral field unit based on a microlens array and fiber bundle works. [Adapted from Figure 9 of Haynes et al. (1999)]. The measured throughput of this IFU is measured to be roughly 50%. However, this is a prototype IFU which was adapted to a pre-existing spectrograph.

Other than diffraction in the pupil plane, the drawbacks to using an IFU are minor; since the spectrograph sees a slit length that is longer than needed for a single slit, it must be designed with a wider field of view. Also, some loss of throughput will result from the reflection or transmission inefficiency of the IFU and any fore-optics required to produce a sufficiently large scale at the IFU.

Following the discussion of spectral resolution, above, the optimal spatial resolution for the IFU and the final spectrograph focal planes depend in part on the total effective area of SNAP and the properties of the spectrograph detectors. If the size of the IFU subregions is too small, the amount of background light will fall below that required for background-limited performance at a given spectral resolution. Sampling of a $2'' \times 2''$ region of the focal plane with $0.''07$ -wide slits would be more than adequate for SNAP. This would require 30 stack layers for an image slicer. Each would be about 30 pixels high, and could be formatted onto a $2k \times 4k$ CCD. Spatial resolution this fine would put the spectrograph in the detector-limited regime of operation for the dimmest targets

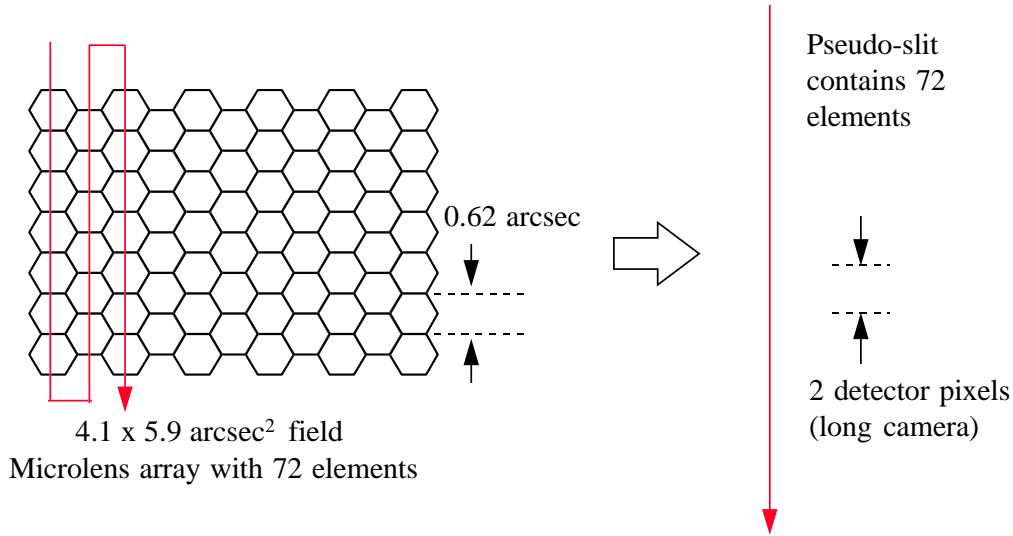


Figure 10.6: Illustration of how a microlens array is used to produce a pseudo-slit from an initially 2-dimensional region of the telescope focal plane. [Adapted from Figure 10 of Haynes et al. (1999)].

for the most desirable resolution using current detectors; therefore some compromise in spatial or spectral resolution would be necessary. Alternatively, optics could be placed in front of the IFU to provide more than one scale; a coarse scale for the faintest objects and a finer scale of brighter objects or bright background (e.g., from the supernova host galaxy) situations.

10.1.5 Optics

A standard astronomical spectrograph consists of a slit, collimator, dispersive element, and camera lens. The SNAP telescope will have an $f/10$ beam, to which the focal ratio of the collimator should be matched. If the focal length of the camera is the same as that of the collimator, the spatial scale at the spectrograph focal plane will match that of the telescope focal plane. However, by choosing different camera lens focal lengths, the spatial scale can be changed to optimally match the properties of the detectors in each arm of the spectrograph.

The spatial scale at the telescope focal plane will be roughly $0.1 \text{ arcsec}/\mu\text{m}$. For a $2''$ square region in the image plane re-formatted as a slit using an IFU, the effective slit length with $0.1''$ slices and a $0.5''$ buffer between slits is $55''$. With such slow optics and limited field-of-view the spectrograph design should be straightforward, and the goal of high efficiency (35%, including detectors) should be attainable. If the spectrograph is fed by an optical-fiber IFU, the collimator focal ratio will be faster than that of the telescope to match the output focal length of the optical fibers. Ordinarily this

would result in a more compact instrument, however diffraction effects will require the optics to be oversized, as discussed above. If a Richardson focusing image slicer IFU is used, the nominal telescope scale will be too small, and magnifying optics would be needed in front of the IFU. This in turn would lead to a longer focal length for the collimator, requiring the camera lens to then demagnify the scale, but would not significantly increase the mass of the spectrograph.

As discussed earlier, the optics (including the image slicer, if placed after the dichroic beam splitters) can be optimized for image quality and throughput for each spectrograph arm. Thus, the design for the spectrograph could be quite different for each arm, if desired. A Phase A spectrograph design is necessary to determine further details and constraints for the spectrograph.

10.1.6 Dispersive Elements

Conventional Gratings and Grisms

The gratings and grisms in common use in astronomical spectrographs typically have efficiencies of 70% at the blaze wavelength, λ_B , and fall to half of peak efficiency at $\sim 2/3 \lambda_B$ and $\sim 3/2 \lambda_B$. These are off-the-shelf and space-ready components. It will be worth exploring higher-efficiency dispersive elements for the SNAP spectrograph.

Volume Phase Holographic Gratings

In the last few years volume-phase holographic gratings have come into use as high-efficiency dispersive elements for astronomical spectrographs. Barden, Arns, & Colburn (1998) have performed extensive studies of the properties of these gratings and their suitability for astronomy. One of these gratings has been put into use at the AAT, with good results (Glazebrook, 1998). These gratings have lower scattered light than ruled gratings — a very desirable feature for obtaining accurate spectrophotometry. It will certainly be worth exploring these as dispersive elements for the SNAP spectrograph. The gelatin medium into which the hologram is imprinted is sealed in glass, so it should be structurally robust in the space environment. One unexplored issue when considering VPH gratings for use in space is the resistance of the gelatine medium to cosmic rays and/or UV radiation; this can be tested quite easily. Presently JPL is having Kaiser Optical Systems space-qualify VPH gratings for a Mars mission (Barden, priv. comm.).

A High-Efficiency NIR Dispersive Element

Oliva (1999) presents an Amici crown-crystal/neobium-flint/crown-crystal prism system, shown in Fig 10.7, which has roughly 85% efficiency over 0.85—2.5 μm . This would be a good starting point for the NIR channel of the SNAP spectrograph.

10.1.7 Very Low-resolution NIR Spectroscopy Option

There are advantages to trading high-efficiency for resolution for some NIR observations. Namely, with such a trade-off, observations of the faintest targets will be

guaranteed to be in the photon-limited regime even if the noise properties of NIR detectors never improve over those currently available. Fig. 10.2 shows that $R \sim 80$ can be productive, and such low resolution might be necessary to overcome HgCdTe detector noise for the faintest, highest redshift SNe Ia ($z \sim 1.7$) for which rest-frame B -band is located at $1.2 \mu\text{m}$ and V -band is at $1.5 \mu\text{m}$. One possible concept for a very low-resolution NIR spectroscopy option would be to feed an $f/30$ or slower beam to an image slicer and then directly on to the above high-index niobium-flint prism and through to the detector, eliminating a collimator and camera. Some optical aberrations may result, and these would have to be quantified in a Phase A study. Such a very low-resolution option would probably have to be separated from the main three-channel spectrograph. The economy and compactness of the design could allow SNAP to accommodate numerous such instruments.

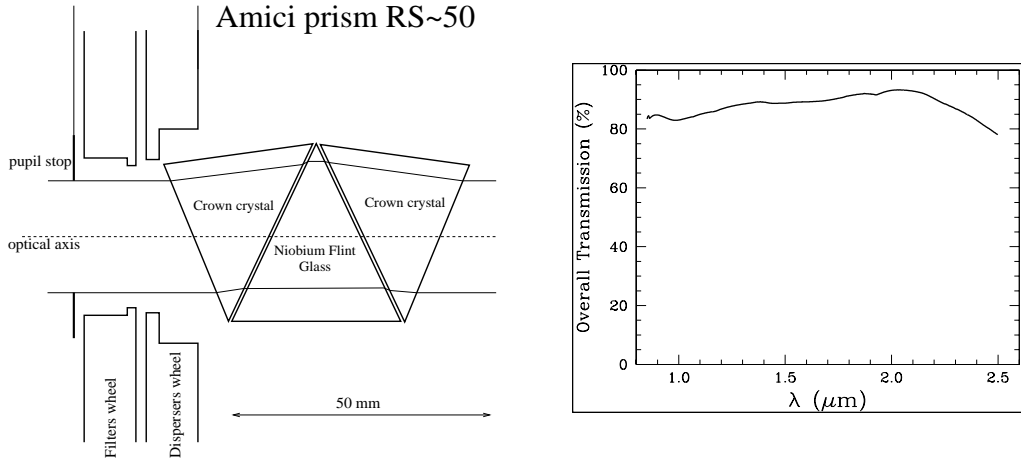


Figure 10.7: Example of a high-efficiency dispersion element which could be useful for the NIR channel of the SNAP three-channel spectrograph, or for a multiplexed very low resolution NIR spectroscopic option on SNAP. [Adapted from Figure 4 of Oliva (1999)].

10.1.8 Internal Adjustment and Calibration

Additional specifications for the spectrograph include an internal calibration module to provide wavelength calibration from arc lamps and pixel-to-pixel sensitivity corrections from a flat lamp, collimator or camera focus control, and possibly tilt control. The internal calibration unit must feed the spectrograph IFU with a beam having the same f-ratio and central obstruction as the SNAP telescope. Also, since the behavior of the dichroics depends on polarization, the internal calibration unit should mimic the (small) polarization of the SNAP telescope. A set of arc and flat lamps optimized for each of the three channels is desirable. The spectrograph focus can be checked using the width of arc lines. The alternative of using shifts in the positions of arc lines

produced by the introduction of a Newall shutter into the collimator beam might be more sensitive, but involves added technical risk since the Newall shutter could stick and thus block half of the collimator beam. Focus control of the collimator is generally preferable over adjusting the camera due to the slower focal ratio of a collimator. Tilt of the detectors with respect to the spectrograph focal planes should be set prior to launch, however, it may be desirable to have tilt adjustments available on-orbit to handle any subsequent mis-alignments.

10.2 Spectrograph baseline

The architecture of both the optical and IR spectrograph is based on an integral field spectrograph with an image slicer. The image slicer eliminates the need for a slit and greatly reduces the pointing accuracy required to place the supernova within the field of view of the spectrograph while preserving photometric accuracy because of the 100% filling factor. The pixel resolution for both spectrographs is set to contain the entire first lobe of the Airy disk within one pixel – this is severe undersampling and may be in conflict with required photometric accuracy and represents a change in scale from the imager. This however, relaxes the requirement for the readout noise of the IR imager, even so the spectrograph is still limited by the performance of the HgCdTe devices for the $z=1.7$ supernovae. Both optical and IR spectrographs will require selectable resolution in order to achieve an optimum of performance and exposure times. Furthermore, the spectral features of the high redshift supernovae are dilated by $1+z$, so that the reduced resolution is a good match to standardizing the performance over all supernovae followed. The performance features of the optical and IR spectrographs are shown in Tables 10.1 and 10.2, respectively. The optical spectrograph is assumed to have two channels, while the IR spectrograph one. The cross-over wavelength between the two optical channels would be determined by the availability of high throughput dichroics. It would be considered highly advantageous to be able to operate the longer wavelength channel of the optical spectrograph simultaneously with the IR spectrograph.

As opposed to the method of obtaining optical photometry on multiple supernovae simultaneously, we assume that the optical and IR spectroscopy is obtained by pointing the satellite at each individual supernova one at a time during its peak brightness. The per pixel resolution ranges from 15Å to 50Å (restframe) for the most distant supernovae in the study. The parameters given in Tables 10.3 and 10.4 assume a 2 meter primary mirror and an overall optical system efficiency of 45% and an IR system efficiency of 35% including telescope obscuration, reflectance, optical transport, and detector quantum efficiency.

Spectrograph architecture	Integral field spectrograph
Wavelength coverage	350 to 600 nm, 600 to 1000 nm
Spatial resolution of image slicer	0.07 arcsec
Field-of-View	2" x 2"
Location	TBD
Photometric Accuracy	1% relative
Resolution (per pixel)	15A, 30A, 60A selectable
Detector Type	High-Resistivity P-channel CCD's
Detector Architecture	2k × 2k, 10.5 micron pixel
Detector Array Temperature	150 K
Detector Quantum Efficiency:	65% @1000nm, 92% @900nm, >85% @400–800nm
Read Noise	2 e ⁻
Dark Current	0.08 e ⁻ /min/pixel
Readout Time	20 sec or longer to optimize readout noise
Exposure control	Mechanical or electrical shutter (TBD)

Table 10.1: Optical Spectrograph Arm Requirements

Spectrograph architecture	Integral field spectrograph
Wavelength coverage	1000 to 1700 nm
Spatial resolution of image slicer	0.12 arcsec
Field-of-View	2" x 2"
Location	TBD
Resolution	30A, 50A, 100A selectable
Detector Type	HgCdTe
Detector Architecture	1k × 1k, 18.5 micron pixel
Detector Array Temperature	130K-150K (to achieve dark current)
Detector Quantum Efficiency:	70% average
Photometric Accuracy	1% relative
Read Noise	≤ 4 e ⁻ (multiple samples)
Dark Current	0.02 e/pixel/s
Readout Time	20 sec
Exposure control	Mechanical or electrical (TBD)

Table 10.2: IR Spectrograph Arm Requirements

<i>Redshift</i>	<i>#SNe follow</i>	<i>Resolution</i> [Angstroms] [(lab frame)]	<i>Peak SNe</i> <i>Flux</i> [e ⁻ /s]	<i>Zodiacal</i> [e ⁻ /s]	<i>TimeSNe</i> [hrs]	<i>Total Time</i> <i>for Peak</i> <i>Spectra [days]</i>
0.1	14	15	6.04	0.0005	0.11	0.1
0.2	44	15	1.27	0.0005	0.11	0.2
0.3	82	15	0.47	0.0005	0.11	0.4
0.4	124	15	0.22	0.0005	0.14	0.7
0.5	162	30	0.24	0.0010	0.23	1.6
0.6	196	30	0.15	0.0010	0.35	2.8
0.7	226	30	0.09	0.0010	0.59	5.6
0.8	250	30	0.06	0.0009	0.84	8.7
0.9	270	30	0.05	0.0009	1.08	12.1
1.0	286	30	0.07	0.0017	1.26	15.1
1.1	298	30	0.05	0.0016	1.69	21.0
1.2	304	30	0.04	0.0016	2.31	29.2
total	2256					97.6

Table 10.3: Optical Spectroscopy

<i>Redshift</i>	<i>#SNe follow</i>	<i>Resolution</i> <i>[Angstroms]</i> <i>[lab frame]</i>	<i>Peak SNe</i> <i>Flux</i> <i>[e⁻/s]</i>	<i>Zodiacal</i> <i>[e⁻/s]</i>	<i>TimeSNe</i> <i>[hrs]</i>	<i>Total Time</i> <i>for Peak</i> <i>Spectra [days]</i>
1.3	30	100	0.039	0.0056	8.1	10.2
1.4	30	100	0.031	0.0053	11.6	14.5
1.5	22	100	0.025	0.0050	16.0	14.7
1.6	16	100	0.020	0.0047	22.3	14.8
1.7	12	100	0.017	0.0045	30.0	15.0
total	110					69.1

Table 10.4: IR Spectroscopy

Chapter 11

Telescope

11.1 Optical Requirements

The preceding material establishes a number of requirements that the SNAP telescope must satisfy. The most important of these are the optical performance specifications that establish the light gathering power, angular coverage, angular resolution, and wavelength coverage needed to deliver our planned supernova discovery rate. We summarize our technical requirements in Table 11.1 below.

11.2 Baseline Optical Design

We have arrived at a baseline optical system configuration after having formulated a list of design considerations including thermal, mechanical, alignment, payload accommodation, and operational factors. We discuss these considerations here, and then present one detailed optical configuration that meets these requirements. We have adopted this as our baseline optical design. We recognize that other solutions may perform as well or better, and those will be explored during the coming year. For purposes of developing plans for cost, mass, and payload accommodation, it is vital to show that there is at least one optical configuration that satisfies our requirements.

One important driver setting the overall envelope of the telescope is the dimensions of a payload that can be launched using a Delta IV rocket. After examining the Payload Accommodation Handbook, we have adopted the nominal 2.0 meter telescope aperture shown in the table above. This dimension is near the minimum optic size that will allow our science goals to be met, and is near the maximum that can be accommodated within limitations imposed by payload mass and cost.

A second driver for our optical design is the requirement for a field of view that supplies a high quality image whose sky area is at least one degree square. Another crucial requirement is a broad bandpass, extending from the near ultraviolet into the near infrared, with no significant chromatic aberration or defocusing. Beyond these, it is advantageous to have our final focal surface flat to simplify the fixturing, metrology, and testing of the CCD array. Because the main CCD array will require a mechanical shutter to provide a dark readout environment, and our multiband photometry imposes

Aperture	2.0 meter
Field-of-view	1 square degree, any compact shape
Optical resolution	diffraction-limited at $1\mu\text{m}$, ~ 0.1 arcsec
Wavelength coverage	350nm - 1700nm
Solar avoidance	70°
Temperature	250-290 K (well below thermal background for $\lambda < 1700\text{nm}$)
Fields of study	North and South Ecliptic Poles
Image stability	0.03 arcsec (3σ) over each exposure
Plate scale	$\sim 100\mu\text{m}/\text{arcsec}$
Effective focal length	$\sim 20\text{m}$
Pupil Obscuration	$\sim 5\%$ diameter
Mirror Coating	Enhanced Silver
Intermediate pupil	Accommodate shutter and filter wheel
Guider	fast CCD not obscured by shutter
Filter Wheel	15 bandpasses + "open"
Articulated secondary	6-axis; Accommodate focus & decenter

Table 11.1: SNAP observatory requirements.

the need for a multiposition filter wheel in the optical train, the optics must offer a reasonably small beam waist optically conjugate to the entrance pupil where this shutter and a filter wheel can be situated. It is desirable that the optical train avoid the use of refractive lenses or correctors, owing to their susceptibility to cumulative radiation damage on an extreme high altitude orbit such as ours, and due to the production of scintillation and Cerenkov light under charged particle bombardment. Thermally, it is highly advantageous to locate the focal plane at the cold side of the payload, where radiative detector cooling is straightforward, thereby avoiding the need for heat pipes or refrigerators.

These requirements eliminate many candidate telescope configurations that otherwise would be considered:

- * A Schmidt camera has serious chromatism from its refractive corrector lens, and has a strongly curved focal surface. Worse, the detector is buried deep within the optical train where radiative cooling is impractical;

- * A Ritchey-Chretien cassegrain telescope has too narrow a field of view;

- * A field-widened Ritchey-Chretien includes a multiple-lens corrector that delivers an image sufficiently large and sharp for our purposes. In addition, if the corrector lenses are made of fused silica, they will be radiation-hard, and could contribute to the radiation shielding for our CCD array. However this configuration lacks a small intermediate beam waist for our shutter and filter wheel.

- * The Paul-Baker (Paul, 1935; Baker, 1969; Angel, Woolf, & Epps, 1982; McGraw et al., 1982) three mirror telescopes are compact and highly corrected over the wide field we desire, and are free of refractive elements. However, these configurations place the focal plane deep within the space between primary and secondary mirrors, where access and thermal control are difficult. Also, these optics impose a severe secondary obscuration amounting to 40% of the primary diameter and therefore produce a diffraction pattern that is larger than desired. These telescopes also lack a small intermediate beam waist.

* The Mersenne-Schmidt (Willstrop, 1984) and Epps-Takeda (Epps & Takeda, 1983) configurations are three mirror systems in which the secondary and tertiary mirrors are enlarged and separated further compared to the Paul-Baker family, with the result that improved geometric image quality is attained. For our purposes however the added length and the inaccessible detector location makes these telescopes even less attractive than the Paul-Baker designs.

* Five compact three mirror anastigmats have been explored by Korsch (1980). Of those, four do not offer the requisite intermediate pupil, and we have not considered them further.

Our baseline configuration is a three-mirror anastigmat in which the tertiary mirror re-images an intermediate cassegrain focus onto the detector plane. This configuration has been analyzed by Cook (1979); Williams (1979), and is the fifth design presented by Korsch (1980). This optical train achieves a large flat focal surface with acceptable image quality without the use of refractive correctors. As with other anastigmats, it is free from spherical aberration, coma and astigmatism. There are further practical advantages to this configuration: baffling against stray light is simpler and the focal plane is more accessible. It possesses two beam waists: one at the cassegrain focus near the primary mirror, and a second midway between the tertiary mirror and the detector plane. This second waist is small, and is an effective location for our filter wheel and CCD shutter.

In addition to the three powered mirrors of the TMA, one or more additional flat mirrors are essential to repack the optical train in such a way as to keep the detector assembly from blocking its own light, and make the payload more compact. The folding mirror(s) can be introduced in the space between the secondary and tertiary, and/or the space between the tertiary and the detector. The choice of folding mirror location and angle determines the overall dimensions of the finished payload package.

Our baseline layout is shown in Figure 11.1. The primary and secondary mirrors are located on the principal axis, as they would be for a conventional cassegrain telescope. The tertiary mirror is on this same axis, far behind the hole in the center of the primary. Immediately behind the primary, a 45 degree flat folding mirror extracts the light from the tertiary and directs it to one side, where it comes to a focus on the planar detector array. This final beam segment has a narrow waist and we have located the folding mirror at this waist to minimize its obscuration of the central part of the field. We utilize the narrow portion of the beam between the folding mirror and the detector to locate the filter wheel assembly and the CCD array shutter. Having the detector located at the cold (shaded) side of the spacecraft permits straightforward passive cooling of the entire CCD array.

Our optical arrangement also allows us to place small additional 45 degree pickoff mirrors in the cassegrain quasifocus plane to feed the precision guider, the spectrometers, and the NIR imager.

We have sized a TMA in this configuration to give a 2.0 meter entrance aperture and a 20 meter focal length, for a plate scale of 100 microns/arcsecond. We have optimized the element curvatures and conic profile shapes to yield the best possible image quality over a one degree diameter field of view. The optical element descriptions for this implementation are as follows:

Side View TMA Baseline Optic

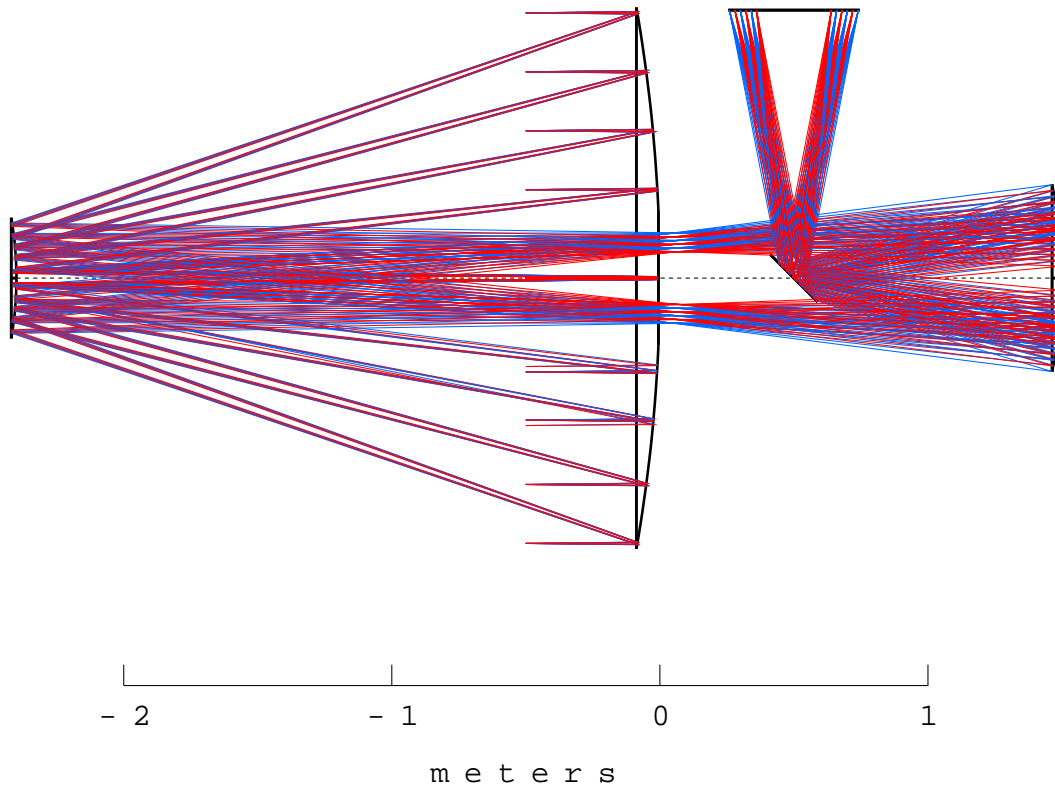


Figure 11.1: Side view of our baseline optical configuration, with a 2.0 meter primary mirror, a 0.45 meter secondary mirror, a folding flat, and a 0.7 meter tertiary mirror.

PRIMARY: concave prolate ellipsoid
 location (X,Y,Z) = (0, 0, 0);
 diameter = 2.0 meters
 curvature = -0.171580 reciprocal meters
 shape = 0.0272532

SECONDARY: convex hyperboloid
 location = (0, 0, -2.4)
 diameter = 0.45
 curvature = -0.7711666
 shape = -1.0335831

```

TERTIARY: concave prolate ellipsoid
location = (0, 0, +1.5)
diameter = 0.70
curvature = -0.6027042
shape = +0.4612502

```

```

FOLDING MIRROR (flat)
location = (0, 0, 0.5)
diameter = oval, 0.25 x 0.18
pitch angle = 45deg

```

```

DETECTOR ARRAY (flat)
location = (+1.0, 0.0, +0.5)
diameter = 0.49
pitch angle = 90deg

```

This optic delivers a root-mean-square image blur of 3 microns over a working field of view extending out to 1.0 degrees off the geometrical axis. The folding mirror selects an annular portion of this circular geometrical field for relaying on to the tertiary mirror. This annulus has an inner radius of 0.4 degrees and an outer radius of 0.7 degrees measured on the sky, and is essentially completely unvignetted. The sky area of this subset of image points amounts to 1.0 square degrees, meeting our current requirements. As with all TMA's, the central zone of the field, while having excellent mathematical image quality, is blocked by the folding arrangement needed to extract the tertiary's beam from the secondary's beam. Consequently we do not use the central part of the field for our wide-field image. This light is however accessible to other guiding and spectroscopy instruments placed behind the aperture in the folding mirror.

We have not performed a detailed tolerance analysis of this optical system, but have found that the design is robust in the sense that a small change made in one place (curvature, for example) can be compensated by a change elsewhere in the system (a spacing, for example).

11.3 Imaging Performance

A set of spot diagrams for the geometrical aberrations (excluding diffraction) is shown as Figure 11.2. This set of spot diagrams has an overall RMS deviation of $3\mu\text{m}$. Overall, 90% of the spot energy can fall within a single nominal 10×10 micron pixel when centered.

The 3 micron RMS average blur figure corresponds to 0.03 arcseconds RMS at our nominal plate scale of 100 micron/arcsecond (20 meter effective focal length). Diffraction will broaden these geometrical image point spread functions. The diffraction blur will increase linearly with wavelength, and will amount to about $12\mu\text{m}$ half-width-zero (HWZ) or 0.12 arcseconds HWZ at a wavelength of $1\mu\text{m}$.

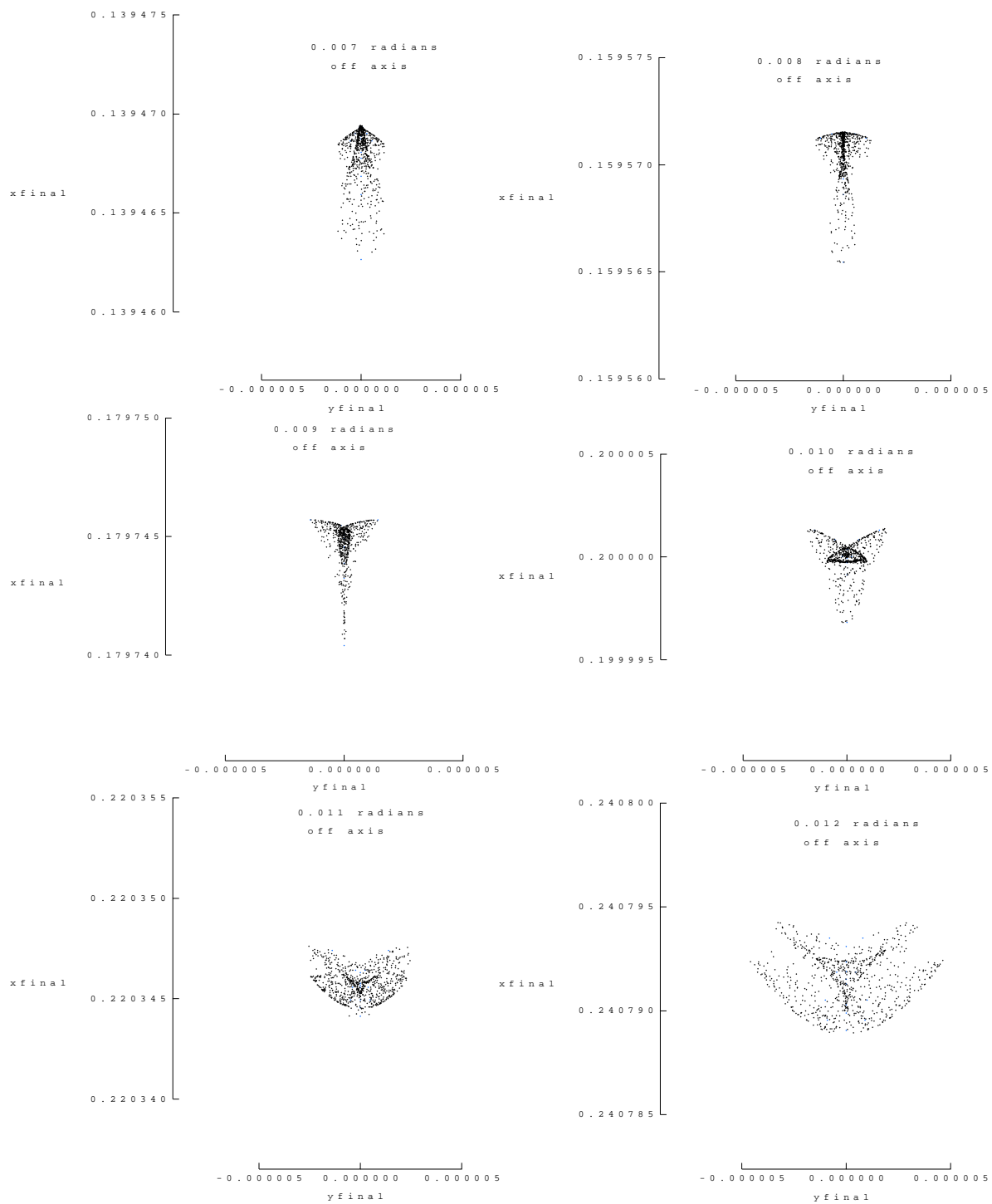


Figure 11.2: Spot diagrams taken at off axis angles ranging from 0.4 to 0.7 degrees. One tick = 0.1 arcsecond.

11.4 Active Steering Mirror

The long exposures of SNAP will require very high stability of the focal plane. This can be accomplished in two ways - both will be examined for performance, cost, and technical difficulty. First, the spacecraft attitude control system will be provided an error signal from the focal plane detectors. This can stabilize the drift of the spacecraft over long periods of time. Second, we can include in our optical path a servo control reflector to stabilize the image over potentially long exposures. An optic that can move in pitch and tilt can simultaneously allow us to stabilize our image in X and Y. For this purpose several CCDs will be located around the periphery of our principal focal plane. Each will be set up for video frame rate image analysis. Because there are ~ 100 stars/square degree at high galactic latitudes brighter than $m_V=15$, and because one star of $m_V=15$ delivers 10000 photons to a 30 ms video frame from a two meter telescope over a $1\mu\text{m}$ bandpass, the combined shot noise and readout noise in the video CCD signal will be the order of a few percent in each video frame. This SNR will give a pointing correction signal whose noise is a few percent of one pixel and will stabilize the image position to within a correspondingly small error box. The star servo concept will not unduly constrain our target field selection because there are seldom fewer than ~ 100 stars per field, any one of which can serve as the servo target.

The amplitude of the angular deviations produced by active steering have to be kept below a few arcseconds because the optimum image plane moves when the steering mirror is tilted away from perfect collimation. Deviations of a few arcseconds or less do not appear to materially degrade our image quality. It appears feasible to divide the correction signal into low frequency and high frequency portions; the high frequency part will move the active steering mirror, and the low frequency part will be passed to the spacecraft attitude control system to keep the principal optical axis stable on the sky.

11.5 Mirror Technology

Because payload launch costs scale with payload mass, it is an important mission cost minimization tradeoff to reduce payload mass to the point where total cost is least. For this reason we have explored current means for manufacturing lightweight optics and optical support structures. Traditional optical element fabrication methods use solid glass blanks that are rough ground, precision ground, and then polished to give the final optical surface profile and finish. The thickness of each element is chosen to be sufficient to guarantee the stability of the surface figure under stress levels ranging from one gravity (for figuring and metrology) to zero gravities (use on orbit).

Newer lightweight elements use innovative fabrication steps to avoid the mass of solid glass components, or to avoid the glass thickness needed to achieve long term rigidity by providing figure control with an active metrology and servo system.

1. **WEIGHT-RELIEVED BLANK:** The starting point for low mass optics is the removal from the backside of 60% to 80% of the mass of a solid glass mirror blank. This is achieved by milling the rear of the mirror blank with an abrasive tool to produce a webbed structure having nearly all the structural stiffness but a fraction of the mass

of the original solid blank. This technique was used on Hubble and other low altitude missions with good results.

This approach is regarded as low risk, but not able to achieve the mass reduction appropriate for a HEO mission.

2. HONEYCOMB SANDWICH: The starting point is a solid disk of Schott Zerodur or Corning ULE glass whose dimensions are close to the desired final dimensions of the mirror. Using abrasive water-jet machining technology, the blank is cut through with numerous hexagonal holes that leave only a thin hexagonal web of glass. Then, a thin solid face sheet and bottom sheet of glass is frit-bonded or fusion-bonded to this honeycomb core. The sandwich is then ground, figured, and polished using advanced low-stress methods such as ion beam milling. The final mirror is typically 95% mass relieved since it is mostly empty space. Its rigidity is determined by the box section stiffness of the core glass component with face sheets. This technology is regarded as proven, since it has become a standard military space-surveillance technique, but can be expensive unless the fixturing and bond-bake cycles have been thoroughly explored.

At present, for the the SNAP project with a two meter aperture, this technology appears to be our best alternative within fixed cost and schedule constraints.

3. ADJUSTABLE FIGURE: The starting point is a rigid lightweight strongback structure made of carbon fiber reinforced epoxy resin. To this structure, dozens or hundreds of electromechanical actuators are fastened. Each of these supports one point of a glass face sheet, typically only a few mm thick, whose surface is the optical mirror. The flexibility of the face sheet allows small surface corrections to be introduced, during the mission, by commands sent to each actuator. The information needed to tune the surface is obtained by image testing using bright stars as the mission progresses. Tuneups might occur monthly, or as the image quality indicates that some kind of surface figure change has occurred.

The figure control method has the cost advantage that the only massive component is the strongback, which is inexpensive to manufacture and need not be manufactured to optical precision. It need only be dimensionally and thermally stable. The servo actuators give the requisite optical surface precision. Moreover, the figure control system in one surface could possibly compensate for figure or positioning errors elsewhere in the optical train. However, for SNAP we regard figure control as more complex than necessary and for this reason do not include it in our baseline system plan. We nonetheless intend to closely follow developments in this field as progress is made.

11.6 Conclusion

During Phase A we will continue to work closely with optics engineers, optical element fabricators, and spacecraft manufacturers to ascertain the confidence with which the optical system performance can be established. This is a complex subject because many factors interact to a considerable extent. For this reason, during the Phase A design period, we shall study the trade-offs between the performance, cost, schedule, and science harvest that alternative optical designs offer the SNAP mission.

Chapter 12

Calibration

12.1 Introduction

SNAP will require excellent photometric, wavelength, and astrometric calibration in order to deliver its full scientific potential. Here the methods of obtaining this calibration are described.

12.2 Imager Photometric Calibration

12.2.1 Internal Calibration

The initial stages of photometric calibration are designed to put all pixels on an equal footing, such that measurements do not depend on where target objects are located on the CCD imager. The required steps are quite standard:

- bias subtraction
- dark current subtraction
- flat fielding.

Bias Calibration

Bias subtraction corrects for the DC offset of the on-chip amplifier and subsequent electronics of each detector. Because the full electronics chain inevitably has imperfect behavior, this offset can vary slightly from pixel to pixel. Therefore, it is standard to obtain a series of zero-length exposures — bias images — with the shutter closed. These are combined and subtracted from science images. The number of bias images required depends on the detector readout noise and the number of particle hits occurring during the readout period, but 10—20 bias images are generally sufficient. Generally the 2-D bias pattern is stable over long periods, so a bias series is probably not required more than once per day. The bias level is likely to be temperature sensitive, but the bias level can be tracked using an 'overscan' region, produced by continuing to clock each CCD through another ~ 50 pseudo-pixels after the real image has been read. This adds a negligible amount to the total readout time. Typically systematic errors in the bias

subtraction should be far below the noise level set by the zodiacal light background, and uncorrelated between supernovae.

Dark Current Calibration

The dark current generated in the CCD silicon substrate will generally show modest 2-D structure, and will depend on temperature, which may vary slightly over the SNAP orbit. In addition, radiation damage incurred over the lifetime of the SNAP mission may result in hot pixels having elevated dark current. Such hot pixels have the potential to masquerade as supernova detections, so some attention must be given to monitoring their locations and stability. For these reasons, long-exposure images with the shutter closed must be taken periodically, and used to subtract the dark current from science images. Dark current images will have noise contributions from detector readout noise, dark current Poisson noise, and particle hits. An UCB CCD has a modest dark current of $\sim .08 \text{ e}^- \text{ min}^{-1}$, and the dark current Poisson noise will equal the $\sim 2 \text{ e}^-$ readout noise after ~ 50 minutes. In this time, the number of particle hits could be considerable. Therefore, dark current images can only last 15–30 minutes, and something like 50 such images requiring up to 25 hours of total integration would be desirable to obtain good signal-to-noise ($S/N \sim 20$; for the imager, the sky background dominates over the dark current, so higher S/N is not needed). Once the temperature dependence of the dark current is established (based on dark current images taken along the SNAP orbit during the initial calibration period), dark current calibration images should require updating only every month or so. The dark current will be much lower than the zodiacal light background, so random and systematic errors due to subtraction of the dark current should be negligible, and uncorrelated between supernovae.

Flat-field Calibration

After subtraction of the bias image, and subtraction of a scaled dark current image, the value of each pixel is directly proportional to the number of photoelectrons originally detected. Since each pixel can have a slightly different sensitivity, the pixel-to-pixel sensitivity must be corrected using a flat-field image in order for the value of each pixel to reflect the correct relative brightness of the astronomical scene. The standard means of obtaining a flat-field image on the ground is to image an illuminated screen in the telescope dome, the twilight sky, or the dark night sky, the idea being to produce a bright, uniformly illuminated scene. In the case of sky flats, astronomical objects are present and must be eliminated by obtaining, e.g. a median, of many sky images obtained for different telescope pointings. The response of each pixel depends on the angle of incidence, so the flat-field light must come from (near) infinity and traverse the complete optical path. In addition, the sensitivity variations between pixels are generally slightly wavelength dependent, so the spectral energy distribution of the flat-field scene should be fairly featureless.

The lack of a projection screen — and source to illuminate it — in space (analogous to a dome flat), or any high surface brightness uniform natural sources (analogous to a

twilight flat), leads us to first investigate whether adequate signal-to-noise and object elimination can be obtained with sky flats with SNAP. Future investigation is required, but it is quite likely that the zodiacal light (sunlight reflected by interplanetary dust) near the northern and southern ecliptic poles is sufficiently uniform to serve as a flat-field source. For the typical zodiacal background near the ecliptic poles, SNAP would require about 18 hrs of exposure in a given filter to collect enough photons to produce a flat-field with Poisson errors of less than 1% per pixel. Accounting for pixels lost due to the presence of astronomical objects and particle hits in individual exposures, up to 30 hrs would realistically be required. Since 30 hrs worth of images would typically be collected in many filters every 2 weeks, flat-fielding using sky flats is a practical method for constructing flat-field images. For less frequently used filters, some extra time above that needed for science observations may be required. It will be essential to achieve excellent elimination of real astronomical sources. Our analysis of the Hubble Deep Field South (HDF-S) indicates that 1 of every 16 pixels of 0.025 arcsec on a side contains light from an astronomical source of sufficient brightness to perturb a sky flat by more than 2%. To meet a requirement that contaminating objects this bright be eliminated from all sky flats over the $\sim 10^9$ pixels of the imager and over the mission lifetime of SNAP, deep exposures at a minimum of ~ 10 different pointings would be needed. The baseline plan calls for SNAP to monitor some 20 fields, so the object rejection requirement for constructing clean sky flats can be met.

Alternatively, it may be possible to construct a reasonably good flat-field module for SNAP. Using quartz-halogen lamps placed behind a diffusing screen on the SNAP secondary mirror support might provide sufficient uniformity to correct sensitivity variations on small spatial scales. Then, smoothed sky flats (requiring much lower S/N per pixel) could be used to make corrections on large spatial scales. Although desirable, it is unlikely that a completely uniform internal flat-field module (such as the *GCAL* calibration unit constructed for the Gemini 8-m telescopes) can be constructed within reasonable cost, size, and weight constraints for such a wide-field imager. Furthermore, there is added risk associated with such a device getting stuck in the optical path.

Yet another alternative would be to use either starring or “streaked” images of Earth or the Moon to map pixel to pixel sensitivity variations. The starring approach would require numerous dithered images (a bare minimum of 60), from which both the correct illumination pattern of Earth or the Moon and the detector sensitivity pattern would have to be determined. Streak flats only provide the pixel to pixel sensitivity variations along a line parallel to the streak. Thus, sky flats or dithering in the cross-streak direction are necessary to determine the marginalized sensitivity function orthogonal to the direction of the streak, and from that, the complete 2D pattern of pixel to pixel variations. The potential advantage of these approaches is that flat-field images could be constructed quite rapidly, although it remains to be seen to what extent sharp, unresolved features (crater rims, clouds, etc.) will cause problems. For a baseline lunar assist orbit (see Section 14.1), the angular extent of the Earth as seen by the spacecraft will range between 2 and 7 degrees, more than filling the imager field of view. The angular size of the Moon as seen by the spacecraft will be much more variable, but should also overfill the imager field of view on occasion. In both cases, most viewing configurations will present only a partially illuminated Earth

or the Moon to the spacecraft, but a minimum illumination of 50% will be available periodically. As seen from Earth, the apparent optical magnitude of the Moon is -12.5. At a pixel scale of $0.1 \text{ arcsec pixel}^{-1}$ the effective brightness in each pixel would be 8.5 magnitudes, requiring the use of a neutral density filter or an aperture stop. The albedo of Earth is $5\times$ that of the Moon, so the Earth will give a brightness of 7 magnitudes per pixel. Flats from the dark Earth (due to atmospheric nightglow) or Moon (illuminated by light reflected from Earth) might also be useful since in these cases a neutral density filter or aperture stop would not be necessary. Such flats may be possible on occasion, and require special configurations of Sun, Earth, Moon, and spacecraft. Potentially severe contrast or sun-avoidance problems would have to be considered however. We note that a project to photometrically calibrate the surface of the moon as seen from Earth at a wide range of lunar phases and over a wavelength range of $0.35\text{--}2.5 \mu\text{m}$ is underway by the USGS (Anderson et al., 1999), and may prove helpful in our planning.

The above discussion makes clear that, unlike bias and dark calibration, some R&D will be required to determine optimal flat-field strategies for the SNAP wide-field imager. Since the CCD quantum efficiency is temperature dependent at the reddest wavelengths, some effort should be made to obtain flat-field images over a range of temperatures. It is worth noting that an external estimate of the quality of a flat-field can be obtained by observing a given field using many dithered pointings and then checking that the photometry of each object is independent of location. Prior to launch it will be important to construct flat-fields for each filter and over a range of operating temperatures, to which flat-fields on-orbit can be compared. The experience of WFPC2 is that the on-orbit flat-fields agree well with those obtained in the lab prior to launch (Holtzman et al., 1995). The principle differences in lab and on-orbit flat-fields for WFPC2 arise from illumination differences and the accumulation of contaminants on the dewar window between decontamination procedures.

Point Spread Function Calibration

Another component of internal calibration which is not necessary for all applications, but which is desirable for the detection and follow-up photometry of supernovae is the determination of the optics point spread function as a function of location on the imager. For detection of supernovae, reference and search images are subtracted from each other, and remaining objects are flagged as potential supernova candidates. In this process, slight differences in the point spread function between these two images can produce spurious candidates, especially around bright objects. A standard procedure is to determine the convolution kernel needed to convolve the higher resolution image to that of the lower resolution image. This convolution kernel is typically a function of location on the imager, if for no other reasons than that diffraction effects will necessarily change slightly over the imager and individual CCD's will be offset slightly from the true focal plane. It will also be a function of time since the focus, and scattering properties of the optics, are likely to drift slightly (behavior seen with HST), and it will be different for each filter. In addition, optimal photometry employs the point spread function for weighting, and to determine the "aperture correction" needed

to account for light in the extended wings of the point spread function which are too weak and contaminated by other sources to measure for each target object individually.

It is desirable to obtain the PSF from its core well out into the wings (say, to a radius with 99% encircled energy). This requires a very large dynamic range, as only the brightest stars will have adequate signal in the wings but they may be saturated in their cores. Moreover, the wings will likely be littered with contaminating objects. By using stars covering a wide range in brightness, or by employing a range of exposure times if performing special calibration observations, the point spread function can generally be determined using stars in each target field. Fig 12.1 shows the number of stars as a function of magnitude from a combination of high Galactic latitude fields observed with HST, scaled to give the number of stars which should be present on each CCD of the SNAP imager. This indicates that each SNAP CCD will have a few stars of sufficient brightness to construct a point spread function. The number of stars bright enough to have good S/N in the wings is low, so variations in the wings of the point spread function will have to be determined by collecting stars from several CCD's.

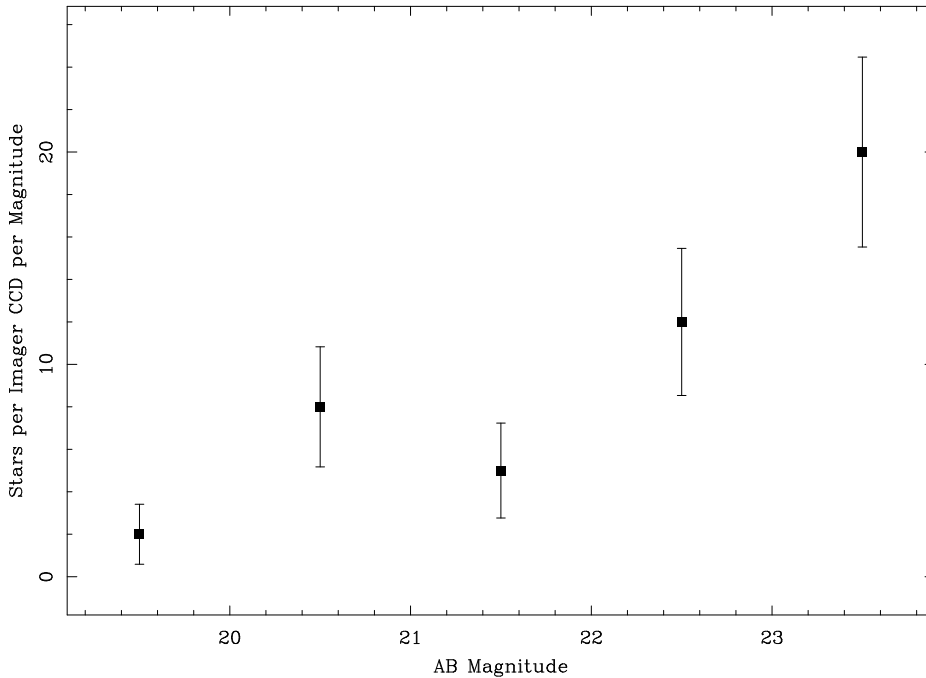


Figure 12.1: The number of stars per magnitude expected on average for each CCD on the SNAP imager. These counts were constructed by combining unresolved objects detected with WFPC2 in the HDF (Williams et al., 1996) and HDF-S, and with STIS in the HDF-S. Fainter than $m_{AB} > 24$ an increasing number of galaxies become unresolved and begin to contaminate the star counts. For typical SNAP search images, stars with $m_{AB} < 24$ will be bright enough to be used to construct the point spread function.

12.2.2 External Flux Calibration

Once the above internal calibration procedures have been applied, target objects can be photometered, giving their correct relative brightnesses in the system defined by the effective instrumental bandpass (optics+filter+CCD) of the imager. Using this information for science requires converting these relative fluxes onto an absolute system. This involves determining a zero-point, as well as a term proportional to the color of each object to allow for differences between standard and instrumental bandpasses.

The most common photometric system employed for ground-based astronomy over the wavelengths to be covered by SNAP is the Johnson $UBVRI, J(H)K$ system, based on Vega and five other bright stars of type A0. Megessier (1995) summarizes numerous subsequent recalibrations of this system and presents preferred absolute fluxes, while Bessell (1979), Bessell & Brett (1988), and Bessell (1990) provide an absolute calibration and filter definitions which include the revised, Kron-Cousins, versions of R and I more commonly in use.

An alternative system in the optical is the Gunn $uvgriz$ system, defined by Thuan & Gunn (1976), and extended by Kent (1985) and Wade et al. (1979). This system is related to the AB magnitude system of Oke (1974) and Oke & Gunn (1983) which provides a direct conversion to flux density, f_ν , with a zero-point also determined by Hayes & Latham (1975). A slightly modified version of the Gunn system is being used to carry out the Sloan Digital Sky Survey (Fukugita et al., 1996).

Systems of secondary and tertiary standards have been set up around the sky using both of these magnitude systems (Landolt, 1983, 1992; Thuan & Gunn, 1976; Kent, 1985). In addition, the number of stars having spectra defined on the Hayes & Latham (1975) system is growing. Bootstrapping from these systems, and aided by accurate model atmosphere calculations, Bohlin (1996) has developed a handful of relatively featureless hot white dwarf and solar-analog stars into spectrophotometric calibrators spanning the UV through NIR. Bohlin (1996) estimates that the absolute calibration is good to 1–2%, and that the error in the relative calibration of his system across the optical–NIR is less than 1%. He also finds that systematic differences of up to 2% exist for some of the other spectrophotometric photometric systems. This analysis is consistent with the extensive independent assessment by Megessier (1995).

The key component of flux calibration for determining cosmological parameters with SNAP is the relative calibration between restframe B and redshifted B . That is, it is important that relative calibration over the range 0.4–1.7 μm be correct to better than the brightness difference from SNAP target 1- σ changes in the cosmological parameters, i.e. $\sim 1\%$. Based on the assessment of Bohlin (1996), the current system of white dwarf and solar-analog spectrophotometric standards — comprised of only 8 stars — can just barely deliver this accuracy. Ideally the core SNAP supernova search fields should be peppered with well calibrated standards. These would serve not only to zero-point the photometry, but to provide a robust check on the accuracy of SNAP photometry. Since bright white dwarfs of the type used by Bohlin (1996) are not common, an improved set of calibration standards for SNAP would require bootstrapping from the Bohlin (1996) stars, perhaps including redoing the absolute calibration, to ensure that after all uncertainties are propagated SNAP photometry will

be flux-calibrated to better than 1%. Establishing secondary standards and redoing the absolute calibration would be a major undertaking in itself, however there is broad interest in the astronomical community in doing this so finding experts to help with such an undertaking should be possible.

12.2.3 Imager Calibration Summary

Internal calibration of SNAP should be relatively straightforward, although some further study of the quality attainable with sky flats would be prudent. The external calibration steps — flux calibration and correction for Galactic extinction — currently have some weak points, to which a wide range of cosmological studies have some sensitivity. These weaknesses are not irreducible, and improvements can be made between now and the launch of SNAP. Our current estimate of the calibration error budget for the SNAP wide-field imager is given in Table 12.1, below. The statistical error quoted refers to the expected worse-case Gaussian/Poisson degradation introduced by each calibration step. The relative systematic error quoted refers to systematic errors between the lowest and highest redshift supernovae due to relative calibration errors over the entire optical to NIR spectral range. The absolute systematic error reflects the accuracy to which the true brightness of supernovae can be determined. These absolute errors do not matter for determination of the cosmological parameters exclusively from the SNAP supernova dataset. They could apply when comparing with ground-based observations (e.g., due to the PSF error).

Calibration Step	Statistical Error	Relative Systematic Error	Absolute Systematic Error
Bias	negligible	negligible	negligible
Dark Frame	negligible	negligible	negligible
Flat-Field	< 1%	< 0.1%	< 0.1%
PSF Calibration	< 3%	< 1%	~ 2%
Flux Calibration	< 1%	~ 1%	~ 2%

Table 12.1: Imager calibration error budget.

12.3 Spectrograph Wavelength and Photometric Calibration

Like the SNAP imager, the spectrograph will require initial subtraction of a bias image and a scaled dark current image. Since the background zodiacal light is dispersed, these corrections require more attention than for the imager. In particular, the dark current from an UCB CCD or HgCdTe device will be comparable to this background level, so the quality of the dark current image will have to be several times better than needed for imaging. For both of these corrections, the precepts discussed for the imager apply, with the additional requirement that the dark current calibration image

have a total exposure time several times longer than the longest target spectrum to prevent degradation of the signal-to-noise ratio.

For flat-fielding of the spectra, the methods used are quite different than for the imager. Because the zodiacal light background will be dispersed and contains numerous stellar features since it is reflected sunlight, sky flats are not suitable for flat-fielding. Rather, the standard approach is to make use of an internal flat lamp. This is much more practical than it would be for the SNAP imager since the spectrograph field is so much smaller. The flat lamp spectrum is fit in the wavelength direction, leaving only the pixel-to-pixel variations. The result is then used to correct for pixel-to-pixel sensitivity variations of the detector. Alternatively, the lamp spectrum can be divided directly into the object spectrum, leaving the true lamp wavelength to be corrected at the flux calibration stage (as described below). A crucial aspect of this procedure is that the functional form of the lamp spectrum in the wavelength direction be well described by a function of modest order, or that it be extremely reproducible. If this is not the case, each flat lamp spectrum would have to be externally calibrated with observations of spectrophotometric standard stars.

After correction by the lamp flat, the resulting spectrum will still contain either the spectrograph response and low-resolution detector response or the (inverse) spectrum of the flat lamp, depending on which of the above flat-fielding methods is used. (Technically, wavelength calibration, described below, is applied prior to flux calibration with a spectrophotometric standard.) Correcting either of these signatures requires observations of spectrophotometric standard stars, such as those of Bohlin (1996) discussed above. This same step provides the absolute flux calibration for the target spectrum. The final accuracy of the relative flux calibration is limited by the 1–2% accuracy of extant spectrophotometric standards. This is further motivation for working to improve this situation. With the use of an integral field unit during the initial SNAP science verification phase, such standard stars should be placed at numerous locations on the IFU to confirm that the lamp flat is providing accurate correction everywhere in the IFU field.

Wavelength calibration uses internal arc lamps — a very straightforward procedure. Slight differences in the optical path of the arc calibration lamps and that of celestial objects can lead to small zero-point errors in the wavelength calibration. This is especially important for very low resolution spectra obtain, e.g., using a dispersive element option for the NIR photometer. Such a zero-point should be quite stable, and can be determined from observations of planetary nebula (having narrow emission lines) or radial velocity standard stars.

12.4 Imager Astrometric Calibration

Astrometric calibration of the wide-field SNAP imager is necessary for the purposes of aligning images prior to subtraction, locating an aperture or point-spread-function for photometry, obtaining correct surface brightnesses for galaxies, or correcting weak lensing shear maps. At a minimum, the orientation and scale of each CCD needs to be determined. Since it is likely that the scale will change slightly across each CCD,

especially near the field edges, higher order fits for the scale will likely be necessary. Lithography mask errors will also be present, as in the 34th row defect on WFPC2. Roughly speaking, there are almost 10^4 terms to solve for, for each filter. By observing a given field with many dithered pointings with offsets as large as one degree, a “plate-overlap” solution can be obtained for these various parameters. In typical SNAP images, objects with $m_{AB} < 25$ should have plenty of signal-to-noise such that centroids can be determined to 0.1 arcsecond or better. Based on HDF number counts there should be more than 10^5 such objects per SNAP field. Multiple dithered fields should easily reduce SNAP astrometric errors to less than 0.01 arcsec. The remaining question then is how often astrometric calibration needs to be obtained; this depends principally on the stability of the optics, optics supports, and CCD mounting plate, etc. Since SNAP will re-observe the same fields every few days, frequent differential adjustments to the astrometry will be possible.

12.5 Spectrograph Astrometric Calibration

In order to reconstruct a spatially and wavelength rectified data cube from spectroscopic observations with an IFU, the relative mapping onto the sky of the slitlets must be known. The exact relative physical locations of the slitlets can be determined from measurements in the lab, however, the telescope and spectrograph optics, and orientation of the detector — which can change once in orbit — will effect the mapping onto the sky. Furthermore, in order to be able to subtract final reference spectra from supernova plus host galaxy spectra obtained at maximum light, the correct relative positions of these spectra in the IFU must be known. This requires that the location of the IFU relative to the wide-field imager be well determined. Obtaining this calibration consists of taking dithered observations in both the wide-field imager and with the IFU spectrograph of a field having a very high surface density of objects, such as the outskirts of a global cluster. The dithering must be large enough so that over the course of the calibration observations the same objects are detected both with the spectrograph and the imager, but needn’t cover nearly the area required for astrometric calibration of the imager. Such calibration should be straightforward.

12.6 NIR Imager Calibration

The HgCdTe detectors to be used for the NIR imager have electronics for each pixel capable of performing non-destructive reads during the course of an exposure. The electronics still have a bias voltage level, as well as dark current and pixel-to-pixel sensitivity variations. These can be addressed in much the same way as for the CCD imager. Because the field of the NIR imager is small, flat-fielding using an internal lamp should be possible. External verification will come from deep sky exposures, and possibly Earth or Moon flats.

Each field observed with the NIR imager will be comparable in size to that of a single CCD on the CCD imager. Therefore, astrometric and point spread function calibration can be accomplished using basically the same methods used for the CCD

imager.

12.7 Extinction from Foreground Dust in the Galaxy

The final step before the absolute photometry can be used to address cosmological questions is to correct for extinction by dust in our own Galaxy. The amount of dust can be estimated by its emission in the far-infrared, as measured by IRAS and COBE (Schlegel, Finkbeiner, & Davis, 1998) (shown in Fig 12.2 and Fig 12.3), or by measuring the column of HI and assuming a constant ratio of dust to gas (Burstein & Heiles, 1982). Using these data as guides, SNAP fields can be chosen which have low amounts of extinction. It is worth pointing out that since discovering lower redshift supernovae ($z < 0.1$) will require searching even larger regions of sky, there is the potential for errors in the dust extinction maps or in the extinction law (relating the extinction at each wavelength to the total column of dust) to cause systematic differences at the level of a few percent. For this reason it will be important to select supernovae of all redshifts over the same regions on the sky. Naturally, any improvements in the dust extinction maps and in verifying the extinction law will be of great benefit. In particular, there is an uncertainty of up to 6% in the minimum B-band dust extinction near the Galactic poles (Schlegel, Finkbeiner, & Davis, 1998). Since a given column of dust absorbs blue light more strongly than red light, such an error will translate into errors in the relative brightnesses of lowest and highest redshift supernovae. SNAP will automatically collect multi-wavelength observations of thousands faint Galactic stars in each field, many of which will lie in the halo of the Galaxy and thus presumably above the dust layer. Of these, ~ 100 should be very hot, featureless subdwarfs whose intrinsic spectra can be calculated fairly well. The calculated spectra can be compared to the observed multi-color photometry allowing the amount of reddening to be determined. Application of a standard dust extinction law gives the total extinction from the reddening (relative) extinction. These, and similar measurements using halo stars (Szomoru & Guhathakurta, 1999; Gilmore, Reid, & Hewett, 1985) should allow an improved determination of Galactic extinction in the SNAP fields. Internal comparison of the extremely deep galaxy counts that will be available across the SNAP survey region will provide a means of obtaining the correct relative Galactic extinction in each color, without having to assume a dust extinction law, using magnitude offsets for the counts in different fields. Ideal SNAP survey regions, having low Galactic extinction and which also have low zodiacal background and are free of very bright stars, are given in Table 12.7.

Field Name	Right Ascension	Declination	Ecliptic Latitude	Galactic Latitude	Blue Extinction
SNAP-North	$16^h 25^m$	$+57^\circ$	$+74^\circ$	$+41^\circ$	~ 0.035
SNAP-South	$04^h 30^m$	-52°	-70°	-42°	~ 0.047

Table 12.2: Survey regions with low zodiacal background.

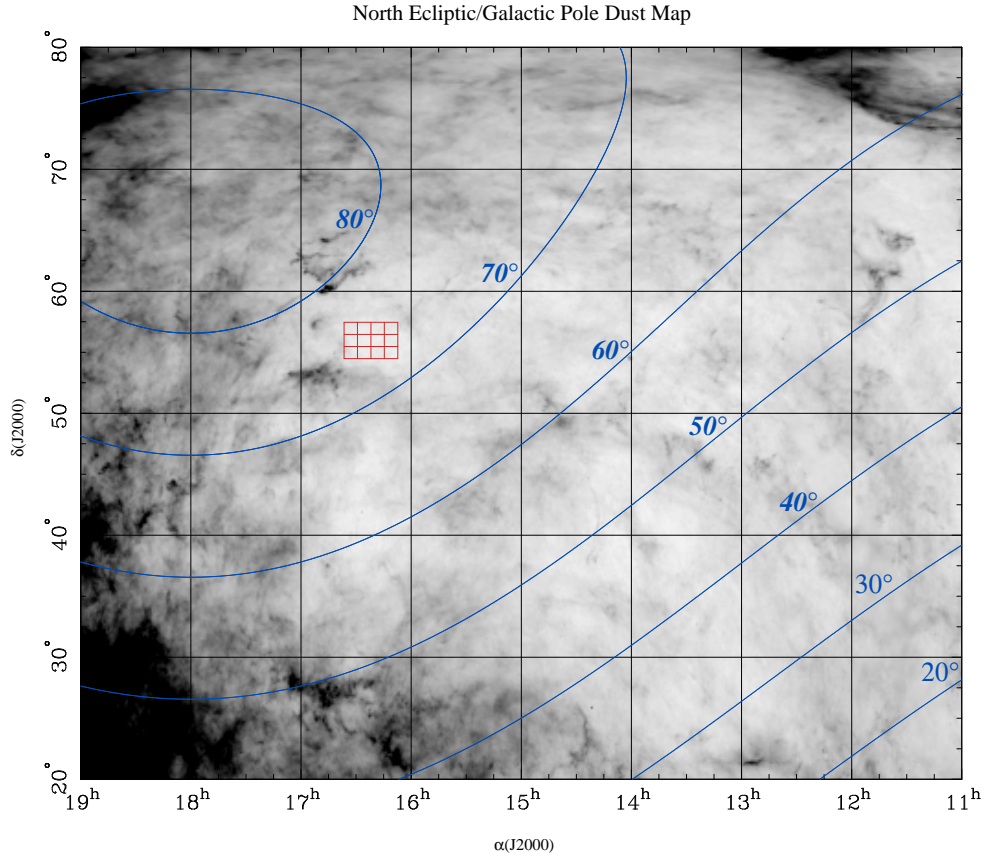


Figure 12.2: Map of the Galactic dust towards the north ecliptic pole and north Galactic pole, from Schlegel, Finkbeiner, & Davis (1998). The greyscale ranges from a B -band extinction of 0.0 (white) to 0.4 (black) magnitudes. The rectilinear coordinate grid is equinox J2000 celestial coordinates. Also shown are lines of constant ecliptic latitude. SNAP fields should be located in regions of low Galactic dust extinction, and at high ecliptic latitude where the zodiacal light background is the lowest, an area such as the one marked off by the grid.

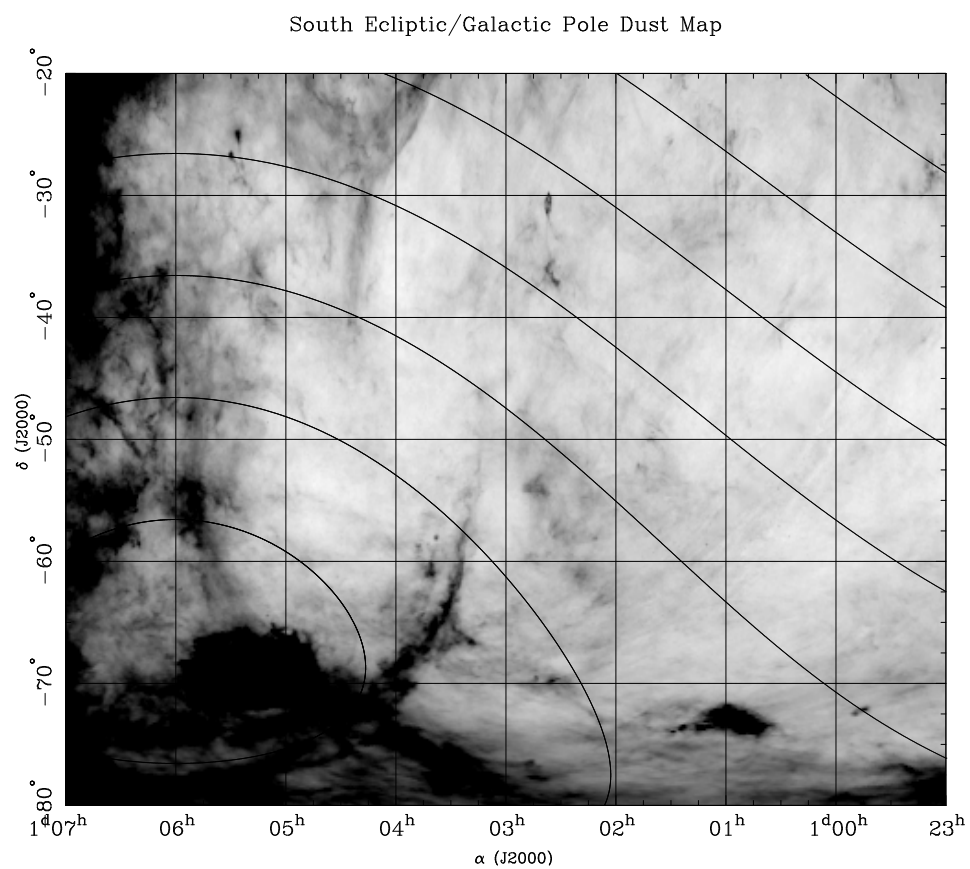


Figure 12.3: Same as Fig. 12.2 for the south ecliptic pole and south Galactic pole.

12.8 Photometric Redshift Calibration

For the SNAP mission there will be a great advantage to knowing in advance the approximate redshifts of newly discovered SNe. With an approximate redshift, an initial guess can be made as to the type (Ia, or other) of a SN, allowing the appropriate follow-up prescription to be executed. This will be especially important for faintest (high redshift) targets, especially since SNAP will have time to observe only a fraction of these.

If a SN candidate can be associated with a host galaxy — which should be true more than 90% of the time — knowledge of the host galaxy redshift provides a good estimate of the SN redshift. The advantage here is that host galaxy redshifts can be measured in advance of any SN explosion. The difficulty is that all galaxies must have redshift determinations since we cannot predict which galaxies will host a SN during the lifetime of SNAP.

Obtaining spectroscopic redshifts for all (10^6) galaxies is clearly out of the question. However, given that galaxies typically have spectra with a few strong features (most notably the “4000 Å break” in the continuum), redshifts can be estimated from broadband photometry. This technique is known as a “photometric redshift”. The accuracy of this technique depends on the number and widths of the filters. In order to cover a large range in redshift, the wavelength coverage of the filter set must also be large.

Photometric redshifts have been determined from UBVRI photometry of galaxies in the Hubble Deep field [HDF; Williams et al. (1996)]. Hogg et al. (1998) present a blind comparison of Keck spectroscopic redshifts with HDF photometric redshifts presented by several groups. In this relatively small sample they find $\sigma_z \sim 0.1$. It is important to note that their sample includes very few galaxies with $z > 1$. This is because LRIS on Keck II has trouble securing redshifts for such distant galaxies due to a lack of prominent galaxy spectral features below the OII 3727Å emission line, coupled with night-sky lines, fringing, and poor response in the red. In principle, with an UCB CCD these Keck redshift surveys should be easily extended, and thus provide training data to at least $z \sim 0.95 \mu\text{m}/0.3727 \mu\text{m} - 1 \sim 1.55$.

Since SNAP will have ~ 11 filters for the wide-field CCD array, it should be able to determine photometric redshifts with a standard deviation of 0.1 out to $z \sim 1.3$. Beyond $z \sim 1.3$ the signal from the 4000Å break will fade away, and by $z \sim 1.5$ it will be redshifted off of the CCD response altogether. This leaves the follow-up program vulnerable to faint SNe with hosts in the range $1.3 < z < 2.2$. Note however that by these redshifts there is a non-negligible distortion of the galaxy continuum due to absorption by Lyman-alpha forest metal lines which can help set redshift limits (this will need to be quantified). The next feature of note is the continuum break blueward of Lyman-alpha, which will enter the B-band at $z \sim 2.3$. Note that CCD response down to 2800Å would be required to enable the Lyman-alpha break to predict redshifts as low as $z \sim 1.3$, which is infeasible.

An alternative approach would be to determine photometric redshifts from the SNe themselves. This approach is mostly unexplored at this time. The expectation would be that various Fe II lines in the restframe UV may present a noticeable photometric

signature. Other techniques might include constraints from early photometry since the SNe will brighten $2\text{--}3\times$ more slowly than in the restframe. Again, further study of this question is needed.

In order to have the photometric redshift estimation in place at the start of the SNAP mission, redshifts of several hundred galaxies in the SNAP fields out to redshift $z \sim 2$ will be needed. These can be obtained using multi-object spectrographs on large ground-based telescopes (e.g., DEIMOS on Keck).

Chapter 13

Electronics

An array of approximately 150 CCD's of 2.5k x 2.5k 10.5 μm pixels will be installed in the focal plane of the SNAP telescope. Single exposure times from 100 to 1000 seconds in the wavelength range of 350-1000 nm are foreseen.

The array of back-illuminated CCDs is read and digitized by low noise electronics in a range from a few to 50,000 electrons at the order of one hundred kHz. The required dynamic range is 16-bit for the electronics and has to be tolerant of 10 krad, under a wide range of temperatures. The current thinking is that the satellite will be able to transmit all images obtained given the availability of high performance Traveling Wave Tube Amplifiers.

The proposed readout architecture comprises:

- Clock Driving for the CCDs,
- Amplification and Correlated Double Sampling (CDS) providing the kT/C on-CCD reset transistor noise reduction.
- Gain selectable amplifiers,
- Analog to Digital conversion,
- Readout control of the analog electronics.
- Compression digital storage.

13.1 CCD Clocking

The CCD capacitance is of the order of 20 nF for the pixel (horizontal) clock lines, and 85 pF for the register (vertical) clock line. A voltage level of 12 V is needed, with a slope depending on the readout speed. Current sources switched to a capacitor can generate the waveform, they have to be heavily buffered to drive the capacitive loads. Corresponding power for CCDs and the clock drivers is of the order of 14 W during a 100 kHz readout. The power for the CCD output stage is 50 mW per channel, 4 channels per CCD. Assuming a duty cycle of 50% for the clock driver chip, the total power for CCDs and clock driver chip are 27 W and 14 W respectively. The CCD and

clock drivers only consume power during image transfer. This power scales with the readout frequency. The clock driver can be integrated using a radiation hard process able to hold 15 V voltages, and deliver large currents. (Dentan et al., 1998, Toronto; Ardelean et al., 1996).

Correlated Double Sampler for CCD Readout

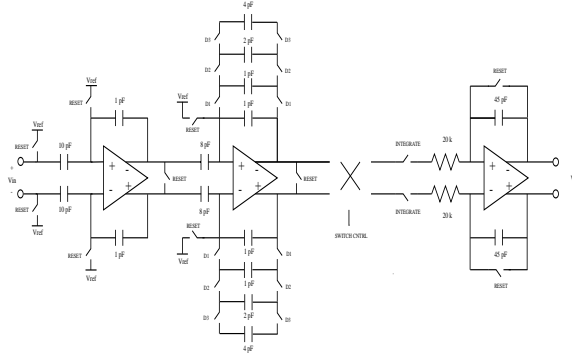


Figure 13.1: Correlated double sampling chain block-diagram.

13.2 Double Correlated Sampling

The present CCD sensitivity is $6 \mu\text{V}$ per electron. In order to reject the low-frequency reset noise, the CCD output is sensed two times, during a clock phase where it is clamped to a voltage reference through a MOS transistor switched on, and when the signal is also present. The Correlated Double Sampler integrates and subtracts the two voltages, resulting in a voltage corresponding to the actual CCD pixel signal. Depending on the sensitivity required by the objects to be observed, a gain of 1, 2, 4, or 8 is selected. This function can be integrated in the same radiation-hard CMOS chip operated with a 5V power supply. The leads to an input referred noise of $3 \text{ nV}/\sqrt{\text{Hz}}$ corresponding to a noise of 1 electron with the actual CCD output sensitivity. This device has been simulated using the DMILL process. The noise/speed performance requires a total power of 50 mW/channel. This function is to be de-powered after CCD have been read, the actual signal levels digitized, and data stored in memory. A block diagram of the correlated double sampler is shown in Figure 13.1.

13.3 Analog to Digital Conversion.

Analog to digital converters that have 16-bit precision and have been measure to survive 10 kRad is limited to the 330k Hz LTC1604 currently on HESSI. Higher speed, or more radiation tolerant devices are currently under investigation as are much lower power 100kHz devices.

13.4 Digital Processing

The huge amount of required data storage dictates the use of dynamic RAM. Synchronous Dynamic RAM (SDRAM) integrated in 3D technology conditioned for space operation are manufactured (e.g. Lockheed-Martin) as solid state recorders and housed in units of 27 GByte (error correction code included) of 80 lb weight, dissipating 110 W for simultaneous Read and Write access, 75 W for Read or Write operations, and 40 W for Data Retention. We assume that twice this memory will be available in the same packaging for SNAP.

13.5 Power

A summary is given in Table 13.1 for CCD readout at 100 kHz. Average power is 60 W, peak power 200 W.

Subsystem	Power peak (W)	Power average	Rad hard
CCD	30	5	yes
CDS Chip	30	5	possible
Clock Drivers	30	10	possible
ADC	5	0	?
Memory	75	40	yes
Total	200	60	

Table 13.1: Power consumption of CCD readout chain.

Chapter 14

Spacecraft Description

14.1 Orbit Properties

The choice of orbit is governed by the effect of the orbit on five aspects of the mission design: 1) The requirement to operate the detectors at 150° K (suggests a high orbit to reduce heat load from the earth and allow the use of a passive radiator system for detector thermal control), 2) The requirement to view in the direction of the ecliptic poles over the entire year without interference from light from the earth, 3) The requirement to maximize viewing time and link margin for the receiving antenna(s) used to downlink science data from the observatory, 4) The requirement to survive the effects of trapped radiation and cosmic rays in the orbit which may degrade performance of the detector systems, and 5) The requirements on the launch vehicle necessary to attain the orbit. A preliminary trade study has examined six potential orbits and a figure of merit has been assigned to each based on how well it meets the requirements imposed in the five categories above. Since the choice of orbit affects the design, weight, power and cost of virtually every spacecraft subsystem, the determination of the optimum strategy is an involved and iterative process which will be re-visited in detail during the forthcoming mission study phase. The result of the present trade study is shown in Table 14.1.

Orbit	Radiation	Thermal	Telemetry	Launch	Stray Light	SCORE
LEO/Polar	High at Poles	Mechanical	High BW	Excellent	Earth Shine	2.9
LEO/28.5	Lowest Dose	Mechanical	High BW	Excellent	Earth Shine	2.9
LEO/Equatorial	Lowest Dose	Mechanical	High BW	Fair	Earth Shine	2.5
HEO/GEO	Poor	Passive	24 hr	Fair	Dark	3.2
HEO/Lunar assist	Very Good	Passive	Low BW	Fair	Dark	3.4
HEO/L2	Very Good	Passive	Low BW	Fair	Dark	3.4

Table 14.1: Orbit trade study matrix.

For the purpose of the present proposal, we will present a solution based on the lunar assist orbit which was one of the high scorers in the trade study and which we believe will meet all mission requirements. Figure 14.1 shows the proposed lunar assist orbit. As is seen from the figure, the strategy involves selection of an orbit which devotes virtually all of the launch vehicle energy to achieving a very high apogee. The

position of the apogee is carefully chosen to interact with the moon in such a way as to bring the perigee up to approximately 122,000 Km on the first apogee pass. Propulsion on the spacecraft is then used to supply a velocity change of 35 meters/second to reduce the apogee to approximately 300,000 Km. The final step is necessary to achieve a final orbit which does not have instability due to interaction with the moon.

Advantages of this orbit are: 1) Since the spacecraft is always far from the earth, the effect of earth albedo on the detector thermal control system, and in causing thermal changes to structural components which would compromise performance of the attitude control system (ACS) is small. 2) The orbit can be designed to go for long periods with out eclipse. This simplifies thermal control, power management, and most importantly, reduces thermally induced disturbances to the ACS. 3) By adjusting the inclination, the orbit can be configured so that the spacecraft is visible from the Berkeley Satellite Ground Station antenna for a substantial fraction of the orbit, while limiting the maximum time between contacts. 4) The orbit is entirely outside the radiation belts.

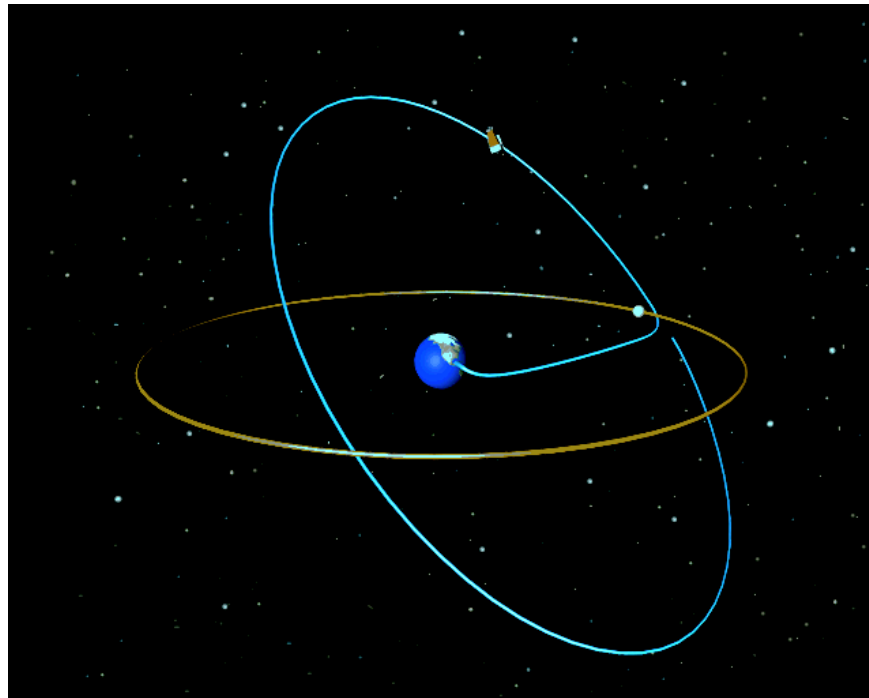


Figure 14.1: Lunar-assisted orbit.

14.2 Spacecraft Description

It is the intent of the SNAP Team to partner with an industrial aerospace firm who would be responsible for providing the spacecraft portion of the SNAP observatory. The option is also being considered to ask this partner or one or more other firms to assist in the design and procurement of portions of the payload. A Letter of Interest/Opportunity for Partnership was sent to a number of companies, five of whom responded with an indication of interest in the project. Discussions were held with these companies and an evaluation made by the SNAP Team determined that two of the firms would likely make a suitable partner. An additional conclusion reached as a result of discussions with the potential teaming partners is that design of the spacecraft for this mission is relatively straight forward, and that the most cost effective approach is to address spacecraft issues in detail following a more precise definition of the payload design and requirements. For this reason during the first part of Phase I of the program we will concentrate on refining the payload design. When the payload has reached a state of maturity which allows the efficient working out of the details of the spacecraft, a teaming partner will be brought on board. Since the final spacecraft design will depend on the particular teaming partner chosen, for this proposal we will present a preliminary design developed by the University of California Space Sciences Laboratory which we believe will meet all mission requirements, and which is consistent with the experience and capabilities of the potential teaming partners. Figure 14.2 is a block diagram of the entire observatory which shows the relationship between the science payload and the various spacecraft sub-systems. The intent in the design is to break the system into a number of sub-systems with well defined requirements and very simple and well defined interfaces. The choice of provider for each block will be made on the basis of the strengths of the teaming partners. The spacecraft portion of the system is comprised of four major functional blocks which are described in the sections below. While for simplicity of presentation a basically single string design is shown, it is recognized that the best interests of the SNAP Program may be served by using redundant designs in a number of areas. During Phase I this question will be examined in detail. A cost-benefit study will be done evaluating the addition of redundancy and cross strapping in the following areas: 1) Communications System 2) Power System 3) ACS System 4) Propulsion System 5) Data Handling System 6) Science Processor System

14.2.1 Power system

The Power System includes 2 solar arrays, each of which has 11 strings of 37 each 2.2 cm square GaAs solar cells. The cells are mounted to array panels and equipped with 1 mm cover glasses for radiation protection. Each array has an overall size of approximately 1 square meter, and when aligned with the sun will produce 209 watts at the beginning of the mission and 170 watts at the end of the mission. OR'ing diodes for each string and power control shunts are mounted on the rear of the panel. The arrays are mounted on panels which swing out from the spacecraft and lock into position with both arrays in the same plane perpendicular to the telescope bore sight.

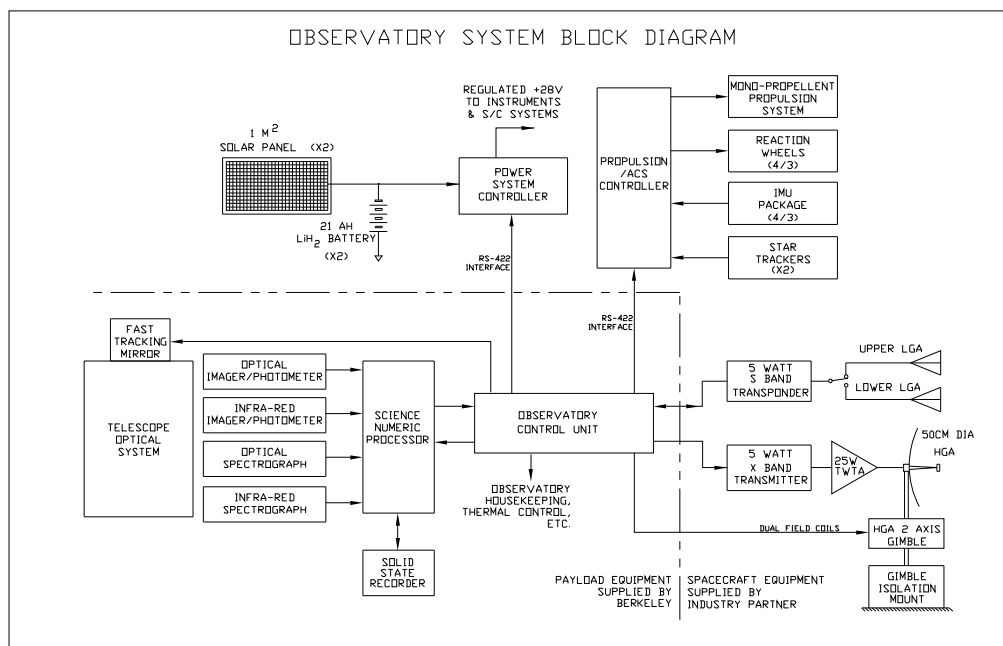


Figure 14.2: Block diagram of the relationship between the science payload and the spacecraft subsystems.

Careful attention is paid to the design of the array support and locking system to keep the frequency of the first vibration mode sufficiently high to avoid degrading the performance of the attitude control system. Since the science targets are generally in the direction of the ecliptic poles, the arrays can be maintained in an orientation approximately normal to the sun direction by controlling the roll of the spacecraft about the telescope bore sight axis. The control of roll angle will also have the effect of keeping the CCD thermal control radiator panels always pointed away from the sun, and by keeping a constant sun direction with respect to the spacecraft will minimize thermally induced distortion of the telescope and structure. The Power System is a direct energy transfer type, with each array connected to one of a pair of 21 AH LiH₂ batteries. The partially redundant system will allow reduced operation of the observatory even in the event of failure of one of the arrays or batteries. A dedicated controller in the power system performs maintenance of the batteries state of charge, provides regulated 28 volt DC power to the other observatory systems, and collects housekeeping and status information on the power system. A single RS-422 interface between the Power System Controller and the Observatory Control Unit (OCU) serves to transfer control information to the Power System, and power system engineering data back to the Observatory Control Unit.

14.2.2 ACS/Propulsion System

The ACS/Propulsion System consists of a pair of star trackers, an Inertial Measurement Unit (IMU), a set of reaction wheels, and a control unit which is used to determine and maintain the attitude of the spacecraft. The ACS control unit also manages a mono-propellant hydrazine system which is used to provide the 35-120 meters/second velocity change needed to circularize the lunar assist orbit, and to provide the angular momentum to unload the reaction wheels. For the preliminary spacecraft design, the ACS components shown in Table 14.2 are suggested.

<i>Description</i>	<i>Mfr & P/N</i>	<i>Mass</i>
Roll Axis Star Tracker	Ball CT 602	6.0 kg
Cross Axis Star Tracker	Ball CT 602	6.0 kg
Reaction Wheel Package	L3 Communications RWA 15 (20 nmsec)	
	with micro balance	
	(Formerly Allied Signal)	
IMU Package	L3 Communications RGA-20	
Controller	TBD	

Table 14.2: Attitude control system components.

The controller uses information from the star trackers and the reaction wheels to generate control signals to the reaction wheels to bring the spacecraft to a specified pointing direction. Experience on previously flown spacecraft indicates that a system based on the components listed in Table 14.2 can achieve a pointing accuracy of approximately 2 arc-seconds on a spacecraft with a suitably rigid structure. This "coarse" pointing supplied by the spacecraft system is augmented by the payload fast tracking

mirror system described in § 11.2 above to achieve the required .03 arc-second observatory system pointing accuracy. An alternative ASC strategy which will be evaluated during Phase I is once pointing to 2 arc seconds has been achieved using the ASC star trackers, the payload would transmit data a tracking star viewed through the main telescope. At the expense of a complication of the interface between the spacecraft and the payload and the testing strategy, this would allow the ASC pointing to be greatly improved with a corresponding relaxation of the requirements or possibly the elimination of the fast tracking mirror system. A careful cost/risk-benefit analysis of this option will be performed.

The mono-propellant propulsion system includes a 5 pound engine which is used to provide the orbit velocity change and a redundant set of six 0.2 pound engines used for reaction wheel management, along with fuel tanks with a total capacity of 49.2 kg of hydrazine and necessary valves and plumbing. The Table 14.3 lists the components with their mass.

<i>Quantity</i>	<i>Description</i>	<i>Mfr & P/N</i>	<i>Mass</i>
1	5.0 lbf Main Engine	Primex MR-50M	.68 kg
12	0.2 lbf Attitude Engine	Primex MR-1003g	12 X .22 kg
3	Latch Valve	Moog 51-204	3 X .36 kg
2	Fill/Drain Valve	Moog 50-837	2 X .02 kg
3	Filter	Wintec 1524-772	3 X .18 kg
2	Pressure X-ducer	Paine 213-76-570-01	2 X .20 kg
4	Bladder Tank	PSI 80266-1	4 X 2.20 kg
A/R	Plumbing		1.0 kg
		TOTAL	13.18 kg

Table 14.3: Propulsion system components.

Approximately 40 minutes of operation of the main engine are required to provide a velocity change of 35 m/sec on a 1550 kg spacecraft. This will consume approximately 25 kg of fuel, leaving 24 kg for orbit injection, reaction wheel management, and margin. The system could be easily modified by the inclusion of additional propellant tanks to provide greater margin, to handle a heavier spacecraft, or larger velocity changes.

Control of the engine catalyst bed heaters, the tank heaters, and the propellant latch valves, as well as the valves on the individual engines is also done by the same controller as performs the attitude control. When the reaction wheels become saturated the attitude control engines are operated by the controller to unload them. The interface between the Propulsion/ACS and the rest of the observatory is a single RS-422 line in each direction between the Propulsion/ACS Controller and the OCU.

14.2.3 Telecommunications System

The Telecommunications System is comprised of two parts. An S-band transponder switched between a pair of mechanically fixed low gain antennas (LGA's) is used for transmission of commands from the ground system to the spacecraft and for low rate

engineering data from the spacecraft to the ground. Science data are transmitted to the ground via a 5 watt X band transmitter driving a 25 watt Traveling Wave Tube Amplifier (TWTA) which is connected to a 50 cm diameter steered high gain antenna (HGA). The high gain antenna is mounted to a 2-axis gimbal tied to the spacecraft structure through an isolation mount which is designed to decouple the vibration modes of the antenna from the spacecraft structure to reduce the demand on the ASC system. Analysis by the UCB/Space Sciences Telemetry Group shows that at a range of 300,000 km, a data rate of 50 megabits per second with a link margin of +3.3 dB can be supported with a 50 cm diameter antenna on the spacecraft transmitting to the UCB/Space Sciences 11 meter dish. Assuming a gain of 1.5 dB for the LGA's, an S band downlink rate of 7 Kb/sec will be supported, and using the 100 watt transmitter in the Space Sciences ground station, an uplink rate of 150 Kb/sec will be possible. While the telecommunications system presented here is single string, it may be desirable to introduce redundancy in the transmitters and/or receiver. This issue will be investigated during the study phase.

14.2.4 Observatory Control Unit

The remaining major spacecraft system block is the Observatory Control Unit (OCU). The OCU serves as the central interface between the other major subsystems and is the interface to the science payload. Functions of the OCU include the receipt and processing of ground commands, the control of the Propulsion/ACS system, the management of ranging operations, and control of the power system. The most computation intensive task of the OCU is management of the science payload systems, and the management and control of the data flow between the science payload and the telemetry downlink. The OCU hardware consists of a RAD6000 processor system coupled to a hardware data processing and interface system based on radiation hardened Actel FPGA's which is used to manage the high speed data flow between the science payload and the X band transmitter. This system architecture is patterned after that used with great success on the FAST spacecraft. The OCU will also collect both spacecraft and payload engineering data and will perform thermal control of the spacecraft and the payload systems.

14.2.5 Spacecraft Structure

The spacecraft structure consists of a disk shaped section approximately 150 cm in diameter and 70 cm thick which makes connection between the science payload and the launch vehicle. The deployable solar array panels are attached to and are considered a part of the structure, as is the HGA isolation mount. The LGA's are attached to the structure, and all Power System, Radio System, and Propulsion/ACS System components are mounted inside it with the exception of a portion of the attitude control engines which are mounted higher on the science payload, and the ASC Startrackers and the IMU Package which are mounted on the reverse side of the Payload optical bench. Mathematical modeling and analysis of the spacecraft structure and the payload will be done as a single unit by the industrial teaming partner, and the results of the

analysis used to refine the designs of all observatory systems, including the ACS, the payload, the solar arrays, and the spacecraft and payload structure.

14.3 Launch Vehicle

While it is expected that the final choice of launch vehicle for the SNAP mission will be made by NASA code L, the Berkeley team has identified a number of candidate launchers. The Boeing Delta IV-M easily meets all SNAP requirements. Figure 2-11 from the Delta III Payload Planners Guide which is reproduced below shows that the Delta III can supply sufficient energy to place a 2850 kg in the initial orbit, well in excess of the current estimated mass of 1550 kg for the SNAP. The Delta IV-M has an even higher lift capacity of 2950 kg. Excess lift capability would be used to relax the mass constraints on the mission and greatly reduce payload development risk and cost.

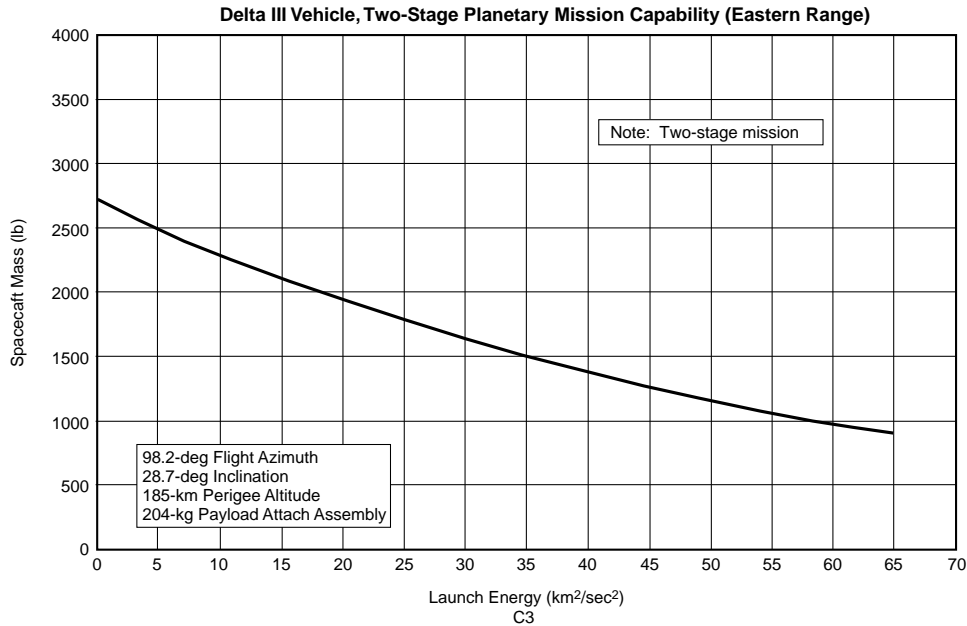


Figure 14.3: Planetary mission capability of the Delta III rocket. The Delta IV-M rocket has a slightly higher lift capacity. A lunar assist orbit requires a $C3 = -2.0 \text{ km}^2/\text{s}^2$ (slightly negative due to the gravity of the moon).

The Delta IV-M will be operated with a single second stage burn to go directly to the lunar intercept orbit. According to Boeing, the orbit injection accuracy for the Delta IV-M is ± 0.03 degrees in both angles, and ± 3 meters/second in velocity. The Propulsion/ASC system on the SNAP spacecraft will be used to perform two mid-course correction maneuvers to achieve the necessary accuracy for the lunar assist

swing-by and will be used again on the first perigee pass to supply the 35 meters/second velocity change needed to lower the apogee to prevent interaction with the moon on subsequent orbits. The Figure 14.4 shows dimensions of the Delta IV-M fairing.

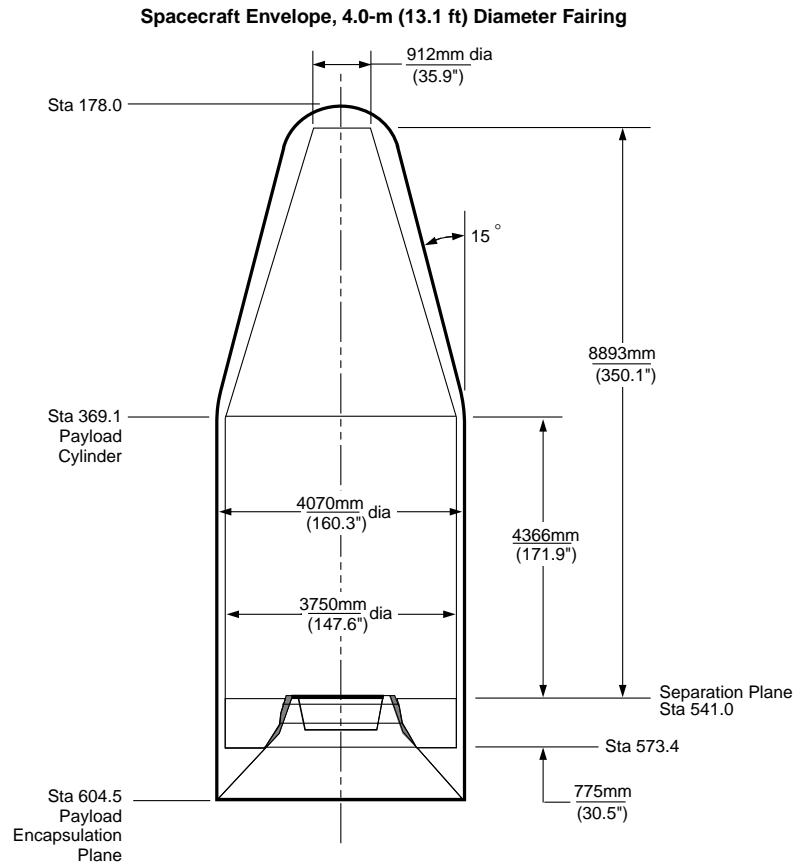


Figure 14.4: The 4.0m diameter composite spacecraft fairing for the Delta IV-M launch vehicle.

14.4 Observatory Integration and Testing

Integration and Test of the SNAP systems is a large and complex task which dictates the need for a carefully developed plan to insure the delivery of a properly functioning observatory with the minimum cost and schedule risk to the program. A detailed I&T plan will be developed during the study phase which utilizes the particular strengths, capabilities, facilities, and experience of the collaboration team, the aerospace partner, and the other sub-contractors involved in development of the observatory components. While the details of this plan will be developed only after a period of careful study and will depend on the particular industry partners(s) chosen, the overall outline is

expected to be as follows: A detailed mechanical mathematical model will be developed early in the program and used to specify limit loads for the various subsystems. Vibration and thermal vacuum testing will be done at the component level by the unit developers. Testing of the optics elements as well as the completed telescope will be done by the optics sub-contractor. Functional testing and operational simulation of the spacecraft components will be done by the spacecraft contractor. A mechanical engineering model of the payload assembly will be provided to the spacecraft contractor to do antenna tests, testing of the ACS, and verification of the structure, including vibration and thermal vacuum testing of the spacecraft components. Mechanical and electrical integration of the payload will be done in the UCB/Space Sciences Laboratory high bay facility. Final mating of the observatory components and the associated electrical testing including end-to-end RF testing, vibration, thermal vacuum, and a final end-to-end optical test will be done in an appropriate facility.

Chapter 15

Mission Operations

15.1 Mission Operations

SNAP mission operations consist of periods of autonomous operation of the observatory coincident with rapid ground analysis of the data collected to determine optimum targets for further observation. Missions operations will be controlled and performed from the SNAP Mission Operations Center (MOC) located at the UCB/Space Sciences Laboratory and at the Science Operations Center (SOC) located at the Lawrence Berkeley Laboratory. Figure 15.1 shows the close coupling existing between the MOC and the SOC which will enable the identification of supernova and redirection of the satellite in a timely manner.

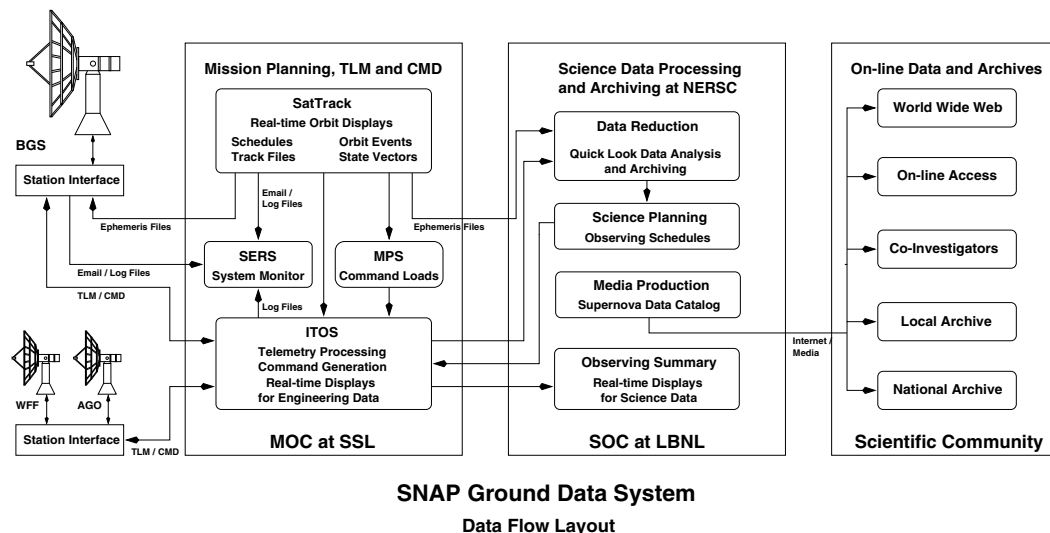


Figure 15.1: Ground system showing the flow of data and the close coupling between the missions operations center and the science operations centers. Data flow from the satellite to the mission operations center, then to the science operations center where new supernova are identified. Commands are then sent to the satellite from the Mission Operations Center to make detailed studies of the newly identified supernova.

Routine operations will be done on a four day period with a command load of approximately 1 megabyte sent up to configure the instruments. Science data will be collected, compressed, and stored in the Solid State Recorder. In parallel with this activity, scientific review and automated ground software will evaluate the transmitted data and build the target lists and instrument configuration loads for the next four day cycle.

15.2 SNAP Operations

Figures 15.2 & 15.3 show the portion of the time that the SNAP spacecraft will be visible from the BGS. Of the approximately 14 hours a day that the spacecraft is visible, it is estimated that about 5 hours a day will be required at a data rate of 50 megabits/sec to download the up to 1 terabit of science data per day. This will allow all mission scenarios including those with no on-board science data compression to be accommodated. Additional bandwidth can be added if needed by adding time on additional ground stations.

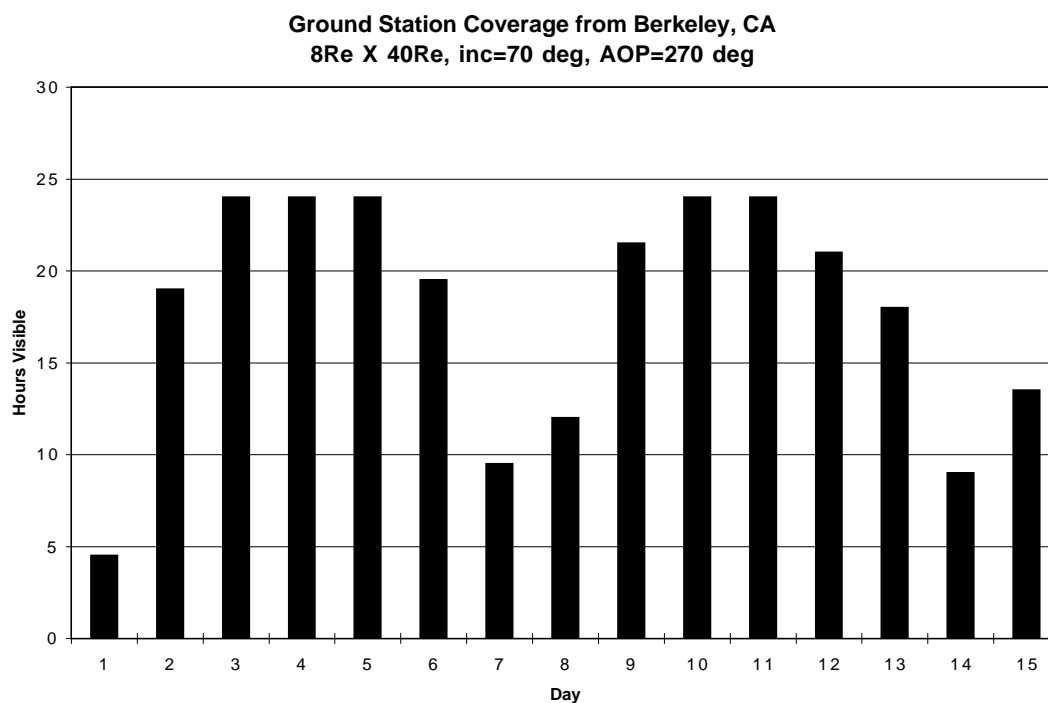


Figure 15.2: Daily coverage from from the UCB/SSL ground station for the lunar assist orbit.

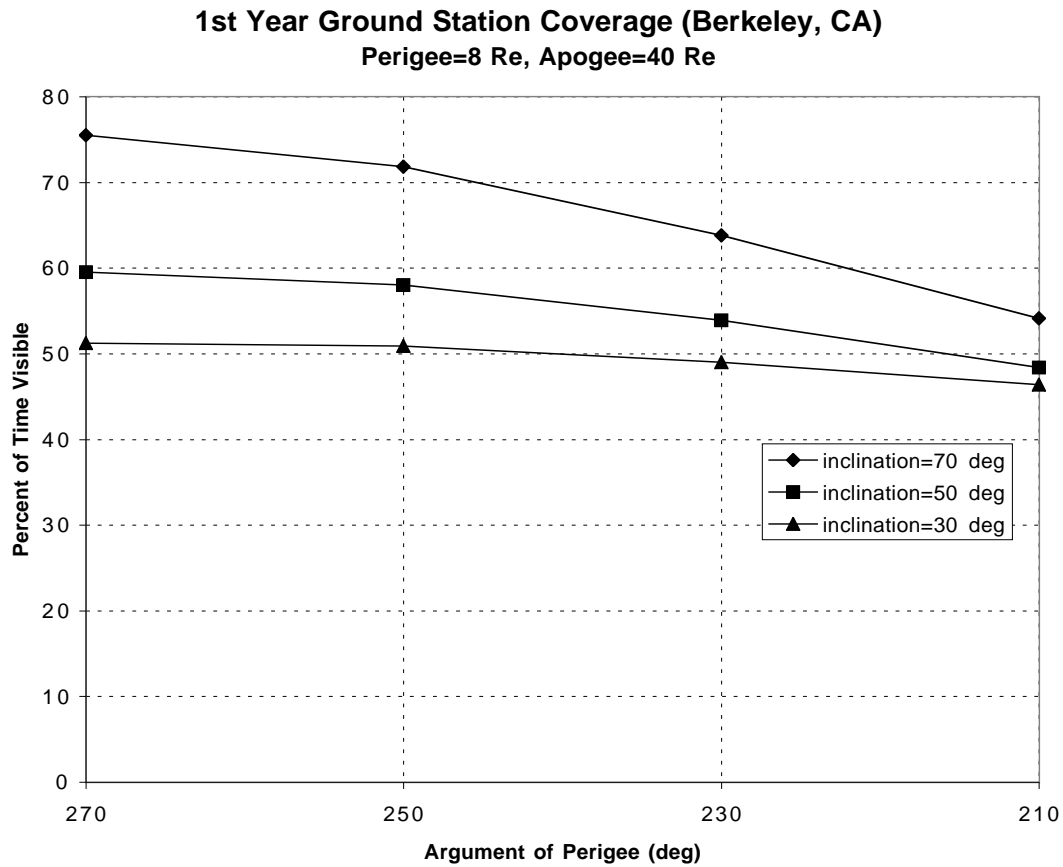


Figure 15.3: Percentage coverage from the UCB/SSL ground station as a function of the lunar assist orbit inclination and for different values of the angle of perigee.

15.3 Data Handling & Signal Processing

The proposed spacecraft and orbit designs support a data bandwidth from the spacecraft of 50 Mbit/s. This rate would permit the transmission of lossless compressed images at the rate of one per 160 seconds. This would reduce the bandwidth requirement on the average four-fold which would allow the elimination of the Traveling Wave Tube Amplifiers from the Communications System. Additionally, transmitted data from the photometry measurements (but not discovery images) can be limited to pixel sets over a 3σ threshold and around locations already identified as being supernova candidates. Analysis of HST images indicate that this will provide a ten-fold reduction in the photometry data. This rate would permit the transmission of lossless compressed images at the rate of one per 160 seconds. This would reduce the bandwidth requirement on the average four-fold which would allow the elimination of the Traveling Wave Tube Amplifiers from the Communications System.

15.4 NERSC

SNAP data is transmitted from the satellite to a receiving station at UCB/Space Sciences Laboratory and then transferred to the Science Operations Center at LBNL. High performance computing and mass storage are locally provided by NERSC, the National Energy Research and Scientific Computing Center. Multiple petabytes of raw and processed data may be stored in HPSS, the NERSC tape robotic facility for long term storage. High speed networks link the mass storage to the CPU farms and supercomputers. Raw data can be extracted for processing, computations performed and then results sent back quickly for uplink to the satellite for mission operations. The NERSC Facilities consist of a very large IBM SP, a Cray T3E, a large Storage System (running HPSS), a computing cluster and the PDSF (a cluster of workstations used mainly for HEP data analysis and simulation). NERSC current capacity is 3 terraflops and 300 terrabytes for computing. These computers are currently being phased out and replaced with new supercomputers and processor farms. Each of these high performance machines has fast networks to a substantial local disk cache and HPSS. A complete description of these facilities, can be found on the NERSC web site: <http://www.nersc.gov/aboutnersc/facilities.html>.

Processing begins by converting the data to a format amenable to analysis and calibrating digital numbers into physically meaningful units. Pattern recognition algorithms reconstruct features in the data such as photon fluxes and spectral-line positions. Data are then reduced with software filters into smaller, signal-enhanced samples based on reconstructed features. All CPU intensive processing is accomplished on the supercomputer so that final analysis can proceed on the average desk-top PC. If additional CPU intensive analysis is required, software systems exist to accommodate the needs of the experimenters.

The essential supernova discovery algorithms have already been run on the NERSC “Millennium Cluster,” and semi-automatically handled ~ 40 Gbytes of data per night for a ground-based low-redshift supernova search. This low-redshift search will be scaled up over the next year and run fully automatically, providing the test-bed for the satellite discovery analysis system, the single most time-critical element of the analysis.

Part IV

Education/Public Outreach

Chapter 16

SNAP Education and Public Outreach

To balance the education goals of the funding agencies for the SNAP mission, we have designed two components for the SNAP education and outreach efforts. The first component addresses the traditional education and public outreach audiences: grades K-14 students and teachers, and the general public.

The second component addresses the need to train the next generation of professional scientists and engineers. This group comprises upper-level undergraduates with declared majors and graduate students pursuing advanced degrees in the sciences and engineering disciplines.

Accordingly, we have divided the education section into two parts. In section 16.1, we present our proposed program for K-14 and public outreach. Section 16.2 contains the training programs for junior and senior undergraduates and graduate students.

16.1 SNAP and Science Literacy

16.1.1 Introduction

The high redshift supernova searches of the Supernova Cosmology Project and the High-Z Team have shown that the expansion of the universe is accelerating. This startling discovery has fired the imaginations of people around the world. The SNAP project provides a unique opportunity for engaging students, educators, and the general public in our rapidly evolving view of the universe.

Major discoveries like the accelerating universe, the origin of gamma ray bursts, the discovery of extra-solar planets, and the most distant quasars regularly appear in the newspapers. When students, teachers and the public are active participants in this exciting experiment, they *are* scientists, gaining first-hand knowledge and experience of the science enterprise.

16.1.2 Identified Need

Research shows that children and adults learn best about science when they actually do science, rather than simply engage in verification exercises. We will make SNAP data – real scientific data – available to learners. Few examples of this kind of outreach program exist.

The constant stream of data from SNAP will be formidable due to the sheer volume of images; storage and analysis of SNAP data will be major challenges for the project. But the actual observing methods and analysis techniques will be accessible. Perhaps most appealing to the layperson, SNAP’s direct images can be studied and appreciated easily, with user-friendly software.

16.1.3 Target Audiences

Our education and public outreach program has as its fundamental operating principle that everyone can participate in the SNAP mission.

Specifically, we have identified these principal audiences:

1) K-12: Students in elementary and secondary schools and home-school students make up this group. We will be guided by the principle of universal access for this audience. This means reaching out to under-served populations.

2) Grades 13 & 14: College freshmen and sophomores comprise another audience. Our focus on this sector of the SNAP program is on undergraduates in two- and four-year colleges who are not science majors, many of whom would otherwise have little or no experience with science research activities and scientists.

3) General Public: Programs geared toward this audience will reach out to all interested citizens – people who are fascinated by the accelerating universe and other cosmological conundrums and who are intrigued by space telescopes, advanced electronics, and technology in general; other outreach audiences include the astronomy, physics and space science communities and the media.

16.1.4 Goals

Science education aims to produce a literate public that appreciates the nature of science. We need educators, journalists, artists, politicians, and business leaders who can recognize and articulate the value of science in society, and in a diverse, high-quality technical work force.

Essential to our effort is outreach to under-served populations, aimed at educating all people about the important role that science and technology play in our lives, as well as helping to ensure that the scientists and engineers of the future come from all sectors of society.

SNAP’s education and public outreach objectives are:

- To have a powerful, positive impact on grades K through 14 science education and increase public understanding of astronomy and cosmology, by making education and public outreach an integral part of the SNAP mission’s professional activities.

We will do this by

- Providing scientific content that is inclusive and age appropriate, with a particular emphasis upon universal access.
- Leveraging our partners' existing programs and activities for maximum impact.

16.1.5 K-14 Activities and Instructional Materials

Science programs are held to particularly high educational standards. Content for elementary, middle, and high schools must meet National Science Education Standards established by the National Research Council. States have their own criteria; California, for example, has set demanding new standards in science and math. Furthermore, material has to be age- and grade-specific to be accessible to students, and has to adhere to the best practices established by discipline-based education research.

All instructional materials have to be evaluated for delivery, pedagogy, and accuracy. This demands a commitment to extensive field testing of curriculum plans and materials, to be accomplished through academic research projects or through sub-contracts with professional education-evaluation firms.

Subject Areas

We will focus on these particular areas:

- Activities in cosmology and observational astrophysics,
- Activities centering on Spaceship Earth,
- Activities centered on SNAP Engineering, Technology and Applied Science,
- Research experiences for undergraduates and educators.

Tools and Activities

- Webcasts and around-the-clock “over-the-shoulder” observation as SNAP images and data come in, covering the electromagnetic spectrum from the ultraviolet to the infrared.
- A virtual science center and virtual field trips to the SNAP mission center.
- A Challenger-style mission to “build” SNAP (see section on partnerships, below).
- Education web pages, with links to public outreach and technical information pages.
- Patches of the sky students can call their own.
- Access to SNAP's library of stored images and data.
- Data processing software with accompanying instructions on data analysis.

16.1.6 Undergraduate Research Experience

Objectives

This opportunity for a research experience is designed for the undergraduate population of students who attend two- and four-year colleges and who otherwise would not have access to research opportunities at their home institutions. In particular, we are targeting socio-economic groups traditionally underrepresented in the fields of science and technology (minorities and women) as well as students with an interest in science who are currently pursuing other majors. The latter group includes, for example, students majoring in business, and economics, and students interested in teaching science in elementary and secondary schools, i.e., education majors.

During a 10-week program, the students will be paired with mentors who are members of the SNAP project team. All students are expected to participate in the activities of their research group. At the completion of their research, students will author a web-based report that will be published on the SNAP web site. Students will be required to make poster and oral presentations to their mentors and colleagues. We will coordinate and integrate this proposed research program with our collaborators' summer programs.

Supporting Students

We will put together a web-based primer consisting of both original material and links to selected existing web sites. The primer will contain FAQ (frequently asked questions) pages in physics and astronomy, asynchronous question-and-answer sessions with mentors, and a virtual tour of the SNAP observatory. This will serve as a reference source for the students as well as for the general public.

We have structured the summer program to include a variety of experiences that provide as much exposure to science research and its applications. Planned activities also include visits to industrial and academic labs and research facilities, seminars, and etc.

Preparing Mentors

Mentors will be coached prior to the start of the program on effective techniques for integrating students into his or her research group. Each mentor will be encouraged to introduce members of the group and collaborators, discuss his or her project goals, as well as the specific problem or project the student will work on with senior researchers. This serves as an ice-breaker while also giving the students a sense of what is expected of them.

Recruitment

We will contact deans, department chairs, job-placement and career offices at two- and four-year colleges and universities nationwide. We will prepare and send information fliers, posters, and application materials. These will also be available on-line on the SNAP web site, with links from the collaborators' web pages.

To meet our own goals of targeting women and underrepresented socio-economic groups, we shall make special effort to contact Historically Black Colleges and Universities, Minority Institutes of Excellence and other minority-serving institutions.

Evaluation

We will evaluate the success of this kind of program from both the perspective of the students as well as the mentors. At the end of the summer, each participating student and mentor will be interviewed individually.

We will continue a longitudinal study of each cohort in this program. An extensive and ambitious evaluation effort is vital for quantifying the effect of this kind of research experience in the future career choices of participating students. Results of the study will be compiled, analyzed and published.

16.1.7 Professional Staff Development

Inservice Teachers

One of the most crucial aspects of science education in the elementary, high school, and lower college grades is effective classroom teaching by motivated and knowledgeable professionals. To this end, we can leverage the Lawrence Hall of Science's expertise in this area, as well as take advantage of their extant programs, such as the Hands-On Universe. The Astronomical Society of the Pacific's Project Astro's nation-wide network of teacher-astronomer partnerships is another resource for professional development of classroom teachers.

Research Opportunities for Preservice Teachers

The way for education majors to develop an understanding of and empathy with scientific and technological enterprises is by participating in them, rather than serving in training exercises alone. They are included in the target audience for the undergraduate research program described in 16.1.6 above.

16.1.8 Public Outreach

Aimed at the widest possible audience, SNAP public outreach will be a logical extension of SNAP's educational science programs, available to all. Some activities are described below.

Public Outreach Web Site

This site will provide shallow-to-deep layers of information on the SNAP mission. The home page will prominently display news updates. The page will link to web versions of the outreach modules (see below), which will be coordinated with educational units. Additional links to related sites such as the Space Science Laboratory's NASA's Science Education Gateway (SEGway), will be included.

Outreach Modules

Outreach modules will contain coordinated materials grouped around key elements of SNAP's mission. These will be regularly kept up to date and assembled for specific purposes. Modules will be organized around different topics, for example, the expanding universe or dark energy and cosmological parameters. Materials may include sets of short, handsome brochures, press releases, pertinent video clips on specific topics, including interview segments with articulate scientists.

Public events

Public events will include briefings and panels at conventions, webcasts, and demonstrations such as the Challenger SNAP mission; many of these will be held at partner institutions such as the Chabot Space and Science Center and other science museums, at locations throughout the country.

A strong linkage between live events and web-based public outreach will be established through partnership with University of California at Berkeley's Space Sciences Laboratory, leader of the Science Education Gateway program (SEGway).

16.1.9 Partnerships

We will form partnerships with groups and institutions that bring unique perspectives and expertise in science education, e.g. the Chabot Observatory and Science Center, the University of California at Berkeley's Lawrence Hall of Science, the Astronomical Society of the Pacific, and professional science-education evaluators. A description of confirmed partners, and some of the activities on which they and SNAP will collaborate follows.

The Chabot Space and Science Center

The Chabot Space and Science Center (CSSC) is a new, 86,000-square-foot, innovative teaching and learning center focusing on astronomy and its interrelationships with other sciences. Its facilities are a place where students, teachers, and the public can imagine, understand, and learn to shape their future through science. CSSC's Challenger Center has a Briefing/Debriefing room, a Mission Control Center patterned after Houston Mission Control, and a Space Station that is equipped to perform basic experiments.

- *Challenger Mission: Journey to a Supernova:* SNAP and CSSC will work together to develop a new Challenger mission, modeled on the SNAP mission – building a space telescope and simulating an intergalactic journey. The Mission Control Center could be used as a Mission Control Center for the SNAP program. Data could be downlinked to the computer consoles for the SNAP team or a specific stream of data could be sent for the public, providing the opportunity for thousands of people to participate or observe the operations of the program. Once developed, the Challenger Center SNAP mission program can be disseminated throughout the United States.

- *SNAP Virtual Science Center*: will be a high- capacity, on-line interactive agent that will provide visitors access to SNAP-related scientific information, curricula, experiments, simulations and models, archival data, educational research information, and scientists, both on-site and by telepresence. It will serve schools, teachers, community organizations and teachers around the world.

The Lawrence Hall of Science

The Lawrence Hall of Science is a nationally and internationally recognized leader in improving science education, having placed its educational materials in one out of four K-8 classrooms in the United States and, with programs like Hands-On Universe, a rapidly expanding high school market. Tens of thousands of teachers have gone through workshops or used materials developed at the Hall, a heritage that would become available to SNAP.

Specific ways that SNAP and the Lawrence Hall of Science could work together include:

The Hands-On Universe: Hands-On Universe is a well-established project with an expanding network of agents who constitute a highly effective teacher training and support system. This system also brings image processing software, a successful database and request system for astronomical images, and a twelve-year heritage of successful classroom work with a broad variety of teachers and students.

- A new Hands-On Universe high school curriculum module, centered on the SNAP project – a streamlined SNAP data analysis system, or “SNAP Lite”, for use by high school students in Hands-On Universe’s High School Supernova Research Project.
- A middle school SNAP module on the expanding universe for HOU’s “Our Place in the Universe”, curriculum units.

Astronomical Society of the Pacific

One of the Astronomical Society of the Pacific (ASP) goals is to improve public understanding of astronomy. Its non-technical publications are: *Mercury*, a magazine; *The Universe in the Classroom*, a newsletter on teaching astronomy in grades 3-12; and a catalog of educational materials that is distributed to over 200,000 teachers and astronomy enthusiasts semi-annually. The ASP’s annual meetings include a national workshop for K-12 teachers, and a weekend exposition and lecture series on new developments in astronomy. The Society sponsors a national symposium on teaching astronomy to college non-science majors every three years.

Project ASTRO is a program that trains professional and amateur astronomers to link with 4th-9th grade teachers and help them bring more astronomy and science into their classrooms. The project now has 13 active sites around the country, and has trained over 650 astronomer-teacher partnerships, reaching more than 50,000 students directly over the last five years. Many of these students are from schools and communities that are traditionally under-served in science, including a number of schools

in Oakland, California, schools in the public housing projects in Chicago, and schools with heavy Native American populations near Tucson, Arizona. A key element of the project is the publication of a series of astronomy resource notebooks, called *The Universe at Your Fingertips*, which collect the best hands-on astronomy activities and teaching resources for the K-12 classroom. It is used by some 15,000 teachers (and astronomers who work with them).

The ASP will partner with the SNAP education and outreach team in the following ways:

- Project ASTRO partners around the country will field-test curriculum modules and activities in appropriate grades SNAP materials will be distributed and tested during workshops and symposia at ASP meetings. After testing, SNAP activities and materials can be distributed through the ASP teachers newsletter, future volumes of *The Universe at Your Fingertips*, and, if appropriate, through the ASP catalog.
- Project ASTRO and ASP education staff will lend their expertise and experience to help SNAP staff in the development of these activities and materials. The ASP has extensive databases of what materials already exist.
- Supernova hunting is an area of astronomy where amateurs have participated, and continue to be very interested. The ASP will help develop materials and training protocols so that amateur astronomers can be goodwill and information ambassadors for the SNAP project specifically, and astronomy and space science in general.

UC Berkeley Space Sciences Laboratory: SEGway

SEGway is a national consortium of science museums, research institutions, and educators working together to adapt the latest scientific research for communication to students, teachers, and the general public. A mature, ongoing program, SEGway is supported by NASA and sustained by in-kind support from its museum partners, the National Air and Space Museum, the Exploratorium, the Lawrence Hall of Science, and the Science Museum of Virginia.

SEGway features include:

- Field-tested, web-based lesson plans featuring NASA data
- Self-guided modules for the public using similar data
- Professional development for teachers
- National dissemination of resources, both through museum web sites and at the museums themselves.

SEGway's museum partners are institutions that have set the standard for science museums around the country, with a loyal constituency of thousands of teachers and millions of members of the general public. Leveraging SNAP's outreach efforts through the SEGway structure will provide our program with an efficient way of serving the needs of both formal and informal education communities.

16.2 SNAP Training Undergraduates Science Majors and Graduate Students

16.2.1 Overview

Students will be involved in hands-on research activities exploiting recent technological advances under the guidance of experts. Examples of the kind of activities include the development of fast electronics for data acquisition and decision making, and computational methods for data handling, processing, simulation and analysis. We have included advanced (juniors and seniors) undergraduates in this program, because we feel that the traditional classroom-dominated curriculum is too narrowly based to allow these students to make a smooth transition into the kind of high-tech research activities they are likely to encounter in their quest for a Ph.D. or a job in industry. We intend to broaden their skills by involving them in on-going research and thereby to familiarize them with the tools of the trade, with the way science is actually done, and to let them share in the excitement of discovery.

16.2.2 Goals and Objectives

A number of research and engineering disciplines rely heavily on advanced instrumentation in the quest for scientific breakthroughs. Among the research areas where intensive instrumentation development activities are actively being pursued are astrophysics, particle physics, and materials science.

Over the last few decades we have seen steady advances in sophistication and complexity of the instrumentation deployed to attack forefront research problems. Lack of adequate training has become an obstacle in incorporating beginning graduate students into our research activities, particularly those that depend heavily on advanced instrumentation. SNAP is one of these projects that incorporates both cutting edge science and complex instrumentation to attack a fundamental question in cosmology: what is the mass-energy density of the universe, what is “dark energy”?

The multidisciplinary nature of this enterprise is clear from the broad spectrum of problems which must be addressed in order for SNAP to be successful. We have been very fortunate in attracting outstanding researchers and engineers from astrophysics to space engineering to work on SNAP. We want students to profit from this symbiosis.

The dominant research goal is to give students hands-on experiences in modern techniques. Students will work with state-of-the art instruments and software. The most important skill we hope to impart to these students is the ability to understand what they are trying to measure, and to develop knowledge of what types of tools are available with which to make measurements. We believe that first class students will become first class scientists and engineers by first learning how to utilize first class equipment and techniques.

Based on past experience with both graduates and undergraduates working in our labs, we know that students with the skills learned while working on these projects are eagerly sought not only by Ph.D. thesis advisors but also by Silicon Valley and related industries.

16.2.3 Training Program

Our program will ensure that students are exposed to key experimental techniques of general use and to the physical basis of modern instrumentation technology. The training programs focus on 1) a summer research experience for undergraduate science majors and incoming graduate students, and on 2) first year graduate students during the academic year.

Over the mission lifetime the number of participating students will increase gradually as we gain experience in running such a program, so that by the end of a five-year period we expect to be able to accommodate 10-12 graduate students, and perhaps 10-15 undergraduates.

We look forward to an evolutionary process where training gradually turns into meaningful collaboration. There are few activities more exciting to a scientist or a student than to be at the forefront of a field and to be able to participate in helping to push back the frontiers. We see this as an essential component of the proposed program.

First Year Graduate Students

First year graduate students will be assigned to one of the several groups on SNAP, e.g. advanced imaging devices, optical design, supernovae or computer science. In addition to learning the key techniques in the lab, during the course of the academic year, students, with their staff mentor will propose and plan a program of summer research experience for junior and senior undergraduates. The participating graduate students will play major roles in preparing and leading the research activities of the undergraduates, and in working closely with them to make meaningful measurements of value to the research program.

Recruitment of graduate students will be limited to students applying for admission to graduate programs in the fields of physics, astrophysics, material sciences, and electrical engineering and computer science, and to graduate students already enrolled at in these departments of our collaborating universities.

A description of the program will be included in the widely distributed informational materials available in hard copy and on the web, and special emphasis will be given to pointing out the benefits of the program for students from schools with limited or no research opportunities. In this way we hope to broaden the base of highly talented applicants to include students who might otherwise be hesitant to tackle technically challenging (or intimidating) Ph.D. programs. The same informational materials will be distributed to first year graduate students already enrolled at collaboration universities, and they, too, would be strongly encouraged to apply to better prepare themselves for their thesis research.

Summer Program: Undergraduates and Incoming Graduate Students

The ten-week summer program for undergraduates and incoming graduate students is intended to provide broad training that yet enables students to come to grips with specific problems. Students work in a research group, under the supervision of the

group leaders and the other researchers in the group. Morning sessions during the first two weeks are devoted to introducing essential concepts and laboratory safety. The rest of the time, full time research is the dominant activity. The students in the various groups would come together with SNAP scientists to participate in joint weekly seminars on current research topics, thereby not only learning more about what is going on, but also enhancing their communications skills. Participating students will be encouraged to attend ongoing seminars that might be of interest to them and visit other research venues of interest (e.g., laboratories on campus and industrial research centers).

We plan to create web-based materials to go with this program. Emphasis is on giving the students a good overview of the field, in making them aware of the relevant literature, in exposing them to the underlying physical principles, and especially in having them participate directly in the experimental programs of the group.

Undergraduates for the summer program will be recruited nationwide. We intend to recruit the best possible students for the program. Hard copy, electronic and personal contacts will be used to reach as wide an audience as possible, and will include special efforts to make students from traditionally underrepresented groups aware of this opportunity (e.g., Southern University, University of Texas at El Paso).

Evaluation

Students will be expected to keep lab notebooks, and to submit to the program administrator a brief written summary of their activities and accomplishments at the end of their participation in the program. Relevant publications, if any, should be appended. We will encourage participants to make written evaluations and other comments about the program to help us to evaluate and improve it. We intend follow the progress of the participating students in their subsequent work as graduate students and elsewhere, and to compare their experiences to those of students who did not participate in this program.

Administration

The SNAP/EPO Operations Center will coordinate this program for the mission, and make arrangements to assure proper supervision of both graduate and undergraduate students participating in the program. Oversight of the program will be provided by a committee consisting of group leaders and the SNAP/EPO coordinator. Day-to-day supervisory responsibility lies with research group leaders with which the students are affiliated. Staff scientists, post-docs, and especially second-year and advanced graduate students will play an important role in working closely with the more junior students, and in guiding their activities. Continuing safety training will be an integral part of the program.

16.3 SNAP Administration of Education and Outreach Programs

SNAP education and public outreach programs, *SNAP and Science Literacy*, will be coordinated by the SNAP/EPO Operations Center, see Figure 17.1. The Operations Center will facilitate the transfer of SNAP data from the mission to the public, connecting the mission scientists and engineers to the education programs. The Operations Center will act as a broker for the SNAP partners. Other roles for the Operations Center is the coordination of the undergraduate research experience (discussed in section 16.1.6) and the training of advanced undergraduates and graduate student programs, discussed in section 16.2.

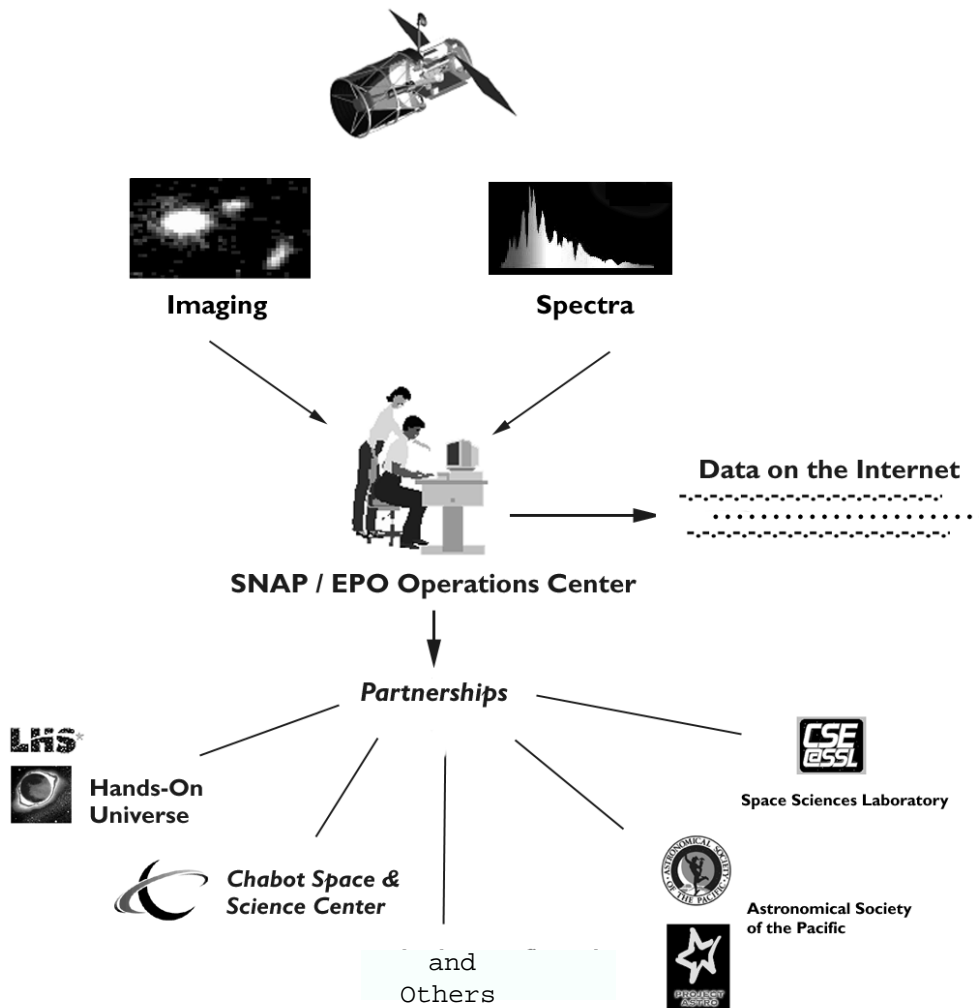


Figure 16.1: SNAP EPO Structure: Broker for Scientists, Partners and the Public

16.3.1 Budget

K-14 Education and Public Outreach: SNAP and Science Literacy

Total cost estimates for baseline infrastructure, the design, development, adaptation and dissemination of the proposed SNAP K-14 education and public outreach materials and activities is roughly 3 percent of total mission cost, well in line with allocations for typical agency education and outreach programs. One third of this cost will be defrayed by cost-sharing from other resources.

Training Programs

We expect to leverage off existing summer research programs of the SNAP collaboration.

16.3.2 Advisory Board

SNAP education and public outreach will have an advisory board with members from a broad cross-section of the science and education communities. Scientists will be drawn from university faculties and research laboratories. The board will advise SNAP's education and public outreach personnel on future directions and opportunities.

16.3.3 Personnel

Dr. Susana Deustua will lead and coordinate the SNAP EPO programs. A scientist with the Supernova Cosmology Project and the SNAP science team at Lawrence Berkeley National Laboratory, she has been active in science education since receiving her Ph.D. in astronomy from the University of Michigan. She recently served on the review panel for the State of California's new science curriculum.

The SNAP K-14 and Public Outreach team consists of professionals in astronomy and science education with some two centuries of experience among them. These are:

Eileen Engel is director of education at the Chabot Space and Science Center. Previously she was Deputy Director of the Partnership for Environmental Technology Education and has served on the Department of Education's Teacher Research Associates Program Advisory Board, among other such activities.

Andrew Fraknoi is director of Project ASTRO and former executive director of the Astronomical Society of the Pacific, chair of the astronomy program at Foothill College. He is co-author of several popular astronomy textbooks, and has edited *Universe at Your Fingertips*. He has organized workshops on teaching astronomy in grades 3-12 for the last 20 years.

Alan Gould is at UC Berkeley's Lawrence Hall of Science, where he is Planetarium Director, co-director of the Hands-On Universe project, and director of the Global Systems Science Project. He has 23 years of experience developing hands-on science activities and teaching guides.

Robert Havlen is executive director of the Astronomical Society of the Pacific. With a Ph.D. in astronomy from the University of Arizona, Havlen has 30 years' of

experience as a research astronomer and professor. He is a member of the Commission on Teaching Astronomy of the International Astronomical Union.

Isabel Hawkins has a Ph.D. in astronomy from UCLA and is Senior Fellow in science education and director of the Center for Science Education at UC Berkeley's Space Sciences Laboratory. She leads several education initiatives including NASA's Sun-Earth Connection Education Forum, and is a member of NASA's Office of Space Science Education Council and Space Science Advisory Committee.

Paul Preuss is with Berkeley Lab's Public Information Department. In over 30 years presenting science to the public, he has made award-winning films for schools and network TV, edited the Exploratorium magazine, and has written numerous articles for science magazines including Discover.

Carl Pennypacker is at UC Berkeley's Lawrence Hall of Science, and is the originator of the Hands-On Universe program and its co-director. He is also a physicist and member of the Supernova Cosmology Project.

Part V

Bibliography

Bibliography

- Aguirre, A. N. 1999, *ApJ*, 512, L19
- Aguirre, A. N., & Haiman, Z. 1999, *astro-ph*, 9907039
- Akerlof, C., et al. 1999, *Nature*, 398, 400–402
- Aldering, G., Knop, R., & Nugent, P. 1999, *AJ*, in press
- Allington-Smith, J. R., Content, R., & Haynes, R. 1998, *SPIE*, 3355, 196–205
- Anderson, J. M., Becker, K. J., Kieffer, H. H., & Dodd, D. N. 1999, *PASP*, 111, 737–749
- Angel, J. R. P., Woolf, N. J., & Epps, H. W. 1982, *SPIE*, 332, 134
- Ardelean, J., et al. 1996, *Nucl. Instrum. Meth.*, 376, 217
- Arnett, W. D. 1982, *ApJ*, 253, 785
- Arnett, W. D., Branch, D., & Wheeler, J. C. 1985, *Nature*, 314, 337
- Baade, W. 1926, *Astr. Nach.*, 228, 359
- Bacon, R., Adam, G., Baranne, A., Courtes, G., Dubet, D., Dubois, J. P., Emsellem, E., Ferruit, P., Georgelin, Y., Monnet, G., Pecontal, E., Rousset, A., & Say, F. 1995, *A&AS*, 113, 347+
- Bahcall, N., & Fan, X. 1998, *ApJ*, 504, 1
- Bahcall, N. A., Ostriker, J. P., Perlmutter, S., & Steinhardt, P. J. 1999, *Science*, 284, 1481+
- Baker, J. 1969, *IEEE Trans.A.E.Systems*, 5, 261
- Balbi, A., Ade, P., Bock, J., Borrill, J., Boscaleri, A., de Bernardis, P., Ferreira, P. G., Hanany, S., Hristov, V. V., Jaffe, A. H., Lee, A. T., Oh, S., Pascale, E., Rabii, B., Richards, P. L., Smoot, G. F., Stompor, R., Winant, C. D., & Wu, J. H. P. 2000. "Constraints on Cosmological Parameters from MAXIMA-1". In Submitted to *ApJ Letters*; 4 pages, 5 figures., pages 5124+
- Barden, S. C., Arns, J. A., & Colburn, W. S. 1998, *SPIE*, 3355, 866–876

- Barkana, R., Blandford, R., & Hogg, D. W. 1999, *ApJ*, 513, L91–L94
- Baron, E., Hauschildt, P. H., Branch, D., Wagner, R. M., Austin, S. J., Filippenko, A. V., & Matheson, T. 1993, *ApJ*, 416, L21
- Baron, E., Hauschildt, P. H., & Branch, D. 1994, *ApJ*, 426, 334
- Baron, E., Hauschildt, P. H., Branch, D., Austin, S., Garnavich, P., Ann, H. B., Wagner, R. M., Filippenko, A. V., Matheson, T., & Liebert, J. 1995, *ApJ*, 441, 170
- Baron, E., Hauschildt, P. H., Branch, D., Kirshner, R. P., & Filippenko, A. V. 1996, *MNRAS*, 279, 779
- Bartelmann, M., & Schneider, P. 1999, *astro-ph/9912508*
- Bartelmann, M., & Schneider, P. 1999, *A&A*, 345, 17–21
- Benítez, N., & Sanz, J. L. 1999, *ApJ*, 525, L1–L4
- Bergström, L., Goliath, M., Goobar, A., & Moertsell, E. 1999, *astro-ph*, 9912194
- Bessell, M. S. 1979, *PASP*, 91, 589–607
- Bessell, M. S. 1990, *PASP*, 102, 1181–1199
- Bessell, M. S., & Brett, J. M. 1988, *PASP*, 100, 1134–1151
- Blandford, R. D., Saust, A. B., Brainerd, T. G., & Villumsen, J. V. 1991, *MNRAS*, 251, 600–627
- Bohlin, R. C. 1996, *AJ*, 111, 1743+
- Bond, J., Efstathiou, G., & Tegmark, M. 1997, *MNRAS*, 291, L33
- Branch, D. 1987, *ApJ*, 320, L27
- Branch, D., et al. 1983, *ApJ*, 270, 123
- Branch, D., & Miller, D. L. 1993, *ApJ*, 405, L5
- Branch, D., & van den Bergh, S. 1993, *AJ*, 105, 2231
- Branch, D., Falk, S. W., McCall, M. L., Rybski, P., Uomoto, A. K., & Wills, B. J. 1981, *ApJ*, 244, 780
- Branch, D., Livio, M., Youngelson, L., F. Boffi, & Baron, E. 1995, *PASP*, 107, 1019
- Branch, D., Romanishin, W., & Baron, E. 1996, *ApJ*, 465, 73
- Bredthauer, R., Pinter, J., Janesick, J., & Robinson, L. 1991, *SPIE*, 1447
- Burke, B., Mountain, R., Harrison, D., Bautz, M., Doty, J., Ricker, G., & Daniels, P. 1991, *IEEE*, 38(5)

- Burke, B. E., et al. 1994, *IEEE Trans. Nucl. Sci.*, 41, 375
- Burke, B. E., et al. 1997, *IEEE Trans. Elec. Dev.*, 44(10), 1633
- Burstein, D., & Heiles, C. 1982, *AJ*, 87, 1165–1189
- Caldwell, R., Dave, R., & Steinhardt, P. 1998, *PRL*, 80, 1582
- Carlstrom, J., et al. 1999, *astro-ph/9905255*
- Coble, K., Dodelson, S., & Frieman, J. 1997, *PRD*, 55, 1851
- Colless, M. 1998. Early Results from the 2dF Galaxy Redshift Survey. In *Wide Field Surveys in Cosmology*, 14th IAP meeting held May 26-30, 1998, Paris. Publisher: Editions Frontieres. ISBN: 2-8 6332-241-9, p. 77., pages 77+
- Content, R. 1998a, *SPIE*, 3354, 187–200
- Content, R. 1998b, *SPIE*, 3356, 122–133
- Cook, L. G. 1979, *Proc. Soc. Photo-Opt. Instrum. Eng.*, 183, 207
- Cooray, A., & Huterer, D. 1999, *ApJ*, 513, L95
- Cooray, A. R. 1999, *A&A*, 348, 31–37
- Cooray, A. R., Quashnock, J. M., & Miller, M. C. 1999, *ApJ*, 511, 562–568
- Copi, C., Schramm, D., & Turner, M. 1995, *Science*, 267, 192
- Costa, E., et al. 1997a, *IAU Circ.*, 6576, 1+
- Costa, E., Feroci, M., Frontera, F., Zavattini, G., Nicastro, L., Palazzi, E., Spoliti, G., di Ciolo, L., Coletta, A., D’Andretta, G., Muller, J. M., Jager, R., Heise, J., & In’T Zand, J. 1997b, *IAU Circ.*, 6572, 1+
- Dalcanton, J. J., Canizares, C. R., Granados, A., Steidel, C. C., & Stocke, J. T. 1994, *ApJ*, 424, 550–568
- Dentan, M., et al. 1998. Industrial Transfer and Stabilization of a CMOS-JFET-Bipolar Radiation-Hard Analog -Digital SOI Technology. In *IEEE NSS98 Conference*. Toronto
- Dodelson, S., & Knox, L. 1999, *astro-ph/9909454*
- Donahue, M., Aldering, G., & Stocke, J. T. 1995, *ApJ*, 450, L45–+
- Eastman, R., Schmidt, B. P., & Kirshner, R. 1996, *ApJ*, 466, 911
- Efstathiou, G., & Bond, J. 1999, *MNRAS*, 304, 75
- Efstathiou, G., Bond, J., & White, S. 1992, *MNRAS*, 258, 1

- Eisenhauer, F., et al. 2000, astro-ph/0001454
- Eisenstein, D., Hu, W., & Tegmark, M. 1999, ApJ, 518, 2
- Epps, & Takeda 1983, Ann.Tokyo Astron. Obs., 19, 401
- Falco, E. E., Kochanek, C. S., & Munoz, J. A. 1998, ApJ, 494, 47+
- Filippenko, A. V. 1997. In 18th Texas Symposium on Relativistic Astrophysics, A. Olinto, J. Frieman, and D. Schramm, editors, Singapore: World Scientific, page 999
- Finger, G., Biereichel, P., Mehrgan, H., Meyer, M., Moorwood, A., Nicolini, G., & Stegmeier, J. 1999. NGST Detector Workshop, April 20-21, 1999
- Frieman, J., et al. 1995, PRL, 75, 2077
- Fruchter, A., & Hook, R. 1998, astro-ph/9808087
- Fruchter, A. S., et al. 1999, ApJ, 519, L13–L16
- Fukugita, M., Ichikawa, T., Gunn, J. E., Doi, M., Shimasaku, K., & Schneider, D. P. 1996, AJ, 111, 1748+
- Garnavich, P., et al. 1998, ApJ, 493, L53
- Gilmore, G., Reid, I., & Hewett, P. 1985, MNRAS, 213, 257+
- Glazebrook, K. 1998, AAO Newsletter, 87, 11
- Goobar, A., & Perlmutter, S. 1995, ApJ, 450, 14
- Groom, D., et al. 1999, SPIE, 3649
- Groot, P. J., et al. 1997, IAU Circ., 6584, 1+
- Gunn, J. E. 1967, ApJ, 147, 61+
- Gunn, J. E. 1995. The Sloan Digital Sky Survey. In American Astronomical Society Meeting, volume 186, pages 4405+
- Hamuy, M., Phillips, M. M., Wells, L., & Maza, J. 1993, PASP, 105, 787
- Hamuy, M., Phillips, M. M., Maza, J., Suntzeff, N. B., Schommer, R. A., & Aviles, R. 1996, AJ, 112, 2391
- Hayes, D. S., & Latham, D. W. 1975, ApJ, 197, 593–601
- Haynes, R., Lee, D., Allington-Smith, J., Content, R., Dodsworth, G., Lewis, I., Sharples, R., Turner, J., Webster, J., Done, C., Peletier, R., Parry, I., & Chapman, S. 1999, PASP, 111, 1451–1468

- Heyes, P. S., Pool, P., & Holton, R. 1997. In *Solid State Sensor Arrays: Development and Applications*, page 201
- Hoekstra, H., Franx, M., Kuijken, K., & Squires, G. 1998, *ApJ*, 504, 636+
- Höflich, P., & Khokhlov, A. 1996, *ApJ*, 457, 500
- Höflich, P., Wheeler, J. C., & Thielemann, F. K. 1998, *ApJ*, 495, 617
- Hogg, D. W., et al. 1998, *AJ*, 115, 1418–1422
- Holder, G., et al. 1999, *astro-ph/9912364*
- Holland, A. 1996, *Nucl. Instrum. Methods*, A337
- Holland, A., et al. 1991, *IEEE Trans. Nucl. Sci.*, 38(6)
- Holland, A. D. 1997, *SPIE*, 3114, 586
- Holland, S. 1989, *Nucl. Instrum. Methods*, A275
- Holland, S., et al. 1996, *IEDM Tech. Digest*, 911
- Holland, S., Wang, N., & Moses, W. 1997, *IEEE Trans. Nucl. Sci.*, 44(3)
- Holland, S. E., et al. 1997. Development of back-illuminated, fully-depleted CCD image sensors for use in astronomy and astrophysics. In *1997 IEEE Workshop on Charge-Coupled Devices and Advanced Image Sensors*
- Holmes-Siedle, A., Holland, A., & Watts, S. 1996, *IEEE Trans. Nucl. Sci.*, 43(6)
- Holtzman, J. A., et al. 1995, *PASP*, 107, 156–178
- Holz, D. E., & Wald, R. M. 1998, *PRD*, 58, 063501
- Hopkinson, G., Dale, C., & Marshall, P. 1996, *IEEE Trans. Nucl. Sci.*, 43(2)
- Hu, W. 1999, *ApJ*, 506, 485
- Hu, W. 1999, private communication
- Hu, W. 1999, *ApJ*, 522, L21–L24
- Hu, W., & Eisenstein, D. 1999, *PRD*, 59, 083509
- Hu, W., & Tegmark, M. 1999, *ApJ*, 514, L65–L68
- Hu, W., Eisenstein, D., & Tegmark, M. 1999, *PRD*, 59, 023512
- Huey, G., et al. 1999, *PRD*, 59, 063005
- Hui, L. 1999, *ApJ*, 519, L9–L12

- Hunten, D. 1974. Part A: "Optical and Infrared. In *Methods of Experimental Physics: Astrophysics*, volume 12, Academic Press, New York
- Iwamuro, F., Maihara, T., Oya, S., Tsukamoto, H., Hall, D. N. B., Cowie, L. L., Tokunaga, A. T., & Pickles, A. J. 1994, *PASJ*, 46, 515–521
- Iye, M., Ebizuka, N., & Takami, H. 1998, *SPIE*, 3355, 417–423
- J. Mohr, B. M., & Evrard, A. 1999, *ApJ*, 517, 627
- Jain, B., et al. 1999, *astro-ph/9901191*
- Jain, B., & Seljak, U. 1997, *ApJ*, 484, 560+
- Janesick, J. 1997, *CCD Astronomy*
- Janesick, J., et al. 1991, *SPIE*, 1447, 87
- Janesick, J., Elliot, T., & Pool, F. 1989, *IEEE Trans. Nucl. Sci.*, **36**(1)
- Janesick, J., Elliot, T., Winzenread, R., Pinter, J., & Dyck, R. 1995, *SPIE*, 2415
- Jordon, P. R., Deltron, J.-M., & Oates, A. P. 1994, *SPIE*, 2198
- Kaiser, N. 1992, *ApJ*, 388, 272–286
- Kaiser, N. 1998, *ApJ*, 498, 26+
- Kaiser, N., Squires, G., & Broadhurst, T. 1995, *ApJ*, 449, 460+
- Kamasz, S., Farrier, M., & Smith, C. 1994, *SPIE*, 2172
- Kent, S. M. 1985, *PASP*, 97, 165–174
- Khokhlov, A. 1991a, *A&A*, 245, 114
- Khokhlov, A. 1991b, *A&A*, 245, L25
- Kim, A., et al. 2000, *ApJ*, in preparation
- Kirshner, R. P., & Kwan, J. 1974, *ApJ*, 193, 27
- Kobulnicky, H. A., & Zaritsky, D. 1999, *ApJ*, 511, 118–135
- Kochanek, C. S. 1996, *ApJ*, 466, 638+
- Korsch, D. 1980, *Appl. Opt.*, 19, 3640
- Kristian, J., & Sachs, R. K. 1966, *ApJ*, 143, 379+
- Landolt, A. U. 1983, *AJ*, 88, 439–460
- Landolt, A. U. 1992, *AJ*, 104, 340–371

- Lange, A. E., Ade, P. A. R., Bock, J. J., Bond, J. R., Borrill, J., Boscaleri, A., Coble, K., Crill, B. P., de Bernardis, P., Farese, P., Ferreira, P., Ganga, K., Giacometti, M., Hivon, E., Hristov, V. V., Iacoangeli, A., Jaffe, A. H., Martinis, L., Masi, S., Mauskopf, P. D., Melchiorri, A., Montroy, T., Netterfield, C. B., Pascale, E., Piacentini, F., Pogosyan, D., Prunet, S., Rao, S., Romeo, G., Ruhl, J. E., Scaramuzzi, F., & Sforza, D. 2000. "First Estimations of Cosmological Parameters From BOOMERANG". In 7 pages., pages 5004+
- Larkin, J., Quirrenback, A., & Graham, J. 2000. Image Slicing with Infrared Fibers. In *Imaging the Universe in Three Dimensions: Astrophysics with Advanced Multi-Wavelength Imaging Devices*, W. van Breugel and J. Bland-Hawthorn, editors, ASP Conference Proceedings
- Lauer, T. 1999a, *PASP*, 111, 1434–1443
- Lauer, T. R. 1999b, *PASP*, 111, 1434–1443
- Le Fevre, O. and the IFMOS Consortium 1999, ESA contract: 13003/98/NL/MS
- Le Louarn, M., Foy, R., Hubin, N., & Tallon, M. 1998, *MNRAS*, 295, 756–768
- Leibundgut, B. 1988. Ph.D. thesis, University of Basel
- Lentz, E., et al. 1999, astro-ph/9906016
- Lesser, M. P., & McCarthy, B. 1996, *SPIE*, 2654
- Link, R., & Pierce, M. J. 1998, *ApJ*, 502, 63+
- Lumb, D. 1990, *Nucl. Instrum.*, A288
- Lumb, D., Chowanietz, E., & Wells, A. 1987, *Optical Eng.*, 26
- Luppino, G. A., & Kaiser, N. 1997, *ApJ*, 475, 20+
- Maihara, T., Iwamuro, F., Yamashita, T., Hall, D. N. B., Cowie, L. L., Tokunaga, A. T., & Pickles, A. 1993, *PASP*, 105, 940–944
- Matz, S. M., McNaron-Brown, K., Grove, J. E., Share, G. H., Hurley, K., Costa, E., Feroci, M., Frontera, F., dal Fiume, D., & Orlandini, M. 1997, *IAU Circ.*, 6578, 1+
- McCann, D., et al. 1980, *SPIE*, 217
- McGraw, J., et al. 1982, *SPIE*, 331, 137
- Megessier, C. 1995, *A&A*, 296, 771+
- Meidinger, N., Struder, L., Soltau, H., & Zanthier, C. 1995, *IEEE Trans. Nucl. Sci.*, **42**(6)
- Melchiorri, A., et al. 1999, astro-ph/9911445

- Meszaros, P., & Rees, M. J. 1999, MNRAS, 306, L39–L43
- Metcalf, R., & Silk, J. 1998, ApJ, 492, L1
- Miller, J., et al. 1992, Lick Observatory Technical Report, 66
- Minkowski, R. 1939, ApJ, 89, 156
- Miralda-Escude, J. 1991, ApJ, 380, 1–8
- Mohr, J. 2000, Private communication
- Murphy, T. W., J., Matthews, K., & Soifer, B. T. 1999, PASP, 111, 1176–1184
- Newman, J., & Davis, M. 1999, astro-ph/9912366
- Nomoto, K., Thielemann, F., & Yokoi, K. 1984, ApJ, 286, 644
- Nugent, P. 1997. Ph.D. thesis, University of Oklahoma
- Nugent, P., et al. 1999, PASP, in preparation
- Nugent, P., Phillips, M., Baron, E., Branch, D., & Hauschildt, P. 1995a, ApJ, 455, L147
- Nugent, P., Branch, D., Baron, E., Fisher, A., Vaughan, T., & Hauschildt, P. 1995b, Phys. Rev. Lett., 75, 394
- Nugent, P., Baron, E., Branch, D., Fisher, A., & Hauschildt, P. 1997, ApJ, 485, 812
- Oke, J. B. 1974, ApJS, 27, 21+
- Oke, J. B., & Gunn, J. E. 1982, PASP, 94, 586+
- Oke, J. B., & Gunn, J. E. 1983, ApJ, 266, 713–717
- Oke, J. B., Cohen, J. G., Carr, M., Cromer, J., Dingizian, A., Harris, F. H., Labrecque, S., Lucinio, R., Schaal, W., Epps, H., & Miller, J. 1995, PASP, 107, 375+
- Oliva, E. 1999, astro-ph/9909108
- Oliva, E., & Origlia, L. 1992, A&A, 254, 466+
- Paczynski, B. 1986, ApJ, 308, L43–L46
- Paul, M. 1935, Rev. Optics, 14, 169
- Peckerar, M., McCann, D., & Yu, L. 1981, Appl. Phys. Lett., **39**(1)
- Perlmutter, S., et al. 1997, ApJ, 483
- Perlmutter, S., et al. 1998, Nature, 391
- Perlmutter, S., et al. 1999, ApJ, 517, 565

- Phillips, M. M. 1993, *ApJ*, 413, L105
- Ramsay, S. K., Mountain, C. M., & Geballe, T. R. 1992, *MNRAS*, 259, 751–760
- Ratnatunga, K. U., Griffiths, R. E., & Ostrander, E. J. 1999, *AJ*, 117, 2010–2023
- Ratra, B., & Peebles, P. 1987, *PRD*, 37, 3406
- Rhodes, J., Refregier, A., & Groth, E. 1999, *astro-ph/9905090*
- Richardson, E. H., Moore, A., Tillemann, T., & Crampton, D. 2000. Focusing Image Slicers: Refractive and Reflective. In *APS Conference Series: Imaging the Universe in Three Dimensions: Astrophysics with Advanced Multi-Wavelength Imaging Devices*, W. van Breugel and J. Bland-Hawthorn, editors
- Riess, A., et al. 1997, *AJ*, 114, 722
- Riess, A., et al. 1998, *AJ*, 116, 1009
- Riess, A., et al. 2000, *astro-ph/0001384*
- Riess, A. G., Press, W. H., & Kirshner, R. P. 1995, *ApJ*, 438, L17
- Riess, A. G., Press, W. H., & Kirshner, R. P. 1996, *ApJ*, 473, 88
- Sandage, A., & Tammann, G. 1995, *ApJ*, 452, 16
- Schlegel, D. J., Finkbeiner, D. P., & Davis, M. 1998, *ApJ*, 500, 525+
- Schmidt, B. P., et al. 1998, *ApJ*, 507, 46–63
- Schmidt, B. P., Kirshner, R., & Eastman, R. 1992, *ApJ*, 395, 366
- Schneider, P., Van Waerbeke, L., Jain, B., & Kruse, G. 1998, *MNRAS*, 296, 873–892
- Starkman, G., Trodden, M., & Vachaspati, T. 1999, *PRL*, 83, 1510
- Steinhardt, P., Wang, L., & Zlatev, I. 1999, *PRD*, 59, 123504
- Stover, R. 1999, private communication
- Stover, R., et al. 1997, *SPIE*, 3019, 183
- Stover, R., et al. 1998, *SPIE*, 3505
- Sze, S. M. 1981. *Physics of Semiconductor Devices*, Wiley
- Szomoru, A., & Guhathakurta, P. 1999, *AJ*, 117, 2226–2243
- Tegmark, M., Taylor, A., & Heavens, A. 1997, *ApJ*, 480, 22
- Thuan, T. X., & Gunn, J. E. 1976, *PASP*, 88, 543–547
- Trimble, V. 1987, *ARAA*, 25, 425

- Tsoi, H. 1985, *IEEE Trans. Elec. Dev.*, **32**(8)
- Turner, E. L., Ostriker, J. P., & Gott, J. R., I. 1984, *ApJ*, 284, 1–22
- Turner, M. 1999, *Physica Scripta* (in press)
- Tyson, J. A., Wenk, R. A., & Valdes, F. 1990, *ApJ*, 349, L1–L4
- Tyson, J. A., Kochanski, G. P., & Dell’Antonio, I. P. 1998, *ApJ*, 498, L107–+
- Umeda, H., et al. 1999, *ApJ*, 513, 861
- Umeda, H., Nomoto, K., Kobayashi, C., Hachisu, I., & Kato, M. 1999, *ApJ*, 522, L43–L47
- Valdes, F., Jarvis, J. F., & Tyson, J. A. 1983, *ApJ*, 271, 431–441
- van Paradijs, J., et al. 1997, *Nature*, 386, 686–689
- Van Waerbeke, L., Bernardeau, F., & Mellier, Y. 1999, *A&A*, 342, 15–33
- Vaughan, T. E., Branch, D., Miller, D. L., & Perlmutter, S. 1995, *ApJ*, 439, 558
- Viana, P. T. P., & Liddle, A. R. 1999, *MNRAS*, 303, 535–545
- Vilenkin, A. 1984, *PRL*, 53, 1016
- Vilenkin, A., & Shellard, E. 1994. *Cosmic strings and other topological defects*, Cambridge University Press
- von Ammon, W., & Herzer, H. 1984, *Nucl. Instrum. Meth.*, A226
- Wade, R. A., Hoessel, J. G., Elias, J. H., & Huchra, J. P. 1979, *PASP*, 91, 35–40
- Walker, M. A. 1999, *MNRAS*, 306, 504–508
- Wang, L. 1999, private communication
- Weinberg, S. 1989, *RMP*, 61, 1
- White, M. 1998, *ApJ*, 506, 495
- Williams, R. E., et al. 1996, *AJ*, 112, 1335
- Williams, S. G. 1979, *Proc. Soc. Photo-Opt. Instrum. Eng.*, 183, 212
- Willstrop, R. V. 1984, *MNRAS*, 210, 597
- Woosley, S. E. 1991. In *Gamma-Ray Line Astrophysics*, P. Durouchoux and N. Prantzos, editors, New York: AIP, page 270
- Woosley, S. E. 1993, *ApJ*, 405, 273–277
- Yamashita, et al. 1997, *IEEE Trans. Nucl. Sci.*, **44**(3)
- Zlatev, I., Wang, L., & Steinhardt, P. 1999, *PRL*, 82, 896
- Zwicky, F. 1937, *Helv. Phys. Acta*, 6, 110

Part VI

Appendix

Appendix A

WBS

1. INSTRUMENT SYSTEMS

- (a) INSTRUMENTS
 - i. IMAGER
 - ii. SPECTROGRAPH
 - iii. INSTRUMENT CALIBRATION
- (b) INSTRUMENT ELECTRONICS
 - i. READOUT ELECTRONICS
 - ii. DATA HANDLING
 - iii. CRATES & POWER MANAGEMENT
 - iv. CONTROLS & STATUS SENSORS
- (c) INTEGRATION & TEST
- (d) GROUND SUPPORT EQUIPMENT
- (e) SUBPROJECT MGM'T & SYS ENG

2. TELESCOPE

- (a) OPTICS
 - i. PRIMARY
 - ii. SECONDARY, ETC.
- (b) STRUCTURE
 - i. METERING STRUCTURE
 - ii. SUN SHIELD & PM BAFFLES
 - iii. M & TM SHIELDS & BAFFLES
- (c) OPTICAL BENCH ASSY
 - i. OPTICAL BENCH
 - ii. FAST STEERING SYSTEM
 - iii. MATCHING OPTICS

- iv. SPLITTERS
 - v. FILTER WHEELS
 - (d) INTEGRATION & TEST
 - (e) GROUND SUPPORT EQUIPMENT
 - (f) SUBPROJECT MANAGEMENT & SYS ENG
- 3. SPACECRAFT
 - (a) ATTITUDE CONTROL
 - (b) PROPULSION
 - (c) MECHANICAL
 - (d) POWER
 - (e) COMMUNICATIONS
 - (f) THERMAL
 - (g) COMPUTING & DATA HANDLING
 - (h) INTEGRATION & TEST
 - (i) GROUND SUPPORT EQUIPMENT
 - (j) SUB-PROJ. MGM'T & SYS ENG
- 4. LAUNCH VEHICLE
 - (a) PROCUREMENT
 - (b) LAUNCH SERVICES
- 5. MISSION INTEGRATION & TEST
 - (a) INSTRUMENT TO TELESCOPE I&T
 - (b) INSTR/TELESCOPE TO SPACECRAFT BUS I&T
 - (c) PAYLOAD TO LAUNCH VEHICLE I&T
- 6. MISSION OPERATIONS CENTER
 - (a) MISSION OPERATIONS CENTER DEVELOPMENT
 - (b) GROUND ANTENNA DEVELOPMENT
 - (c) REPARATION FOR DATA HANDLING/SOC
- 7. OPERATIONS
 - (a) LAUNCH & EARLY ORBIT SUPPORT(30 Days)
 - (b) POST-LAUNCH SUPPORT
 - (c) FACILITY MAINTENANCE
 - (d) SOFTWARE MAINTENANCE

- (e) PERSONNEL TRAINING
- (f) INSTRUMENT TROUBLE SHOOTING/REPAIR
- (g) MISSION GROUND STATION OPERATIONS
- 8. SPECIAL STUDIES
- 9. SCIENCE TEAM
 - (a) SCIENCE REQUIREMENTS DEVELOPMENT
 - (b) IMPLEMENTATION
 - (c) DATA ANALYSIS
 - (d) EDUCATION & PUBLIC OUTREACH
- 10. PROGRAM MANAGEMENT
 - (a) TECHNICAL
 - (b) PLANNING
 - (c) TRACKING
 - (d) SUBCONTRACTING & PROCUREMENT
 - (e) DOCUMENT CONTROL
 - (f) PERFORMANCE/QUALITY ASSURANCE
 - i. CALIBRATION
 - (g) ES&H
 - i. INSTRUMENT & TELESCOPE EH&S PROGRAM
 - ii. GLOBAL SPACECRAFT EH&S PROGRAM
 - iii. ORBITAL DEBRIS ASSESSMENT
 - (h) SUPPLIES & EQUIPMENT
 - (i) REVIEWS, MEETINGS & TRAVEL
 - (j) BUDGET RESERVE/CONTINGENCY
 - (k) CONFIGURATION CONTROL BOARD
- 11. SYSTEMS ENGINEERING
 - (a) REQUIREMENTS DEVELOPMENT & CONTROL
 - (b) CONFIGURATION & INTERFACE CONTROL
 - (c) TRADE STUDIES
 - (d) SYSTEM ANALYSIS
 - (e) MATERIALS & PROCESS CONTAMINATION CONTROL
 - (f) SYSTEMS QUALIFICATION
 - (g) INTEGRATION & LOGISTICS

Appendix B

Fully Depleted High Resistivity CCDs

B.1 Overview

A key technological innovation in the SNAP instrumentation is a large one billion pixel camera. In order to maximize the sensitivity of SNAP to discover high red-shift supernova ($z < 1.7$) this camera requires excellent sensitivity in the I or Z optical bands. Consequently, we have assumed in the baseline design the use in this camera of a new kind of CCD with excellent I and Z-band sensitivity.

We have successfully developed a new type of large-format CCD's on n-type high-resistivity silicon. The back-illuminated CCD's are fabricated on 300 μm thick silicon substrates. The substrate is fully depleted by the application of an independent voltage through an optically transparent backside contact. Multiple science-grade $2\text{k} \times 2\text{k}$ pixel ($15 \mu\text{m}^2$ pixels) CCD's have been fabricated and tested (Fig. B.1). Furthermore, devices on these wafers have shown excellent charge transfer efficiency (> 0.999995), read noise of $4.3 e^-$, dark current of $0.003 e^-/\text{pixel/s}$, and a well depth of $300,000 e^-$ ($15 \mu\text{m}^2$ pixels). With back illumination, the QE at 1000 nm is 65% ($T = 150^\circ\text{K}$). As shown in Fig. B.2, commercially available CCD's with proper coatings reach 15% or less at 1000 nm at this temperature. This is a major achievement in the development of n-type high-resistivity CCD's (Holland et al., 1996; Stover et al., 1997; Holland et al., 1997).

Early measurements indicate that as expected [J. Janesick, private communication] this technology results in significantly improved radiation tolerance of the CCD. For long duration missions this could prove to be a major benefit. Since devices do not need to be thinned, the CCD's are self-supporting and four-side buttable (with back-illumination thinned devices require an underlying mechanical support that interferes with traditional wire bonding). Consequently, the new CCD's are ideal for a wide-field mosaic array. A space-based wide-field imager taking advantage of the 4-side abutment would require much smaller pixel sizes than ground based telescopes for reasonable cost and weight of the optics. In this context, we currently have in fabrication large-format, smaller pixel size (10.5 and 12 μm) devices, and we are exploring light weight four-side

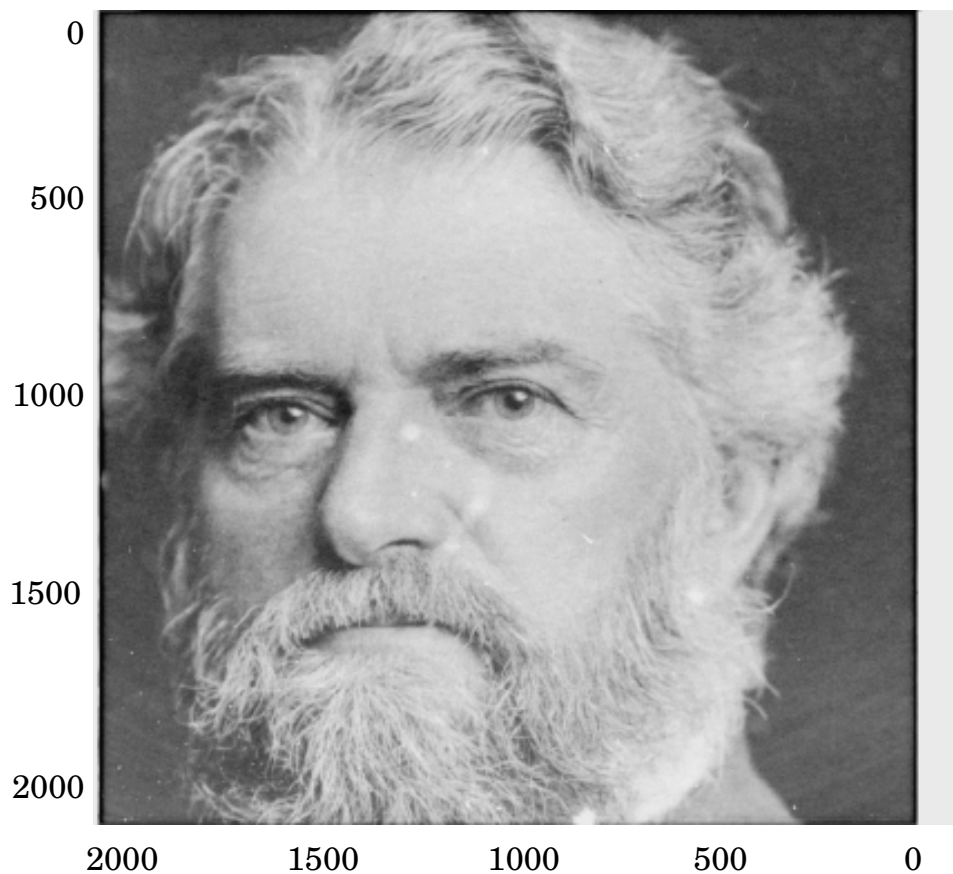


Figure B.1: Raw test image obtained at Lick Observatory of a back-illuminated $2k \times 2k$ ($15 \mu\text{m}^2$ -pixel) UCB high-resistivity CCD. The chip is cosmetically and electrically perfect. A 20V bias voltage transports the charge from the rear surface through the fully-depleted substrate to the CCD potential wells on the front surface. The substrate is $300 \mu\text{m}$ thick. Parallel CTE is 0.999998 and serial CTE is 0.999999, well depth is $300,000 e^-$, and the read noise is $4.3 e^-$.

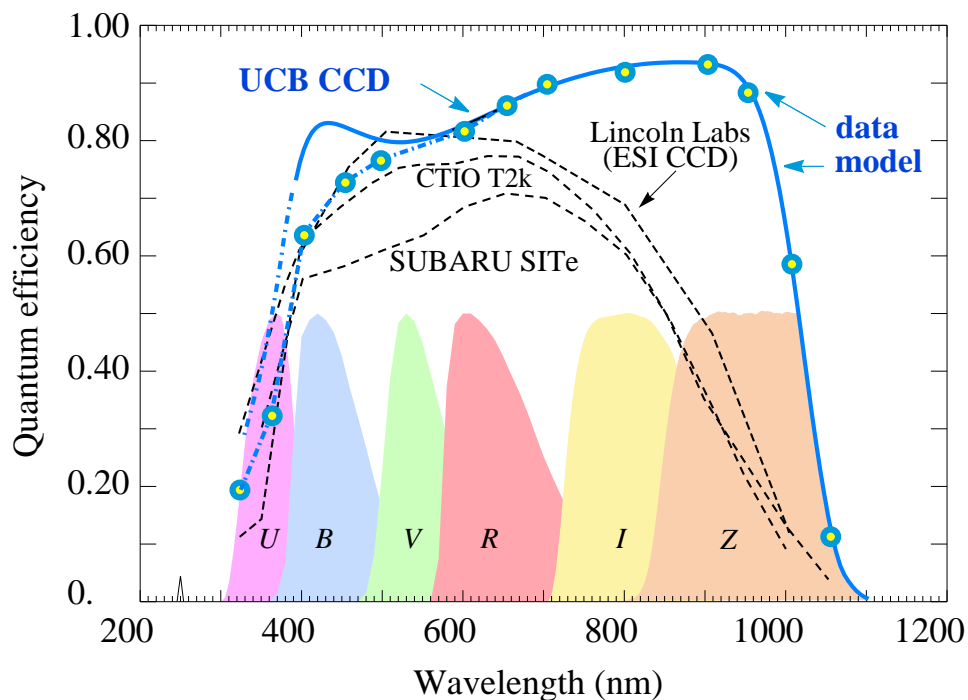


Figure B.2: Measured response of the UCB “fully-depleted” CCD at -100°C (open circles) for an unoptimized two-layer AR coating (the dark curve through the points is a model calculation). Response is expected to be significantly higher for optimized AR coatings. For comparison, measured response of the $2\text{k} \times 4\text{k}$ “deep-depletion” back-illuminated MIT/Lincoln chip on Keck ESI is shown, as are measurements for two different SITe CCD’s on SUBARU and CTIO. Relative spectral responses of standard wide-band filters are shown.

abutment packaging technologies.

This technology is currently being transferred to a commercial vendor, Mitel Corp, Bromont Canada. Mitel is currently in the middle of two simultaneous processing runs that will evaluate the process at their foundry. The two runs consist of 1) an adaptation of the UCB process recipe for the Mitel process equipment that is fairly true to the original recipe, and 2) a version that is highly optimized for the standard Mitel CCD process flow and would produce the devices at higher volume. This is the second vendor that has taken this process over for device fabrication. The first vendor Digirad, has now been successfully using the process for the manufacture of photodiode arrays. From this experience we would expect Mitel to be able to manufacture CCD's in volume to our specification in approximately twelve to eighteen months. This time is needed to optimize furnace recipes, validate process steps and characterize intermediate devices. If funds were available this time period could be greatly accelerated as the development work is currently paced by funding.

UCB is also engaged in further in house fabrication runs. Now that the process steps have been completed for fabrication, development of specific science devices is underway. Currently, we have devices in use or about to be in use at Lick Observatory and we have a $2k \times 4k$ pixel device in fabrication for the ESI spectrograph at Keck Observatory. With the completion of the process development we have hired a process technician to help us with regular manufacture. The time expected now to process a lot (25 wafers) is 6 months. To date we have been able to obtain one science grade large format device per wafer.

Were SNAP to proceed into an R&D phase we would very seriously consider other options available to mitigate the technical risk present in the new technology for the imager. For slightly higher cost and lower performance we would seriously consider EEV or Sarnoff deep-depletion devices. These thinned devices, when back-illuminated and placed over a mirrored surface (effectively doubling the apparent thickness) can achieve 30% quantum efficiency at 1000 nm ($T = 150^\circ\text{K}$). Design of the imager would proceed such that these devices could be substituted if necessary.

B.2 Benefits and Goals

Although the UCB CCD's use a normal three-phase gate structure, the CCD's differ dramatically from the thinned CCD's currently used in astronomy. They are made on float-zone refined high-resistivity ($\sim 10,000 \ \Omega\text{-cm}$) n-type silicon $300 \ \mu\text{m}$ thick. Holes, rather than electrons, are collected in the potential wells. An indium-tin oxide coating on the back surface provides three functions: (a) as a contact to which an up to $\gtrsim 80 \ \text{V}$ bias is applied to deplete the substrate completely, so that photo-generated charge from the whole volume is collected, (b) as a transparent window, permitting back illumination for normal operation, and (c) as part of the back-surface anti-reflective (AR) coating. The photo-produced charge from near the back surface is then collected in the potential wells. Since the devices are thick, they exhibit excellent quantum efficiency, as shown in Fig. B.2, until just below the silicon bandgap at 1050 nm, and at the same time interference "fringing" is completely absent.

Since blue light is strongly absorbed in the gate structure of any front-illuminated CCD, the CCD's used in astronomy are usually thinned and back-illuminated. For most devices (with a 20 μm thick 10 to 50 $\Omega\text{-cm}$ epitaxial layer), this means thinning to about 20 μm . The thinning results in transparency in the red, resulting in a loss of quantum efficiency (QE) and "fringing" due to multiple reflections. For the UCB devices this expensive, time-consuming, and low-yield thinning process is both unnecessary and undesirable. Advantages of the novel UCB CCD's include:

- a. High quantum efficiency (QE) up to wavelengths approaching the silicon bandgap at just above 1050 nm, where silicon becomes transparent.
- b. Absence of fringing. The interference patterns that are present in thinned spectroscopic CCD's are completely absent in these thick devices.
- c. Good blue response without special processing and without UV flooding. A normal CCD exhibits field inversion near the back surface, resulting in the loss of QE for blue light, where the absorption length is very short. A variety of methods have been invented to avoid this problem. Since holes, rather than electrons, are collected in the UCB CCD's, the problem does not exist and the fully-depleted substrate has no field-free region.
- d. The very low concentrations of phosphorus and oxygen in the n-type high-resistivity device result in excellent radiation tolerance. Preliminary measurements at the 88" cyclotron indicate that these devices have superior tolerance compared to previous CCD technologies.
- e. Exceptionally large well-depth of 300,000 e^- (15 μm^2 pixels) with low noise readout can be traded-off for smaller pixel sizes.
- f. Capitalizing on the device thickness, the CCD's can be readily packaged for four-side abutment with standard wire bonding techniques enabling the manufacture of very large mosaic arrays.
- g. The new CCD's can be manufactured at low cost in a traditional CCD foundry. Since no thinning is required, the overall cost will be significantly less than conventional thinned devices.

B.3 Uniqueness of Fully-Depletion Devices

To overcome a variety of technical problems high-performance CCD's for astronomy are obtained by "thinning" conventional CCD's (where the active region is a thin 30–50 Ωcm epitaxial layer grown on a lower-resistivity p-type substrate), leaving only the epitaxial layer and gate circuitry. After back-surface preparation they are used with back illumination. There are severe cost, quality, and availability problems associated with the process. For example, a defect-free 2048×2048 pixel CCD in a modern mosaic camera costs approximately \$50,000, about an order of magnitude higher than the cost of the CCD as it leaves the foundry (Janesick, 1997).

All of these problems are avoided by the full-depletion technology, in which the final CCD emerges directly from the MOS foundry. There are additional gains: high blue sensitivity is achieved with standard technologies, therefore easing the transfer of the technology to a commercial foundry. These CCD's are more radiation resistant

than standard CCD's because boron, rather than phosphorus, is used for doping, and because the high-resistivity substrate contains comparatively little oxygen. Because they are thick, red sensitivity is extended to near the bandgap cutoff at 1050 nm ($T = 150^\circ\text{K}$) (Sze, 1981). No other MOS CCD process offers these improvements.

These "fully-depleted" 300 μm thick high-resistivity MOS CCD's exhibit significantly improved performance over existing "deep-depletion" CCD's which still require thinning to 40–50 μm for good performance and are technically quite different.

Full depletion of a standard low-resistivity silicon substrate is not technically feasible, so the technical developments for expanding the wavelength sensitivity of scientific CCD's have focussed on high-resistivity substrates. Unique among MOS CCD developers is the use at UCB of a lightly doped high-resistivity n-type silicon substrate. The community of developers of MOS CCD's on high-resistivity silicon is small, limited to UCB, Sarnoff Laboratory, MIT/Lincoln Laboratory (Burke et al., 1997, 1994, 1991), and EEV Ltd (Heyes, Pool, & Holton, 1997; Holland, 1997, 1996; Lumb, 1990; Lumb, Chwanietz, & Wells, 1987).

The MOS CCD's developed at MIT/Lincoln Laboratory, Sarnoff Laboratory, and EEV Ltd. are of the "deep-depletion" type. In these devices partial depletion of the substrate is achieved to depths of typically 40–80 μm through the potential applied at the charge transfer gates. The devices must still be thinned to 40–50 μm in order to eliminate the field-free region between the depletion layer and the backside (Burke et al., 1997; Heyes, Pool, & Holton, 1997). Thinning unfortunately undermines the long wavelength sensitivity and introduces large amplitude interference fringes at long wavelengths. The need to apply the depletion potential at the charge-transfer gate makes these devices harder to optimize.

In contrast, the UCB "fully-depleted" CCD utilizes conventional MOS technology. This implies that technology transfer to any of a number of CCD manufacturers is possible without the need for customized fabrication equipment to handle the double-sided lithography. The major difference for wafers used by UCB compared to industry standard wafers is the thickness (300 μm versus industry standard 550 μm for 4 inch diameter). However, we have shown that conventional lithography tools used in CCD manufacturing can operate with both wafer thicknesses (demonstrated on both 1:1 scanners and 5:1 steppers) and our expected commercial partner has already agreed to work with the 300 μm thick substrates. The "fully-depleted" thick MOS CCD's will in the future be inexpensive to manufacture due to the lack of thinning and backside lithography.

B.4 Comparison of CCD's

The CCD design dilemma is summarized in Fig. B.3. At the atmospheric cutoff at the blue end ($\lambda \equiv 320$ nm), the absorption length of light in silicon is about 10 nm. It is four orders of magnitude larger, or 100 μm , at $\lambda = 1000$ nm. The problem at the blue end is to collect electrons (or holes, in the case of this work) produced very near the entrance window. At the red end, quantum efficiency (QE) decreases as the device becomes transparent. In the case of a thinned device, the loss of QE is accompanied

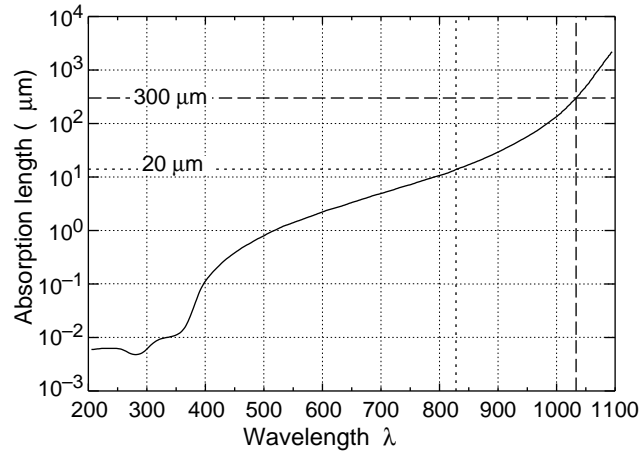


Figure B.3: Absorption length of light in silicon (solid curve). Except at wavelengths approaching the bandgap cutoff at $\lambda_b \approx 1100$ nm, essentially all absorbed photons produce e-h pairs. The sensitive region of a conventional CCD is the ≈ 20 μm -thick epitaxial layer, indicated by the dotted line, while in the UCB high-resistivity CCD's the fully-depleted 300 μm substrate is active (dashed line).

by the production of interference fringes due to multiple reflections. Typical QEs for astronomical CCD's are shown in Fig. B.2, along with the predicted QE for the UCB CCD with a two-layer AR coating.

The “fully-depleted” thick CCD's have a wider range of wavelength sensitivity than backside illuminated conventional CCD's or “deep-depletion” CCD's, including improved blue response due to the optical contact, and significantly better IR response. The best MIT/Lincoln Laboratory “deep-depletion” CCD is measured to have 16% quantum efficiency at 1000 nm (Stover, 1999, private communication) whereas our devices have a 65% quantum efficiency at 1000 nm and $T = 150^\circ\text{K}$.

In Table B.1 the characteristics of UCB CCD's are given along with the performance characteristics of other competitive devices. One favored substitute for CCD's in the near-IR region are HgCdTe active pixel devices. A HgCdTe array is grown on a sapphire substrate, illuminated through the sapphire, and indium bump-bonded to silicon readout chips. Charge transfer efficiency (CTE), quantum efficiency (QE) as a function of wavelength, noise, and full well capacity, have been characterized on the $2k \times 2k$ prototypes. The CCD's were characterized in detail at the Lick Observatory CCD Laboratory. Measured serial and vertical CTEs were 0.999999 and 0.999998, respectively. Fig. B.4 shows a test pattern imaged by a back-illuminated $2k \times 2k$ CCD tested. Excellent CTE was also measured on an 1100×800 CCD. (Holland et al., 1996; Stover et al., 1997; Holland et al., 1997; Stover et al., 1998)

Astronomical images using a 200×200 pixel back-illuminated high-resistivity CCD fabricated at UCB were first obtained on 1996 Dec 4. In a test at the Lick Observatory 1 m telescope, a heavily obscured region of the Orion Nebula was imaged using an R filter, which has maximum transmission near 600 nm, and a narrow bandpass 1000 nm

Characteristic	UCB measured	UCB future	Typical CCD [‡]	MIT/Lincoln*	HgCdTe [†]
Typical format	2k×2k	2k×4k	2k×2k	2k×4k	2k×2k
Pixel size	15μm×15μm	8μm×8μm	15μm×15μm	15μm×15μm	18μm×18μm
Operating Temp.	150K	150K	150K	150K	78K
CTE	> 0.999995	> 0.999995	> 0.999995	> 0.999995	—
Read noise	4.3 <i>e</i>	2 <i>e</i>	3–6 <i>e</i>	2–4 <i>e</i>	4 <i>e</i>
Dark current	0.18 <i>e</i> /m/pix	0.05 <i>e</i> /m/pix	0.03 <i>e</i> /m/pix	0.03 <i>e</i> /m/pix	1 <i>e</i> /m/pix
Full-well (<i>e</i> 's)	300 k	100k	150k (non-MPP)	105k	90k
Fringing @ 800 nm	0%	0%	9%	9%	—
Fringing @ 900 nm	0%	0%	22%	22%	—
Fringing @ 1000 nm	< 2%	< 2%	46%	46%	—
QE @ 900 nm [◊]	92%	92%	38%	47%	—
QE @ 1000 nm [◊]	65%	65%	5–10%	11%	56%
QE Variation @ 350 nm 0% **		0% **	45%	45%	—
QE Variation @ 500 nm 0% **		0% **	2%	2%	—
Cost	—	10K	50-100K	—	300K

UCB 2k×2k CCD's measured at UCO/Lick, expected performance taken from Groom et al. (1999).

[‡] Thinned CCD, <http://sauron.as.arizona.edu/ccdlab/>

* <http://gardiner.ucolick.org:80/~ccdev/lincoln>

[†] Hawaii-2 array prospects/cost as reported by K. Hodapp (priv. comm.), QE is from Hawaii-1 array

[◊] At cold temperatures ($T = 150^\circ\text{K}$) where QE drops due to bandgap widening Lesser & McCarthy (1996).

** expected

Table B.1: UCB $2k \times 2k$ ($15 \mu\text{m}$)² CCD's as compared with other detectors.

filter obtained especially for these tests. The examples shown in Fig. B.5 show stars obscured at 600 nm but which are visible at 1000 nm. When scaled by the respective bandpasses the counting rates indicate comperable quantum efficiencies at the two wavelengths. To the best of our knowledge, this is the first demonstration of high-QE imaging at 1000 nm with a CCD.

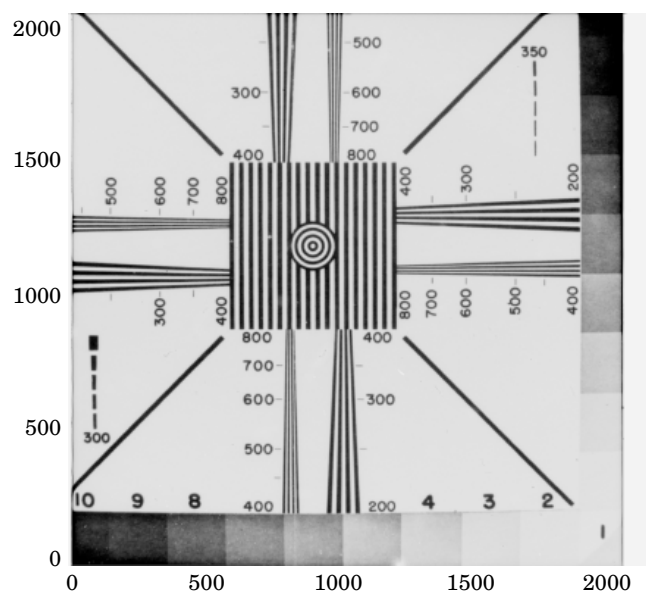


Figure B.4: Back-Illuminated test pattern imaged a back-illuminated $2k \times 2k$ UCB high-resistivity CCD tested at Lick Observatory. The CCD is cosmetically perfect.

B.5 Technical features of high-resistivity CCD's

Fig. B.6 shows the basic concept for the back-illuminated, fully-depleted CCD. A conventional three-phase, buried-channel CCD is fabricated on a high-resistivity silicon substrate of nominal thickness $300 \mu\text{m}$. A bias voltage is applied to the backside contact in order to fully deplete the $300 \mu\text{m}$ thick substrate. This contact is also the illumination entrance window. An antireflective coating is added to maximize transmission over the extended optical region.

The use of a high-resistivity substrate permits fully depleted operation at reasonable bias voltages. The effect of the bias voltage is to remove the mobile electrons resulting from the extremely small number of dopant atoms (phosphorus) in the high-resistivity silicon. The resistivity, $\approx 10,000 \Omega\text{-cm}$, corresponds to a doping density in the mid- 10^{11} cm^{-3} range, about four orders of magnitude smaller than in conventional CCD's. The substrate thickness used here, $300 \mu\text{m}$, is significantly thicker than previous conventional, deep-depletion CCD's with typically $40\text{-}80 \mu\text{m}$ thick depletion regions (Burke et al., 1997, 1994, 1991; Heyes, Pool, & Holton, 1997; Holland, 1997, 1996; Lumb, 1990; Lumb, Chowaniec, & Wells, 1987; Kamasz, Farrier, & Smith, 1994;

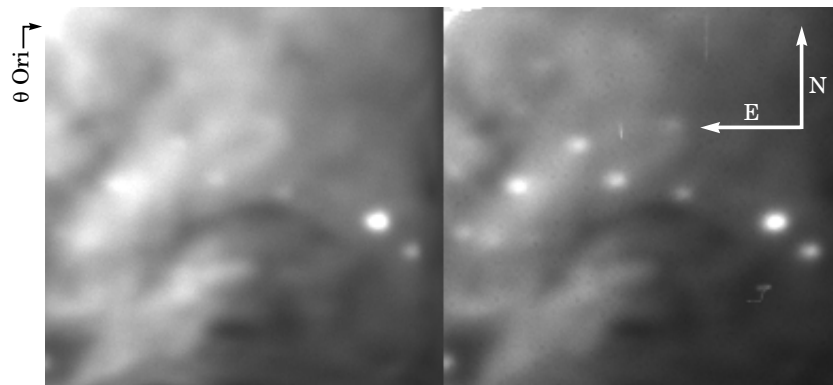


Figure B.5: Lick test CCD images of a heavily obscured region in the Orion Nebula, observed under poor conditions on 1996 Dec 4 with the Lick Observatory 1-m telescope on Mt. Hamilton. The left image was a 50 s exposure with a Harris R filter, with a peak transmission at 600 nm and a FWHM of 120 nm. The right image was a 100 s exposure through a special filter with maximum transmission at 1000 nm and FWHM 88 nm. Each field is about 57 arc-sec squared.

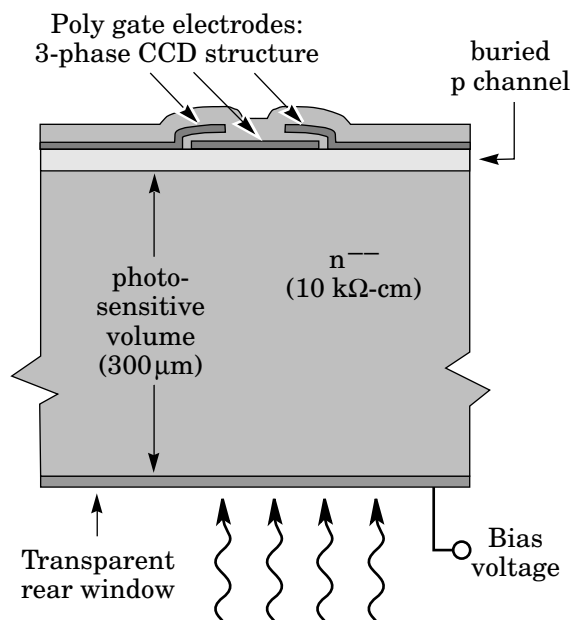


Figure B.6: Cross-section of the back-illuminated, fully-depleted CCD. A conventional buried channel CCD is fabricated on a high-resistivity silicon substrate. A bias voltage applied to the backside contact results in full depletion of the substrate.

Tsoi, 1985).

The removal of the mobile electrons from the substrate results in an electric field

due to the dopant atoms that are now ionized and positively charged. This electric field extends essentially all the way to the backside contact, hence the term full depletion. This element is key to the proper operation of the back illuminated CCD. Short wavelength light is absorbed very near the backside contact. In order to minimize the loss of spatial resolution due to thermal diffusion, it is important that the photo-generated charge be directed towards the CCD buried channels by an electric field.

In order to realize the benefits of such a CCD, several technical challenges needed to be overcome. One concern was maintaining low dark currents with a substantially thicker depletion region as compared to thinned CCD's. A technique for processing high-resistivity silicon while maintaining low dark currents had been previously developed for high-energy physics detectors (Holland, 1989), and this active gettering technique was also used for the CCD fabrication. It consists of the deposition of a phosphorus-doped, backside polycrystalline silicon layer which getters harmful impurities during the fabrication process. High dark currents were a significant problem with initial attempts to develop CCD's on high-resistivity substrates (McCann et al., 1980; Peckerar, McCann, & Yu, 1981).

Another significant challenge was the development of a transparent back-side window that allows transmission of short-wavelength light and application of the bias voltage necessary for full depletion of the substrate. A backside window consisting of a thin layer of in-situ doped polysilicon with an indium-tin oxide antireflection coating was developed (Holland et al., 1996; Holland, Wang, & Moses, 1997).

B.6 Radiation Tolerance

Radiation damage is relevant to space applications. J. Janesick has been pointed out (private communication) that the major bulk damage effect due to space protons, for example, is the generation of trapping states due to formation of phosphorus-vacancy centers (Janesick et al., 1991; Janesick, Elliot, & Pool, 1989; Yamashita et al., 1997; Holmes-Siedle, Holland, & Watts, 1996; Hopkinson, Dale, & Marshall, 1996). This defect results in hot pixels (high dark current) and degrades CTE. Typical CCD's have phosphorus implanted channels, with peak phosphorus concentrations in the low 10^{16} cm^{-3} range (Janesick et al., 1995). Our p-channel CCD has a boron implanted channel, and the background phosphorus concentration is extremely small in the high-resistivity substrate (in the low 10^{11} cm^{-3} range). Therefore it is expected that P-V centers will not limit radiation hardness, but instead oxygen-related defects as observed by Meidinger et al. (1995). High-resistivity silicon has significantly reduced oxygen levels as well (von Ammon & Herzer, 1984). The type of CCD under development here should have significantly improved radiation hardness when compared to conventional CCD's. A 200×200 prototype has been irradiated at the LBNL 88" cyclotron with 55 Mev protons to a fluence of $1 \times 10^9 \text{ cm}^{-2}$. The equivalent 10 Mev fluence was $5 \times 10^8 \text{ cm}^{-2}$, and the CTE degradation was below the level of detection 2×10^{-6} . This limit is already is a factor of ten less than that reported in the literature for CCD's on p-type silicon with the same dose (Holland et al., 1991).

Detailed radiation hardness studies will require use of the LBNL 88" 55 MeV proton

cyclotron to make systematic studies of dark current and CTE as a function of proton fluences.

The Non-Ionizing energy loss (NIEL) for 55 MeV protons at $1 \times 10^9 p/cm^2$ that the CCD has been tested to is 3.7×10^6 MeV/g. For the SNAP mission, if we assume a 3 year mission during solar maximum outside the earth's geomagnetic field, the NIEL behind a nominal 1" of aluminum shielding is 1.85×10^7 MeV/g – a factor of 5 higher than what the device has been tested to.

If we assume the mission runs during solar minimum, then the current models would predict no coronal mass ejections and thus, no solar proton damage. Computing the NIEL for the cosmic ray protons for a 3 year period gives 6.7×10^5 MeV/g – much lower than what the device has been tested to. Clearly, a flight during solar minimum is best from a total radiation damage point of view.

High CTE is essential for such large area devices, and several design and process techniques have been implemented in the current mask set in order to enhance CTE in a radiation environment (not present in the previous radiation tests). The channel implant region, where the charge carriers reside, is slightly offset from the channel stop region in order to avoid possible trapping sites at the channel to channel stop interface (Janesick et al., 1995). The serial register is wider than the imaging channel in order to allow for on-chip binning with large full well capacity. However, this results in a larger volume for charge trapping in the serial register. A second implant, 3 μm wide, is included in the serial register in order to improve CTE, especially for small signals (Bredthauer et al., 1991).

B.7 Cosmic Rays

Fully-depleted CCD's have an increased sensitivity to cosmic rays due to the thicker active region so that a passing particle will leave a longer trail of particles in the detector eventually destroying any accumulated optical image. This phenomena is well known in previous and current space flights and we are currently beginning to receive excellent data from Chandra on the performance of the "deep-depletion" devices, particularly numerical values of the cosmic ray fluence. This can be used for engineering numbers in determining our expectation for CCD's in SNAP.

Our current best estimate for the worst case cosmic ray fluence in high earth orbit (assumes 0.1" aluminum shielding) is 4.4 protons/cm²/s at solar min (drops to 1.5 protons/cm²/s at solar max). This flux of protons, shown in Figure B.7, peaks around 300 MeV and is consequently difficult to shield further.

Solar Condition	Al Shielding	Integrated Flux/cm ² /s
Maximum	None	1.7
Maximum	100 mil	1.6
Maximum	1 inch	1.5
Minimum	None	4.7
Minimum	100 mil	4.4
Minimum	1 inch	4.2

Table B.2: Lunar-assist orbit cosmic ray hit rate.

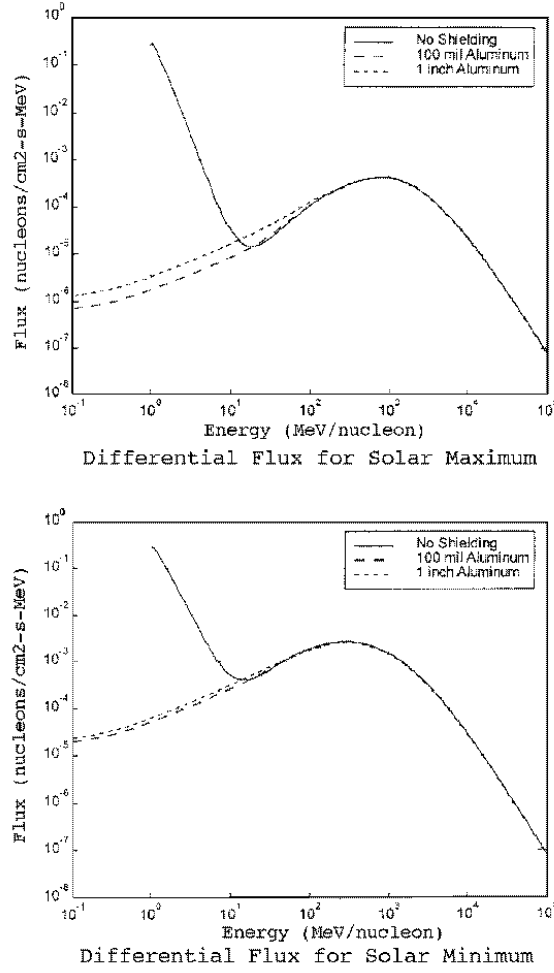


Figure B.7: Differential proton flux in high earth orbit for solar maximum and solar minimum for different shielding thicknesses calculated using CREME96.

With a typical 45 pixels/particle contaminated by the passage of the ionizing trail in a CCD with $10.5 \mu\text{m}$ pixels, then 10% of the image will be contaminated after a 500 second exposure. This calculation is consistent with the assumptions used for NGST. This level of contamination is acceptable and we assume that multiple images of the same region of space must be taken in order to obtain a single “clean” image. The methods for removing cosmic ray signatures from images are well known.

B.8 Packaging with 4-side Abutment

For a normal thinned CCD, pad contacts are etched through the wafer and are available at the back surface. The packaging normally includes a circuit board which substantially extends the dimensions on any CCD edge with pads. External wiring is attached to this board, as are the wire-bond connections to the CCD. Thus if a CCD mosaic is extended in the direction of any pad-containing edge, close abutment along this direction is impossible and the wiring obstructs light. These problems are normally dealt with by (a) making the connections on only two of the four sides and achieving two-side abutment; (b) using rectangular 3-side abutable CCD's with all the connection pads on the narrow end, so that the array is two CCD lengths wide and four or more wide; or (c) allowing wide gaps between the CCD's, as is done in the Sloan Digital Survey mosaic.

For our thick, totally-depleted CCD's, back surface access to the pads is out of the question. In a packaging scheme under consideration, the edges cantilever from a 3-layer aluminum oxide structure. The first is a thin insulating layer cemented to the front of the CCD. The second is a ceramic circuit board with edge pads to which the CCD pads are wire-bonded. The traces go to a center miniature connector through which wiring is brought out perpendicular to the CCD package and through the cold plate. The third layer is an additional insulator which also captures three indexing pins. Screw-on extensions facilitate installation and removal without hitting adjacent CCD's. Four-side abutability and a certain amount of assembly jigging is therefore automatic. This scheme is shown in Fig. B.8.

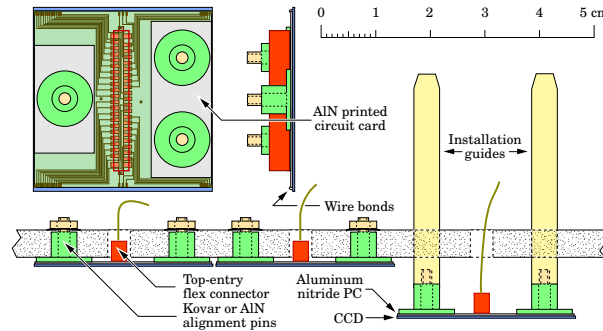


Figure B.8: Conceptual design for “fully-depleted” CCD packaging. The CCD is cemented to a three-layer aluminum oxide substrate. The middle layer is a circuit board to which the cantilevered CCD pads are wire-bonded. Connections exit through the cold plate via a miniature connector in the center of the board. The third layer provides insulation and captures three indexing and mounting pins